Investigation of Jitter on Full-Field Amplitude Modulated Continuous Wave Time-of-Flight Range Imaging Cameras

A thesis submitted in fulfilment
of the requirements for the degree of

Doctor of Philosophy

in Electronics

by

Gehan Anthonys

THE UNIVERSITY OF
WAIKATO
Te Whare Wānanga o Waikato

2021

Abstract

The time-of-flight (ToF) range imaging cameras indirectly measure the time taken from the modulation light source to the scene and back to the camera and it is this principle that is used in depth cameras to perform depth measurements. This thesis is focused on ToF cameras that are based on the amplitude modulated continuous wave (AMCW) lidar techniques which measure the phase difference between the emitted and reflected light signals. Due to their portable size, feasible design, low weight and low energy consumption, these cameras have high demand in many applications. Commercially available AMCW ToF cameras have relatively high noise levels due to electronic sources such as shot noise, reset noise, amplifier noise, crosstalk, analogue to digital converters quantization and multipath light interference. Many noise sources in these cameras such as harmonic contamination, non-linearity, multipath interferences and light scattering are well investigated. In contrast, the effect of electronic jitter as a noise source in ranging cameras is barely studied.

Jitter is defined to be any timing movement with reference to an ideal signal. An investigation of the effect of jitter on range imaging is important because timing errors potentially could cause errors in measuring phase, thus in range. The purpose of this research is to investigate the effect of jitter on range measurement in AMCW ToF range imaging. This is achieved by three main contributions: a development of a common algorithm for measurement of the jitter present in signals from depth cameras, secondly the proposal of a cost effective alternative method to measure jitter by using a software defined radio receiver, and finally an analysis of the influence of jitter on range measurement.

Among the three contributions of this thesis, first, an algorithm for jitter extraction of a signal without access to a reference clock signal is proposed. The proposed algorithm is based upon Fourier analysis with signal processing techniques and it can be used for real time jitter extraction on a modulated signal with any kind of shape (sinusoidal, triangular, rectangular). The method is used to measure the amount of jitter in the light signals of two AMCW

ToF range imaging cameras, namely, MESA Imaging SwissRanger 4000 and SoftKinetic DepthSense 325. Periodic and random jitter were found to be present in the light sources of both cameras with the MESA camera notably worse with random jitter of (159.6 $\pm$ 0.1) ps RMS in amplitude.

Next, in a novel approach, an inexpensive software defined radio (SDR) USB dongle is used with the proposed algorithm to extract the jitter in the light signal of the above two ToF cameras. This is a cost effective alternative to the expensive real-time medium speed digital oscilloscope. However, it is shown that this method has some significant limitations, (1) it can measure the jitter only up to half of the intermediate-frequency obtained from the down shift of the amplified radio frequency with the local oscillator which is less than the Nyquist frequency of the dongle and (2) if the number of samples per cycle captured from this dongle is not sufficient then the jitter extraction does not succeed since the signal is not properly (smoothly) represented.

Finally, the periodic and random jitter influence on range measurements made with AMCW range imaging cameras are studied. An analytical model for the periodic jitter on the range measurements under the heterodyne and homodyne operations in AMCW ToF range imaging cameras is obtained in the frequency domain. The analytical model is tested through simulated data with various parameters in the system. The product of angular modulation frequency of the camera and the amplitude of the periodic jitter is a characteristic parameter for the phase error due to the presence of periodic jitter. We found that for currently available AMCW cameras (modulation frequency less than 100 MHz), neither periodic nor random jitter has a measurable effect on range measurement. But with modulation frequency increases and integration period decreases likely in the near future, periodic jitter may have a measurable detection affect on ranging.

The influence of random jitter is also investigated by obtaining an analytical model based on stochastic calculus by using fundamental statistics and Fourier analysis. It is assumed that the random jitter follows the Gaussian distribution. Monte Carlo simulation is performed on the model obtained for a 1 ms integration period. We found increasing the modulation frequency above approximately 400 MHz with random jitter of 140 ps has a measurable affect on ranging.

Acknowledgements

I wish to express my gratitude to chief supervisor Associate Professor Michael J. Cree for his great fruitful, patience and stimulating discussions during the last four years for making this research success. Then, to my co-supervisor Dr Lee Streeter for his valuable suggestions and support. Next, I would like to thank for the University Grants Commission (UGC) of Sri Lanka for the first three years of tuition fees under the grant number UGC/DRIC/PG/20l5(ii)/ OUSL/02.

My fellow PhD student Carl Lickfold in Time of Flight Range Imaging Group (ToFRIG), has provided enjoyable discussions. I am also grateful to Mary Dalbeth, Natalie Shaw and Tanya Mete for their administrative supports during my studies.

Finally, I extend my wholehearted gratitude to my family for their encouragements that enabled me to succeed in this effort.

Dedication

To my family and all teachers.

Contents

List of Figures

List of Tables

List of Symbols

Standard Operations

$\lvert x \rvert$	absolute value of x
x^*	complex conjugate of x
$\lfloor x \rfloor$	floor of x
$x * y$	convolution between x and y

Standard Types of a Variable

$\mathbb{C}$	set of complex numbers
$\mathbb{N}$	set of natural numbers beginning at zero
$\mathbb{R}$	set of real numbers
$\mathbb{Z}$	set of all integers
$\mathbb{Z}^*$	set of all integers without zero
$\mathbb{Z}^+$	set of positive integers without zero

Variables and Functions

d	radial distance from the camera to the scene
d_{err}	range error for d
δt	the Dirac delta function
f, f_m, f_l, f_s	modulation frequency of the camera
f_{PJ}	frequency of the periodic jitter
$\hat{f}$	an estimation of the probability density function of f
i	imaginary unit, given as $\sqrt{-1}$
j, k, m, n, p, q	indices for set of variables
$l(t, \phi)$	modulated light reflected signal of the camera
$s(t), s(t, \theta)$	shutter signal of the camera
w_H	the Hann window function

A	amplitude of the illumination signal
A_H^{cf}	amplitude correction factor for the Hann window
A_{PJ}	amplitude of the periodic jitter
B	an offset due to background illumination
$\mathcal{C}_i$	weighting coefficients for the Savitzky and Golay algorithm
$C(\theta_k)$	correlation between the light reflected back and shutter signals for kth phase step
E_H^{cf}	energy correction factor for the Hann window
f_X	cumulative distribution function of the random variable X
$\mathscr{F}$	the Fourier transform
$\mathscr{F}^{-1}$	inverse Fourier transform
I_k	raw intensity at the kth phase step
$J_m(x)$	the Bessel function of the first kind of order m of argument x
K, M, N, P, Q	positive integers
$\mathcal{K}(x)$	a kernel density function of argument x
$\mathcal{N}(\mu, \sigma^2)$	a Gaussian distribution with mean μ and variance σ^2
$N_{\Delta t}^{cal}$	calculated number of jitter cycles
$N_{\Delta t}$	floor of the number of jitter cycles
$[\mathcal{R}]$	Richardson extrapolation matrix
$\Re[z]$	real part of the complex number z
T	integration period of the camera
ΔA	amplitude noise
Δt	timing jitter
$\varepsilon(t)$	a random process which follows the Gaussian distribution
ϕ	time of flight phase shift in radian
ϕ_{err}	phase error for ϕ in radian
ϕ_{PJ}^{s}	phase difference of the periodic jitter in shutter signal w.r.t. the light signal in radian
σ_{RJ}	root-mean-square of the random jitter
θ	phase step in radian
ϑ	angular frequency conjugate to θ in units of per radian
Θ	frequency conjugate to θ

Constants

c	speed of light 299792458 m/s
e	the base of the natural logarithm 2.718281828...

Glossary

AM	amplitude modulation
AMCW	amplitude modulated continuous wave
ADC	analogue to digital converter
BER	bit error ratio
BERT	bit error ratio tester
BNC	Bayonet Neill-Concelman
BUJ	bounded uncorrelated jitter
CCD	charged coupled device
CMOS	complementary metal oxide semiconductor
CNN	convolutional neural network
CW	continuous wave
DDJ	data dependent jitter
DJ	deterministic jitter
DUT	device under test
DDC	digital down converter
DAC	digital to analogue converter
DSP	digital signal processing
DC	direct current
DFT	discrete Fourier transform
DCD	duty cycle distortion
FFT	fast Fourier transform
FM	frequency modulation
FPN	fixed pattern noise
FT	Fourier transform
GCD	greatest common divisor
IF	intermediate frequency
ISI	inter symbol interference

IFFT	inverse fast Fourier transform
IQR	interquartile range
KDE	kernel density estimation
LED	light emitting diode
LO	local oscillator
LOTUS	law of the unconscious statistician
MCS	Monte Carlo simulation
MLE	maximum likelihood estimation
MGF	moment generating function
MPI	multipath interference
NA	not available
PB	pulse based
PJ	periodic jitter
PLL	phase locked loop
PM	phase modulation
PMD	photonic mixing device
PN	pseudo-noise
PSD	power spectrum density
PDF	probability density function
RJ	random jitter
RF	radio frequency
RV	random variable
RMS	root mean square
RMSE	root mean square error
SDR	software defined radio
SE	standard error
SG	Savitzky-Golay algorithm
SMA, SMB	SubMiniature version A, version B
SNR	signal to noise ratio
SRA	sparse reflections analysis
TLC	time lag correlation
ToF	time-of-flight
USB	universal serial bus
UI	unit interval

Chapter 1

Introduction

From the twenty first century, depth (range) sensors have been improving in the camera manufacturing industries (Blais, 2004; Li, 2014). The time-of-fight (ToF) range imaging cameras measure the time taken from the modulation light source to the scene and back to the camera and it is this principle that is used in depth cameras to perform depth measurements. Based on the modulation light source, ToF range imaging cameras are categorised as (1) continuous wave (CW) modulation; (2) pulse based (PB) modulation; and (3) pseudo-noise (PN) modulation (Jähne, 2000).

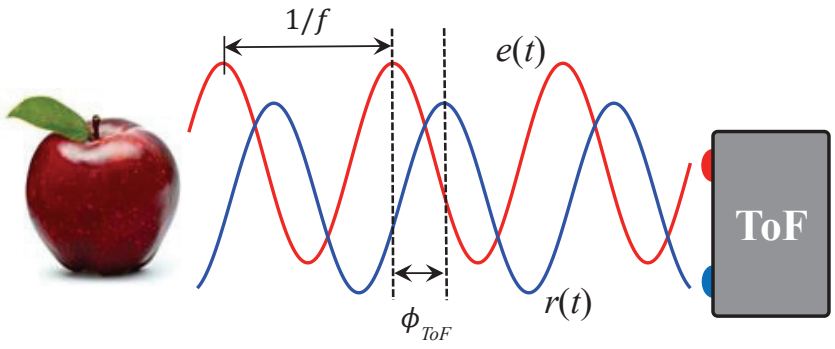

Figure 1.1: Continuous wave modulated operation in time-of-flight camera.

Continuous wave ToF cameras send a (usually infra-red) optical signal $e(t)$ modulated by a sinusoid or square wave. Signal $e(t)$ is reflected back by the scene surface and travels back towards a receiver co-positioned with the emitter. The signal $r(t)$ is delayed due to the propagation distance thus a phase delay is induced on the received signal (Dal Mutto *et al.*, 2012). CW ToF cameras measure the phase difference ϕ_{ToF} between the emitted signal $e(t)$ and received signal $r(t)$ as shown in Figure 1.1. The cross-correlation between the two signals allows phase estimation which is directly related to the distance

between the camera and scene (Beheim and Fritsch, 1986). The range resolution of this method is inversely proportional to the modulation frequency f of the light source. Some advantages of this type of camera are acquisition range and amplitude images, applicable to different modulation techniques (amplitude (AM), phase (PM) and frequency (FM)) and the availability of different light sources (e.g., LED, laser). On the other hand, in order to reduce noise, the camera integrates the received optical signal over time, which causes motion blur in the system, and limits the frame rate. These are some of the disadvantages of this type of camera (Jin and Zeng, 2016).

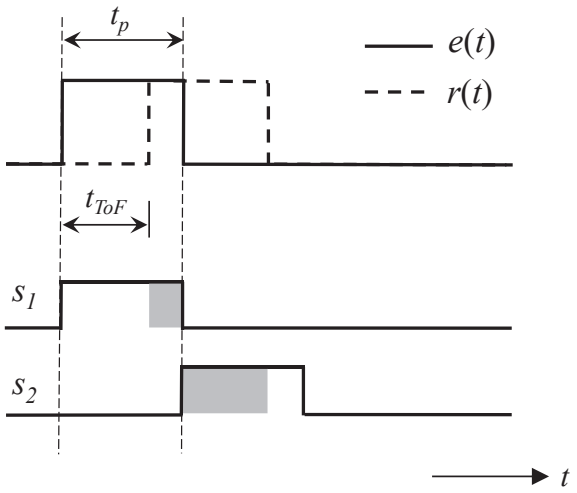

Figure 1.2: Timing diagram for pulse based modulated operation in ToF camera. The shaded areas represent the time period that received the pulse light.

Figure 1.2 shows the timing diagram for the PB modulation technique which measures the absolute time t_{ToF} (direct ToF) of the light pulse that needs to travel from the source into a scene and back to the sensor of the camera. The sensor contains two shutters s_1, s_2 for each pixel. A pixel is accumulating the light in a short and a long interval. When the first shutter s_1 is accumulating with the light in the sensor then the second one s_2 is active until the whole pulse is returned. The two intervals are used to obtain the corresponding distance calculation (Moring *et al.*, 1989). The range resolution of this method is proportional to the pulse width t_p of the light source. These cameras allow long-distance measurements. Thus, the camera needs very short light pulses with fast rise and fall times and with high optical power lasers which reduce the influence of background illumination (Zanuttigh *et al.*, 2016). The arrival time must be detected very precisely (i.e., high accuracy). However, these cameras typically have low repetition rates for pulses and the measurement of light pulse return may not be accurate due to light scattering.

Recently, Sarbolandi *et al.* (2018) investigated some error sources such as temperature drift, multipath effects, motion artefacts, linearity error and depth inhomogeneity in a pulse based ToF camera prototype based on the Hamamatsu area sensor S11963-01CR[1]. A quantitative partial comparison for the above intrinsic parameters with their previous study (the Microsoft Kinect V1 based on structured light and Microsoft Kinect V2 based on the ToF principle of the range sensor (Sarbolandi *et al.*, 2015)) is also included.

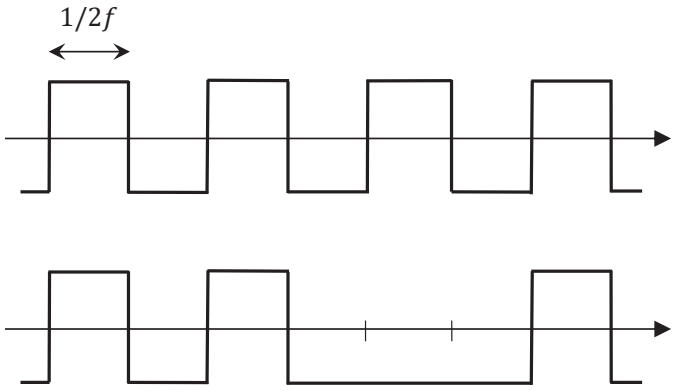

Figure 1.3: A portion of (top) the reference range-clock for a square wave and (bottom) the ranging sequence wave for the binary pattern $\cdots + 1 - 1 + 1 - 1 - 1 - 1 + 1 \ldots$, for pseudo-noise modulated operation in ToF camera.

PN modulation uses a repeating pattern of binary coding of the data signal (Büttgen *et al.*, 2007). The receiver demodulates the waveform to extract the original data as shown in Figure 1.3. However, this modulation has lower precision than the other two types and the precision is proportional to the modulation frequency of the light source (Whyte *et al.*, 2010). A detailed overview of the operational principle of CW, PB and PN modulation ToF sensors is investigated by Jin and Zeng (2016), Zanuttigh *et al.* (2016) and Consultative Committee for Space Data Systems (2014), respectively. The technology and performance of depth cameras are reviewed by Langmann *et al.* (2012).

ToF cameras can also able in low light conditions since the sensor uses infrared light to discover the distance to the scene; it could help with applications even in a pitch black environment. Furthermore, some versions of the AMCW ToF cameras such as MESA Imaging SwissRanger[2] 4000 and 4500, allow multiple cameras to operate simultaneously. In the last few years, the ToF cameras have become commercially available at reasonable prices (i.e., a

[1] `https://www.hamamatsu.com/resources/pdf/ssd/s11963-01cr_kmpd1142e.pdf`
[2] `https://acroname.com/sites/default/files/assets/sr4000_sr4500_manual.pdf`

couple of hundred US dollars). Besides, these cameras have interesting properties such as portable size, feasible design, low weight and low energy consumption (He *et al.*, 2017) leading to high demand in many areas such as mobile robotics (May *et al.*, 2006; Schamm *et al.*, 2009), medical imaging (Karp *et al.*, 2008; Soutschek *et al.*, 2008), 3D reconstruction (Henry *et al.*, 2010), human identification (Liu and Fujimura, 2004; Tong *et al.*, 2012), human motion capturing (Ganapathi *et al.*, 2010), computer graphics (Kolb *et al.*, 2010) and plant breeding (Klose *et al.*, 2009; Busemeyer *et al.*, 2013).

1.1 Motivation and Objectives

Commercially available AMCW ToF cameras have low resolution and relatively high noise level due to electrical sources such as shot noise, reset noise, amplifier noise, crosstalk, analogue to digital converters (ADC) quantization, clock jitter, and due to multipath light interference. These noise sources directly affect the signal to noise ratio of the range measurements. Many noise sources in these cameras such as harmonic contamination (Kahlmann *et al.*, 2006; Streeter and Dorrington, 2015), non-linearity and multipath interference (Godbaz *et al.*, 2011; Freedman *et al.*, 2014; Jiménez *et al.*, 2014; Whyte *et al.*, 2015), and light scattering (Mure-Dubois and Hügli, 2007; Schäfer *et al.*, 2014) are well studied. Another potential noise source is jitter which arises because of mistiming in electronic signals on the camera sensor such as in the ADC. Jitter is defined as any timing movement with reference to the timing of the intended (ideal) signal. The effect of electronic jitter as a noise source in ranging cameras is barely recognized or addressed in the literature (Streeter *et al.*, 2013; Seiter *et al.*, 2014).

But now we believe the amount of jitter is also impacting on ranging. At present, the depth sensors for the ToF systems have been rapidly improved in camera manufacturing industries by increasing the resolution of the camera range with higher modulation frequencies and higher frame rates. These improvements are potentially more affected by the mistiming of electronic signals and thus, by jitter. In addition, due to the above mentioned properties of the ToF cameras, the depth sensors will further contribute in various applications where not much use at present such as smartphones[3], smart buildings[4] has been made. These applications may need very accurate range measurements,

[3]https://www.pocket-lint.com/phones/news/147024-what-is-a-time-of-flight-camera-and-which-phones-have-it

[4]https://lidarmag.com/2019/04/16/terabee-introduces-latest-3d-time-of-flight-camera/

thus the investigation of the jitter on ToF measurements (ranging data) is timely, because they can cause errors in the measurements.

Once the error sources are examined, the noise and jitter performance can be improved and we can correct for these effects on ranging data. The ultimate goal of this thesis is to investigate the jitter measuring, extracting and influencing on range measurements in full-field AMCW ToF range imaging cameras.

1.2 Contributions of the Thesis

This thesis makes the following original contributions:

- an algorithm for real time jitter extraction on the emitted light source signal of the AMCW ToF range imaging cameras. The proposed algorithm can be used to jitter extract on any modulated signal (digital or analogue) with any kind of shape (sinusoidal, triangular, rectangular) for which the reference clock is not available,
- a methodology of periodic and random jitter measurement in AMCW ToF systems by an inexpensive software defined radio USB dongle with the above proposed algorithm, providing an alternative to the order of magnitude more expensive real-time oscilloscope. This technique does have significant limitations and can only uncover lower frequency jitter,
- an analytical model for the correlation function of the range imaging system based on Fourier analysis to investigate the influence of the periodic jitter on the range measurements under the heterodyne and homodyne operations in AMCW ToF range imaging cameras and
- a stochastic model for the correlation function based on Fourier analysis and Monte Carlo simulation to investigate the influence of random jitter on the range measurements in heterodyne and homodyne operations in AMCW ToF range imaging cameras.

1.3 Thesis Overview

This thesis is structured across nine chapters with three main sections: literature review, jitter measurement and jitter influence in AMCW ToF range imaging, as summarized in Figure 1.4. The major contributions in each chapter are pointed out with the four appendices in the figure. In addition to that, a brief description of each chapter is also presented.

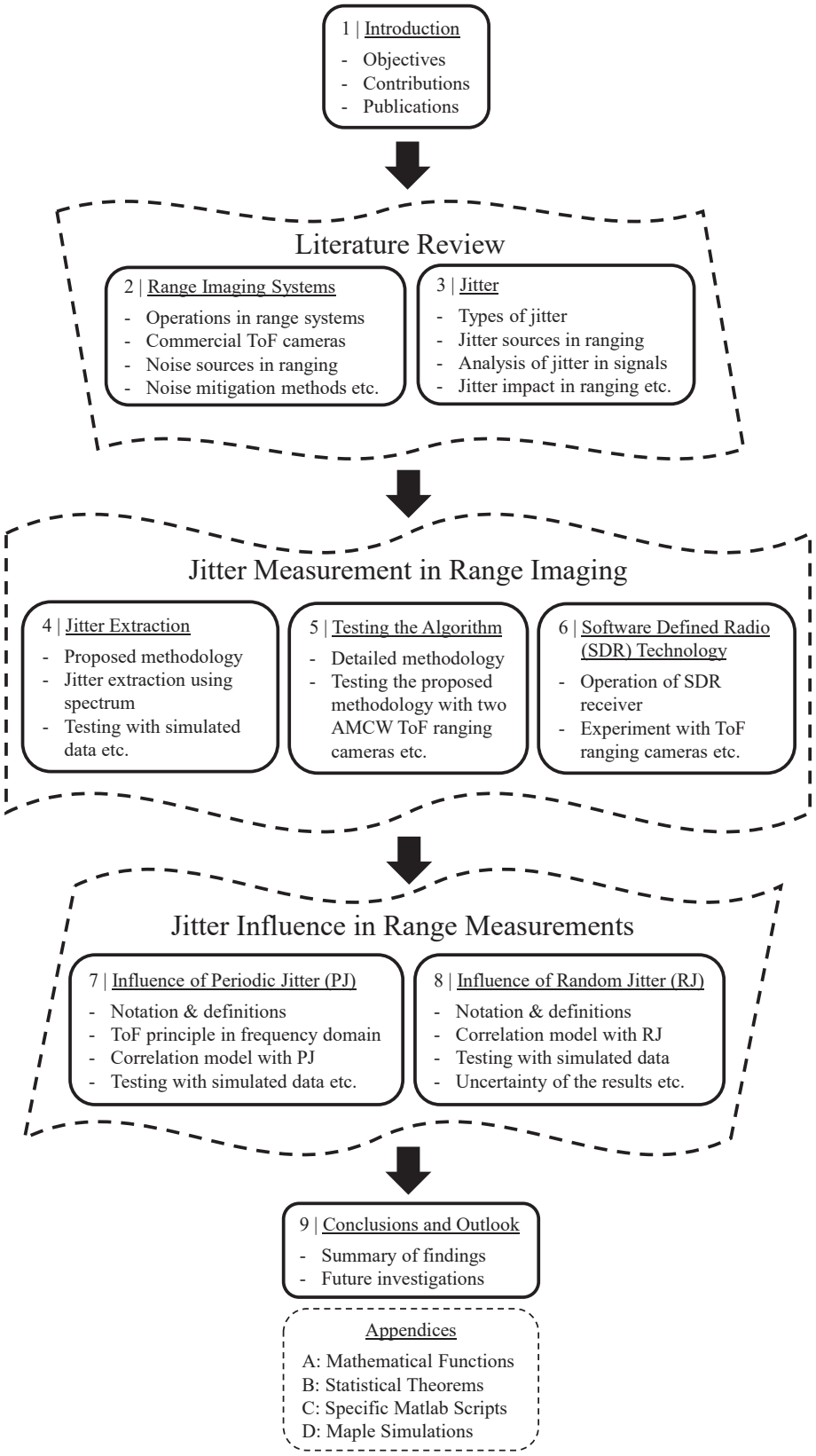

Figure 1.4: Summary of the chapters of the thesis.

Chapter 2 contains one of the literature review chapters of this thesis. This chapter mainly focuses on the details about range imaging systems and their measurement errors. The working principles of ToF ranging systems, including homodyne and heterodyne operation are described and the specifications of selected commercial ToF ranging cameras are briefly summarized. Among them, the details of two AMCW cameras which are used in this thesis are separately pointed out. Next, the definitions of noise and jitter with the noise sources in ranging cameras are analysed. Furthermore, noise mitigation techniques in ToF ranging systems are briefly reviewed. Finally, noise and jitter extraction techniques for ToF cameras in the literature are summarized in tabular form.

Chapter 3 is focused on jitter and outlines the types of jitter in signals, the random and periodic jitter sources in ranging systems and jitter analysis techniques in signals such as using graphical approaches, in time and frequency domains, with the statistical and signal processing approaches. Finally, the impact of jitter on range imaging reported in the literature is described.

The next three chapters comprise the section of the thesis on jitter extraction and measurement. **Chapter 4** describes a proposed novel algorithm to extract the periodic and random jitter present in the light source of the AMCW ToF ranging cameras. The most important advantage of this method is that it does not require a reference or sampling clock signal to trigger the time measurement unit. Instead, signal processing techniques with Fourier analysis are used. This algorithm is camera independent and can be used in real-time jitter investigation in most of the ToF systems where it is impossible to access their clock signals. Finally, the proposed algorithm is tested on simulated data in this chapter.

The measurement of jitter present in two commercial AMCW ToF cameras is reported in **Chapter 5**. Evidence that random jitter and periodic jitter at multiple frequencies are present in both cameras is presented.

The oscilloscope for the experiments used in Chapter 5 is an expensive instrument. Can one replace the oscilloscope by a much cheaper instrument? **Chapter 6** is an investigation of the possibility of re-purposing a vastly cheaper software defined radio (SDR) USB dongle for jitter extraction in signals. The operational principle of the receiver side of the SDR technology is described and the results of experiments on same two AMCW ToF cameras is presented. Comparison is made with the results in Chapter 5, and the limitations of the SDR technique are described.

The next two chapters comprise the section on the investigation of influence of two types of jitter, in ToF ranging systems. **Chapter 7** is an investigation of the influence of the periodic jitter on range measurements. The primary contribution is the derivation of an analytical model in the Fourier domain. The heterodyne operation principle of the correlation model of the AMCW ToF cameras is obtained in the Fourier domain. Then, a novel analytical model for the correlation function with periodic jitter for both heterodyne and homodyne operations in ToF systems are investigated. In order to verify the results, two common numerical approaches are described. Lastly, the remarkable findings of this novel investigation are included at the end of this chapter.

Chapter 8 is an investigation of the effect of random jitter on range measurements. Using Fourier analysis and standard statistical theorems, benchmark stochastic models for the influence of random jitter in the heterodyne and homodyne operations of the AMCW ToF cameras are constructed. The model is tested with the Monte Carlo method through the simulated data with various parameters such as modulation frequency and the RMS of random jitter in the model. Two non-parametric estimations are performed to find the probability density function for the standard deviation of the phase error which is the characteristic parameter for random jitter in the correlation model. Finally, interesting findings for present and predictions for future AMCW ToF cameras on range measurements due to the random jitter are figured out.

Chapter 9 concludes the significant contributions of this thesis, summarises the findings in each chapter and suggests some potential future investigation. In addition, four appendices: mathematical functions, statistical theorems, specific Matlab scripts and Maple simulations are included.

1.4 Publications

A journal article based on Chapter 7 is in preparation and is intended to be submitted to the Journal of Photogrammetry and Remote Sensing (ISPRS). In addition, the following publications were prepared and presented during the course of this research:

- G. Anthonys, M. J. Cree and L. Streeter, "Jitter Measurement in Digital Signals by Using Software Defined Radio Technology," 2019 IEEE International Instrumentation and Measurement Technology Conference (I2MTC), Auckland, New Zealand, 2019, pp. 1-5. (Anthonys *et al.*, 2019)

- G. Anthonys, M. J. Cree and L. Streeter, "Signal Processing Approaches for Jitter Extraction in Time-of-Flight Range Imaging Cameras," 2018 IEEE 12th International Conference on Signal Processing and Communication Systems (ICSPCS), Cairns, Australia, 2018, pp. 1-9. (Anthonys *et al.*, 2018b)

- Anthonys, G., Cree, M. J. and Streeter, L., 2018. "Jitter Extraction in a Noisy Signal by Fast Fourier Transform and Time Lag Correlation," In Applied Mechanics and Materials (Vol. 884, pp. 113-121). Trans Tech Publications. (Anthonys *et al.*, 2018a)

The following publication was contributed during the course of this PhD but does not form a contribution to this thesis.

- M. J. Cree, J. A. Perrone, G. Anthonys, A. C. Garnett and H. Gouk, "Estimating heading direction from monocular video sequences using biologically-based sensors," 2016 International Conference on Image and Vision Computing New Zealand (IVCNZ), Palmerston North, 2016, pp. 1-6.

Chapter 2

Range Imaging Systems and Measurement Error

The precision and accuracy of time of flight (ToF) range imaging cameras are important for many applications, however, the cameras have many noise sources that degrade both precision and accuracy. The commercial ToF range imaging cameras have noise and jitter sources in different amounts which potentially affect range measurements. In this chapter, first, a development of the ToF camera with a typical model is briefly reviewed. Next, an operational principle and the theoretical framework for homodyne and heterodyne operations of range imaging systems are described. Then the specifications of the commercial ToF range imaging cameras are pointed out in the tabular form. In addition, the noise error sources related to the commercial ToF cameras are investigated. Finally, the noise mitigation techniques in range measurements are pointed out.

2.1 Background

In 1977, the first ToF ranging cameras for scene analysis were invented by Stanford Research Institute (presently SRI International) (Nitzan *et al.*, 1977). In the 1990s, the invention of the lock-in charge-coupled device (CCD) technique enabled fast sampling of received light (Spirig *et al.*, 1995). This technique was used by Schwarte (1997) to investigate a method of measuring the phase and magnitudes of electromagnetic waves. As a result of that, in 1999, his team invented the first CCD-based ToF camera prototype (Lange *et al.*, 1999). Following that, ToF cameras were rapidly improved over the last couple of decades (He *et al.*, 2017).

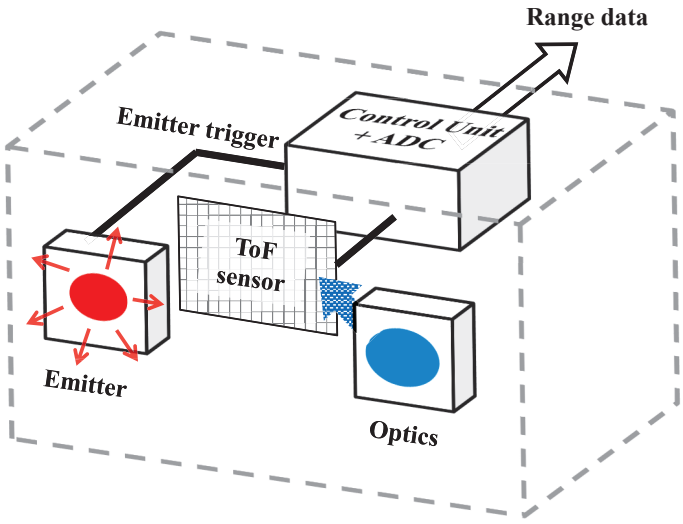

Figure 2.1: A typical block diagram of a common ToF system.

A typical building block of a ToF camera is illustrated in Figure 2.1. These cameras have three main components: a modulation source (an emitter), a lens (optics) and a depth sensor. Typically, the modulation source is based on solid-state laser or light emitting diode (LED) to produce an unobtrusive infrared that drives an illumination source. The lens collects the light reflected back from the target. A depth sensor is composed of an array of shuttered photo-detectors or CCDs (pixels) that are capable of distance measurements. The shutter is driven by the modulation source usually at the same frequency as the light source. Then, either indirect time measurement through the phase difference of the modulation signal or direct time measurement with the laser pulse is used to interpret the distance to the scene. Finally, the sensor interface communicates with the external world such as a PC. In addition to these three, there are other components such as the power supply, corresponding biasing current or voltage signals, control unit, and reading out from the sensor data stream (Remondino and Stoppa, 2013).

2.2 Range Imaging Systems

In amplitude modulated continuous wave (AMCW) operation, the ToF camera illuminates the scene with a modulated light source (using solid-state laser or a LED), and captures (typically, using infra-red CCD/CMOS sensor) the reflected light via a shuttered pixelated sensor in the camera resulting in distance information and a picture of the complete scene simultaneously. Figure 2.2 illustrates the operation of a ToF camera system.

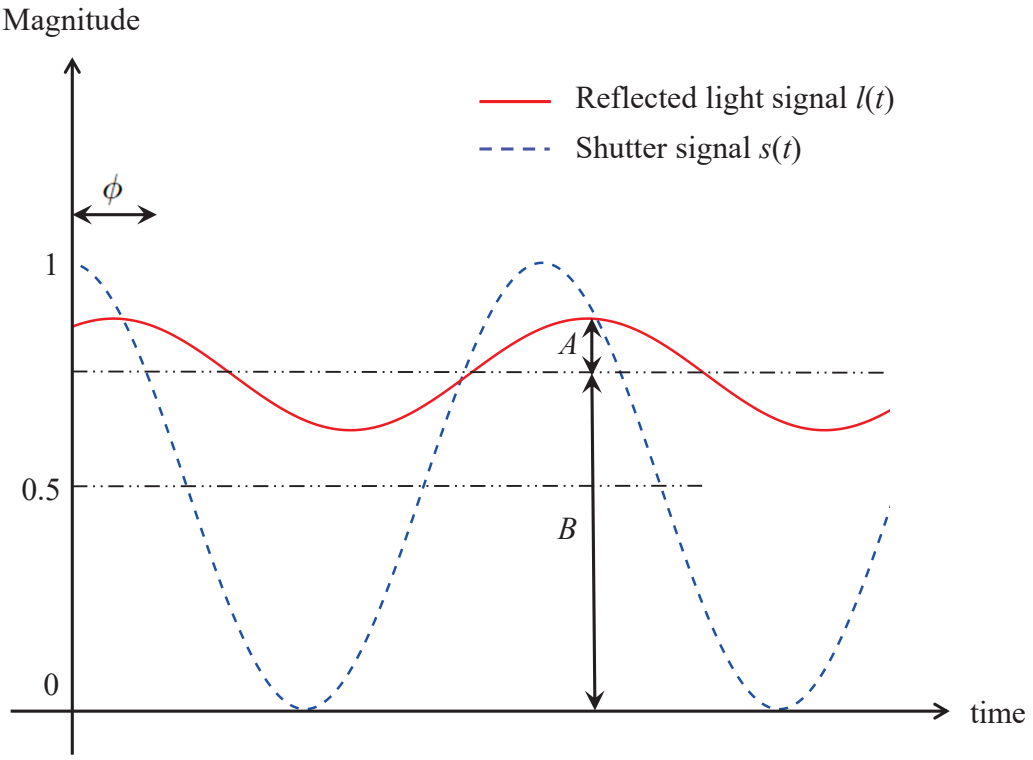

Figure 2.2: Light and shutter signals relationship in a ToF camera.

The relation between the phase difference ϕ due to the time of flight between the illumination and the reflection is measured, and from that the radial distance to the scene d can be expressed as (Lange and Seitz, 2001)

$$d = \frac{c\,\phi}{4\pi f}, \tag{2.1}$$

where c is the speed of light ($2.9979\ldots \times 10^8$ m/s) and f is the modulation frequency of the emitted light source (illumination) and camera sensor.

The received reflected light back from the scene with modulation frequency f is described by,

$$l(t, \phi) = A\cos(2\pi f t - \phi) + B, \tag{2.2}$$

where A is the amplitude of the reflected light which depends on the scene's reflectivity and the sensor's sensitivity, B is the offset due to the background illumination and the phase shift ϕ is directly related to the time of flight. The shutter operates as high/low states and its signal is given by

$$s(t) = \tfrac{1}{2}\cos(2\pi f t) + \tfrac{1}{2}. \tag{2.3}$$

In practice, the phase shift cannot be measured directly. Therefore, the phase shift ϕ due to the time of flight between the illumination and reflection is measured by correlating the two signals. As there are three unknowns variables, at least three measurements of the scene must be made. This is achieved by including an extra added phase delay θ_k for the kth phase acquisition, which the camera controls. Then, the correction function is given by

$$C(\theta_k) = \lim_{T\to\infty} \frac{1}{T} \int_{-T/2}^{T/2} s(t, \theta_k)\, l(t, \phi)\, dt, \tag{2.4}$$

where T is the integration time. Substituting Equations 2.2 and 2.3 into Equation 2.4, with simplification, leads to

$$C(\theta_k) = \frac{1}{2}\left(\frac{A}{2}\cos\left(\phi + \theta_k\right) + B\right). \tag{2.5}$$

For convenient performance of the phase shift ϕ in Equation 2.5, the phase step θ_k should be spaced over 2π radians (Monson *et al.*, 1999). For simplicity, if the samples are evenly spaced, the phase step is given by

$$\theta_k = \frac{2\pi k}{K}, \quad k = 0, 1, \ldots, K-1. \tag{2.6}$$

Then, this correlation measurement (Equation 2.5) is repeated K times with a phase step of θ_k, introduced to the camera sensor or light source.

2.2.1 Homodyne Operation

In homodyne operation the modulation frequency of the emitted light source and sensor signals are identical. In this mode the phase-shifted illumination is mixed with the camera shutter to produce a constant intensity level. Even though three measurements of phase frames are sufficient to perform a single calculation of range, traditionally four samples in the period of the reflected signal are sequentially acquired for each pixel of the sensor, since the multiple of $\pi/2$ radians phase frames can be easily generated electronically, and the calculation is also straightforward (Lange and Seitz, 2001) as

$$I_k = C(\theta_k) \quad \text{for} \quad \theta_k = \pi k/2, \quad k = 0, \ldots, 3, \tag{2.7}$$

giving,

$$\begin{aligned} I_0 &= 0.5A\cos\phi + B, \qquad I_1 = -0.5A\sin\phi + B, \\ I_2 &= -0.5A\cos\phi + B, \qquad I_3 = 0.5A\sin\phi + B, \end{aligned} \tag{2.8}$$

where $I_0, \ldots, I_3$ are the raw intensities as shown in Figure 2.3.

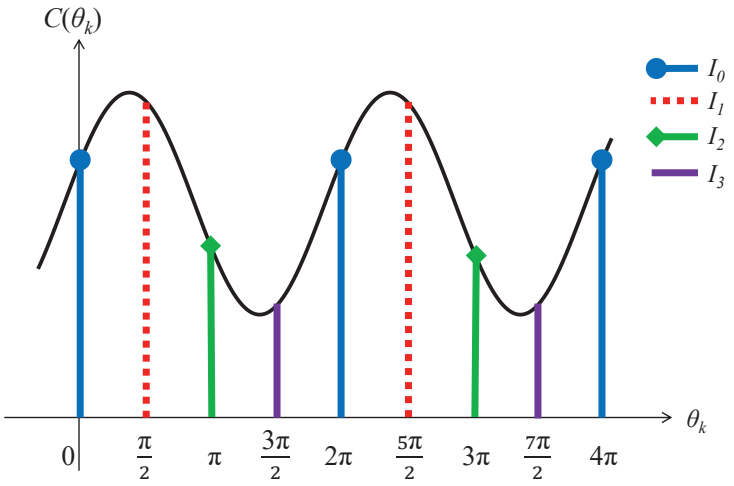

Figure 2.3: Estimation of four samples of the correlation function.

The solutions for the three unknowns can be obtained as

$$\phi = \tan^{-1}\left(\frac{I_3 - I_1}{I_0 - I_2}\right), \tag{2.9a}$$

$$A = \frac{1}{2}\sqrt{(I_0 - I_2)^2 + (I_3 - I_1)^2}, \tag{2.9b}$$

$$B = \frac{1}{4}\sum_{k=0}^{3} I_k. \tag{2.9c}$$

Alternatively, the discrete Fourier transform (DFT) over the integration period T can be used to calculate the three unknowns. The phase and amplitude of the first frequency bin contains the ϕ and A, respectively, while the DC component of the spectrum gives B (Payne, 2008).

2.2.2 Heterodyne Operation

When the modulation frequencies of the two signals are different, the camera is in heterodyne operation. In this mode, the phase difference of the illumination signal is maintained in the low frequency beat and the camera can be performed by taking at least four synchronous samples per cycle for each pixel of the sensor. The phase shift can be determined through analysis of the time varying intensities for each pixel using a more general form than in the homodyne case

(Conroy *et al.*, 2009). Then, from DFT, the unknowns ϕ, A and B can be found from the phase and amplitude of the beat frequency bin, and the DC component of the spectrum, respectively, (Payne, 2008) as

$$\phi = \tan^{-1}\left(\frac{\sum_k I_k \cos\theta_k}{\sum_k I_k \sin\theta_k}\right), \tag{2.10a}$$

$$A = \frac{1}{2}\sqrt{\Big(\sum_k I_k \cos\theta_k\Big)^2 + \Big(\sum_k I_k \sin\theta_k\Big)^2}, \tag{2.10b}$$

$$B = \frac{1}{K}\sum_k I_k, \qquad k = 0, 1, \ldots, K-1. \tag{2.10c}$$

A continuous phase shift in heterodyne operation is an effective result rather than the discrete phase steps between samples of the homodyne method. However, the signal amplitude is reduced by the phase shift during the sensor integration period, in particular attenuating higher frequency harmonic components which can contaminate the phase measurement (Jongenelen *et al.*, 2009). By changing the beat frequency, the ability of the system to easily alter the value of K from three to several hundred is an another advantage. This allows the user to select between high-speed, high-precision measurements with K large (many frames) or reduced-precision measurements with K small (few frames).

Once the phase shift ϕ is known, the depth measurements (the radial distance to the scene d) can be obtained via Equation 2.1.

2.3 Commercial ToF Ranging Cameras

The technologies used to build depth sensors of AMCW lidar systems have rapidly improved in camera manufacturing industries in recent years (Blais *et al.*, 2000; Horaud *et al.*, 2016). Each pixel of the sensor captures both grey-scale image measurement (intensity) and distance to the scene at a frame rate. Both the depth accuracy and the frame rate are limited by the required integration period of the camera. The appropriate tuning of the integration period is very important in ToF measurements. Long integration periods lead to good ToF depth measurements repeatability (Fürsattel *et al.*, 2016). During the last decade, significant progress has been made in increasing the resolution and the sensitivity of the camera sensor (Kraft *et al.*, 2004). At present, modulation frequencies of the ToF cameras are relatively small (less than 100 MHz) and

all these cameras have different accuracy and precision levels (McCarthy *et al.*, 2013; He *et al.*, 2017). There are a number of commercial ToF cameras available in the market. Most of them (MESA Imaging AG[1,2,3], SoftKinetic[4], PMD Technologies[5] and Panasonic[6]) use the AMCW phase-shift method while others (Advanced Scientific Concepts[7], Hamamatsu Photonics K.K.[8]) use direct measurement time of flight (i.e., pulse method) to measure distances.

The price of commercial ToF cameras varies enormously and different technologies are used in their design. ToF cameras with high accuracy in ranging are very expensive while the cameras with substantial inaccuracies in ranging are relatively cheap. Therefore, some ToF cameras are not suitable for applications that need greater accuracy levels. In this thesis, we are using two AMCW ToF range imaging cameras, namely, MESA Imaging SwissRanger 4000[2] (US $10000) and SoftKinetic DepthSense 325[9] (US $25) during the experiments will be stated in Chapters 5 and 6. The modulation frequencies of these cameras are self generated inside.

2.3.1 MESA Imaging SwissRanger 4000

A picture of a MESA Imaging SwissRanger 4000 is given in Figure 2.4. This camera uses infrared LEDs for its illumination source and uses a four-sample homodyne operation. The illumination process includes an optical feedback system. The optical feedback redirects some of the LED illumination directly back to the sensor region. In SR4000, the LEDs appear relatively bright with the wavelength of 850 nm and affect very low sensitivity to the human eye and the camera has been verified for eye-safety.

The SR4000 was manufactured in two versions. From one version, the user can select the modulation frequency among 29, 30 and 31 MHz. For the other version, the modulation frequency can be chosen among 14.5, 15 and 15.5 MHz. The calibrated ranges for 30 and 15 MHz are 0.8−5.0 m and 0.8−8.0 m, respectively. The size of the image captured from this camera is 176×144 pixels and the integration time can be controlled by the user. In addition, SR4000

[1] https://aiweb.techfak.uni-bielefeld.de/files/SR3000_manual_V1.03.pdf
[2] http://www.adept.net.au/cameras/Mesa/pdf/SR4000.pdf
[3] http://www.adept.net.au/cameras/Mesa/pdf/SR4500.pdf
[4] https://www.sony-depthsensing.com/Depthsense/DepthsenseSensors
[5] https://pmdtec.com/picofamily/
[6] https://www.digikey.com/product-detail/en/panasonic-electric-works/
[7] https://www.advancedscientificconcepts.com/products/overview.html
[8] https://www.hamamatsu.com/jp/en/product/index.html
[9] https://www.softkinetic.com/Portals/0/Documents/PDF/WEB_20130527_SK_DS325_Datasheet_V4.0.pdf

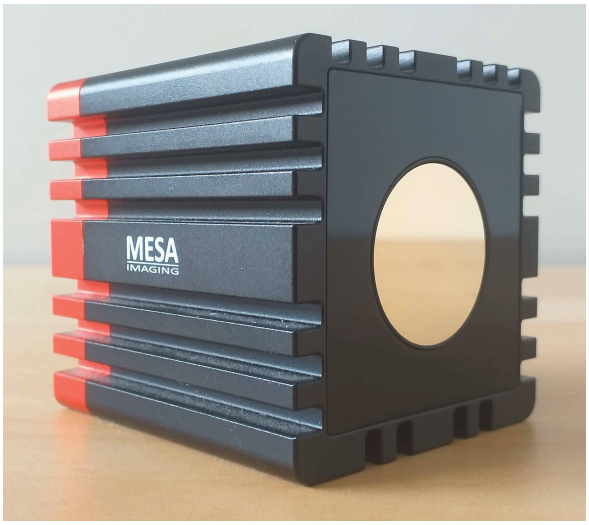

(a)

(b)

Figure 2.4: The MESA SwissRanger 4000 with power (a) off and (b) on.

allows multiple cameras to operate simultaneously. This camera operates with a maximum frame rate of 50 fps. The MESA SR4000 depth camera is now discontinued in the market.

2.3.2 SoftKinetic DepthSense 325

A picture of a SoftKinetic DepthSense 325 is shown in Figure 2.5. This camera uses infrared laser (diffused) light for its illumination source and uses the homodyne operation. The camera has been verified for eye-safety and has a low intensity signal. DS325 has the capability of a short range distance, 0.15 – 1 m only. The modulation frequencies for this camera are 50 and 60 MHz with

(a)

(b)

Figure 2.5: The SoftKinetic DepthSense 325 with power (a) off and (b) on.

the frame rates 25 and 30 fps, respectively. The size of the image captured from DS325 is 320×240 pixels and the integration time is fixed. New versions of this camera are available in the market today[10].

Regardless of whether LEDs or laser diodes are used, the emitted light is modulated with a modulation signal by its specific frequency, whose characteristics are used for measuring of the depth. LEDs are cheaper and often smaller than lasers. However, some commercial ToF ranging cameras allow the simultaneous implementation of the ToF principle for several range measurements at the same time. Therefore, each pixel in here represents an own range measurement system.

All cameras performance with their own configurations. The relevant camera parameters such as resolution, maximum range, frame rate, modulation frequency and precision/accuracy, of the selected commercial ToF cameras, are tabulated in Table 2.1.

[10] `https://www.sony-semicon.co.jp/products_en/index.html`

Table 2.1: Specifications of the selected commercial time-of-flight range imaging cameras

Manufacturer and ToF camera		**Image size [pixel×pixel]**	**Modulation freq. [MHz]**	**Maximum range [m]**	**Max. frame rate [fps]**	**Precision or accuracy [mm]**
Amplitude modulated continuous wave (AMCW) ToF cameras						
MESA Imaging SwissRanger	SR3000	176×144	20	7.5	25	NA
	SR4000		29, 30, 31	5	54	±10
			14.5, 15, 15.5	10	50	±15
	SR4500		15 – 30	9	10 – 30	±20 for ≤ 5 m ±40 for > 5 m
SoftKinetic DepthSense	DS311	160×120	20	1.5 – 4.5	60	< 300 at 3 m
	DS325	320×240	50, 60	1.5 – 3.0	30	< 14 at 1 m
	DS525	320×240	Not Available	0.15 – 1.0	25 – 30, 50 – 60	< 14 at 1 m
	DS536A	78×58	NA	0.1 – 5.0	5 – 60	NA
Microsoft Kinect	V1 – (uses structured light)	640×480	NA	0.4 – 4	30	NA
	V2	512×424	16, 80, 120	0.5 – 4.5	30	±30 at 2 m

Continued on next page

Table 2.1 – continued from previous page

Manufacturer and ToF camera		Image size [pixel×pixel]	Modulation freq. [MHz]	Maximum range [m]	Max. frame rate [fps]	Precision or accuracy [mm]
Amplitude modulated continuous wave (AMCW) ToF cameras						
PMD Technologies GmbH	PMD19k	160×120	20	7.5	15	±30
	CamCube3.0	200×200	21	15	15	±30
	CamCube3.0	200×200	21	15	15	±30
	A2	64×16	16	15	15	±100 for < 40 m
PMD Technologies CamBoard	pico monstar	352×288	100	0.5 – 6.0	60	≤ 1%
	pico flexx	224×172	NA	0.1 – 4.0	5 – 45	≤ 1% at 5 fps ≤ 2% at 45 fps
Panasonic D-Imager	EKL3104	160×120	3 modes — the selection is available using application software.	9	30	±40, σ=30 (low ambient) ±40, σ=140 (high ambient)
	EKL3105			1.2 – 5 1.5 – 5		σ=20 (low ambient) σ=50 (high ambient)
	EKL3106			1.2 – 5 1.5 – 5		σ=30 (low ambient) σ =140 (high ambient)

Continued on next page

Table 2.1 – continued from previous page

Manufacturer and ToF camera		**Image size [pixel×pixel]**	**Modulation freq. [MHz]**	**Maximum range [m]**	**Max. frame rate [fps]**	**Precision or accuracy [mm]**
Pulse modulation ToF cameras						
Advanced Scientific Concepts Inc.	3D Flash LIDAR	128×128	NA			
	Portable			70 – 1100	15	NA
	TigerEye			60 – 1100	30	± 40 at 60 m
	TigerCub			NA	30	NA
	DragonEye			1500	10	$< \pm 100$, $3\sigma = \pm 150$
	GoldenEye			3000	10	$< \pm 100$, $3\sigma = \pm 150$
	Peregrine	128×32		Lens depend	20	NA
Hamamatsu Photonics K.K.		160×120	NA	Depends on integration time (IT)		NA
Distance area image sensor - S11963-01CR[11]				and readout time (RT), frame rate = 1/(IT + RT)		

[11] https://www.hamamatsu.com/jp/en/product/type/S11963-01CR/index.html

2.4 Noise and Jitter

The raw intensities in either Equations 2.9 or 2.10 that are used to compute A, B and ϕ are subject to noise. As a result, the modulation amplitude, background offset and the range information that one gets from the camera signals are also noisy. Any signal can deviate from its ideal occurrence in any of magnitude and timing as shown in Figure 2.6.

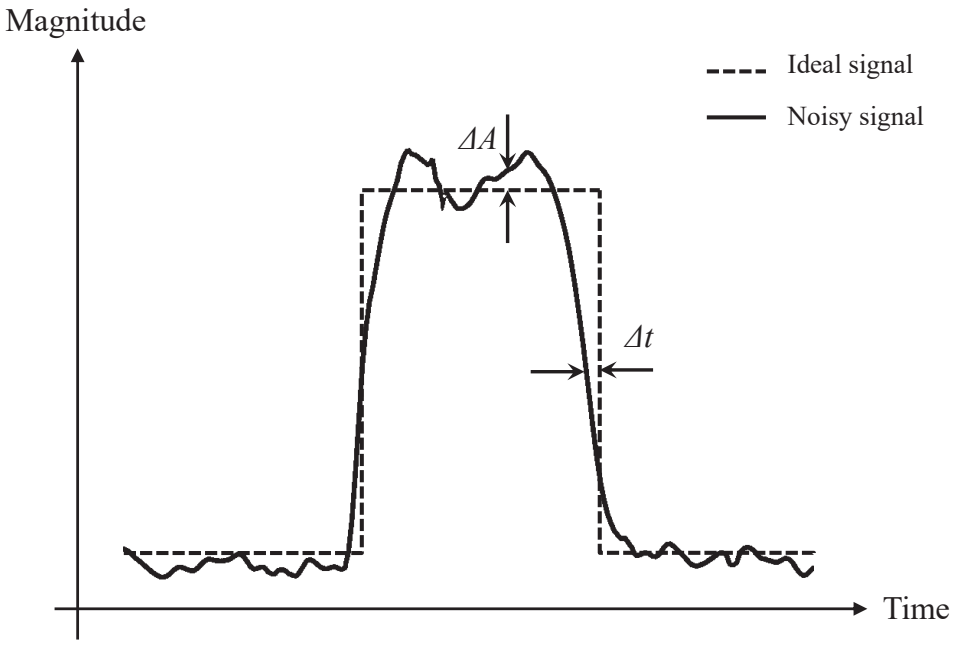

Figure 2.6: A noisy signal and its ideal signal.

If the deviation is in magnitude, it is said to be noise (or amplitude noise ΔA), whereas if the variation is in timing, it is said to be jitter (or timing jitter Δt). These definitions are used throughout this thesis. Often both noise and jitter occur at the same time. Jitter reveals itself as variations in phase, width, duty cycle, or period (Li, 2007). To reduce the uncertainty in depth measurements, it is useful to understand some of the common error sources of noise and jitter in ToF range imaging cameras. There are significant sources that are present in almost every measurement of instrument precision and accuracy, electronic noise and jitter. Therefore, the rest of this chapter focuses on the noise sources in ToF ranging cameras and noise mitigation techniques.

2.5 Harmonic Cancellation

The generation of perfect sinusoids of the relevant frequency is impossible. Sampling a received signal takes a finite non-zero time, thus the sampling of

the received signal is not ideal. This causes harmonic distortion in the received signal, which negatively impacts on the quality of the measured data. Typically a calibration is performed to correct these errors. In addition, the unwanted harmonics in the received signal considerably impacts the depth measurements. By using a lookup table, Kahlmann *et al.* (2006) described a method to calibrate for this kind of error while Lindner and Kolb (2006) used a fitted cubic B-spline in their method. However, if the temperature changes in the system, the calibration methods can be invalidated. Therefore, a phase encoding approach that attenuates the harmonics during the sampling process, was introduced by Payne *et al.* (2010). That method is independent of the amplitude modulation waveform shape. Moreover, Streeter and Dorrington (2015) demonstrated a simple method to remove the third harmonic that typically causes the main harmonic error in AMCW based ToF cameras. They verified that the standard deviation of the noise results has not been significantly changed after applying the method and recommended that the method can be applied to the higher-order harmonics as well.

2.6 Noise Sources in Ranging Cameras

It is clear that the depth measurements depend on the phase angle and modulation frequency in the system. Therefore, it is more important to investigate what factors contribute (for ϕ and f) directly or indirectly to the precision and accuracy of ToF range measurements, because, the noise sources affect the precision while the measurement errors affect the accuracy. In ToF cameras, the noise can be categorised as systematic and non-systematic (random) errors (Falie and Buzuloiu, 2007; Foix *et al.*, 2011). Systematic errors can be further categorised according to their source in the process of range measurement. Noise sources are due to random pixel noise, temperature noise, built-in pixel-related noise, the amplitude of reflected light and depth distortion.

2.6.1 Integration-Time Related Noise

It is noticed that there is a relationship between the integration time and the depth measurements for the same scene (Foix *et al.*, 2011). This affects the range of depths that the camera is sensing with more precision. Too long an integration time leads to saturation while short integration time increases the noise level. The effects of the integration time on the data measurements of various ToF cameras have been investigated in literature (Piatti and Rinaudo,

2012; Pfeifer *et al.*, 2013). Many range cameras use the four-phase shift algorithm (Servin *et al.*, 2009) which needs four samples to produce the phase measurement. This requires four separate integration periods. Some cameras use even more integration periods, therefore the total time required to capture a depth image is three (or more) times the integration time, plus three (or more) times the readout time. This is reflected in the achievable frame rate for given integration time. Integration time can typically be set by the user and is adjusted to the observed scene.

2.6.2 Temperature Noise

The inside and outside temperatures of ToF cameras are always unstable, therefore it will take some time to stabilise at some level after turn on. Until the temperature of the camera is stabilised, the depth measurements can drift. The warm up effects on different cameras have been investigated by Kahlmann and Ingensand (2008), Chiabrando *et al.* (2009) and Pfeifer *et al.* (2013). As an example, Pfeifer *et al.* (2013) explored the warm up effect in MESA SwissRanger 4000 and showed that there is a 2 mm shift in measurement over the first hour of operation. After one hour the measurement is much more stable. The inside heating of ToF cameras may be increased if the camera is running for long hours. This causes a change in the behaviour of the materials inside the camera. Furthermore, the effect of the warm up of some ToF cameras have been investigated by Kahlmann *et al.* (2006) and Piatti and Rinaudo (2012). As an example, Kahlmann *et al.* (2006) pointed out the influence of the integration time and temperature on measured distance by SwissRanger.

2.6.3 Built-in Pixel-Related Noise

This kind of error occurs in the sensor array due to properties of different material in the complementary metal-oxide-semiconductor gates or charge-coupled device, and the time delays of capacitor charge during the signal correlation process. As results of these, two neighbouring pixels that measure the same real depth may nevertheless provide different depth measurements (Kahlmann *et al.*, 2006; Falie and Buzuloiu, 2007).

2.6.4 Intensity of Reflected Light

Since the ToF measurements are based on the light reflected from the scene, the accuracy of the measurements is highly related to the amount of incident

light. The higher reflected intensity implies higher depth accuracy. On the other hand, saturation of the sensor can occur when the scene is too close to the camera and invalidates the measurement (Oprisescu *et al.*, 2007; Foix *et al.*, 2011).

2.6.5 Depth Distortion

Depth distortion is referred to as wiggling or circular error (Foix *et al.*, 2011). In practice, the emitted infra-red light cannot be exactly generated in the modulation process as described in the theory. This causes errors in the depth measurements and depends only on the measured depth for each pixel. This type of error can be addressed either by considering the average values from multiple relative measurements or by comparing the depth measurements with a reference truth distance (Fuchs and May, 2008; Fuchs and Hirzinger, 2008).

On the other hand, several non-systemic errors in ToF cameras can be identified as light scattering, multipath interference, motion blurs and distortion in signal-to-noise ratios.

2.6.6 Multipath Interference

This is due to the interference of multiple light reflections captured at each pixel of the sensor. Multipath interference (MPI) is highly scene dependent, and is one of the major problems in ToF measurements, because (1) it is ambiguous and difficult to prevent, (2) it can produce large errors in range, and (3) we do not know the scene until we have measured it. MPI is mainly due to the presence of surface edges, reflections of translucent objects (e.g. glass, white sheet), volumetric scattering (e.g. fog, dust) and inter-reflections of objects in the surrounding area (Fuchs *et al.*, 2013; Bhandari *et al.*, 2014). The behaviour between phase and amplitude is not linear with the frequency when MPI is present. The impact of multipath interference in ToF systems is well explored in literature (Dorrington *et al.*, 2011; Godbaz *et al.*, 2012; Whyte *et al.*, 2014a,b). The non-linearity and multipath interference in the signal is one of the major problems in AMCW ToF ranging systems.

2.6.7 Motion Blurs

This is another type of error that more adversely affects ranging after the MPI. Due to the movement of the scene or the camera during the integration time, the measurement of the scene is blurred. Also, the motion that occurs between

integration periods is a major problem. Lottner *et al.* (2007) have used a combination of a photonic mixing device (PMD) camera and a conventional 2D image sensor to detect lateral motion artefacts. Also, Lindner and Kolb (2009) have investigated compensation methods for motion artefacts for ToF cameras. If the motion is restricted to a single direction then the correction process is relatively faster than the motion in multiple directions (Hussmann *et al.*, 2010, 2011). Streeter and Dorrington (2014) have investigated both motion blur within each frame and errors arising due to changes between frames.

2.6.8 Signal-to-Noise Ratio

The signal-to-noise ratio (SNR) compares the levels of signal power to noise power and is most often expressed in decibels (dB). The achievable SNR varies between cameras and scenes since some cameras have a stronger emitted signal than others. When this ratio is increasing with time, it is called that the system is in the better specification, since there is more useful data (the signal) than the unwanted data (the noise) (Foix *et al.*, 2011).

2.6.9 Random Noise

The random noise in the radial motion in ToF ranging was investigated by Streeter (2017). Two methods were developed: one was by using the maximum likelihood estimation (MLE) and a new method based on the measured correlation signal and its derivative. The author concluded that the MLE performed better than the other in terms of random noise, but MLE was slower and was not able to provide an estimate in every example used. In contrast, the other method always produces an estimate of radial motion.

2.7 Noise Mitigation Techniques

There are different types of de-noising techniques for the error sources in ToF systems. A mathematical model to predict systematic errors and statistical uncertainties of ToF camera was investigated by Rapp *et al.* (2008). An error propagation model from the measured data is used to analyse them. The pixel base non-uniformity of the depth signal was also examined. The amplitude was used for pixel validation purposes and temperature noise was not considered in their work. Let us briefly consider other corresponding de-noising techniques as follows.

2.7.1 Temperature Noise

With increases in temperature, a higher rate of thermally generated electrons is present in range sensors technology. In CCD and CMOS photo sensors increased internal heating causes a larger number of thermal generated electrons (Kahlmann *et al.*, 2006). Even though some cameras have a cooling process, it remains a small effect and can be factored in the calibration.

2.7.2 Depth Calibration

Due to the systematic appearance of sources of noise errors, there is a deviation of actual depth and depth measured by the ToF camera. Thus, a thorough depth calibration has to be performed to record accurate data. Zhang (2000) developed a flexible technique for the calibration of radial distance to the scene which is based on a closed-form solution, followed by a non linear refinement based on the maximum likelihood criterion. Kahlmann *et al.* (2006) and Kahlmann and Ingensand (2008) introduced a calibration pattern consisting of filled white circles on a black background while Fuchs and Hirzinger (2008) used a classic checkerboard pattern where both methods are suited to accurately determine the intrinsic parameters such as the depth measurement distortion and focal length, and the pose of the camera. However, Kahlmann *et al.* (2006) presented a parameter based calibration approach while Kahlmann and Ingensand (2008) used a differential measurement principle setup. Both of them were considered a photogrammetric camera calibration and a distance system calibration with respect to the reflectivity and the distance itself.

Fuchs and Hirzinger (2008) introduced a calibration procedure based on the distance and amplitude measurements with respect to an external positioning system. They simultaneously estimate the distance parameters and the extrinsic parameters (e.g. optical tracking system or a robot) with respect to the external positioning system for a ToF camera. Lindner *et al.* (2010) presented a lightweight calibration framework in which intrinsic calibration, wiggling error calibration and reflectivity related depth error calibration is integrated. The method is based on analysis-by-synthesis, a planar checkerboard pattern with different levels of reflectivity. Furthermore, Hansard *et al.* (2012) introduced an automatic detection of calibration grids of ToF images with checkerboard pattern. They used the Hough transform which is based on careful reasoning about the global geometric structure of the board, before and after perspective projection.

2.7.3 Camera Distortion

Due to the wiggling effect of the camera, the depth measurements offset can be distorted. To overcome this offset, some researchers choose one integration time and perform the depth distortion calibration process with the same value (Oprisescu *et al.*, 2007; Kim *et al.*, 2008). On the other hand, high integration time was used to compensate the higher optical output power of their proposed illumination module and implemented the model by using pseudo four-phase shift algorithm (Hussmann and Edeler, 2010). Longer integration times cause a higher temperature of the sensor therefore some 3D cameras have an auto mode settings for the integration time. Hussmann *et al.* (2014) described a CW modulation method based on sine waves with various higher integration time for their noise distribution model.

2.7.4 Built-in Pixel-Related Noise

A simple model which predicts how the distance error at one pixel depends on image intensity at that pixel and on the distance itself is introduced by Falie and Buzuloiu (2007). The model is based on shot noise (correlated with a light source) with additional noise source (due to the presence of dark pixels). They experimented on three features: intensity-dependent variance of the noise, intensity-dependent distance error and surround-dependent distance errors of ToF cameras. They concluded that due to the non-linearity in the phase-shift estimation, the darker objects seem to be either further away or closer depending on the distance. This error can be obtained by comparing the calculated depths with a reference distance, and representing them as a table or matrix, knowing as a Fixed Pattern Noise (FPN) matrix. This matrix depends on the integration time in the system and has to be determined for every different integration period (Kahlmann *et al.*, 2006).

2.7.5 Light Scattering

Jamtsho and Lichti (2010) noticed that the light scattering is highly dependent on the surface area and the distance of the scattering object from the camera and the background scene. They concluded that scattering range bias is independent of the integration time while the scattering amplitude bias monotonically increases with the integration time. However, they tested only for MESA SwissRanger 3000 and 4000 ToF ranging cameras. On the other hand, Schäfer *et al.* (2014) presented a new model, based on raw data cal-

ibration with only one additional intrinsic camera parameter and have shown that their approach effectively removes the errors of in-camera light scattering. They however assumed a constant scattering parameter that can be averaged for every pixel in the measurement area.

2.7.6 Non-Linearity and Multipath Interference

Godbaz *et al.* (2011) show that the standard amelioration methods such as lookup tables and B-spline models are invalidated due to temperature changes. They consider heterodyning and harmonic cancellation as partial solutions to non-linearity issues in practical systems. Commonly, there are two types of algorithms to describe multi-path interference (MPI) in the literature. One type is focused on *diffuse* multipath, arising from Lambertian surfaces (i.e., uniformly all pixels to all pixels) (Fuchs *et al.*, 2013; Jiménez *et al.*, 2014) and other the type is focused on *two-path* multipath, which arises from specular surfaces (i.e., per pixel basis) (Dorrington *et al.*, 2011; Godbaz *et al.*, 2012).

Jiménez *et al.* (2014) have proposed a radiometric model that represents the working principle of ToF cameras, including the MPI phenomenon. They show the original scene can be recovered from contaminated measurements from the ToF camera, with an iterative method that converges to a depth correction. It reduced highly the MPI influence on the results. Godbaz *et al.* (2012) proposes two models; one is based on a Cauchy distribution over the range and uses four measurements at different modulation frequencies to determine the amplitude, phase and reflectivity distribution of up to two component returns within each pixel. The other method is based on the attenuation ratios to determine the amplitude and phase of up to two component returns within each pixel.

Freedman *et al.* (2014) introduced an algorithm based on sparse reflections analysis. They show the method can be used with many types of multipath interference. The investigation of the properties of a binary sequence as the modulation waveform is another technique available that is commonly used. Moreover, Whyte *et al.* (2015) resolved these errors by using the direct and global separation methods; a technique that is also applicable to normal camera images. It is considered that the multiple paths are a direct return which is the return from shortest path length, and a global return which includes all other returns. Recently, Marco *et al.* (2017) has proposed a different approach, a convolution neural network (CNN) based on depth reconstruction methods for the correction of MPI by using an unmodified, off-the-shelf camera, with a single frequency in real time. A encoder-decoder (convolutional-

deconvolutional) neural network with a two-stage training process is designed using both captured and synthetic data. The network is trained by synthetic depth data with MPI as input and it returned the corrected depth map. This investigation was worked in several real world scenarios with more general reflections and it failed for extremely transparent or glossy surfaces.

2.7.7 Motion Blurs

Lottner *et al.* (2007) recommended two possible approaches to minimise the affect due to the motion blurs without discarding the corrupted data. One is to take two-phase depth computation after the phase sampling of the images and the other is to take an average of positionally weighted neighbouring pixels. In addition, the usage of coded exposure and optical flow techniques together in AMCW range measurement is used by Streeter and Dorrington (2014). In addition, Jimenez *et al.* (2014) have proposed a method that removes motion artefacts from a single frame captured by a PMD ToF camera without altering current hardware. They recovered the depth of each pixel by exploiting consistency of the correlation samples and local neighbours of the pixel. Recently, Streeter (2018) used the Kalman filter to perform noisy time-series analysis for the problem of transverse motion by raw ToF data.

2.7.8 Signal-to-Noise Ratio

To increase the signal-to-noise ratio (SNR), the average value can be computed with a certain accuracy threshold with respect to the pixel's variance or simply removing the corrupted values by using the low amplitude filtering method (Falie and Buzuloiu, 2007). Fuchs and May (2008) used a procedure to decide the optimal integration time depending on the required areas. Mufti and Mahony (2011) proposed SNR estimator for ToF cameras based on statistical modelling and maximum likelihood estimation. They provided noise models for the three parameters of amplitude, phase and intensity. The model was used for prediction of errors in a ToF camera under various SNR conditions.

Among those error sources, light scattering and depth distortion can be easily mitigated. In addition to that, the effect of SNR can be easily overcome. Table 2.2 is a summary of some selected error reductions related to ToF systems attained by the main compensation approaches in the literature.

Table 2.2: Noise and jitter extraction techniques for time-of-flight range imaging cameras

Investigation on	**Paper**	**Methodology/Algorithm**
Harmonic cancellation	Kahlmann *et al.* (2006)	Lookup table
	Lindner and Kolb (2006)	Fitted cubic B-spline
	Payne *et al.* (2010)	Phase encoding method
	Streeter and Dorrington (2015)	Modification on the data acquisition process
Wiggling and reflectivity error calibration	Lindner *et al.* (2010)	Checker-board pattern and an Analysis-by-Synthesis method
Depth distortion and amplitude	Oprisescu *et al.* (2007)	Spatially and adaptive neighbourhood filters
	Fuchs and Hirzinger (2008)	B-Splines and multiple range amplitudes
	Kim *et al.* (2008)	6-degree polynomial and radial pattern
	Hussmann and Edeler (2010)	Pseudo four-phase shift algorithm
	Hussmann *et al.* (2014)	A CW modulation based on sine waves
Photogrammetric and distance calibrations	Kahlmann *et al.* (2006); Kahlmann and Ingensand (2008)	A parameter based approach; differential measurement principle
Distance calibration	Zhang (2000)	Closed-form solution & maximum likelihood estimation (MLE)

Continued on next page

Table 2.2 – continued from previous page

Investigation on	**Paper**	**Methodology/Algorithm**
	Fuchs and Hirzinger (2008)	Checker-board pattern and a non-linear optimisation algorithm
	Hansard *et al.* (2012)	Checker-board pattern and Hough transform
Built-in pixel & integration time	Kahlmann *et al.* (2006)	Fixed Pattern Noise (FPN) matrix and look-up table
	Lindner and Kolb (2006)	FPN matrix with constant integration time
	Falie and Buzuloiu (2007)	Shot noise and correlated with light source
	Fuchs and Hirzinger (2008)	Pan and tilt coefficient with different integration time
Lateral motion artefacts	Lottner *et al.* (2007)	Classical 2D image edge detector
Motion artefacts	Schmidt and Jähne (2011)	Analysing the temporal raw data signal
	Jimenez *et al.* (2014)	A single frame (i.e., 4 phase images)
Axial and lateral motions	Lindner and Kolb (2009)	A theoretical model
Motion blur	Hussmann *et al.* (2010, 2011)	Optical distance measurement and phase-shift algorithm
	Lee (2014)	Pixel-wise motion blur elimination method

Continued on next page

Table 2.2 – continued from previous page

Investigation on	**Paper**	**Methodology/Algorithm**
Transverse motion	Streeter and Dorrington (2014); Streeter (2018)	Coded exposure and optical flow techniques; Kalman filter
Light scattering	Mure-Dubois and Hügli (2007)	Hypotheses of linearity and space invariance
	Jamtsho and Lichti (2010)	An analytical compensation method
	Schäfer *et al.* (2014)	A model, based on raw data calibration and one additional intrinsic camera parameter
Nonlinearity	Godbaz *et al.* (2011)	Harmonic cancellation and heterodyning
Multipath interference	Dorrington *et al.* (2011)	Mixed pixel restoration and multi-path separation algorithm
	Godbaz *et al.* (2012)	Cauchy distribution over range and attenuation ratios
	Fuchs *et al.* (2013)	Photometric calibration and environment integration
	Freedman *et al.* (2014)	Sparse Reflections Analysis algorithm
	Bhandari *et al.* (2014)	Spectral estimation theory

Continued on next page

Table 2.2 – continued from previous page

Investigation on	Paper	Methodology/Algorithm
	Jiménez *et al.* (2014)	Radiometric model under some mild conditions to the surfaces and lights in the scene
	Whyte *et al.* (2015)	Direct and global separation methods
	Marco *et al.* (2017)	Convolutional-deconvolutional neural network
Signal-to-noise ratio	Falie and Buzuloiu (2007)	Low amplitude filtering method
	Gudmundsson *et al.* (2007)	Compare the average of data with a fixed threshold
	Fuchs and May (2008)	Optimal integration time parametrization
	Mufti and Mahony (2011)	Rice distribution and MLE
Random noise	Streeter (2017)	MLE and based on the derivative of correlation signal
Global jitter and/or drift	Streeter *et al.* (2013)	Spatial filtering methods
Cycle-to-cycle jitter	Seiter *et al.* (2014)	Gaussian & triangular-shaped distributions

2.8 Chapter Remarks

AMCW ToF cameras measure three independent parameters of intensity, amplitude and phase which are primarily used for range estimation. Most of these cameras are used in the homodyne operation. The precision and accuracy of ToF full field ranging cameras are important for many applications, however, several noise sources degrade both precision and accuracy. These errors arise primarily due to the factors such as the hardware inadequacies in camera design leading to problems, and light travelling multiple paths in the scene.

This chapter was focused on the introduction of the ToF range imaging cameras and a sufficient investigation of their noise sources with noise mitigation techniques. These error sources directly affect the range measurement and many of them are well examined in the literature. Among those error sources, the motion blurs, non-linearity and multipath interference more adversely affect ranging. Some error sources in these cameras can be mitigated by calibration techniques.

Chapter 3

Jitter and Measurement of Jitter

The previous chapter focused on the noise analysis in range imaging systems. The jitter also affects the noise, and often both noise and jitter occur at the same time. Therefore, in the literature, it is important to investigate the behaviour of jitter in signals of range measurements. This chapter contributes by investigating the jitter in ranging systems. First, a mathematical representation of jitter, the noise-jitter relation and types of jitter in signals are stated. Then jitter sources in ranging systems and three types of approaches, namely, *graphical representation, time and frequency domains*, and *statistical and signal processing domains* for analysing the jitter in signals are described. Next, the jitter impact on range imaging systems and currently available jitter measurement studies relevant to the AMCW ToF range imaging cameras are reviewed. We found only a couple of studies of jitter that related to range measurements in the literature. Those methods are camera dependent and cannot be used for jitter measurement in all ToF range imaging cameras.

3.1 Jitter

As stated in Chapter 2, jitter is the variation in timing. Figure 3.1 shows a signal with jitter (without noise) and its ideal signal. The deviation of the signal nth timing event t_n, from its ideal occurrence in time, is given by

$$\Delta t_n = T_n + \Delta t_{n-1} - T, \tag{3.1}$$

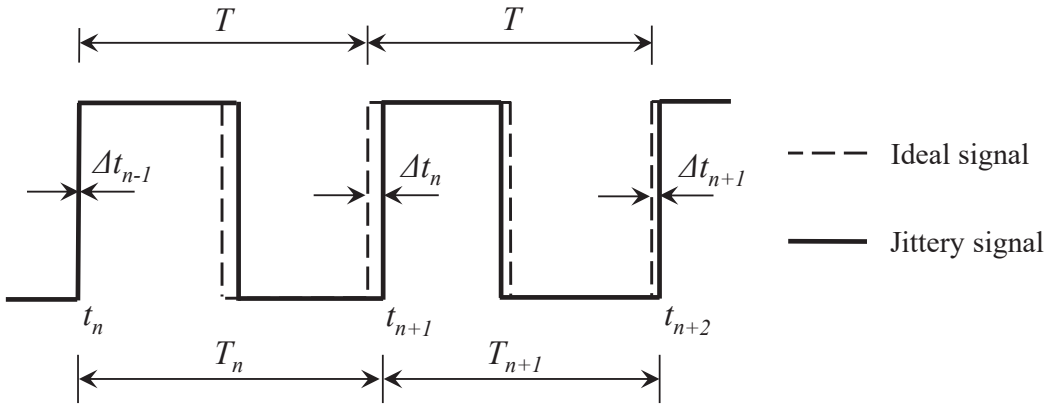

Figure 3.1: Graphical representation of jitter.

where T_n is the nth period (cycle) of the signal given by

$$T_n = t_{n+1} - t_n, \tag{3.2}$$

and T is the period of the ideal signal.

3.2 Impact of Jitter Relation to Phase-Noise

Generally, noise and jitter can affect system performance all the time and often both of them occur at the same time. The impacts of jitter and noise are not linear. Let us consider a sinusoidal signal with the phase modulated by random phase fluctuation $\theta(t)$ is given by

$$\begin{aligned} s(t) &= \sin\left(2\pi f t + \theta(t)\right) \\ &= \sin\left(2\pi f\left(t + \frac{\theta(t)}{2\pi f}\right)\right), \end{aligned} \tag{3.3}$$

and the phase jitter Δt is (Semiconductor, 2007)

$$\Delta t = \frac{\theta(t)}{2\pi f}. \tag{3.4}$$

This gives a mathematical relationship between the jitter and phase-noise in the signal. From this relationship, it is clear that for a given frequency f of the signal, the phase jitter amount increases (or decreases) when the phase fluctuation $\theta(t)$ increases (or decreases). Thus, the phase jitter in a signal is the impact on the phase fluctuation and vice versa causing the effect of the jitter on other noise sources in range measurements.

In practice, the total phase of sinusoidal signals is influenced by several factors such as frequency drift, frequency offset and random phase fluctuations. However, we are considering the signals with the form

$$s(t) = A(t)\sin\left(\Phi(t)\right), \tag{3.5}$$

where $A(t)$ is amplitude of the signal and $\Phi(t)$ is the total phase as

$$\Phi(t) = 2\pi f\big(t + \Delta t^{RJ}(t) + \Delta t^{PJ}(t)\big) \tag{3.6}$$

where $\Delta t^{RJ}(t)$ and $\Delta t^{PJ}(t)$ are the random jitter and periodic jitter, respectively which are introduced in Section 3.3 following and formally defined with mathematical expressions in Section 4.3.

3.3 Types of Jitter in Signals

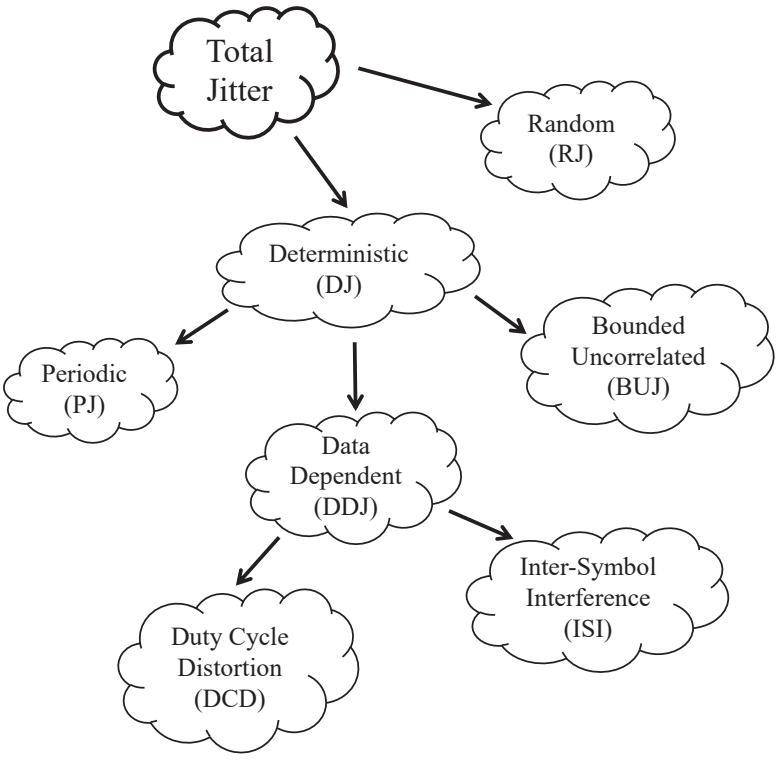

Figure 3.2: Classification of jitter.

The total jitter in a signal is specified by the sum of the components of non-deterministic jitter and deterministic jitter as shown in Figure 3.2. Non-deterministic jitter is due to the random process and is referred to as random

jitter (RJ). This type of jitter often follows a Gaussian distribution and can be characterized by its root-mean-square (RMS) value. In contrast, the deterministic jitter is due to deterministic processes and is linearly additive with a predictable function. It can be characterized by its peak-to-peak (or peak) value. Periodic jitter (PJ), bounded uncorrelated jitter (BUJ) and data dependent jitter (DDJ) which consists with duty cycle distortion (DCD) and inter symbol interference (ISI) are sub-categories of the deterministic jitter (Li, 2007). Many of these jitter types are only relevant to a communication system carrying data. No jitter depends on the data in the modulation light signal of the AMCW ToF cameras.

PJ refers to periodic variations of signal edge positions over time and is often due to electromagnetic interference sources such as power supplies. There can be multiple PJs of various frequencies and these follow the superposition rule, and each can be characterised by its amplitude and frequency. BUJ is typically caused by coupling from adjacent data-carrying links. This type of jitter is bounded due to coupling strength, and uncorrelated because there is no correlation to the channel's data pattern. The models depend on the data pattern, coupling signal and its mechanism (Kuo *et al.*, 2005).

The DDJ corresponds to a variable jitter that depends on the bit pattern transmitted on the link under test. In addition, DCD describes a jitter amounting to a signal having unequal pulse widths for high and low logic values, this means that the duty cycle of the high speed clock will be directly translated into the overall DCD. ISI refers to the band limited characteristic of the transmitted patterns (i.e., cable, driver, connectors); this effect is proportional to the number of consecutive equal transmitted bits and patterns on the same trace. Various edge patterns have various frequency components. Because of the conductors filtering effects, different patterns propagate at different speeds through the conductors. This difference in propagation speeds causes bits to smear into adjacent bits, resulting in ISI (Kuo *et al.*, 2004; Li, 2007).

3.4 Jitter Sources in Ranging Systems

All the jitter types described in Section 3.3 occur in signals carrying the data such as in a telecommunication system. The modulation signal of the ranging camera contains certain types of jitter since it carries only an unchanging datum (i.e., the phase only) therefore, DDJ and BUJ which depend on transmission data do not occur in the modulation signal of ranging cameras. The

jitter sources in ToF cameras are related to the behaviour of the camera sensor, light source and transmission media. Let's consider the jitter sources for the two major components: random and deterministic.

3.4.1 Sources for Random Jitter

Random jitter is due to random noise inherent in electronic circuits and typically follows a Gaussian distribution. Also, stochastic sources such as white noise, thermal noise, shot (Poisson) noise, flicker noise, and other high-order noise processes are lead to present the random jitter (Rapp *et al.*, 2008; Patrin and Li, 2002).

3.4.1.1 Thermal Noise

This is associated with electron flow in conductors and increases with bandwidth, temperature, and noise resistance. When limited to a finite bandwidth, thermal noise has a nearly Gaussian distribution. This type of noise is also refereed as Johnson-Nyquist noise (Johnson, 1927).

3.4.1.2 Shot or Poisson Noise

This is a type of electronic noise which can be modelled by a Poisson process. In electronic shot noise originates from the discrete nature of the electric charge. This also occurs in photon counting in optical devices which is associated with the particle nature of light.

3.4.1.3 Flicker Noise

This is proportional to the reciprocal of the frequency. It is only of concern in low frequency measurements. It is normally found in resistors, diodes, switches and transistors, among other components. Typically, it must be measured empirically (by observation).

3.4.2 Sources for Deterministic Jitter

Generally, due to the imperfections in the behaviour of the device or transmission media that occur the deterministic jitter. In addition, signal modulation, crosstalk and reflections on signals can all lead to deterministic jitter on the light and shutter modulation signals (Falie and Buzuloiu, 2007).

3.4.2.1 Crosstalk

This arises by accidental coupling of a magnetic and/or electric field to an adjacent conductor carrying a signal. The unwanted components are added to the original signal altering its bias determined by the amount of the interference signal.

3.4.2.2 Electromagnetic Interference

This results from conducted and radiated emissions undesirably radiated from the system. Switching power supplies which radiate strong, high frequency magnetic and electric fields conducting a large amount of electrical noise are some common sources that lack adequate shielding and output filtering in the system. These sources are related to periodic jitter.

3.4.2.3 Reflection

This is caused by interference of the signal with itself occurring when impedance mismatches exist. A portion of the energy is reflected back to the transmitter if an impedance mismatch exists at the receiver, coming from uncontrolled stubbing and incorrect terminations. Likewise, if the mismatch is at the transmission end, it ingests part of the reflected energy, and the receiver gets reflected the remainder. Ultimately, the receiver gets the delayed signal out of phase with the original one which is algebraically added with the first arriving signal.

3.4.2.4 Data-Dependent Phenomena

This is often caused by the frequency response of a cable or device. Amplitude offset errors, turn on delays and saturation may be some of the causes of DCD. ISI occurs when the frequency component of the data is propagated at different rates by the transmission medium.

3.5 Analysis of Jitter in Signals

Total jitter, namely both deterministic and random are mixed. In a signal with jitter, the zero-crossing transitions of the cycles are seen to vary in time from the ideal clock timing. Jitter can be characterised, depending on the type of jitter, by parameters such as the amplitude and frequency of the jitter. Jitter amplitude is a measure of the typical time displacement in units of time. If the

jitter values are repetitive then the frequency of the repetition is of interest. The time displacement of a digital signal is equivalent to variations in the signal's phase.

Controlling jitter is a valuable task because jitter can degrade the performance of electronic systems. Measurement of jitter can be performed in the time-domain or frequency-domain with the help of statistical and signal processing techniques. In addition, various kind of jitter measuring instruments are commercially available such as the pulse/pattern generator, spectrum analyser, real-time sampling oscilloscope, digital communications analyser and the bit error ratio tester (Hancock and Draving, 2004; Cohen, 2005). All of these instruments require an accurate reference clock to trigger the time measurement unit to measure jitter. The rest of this section briefly describes three common approaches to analyse the jitter in signals: (1) graphical, (2) time and frequency domains and (3) statistical and signal processing techniques.

3.5.1 Graphical Approaches

Jitter in a signal can be analysed by graphical representation techniques such as the *eye diagram, histogram* and *bathtub plot* with each having limitations (Shinagawa *et al.*, 1990; Kuyel, 2003; Hancock *et al.*, 2004; Dou and Abraham, 2006). The accuracy of these techniques can only be guaranteed if the jitter measurement is carried out on realtime measuring instruments with very large memory depth to acquire sufficient data.

3.5.1.1 An Eye Diagram

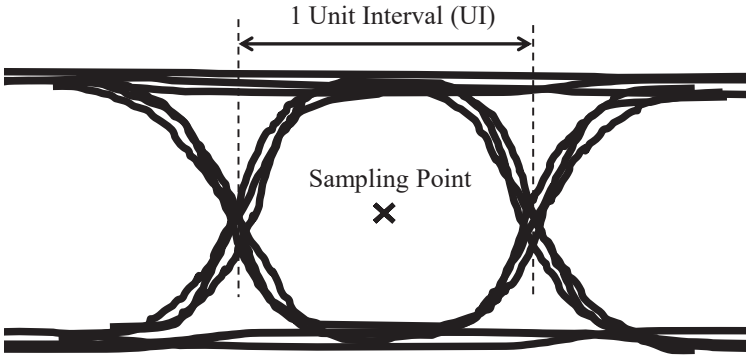

Figure 3.3: A picture of an eye diagram.

The effect of both noise and jitter can be represented by the eye diagram, in which many data voltage levels (bit periods) and edge transitions are super-

imposed over a one unit interval (UI) range as shown in Figure 3.3 (Li, 2007). An eye diagram gives an overall statistical qualitative view of the quality of the signal under test. It helps for both quantitative and qualitative insight regarding the data signal path itself and what might be affecting signal integrity. The horizontal and vertical eye openings are important characteristics of the eye diagram that aid in measuring the signal quality. The horizontal eye opening is expressed as a percentage of the bit interval while vertical eye opening is expressed as a percentage of the full eye height. A large, wide-open eye in the centre (marked by $\times$) shows the ideal location for sampling each bit. At the sample point, the waveform should have settled to its low or high value and this indicates that the data stream has very little noise and jitter. As the sum of skew and noise increases, the eye closes and data is corrupted. An eye diagram with a small opening (eye closure) indicates that the data is affected greatly by jitter. Lowering the height enters the input voltage threshold while closing the width decreases the time available for accurate reception. Both opening and closure of the eye add up to 100% (Säckinger, 2005).

3.5.1.2 Histogram

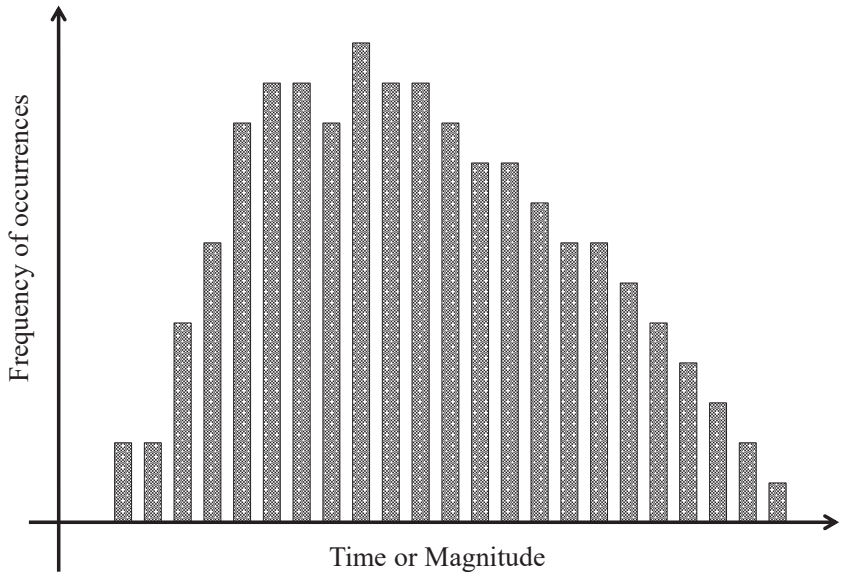

Figure 3.4: A picture of a histogram.

The histogram plots the frequency of occurrence of jitter presentable versus the range of values (bins) of a chosen parameter (time or magnitude). This is also known as a jitter histogram. It shows the shape of the statistical distribution of parameter values as illustrated in Figure 3.4. The histogram

provides a level of insight that the eye diagram cannot, such as a separating random jitter from deterministic jitter types. Histograms are essential data sets for jitter-separation routines required by various digital bus standard (Hancock *et al.*, 2004). If the histogram is normalized such that the integral is unity, it may become an approximate probability density function (PDF) of jitter. However, this PDF does not always give the actual PDF, sometimes it makes large errors (e.g. when the number of bins is not sufficient).

3.5.1.3 Bathtub Curve

This is usually created with bit error ratio testers (BERT), therefore it is referred to as BERT scan and presumably is only relevant to a communication channel. A BERT generates data to pass through a device under test (DUT) and then measures the transmitted data and compares for errors, thus determining the bit error ratio (BER) as depicted in Figure 3.5. As the measurement location (i.e., sampling point) is swept across a unit interval (UI), a plot of BER as a function of the UI is constructed. This plot typically resembles a cross section of a bathtub, thus the name *bathtub curve*.

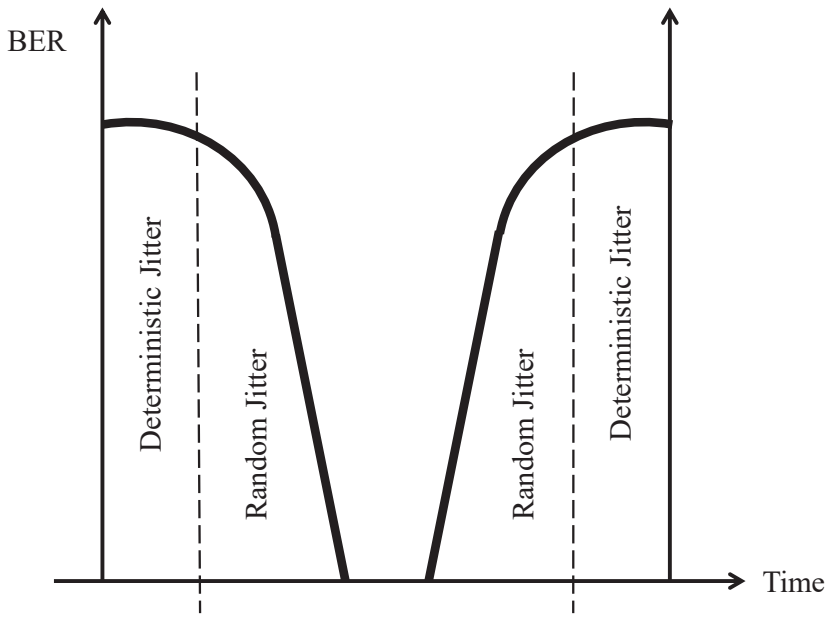

Figure 3.5: A picture of a bathtub curve.

When the sampling point nears the transition points, this curve is fairly flat which is dominated by deterministic jitter. As the sampling point moves inward from both ends of the UI, the BER drops very steeply which is caused

by random jitter. Thus, the bathtub curve can also be used to separate random and deterministic jitter in communication signals (Hancock *et al.*, 2004).

In addition to these graphical analyses, there are other jitter measurement methods in the time domain and frequency domain with statistical and signal processing approaches.

3.5.2 Time and Frequency Domains

Jitter can be calculated in the time domain and/or frequency domain by Fourier transform (FT) and power spectrum density (PSD). Cosart *et al.* (1997) described the measurement of phase modulation and noise using time domain techniques. They presented a model for the relationship between zero crossings and phase on a signal and concluded measurements can be made on data signals eliminating the need for external data clock recovery. Later, a time-domain jitter separation method was introduced by Li *et al.* (1999) as a general-purpose automated search and non-linear fitting algorithm for both deterministic and random jitter components. They fitted the tail parts of the jitter histogram with non-linear jitter models and calculated bit error rate for each category. To reduce deterministic jitter, adding pre-emphasis (or de-emphasis) helps by improving the signal's high-frequency content (i.e., improves SNR). For random jitter, there comes a point where these techniques would not provide enough compensation. The solution is re-clocking, which requires a phase-locking technique.

An analytic signal method to extract both RMS and peak-to-peak jitter values from phase-locked loops (PLLs) was presented by Yamaguchi *et al.* (2000). This method relied on the extension of a real signal into an analytic signal by utilizing the Hilbert transform. The authors considered the jitter as the variation of the edge position (or zero crossing) at each cycle. Later, Yamaguchi *et al.* (2001) extended this method for measuring the cycle-to-cycle period jitter in PLL output signals and verified the relationship with the power spectral density of total phase. The more widely the cycle-to-cycle period jitter spreads power into the sidebands of the phase noise spectrum. This method has been used for measuring jitter of the bit clock signal in telecommunication devices operating at 10 Gbps (Yamaguchi *et al.*, 2002).

Jitter can also be analysed in the frequency domain by using the Fourier transform, then the energy of the resulted jitter spectrum can be used to calculate the jitter components by application of one of several techniques (Yamaguchi *et al.*, 2002, 2007; Pang *et al.*, 2009). Some require a jitter-free

sampling clock signal (or reference signal) to perform spectral analysis on the signal. As an example, the fast Fourier transform (FFT) and time lag correlation (TLC) functions have been used by Pang *et al.* (2009) to measure jitter in simulation experiments. Yamaguchi *et al.* (2007) proposed an algorithm based on FFT and probability density function *blind separator* to estimate both random jitter (RJ) and deterministic jitter (DJ). They assumed that the probability density function noise is distributed at high frequencies while both RJ and DJ is distributed around low frequencies (or DC).

The TLC functions and FFT with TLC functions have been used by Dou and Abraham (2006) and Pang *et al.* (2009), respectively, on simulation experiments. Both of them have used a reference clock signal for the ideal signal. To reduce the number of equations, Pang proposed using the FFT which reduces the calculation time. The relationship between the time domain jitter measurements and the power spectrum of the phase jitter by using fundamental Fourier properties with basic random variables analysis were presented by Moon *et al.* (2002). They concluded that the phase jitter for a specific number of clock cycle delays in any self-referenced measurements can be extended to define other jitter measurements.

In addition, random and periodic jitter is measured in simulated noisy signals by using the frequency spectrum and calculating the energy of the jitter spectrum (Anthonys *et al.*, 2018a). Instead of the reference clock, they used Fourier analysis to obtain the corresponding ideal signal for the simulated signal.

3.5.3 With Statistical and Signal Processing Techniques

It is well known the statistical analysis and digital signal processing are common methods to investigate the signal filtering in any field of use. In the literature, the statistical analysis for jitter measurement is used in the time domain or frequency domain. The effects of independent additive noise on timing jitter for pulse amplitude modulation data signals were evaluated by Franks and Bubrouski (1974). They have shown the minimum variance of the timing wave was increased by a Gaussian additive noise term similar in form to the constant term in the noise-free case.

For the random jitter in sampling systems, Souders *et al.* (1989) has used the sample mean as the Markov estimator and approximated in the frequency domain by a simple filter function. They have proven the Markov estimator is asymptotically converged to the population median and it is, therefore, an

unbiased estimator for monotonic waveforms sampled with jitter distributions having a median of zero.

Most of the literature on statistical analysis for the noises and signal measurements in ToF cameras assumes that the signals are in Gaussian distribution (Moller *et al.*, 2005; Büttgen *et al.*, 2005). However, an individual statistical distribution of the modulated samples is considered to formulate a statistical model for the parameters of amplitude, phase and intensity by Mufti and Mahony (2011). They used the effect of photon shot noise to analyse ToF measurements under various SNR conditions, which is a key parameter for the reliability of the range measurements. The authors have concluded that the proposed SNR estimator based on maximum likelihood estimation has better performance than based on Gaussian assumption. They used the Rice distribution (Rice, 1945), which has the uniqueness and unbiased maximum likelihood estimators for large data sets (Carobbi and Cati, 2008).

Moreover, a statistical model for simulation of direct time of flight for 3D imaging and ranging applications has been presented by Nguyen *et al.* (2013). Four different peak-detection algorithms have been used for quantifying the data and then have determined the effect of signal, noise and jitter levels on the depth resolution achievable by the system. The comparison between the tail fitting algorithm and spectrum analysis on jitter estimation were investigated by Sharma *et al.* (2014). They concluded that using the tail fitting algorithm in presence of DDJ was caused an error while in spectral analysis; error percentage was large in the presence of high frequency PJ.

Tarczynski and Allay (2004) proposed two algorithms, named, the weighted sample and weighted probability density functions to find digital alias-free estimation signal spectrum. They limited the usage of the algorithms on two factors: the level of the spectrum estimation error and sampling instant jitter. They concluded the spectrum estimation error resembles a wideband noise while the jitter introduces bias to spectrum estimation.

A method for jitter estimation in ADC has been introduced by Wu *et al.* (2012). They used a single high frequency test without coherent sampling to significantly save the hardware and data acquisition time. Later, this method has been extended by Wu *et al.* (2015b) for jitter and noise separation in ADC test, based on the property that jitter is modulated by the slope of the input signal. Wu *et al.* (2015a) have applied this method to separate the random and periodic jitter in ADC output by involving only one FFT and one IFFT operation.

3.6 Impact of Jitter on Range Imaging

Researchers have barely investigated jitter related to the AMCW ToF ranging systems. A couple of studies that affect the jitter on range measurements were found and both of them are related to random jitter (Streeter *et al.*, 2013; Seiter *et al.*, 2014). The investigations on the periodic jitter in ToF range imaging cameras are not studied in the literature.

The possibility of the jitter and/or drift between the modulation signals and the camera shutter was investigated by Streeter *et al.* (2013). The variations in phase and frequency were modelled in a linear model by using an algorithm which is used for jitter correction. The model is solved after computing the jitter parameters of the current frame with respect to the reference frame by using linear regression. The root-mean-square error (RMSE) values with respect to the reference image are analysed to consider the effect of those filtering methods. They concluded that the combination of the filters *Bilateral* and *Non-local means* perform well with their de-jitter algorithm, which depends only on the assumption that jitter affects equally all pixels in the scene.

Seiter *et al.* (2014) investigated the impact of two common types of cycle-to-cycle jitter distributions, namely, a random Gaussian and discrete jitter distributions on the performances of ToF measurements. They proved a discrete jitter has a strong impact while the random Gaussian jitter has a negligible impact on the performances, by analysing the standard deviation of the obtained measurements. There is therefore a disagreement between those two papers, on the importance of different types of jitter on range measurement.

3.7 Chapter Remarks

The noise and jitter in a signal can be analysed by different approaches in time and frequency domains with the help of statistical and signal processing techniques. Many of the noise sources such as nonlinearity, multipath interference and harmonic cancellation are well investigated in the literature, but the jitter related to the ToF ranging systems is barely investigated. We found only a couple of studies and there is a disagreement between those two studies regarding the importance of different types of the jitter in ToF range imaging cameras (Streeter *et al.*, 2013; Seiter *et al.*, 2014).

Thus, there is a huge gap in the knowledge of jitter investigation in the AMCW ToF range imaging cameras such as extraction and how effect, type

and amount of jitter has most effect on range measurements. All of these are unanswered investigations in the literature. In addition, these investigations are important in the depth sensor manufacturing industries as well. Therefore, the jitter investigation of the AMCW ToF range imaging is highly significant for the exploration of reducing the aforementioned gap in ToF ranging systems. Thus, the rest of the chapters of this thesis contribute to minimizing this gap as much as possible.

In contrast, in Chapter 4, we will propose a common algorithm (camera independent) to extract the jitter in the AMCW ToF ranging systems without using a sampling clock to trigger the time measurement unit. Instead, we use signal processing techniques in the proposing algorithm.

Chapter 4

Algorithm for Jitter Extraction in AMCW ToF Range Imaging

As described in the last chapter, jitter in ToF ranging systems has barely been investigated in the literature. This chapter proposes an algorithm for extraction of the periodic and random jitter in the light source of any AMCW ToF range imaging cameras. This algorithm can be used for jitter extraction in any analogue or digital signal without requiring a reference or sampling clock signal to trigger the time measurement unit. In addition, the algorithm is tested on the generated simulation data with various numerous values for the characteristic parameters of the signal and jitter. The corresponding results with discussion are included at the end of the chapter.

4.1 Background

There are only two studies that the author is aware of that investigate the effect of jitter in ranging with AMCW ToF range imaging cameras (Streeter *et al.*, 2013; Seiter *et al.*, 2014). These studies considered only the effect of random jitter on measurement in specific ToF cameras. The author is not aware of any investigations on the extraction of periodic jitter in the light signal of ToF cameras in the literature. It is a very challenging task to completely extract the sources of jitter in range imaging applications, because it is impossible to get to the internal signals without disassembling the camera, and even then, specific signals may not be accessible. Therefore, we focus on jitter in the emitted light signal which is sensible since the light signal of the camera is relatively straightforward to access. However, it was noted in the last chapter that an accurate reference clock is needed to enable jitter extraction in a signal.

Since we have no access to the reference clock, we develop a method here to generate the reference clock (ideal signal) for the camera from its measured data without involving any other signal or data and this is the novelty of the proposed algorithm. Fourier analysis and signal processing techniques for generating the reference clock signal are described in the following sections.

4.2 Proposed Methodology

The main steps of the methodology used to extract the jitter components in the ToF cameras we tested are shown as a flowchart in Figure 4.1. This proposed method can be used for real time jitter investigation for all AMCW ToF range imaging cameras since the light sources of these cameras are directly accessible. The detailed description for step ① to step ⑥ of this flowchart will be discussed in the next subsections while step ⑦ is separately explained in Section 4.3. In addition, they are illustrated with sub steps as a descriptive flowchart in Figure 5.1 of Chapter 5.

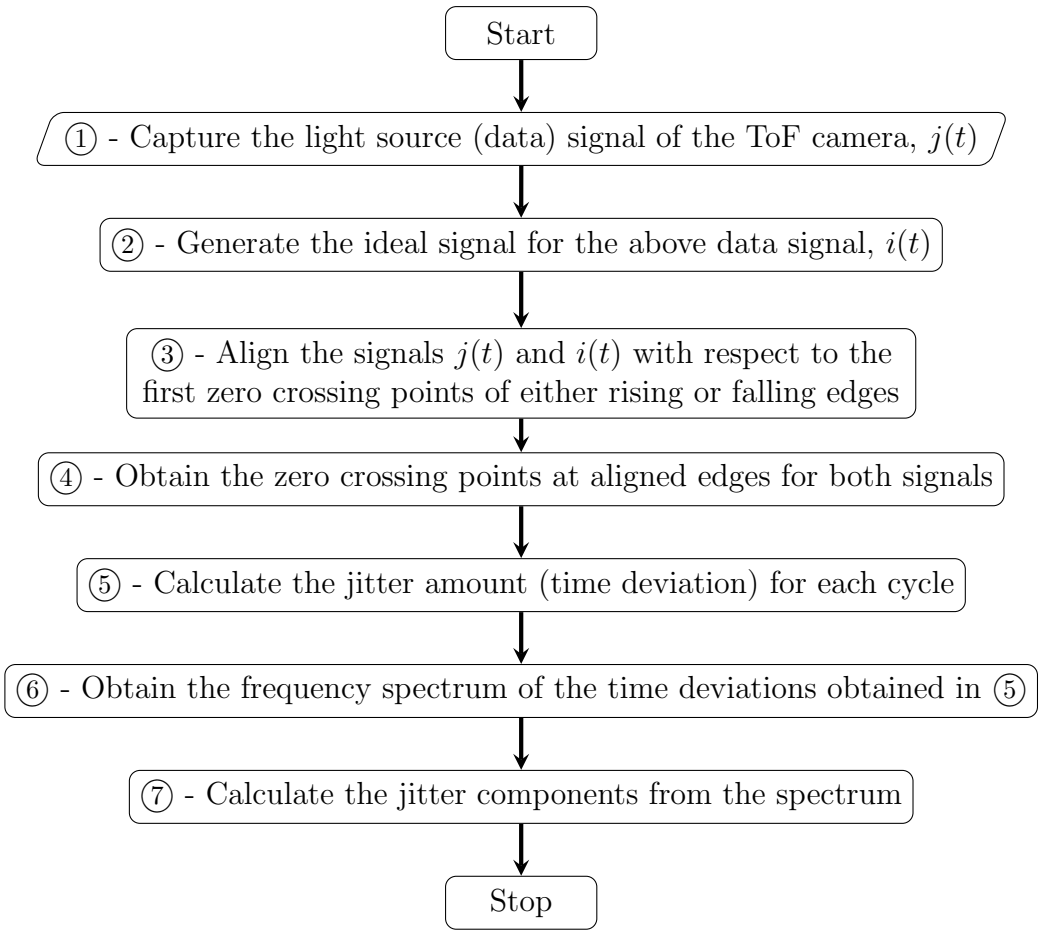

Figure 4.1: Algorithm for jitter extraction in ToF range imaging cameras.

In step ①, we capture the data signal from the light source of the camera. In general, this signal consists of noisy data at the intersections of the time axis (zero crossing points). Therefore, in order to clearly identify the zero crossings of the data signal, we smooth it by using the Savitzky-Golay filtering algorithm (Savitzky and Golay, 1964) with minimal impact on the signal.

4.2.1 Signal Smoothing

The main idea of this method is to find the weighting coefficients (i.e., convolution integers) to carry out the smoothing operation by fitting the data y_k to a polynomial for each value of the data with $2m + 1$ neighbouring points (including the point to be smoothed), with m being equal or greater than the order of the polynomial. Savitzky and Golay have shown that a moving polynomial fit can be numerically handled in exactly the same way as a weighted moving average, since the coefficients of the smoothing procedure are constant for all y_k (Savitzky and Golay, 1964). Let $\mathcal{C}_i$ for $i = -m, -m + 1, \ldots, m$ be $2m + 1$ weighting coefficients for data y_k. Then, by using the weighted moving average method, the smoothed data $y_k^{(s)}$ can be computed by (Orfanidis, 1996)

$$y_k^{(s)} = \frac{\sum_{i=-m}^{m} \mathcal{C}_i \, y_{k+i}}{\sum_{i=-m}^{m} \mathcal{C}_i}. \tag{4.1}$$

The Savitzky-Golay algorithm finds the weights $\mathcal{C}_i$ that are optimal in the sense that they minimize the least-squares error in fitting a polynomial to frames of noisy data. The advantages of the SG algorithm include that it smooths the fluctuations and increases the signal-to-noise ratio without significant distortion of the analysed data. Also, the SG algorithm uses all data and does not exclude outliers, and the smoothed values can be expressed as a linear transformation of the input values (Kawala-Sterniuk *et al.*, 2020).

For step ②, we generate the corresponding sinusoidal ideal (reference) signal for the camera. For that, the relevant frequency and amplitude of the ideal signal have to be found. First, we obtain the Fourier spectrum of the smoothed data signal, find the relevant frequency at the maximum magnitude, and perform quadratic interpolation with its neighbours to find the frequency of the ideal signal.

4.2.2 Frequency Estimation for the Ideal Signal

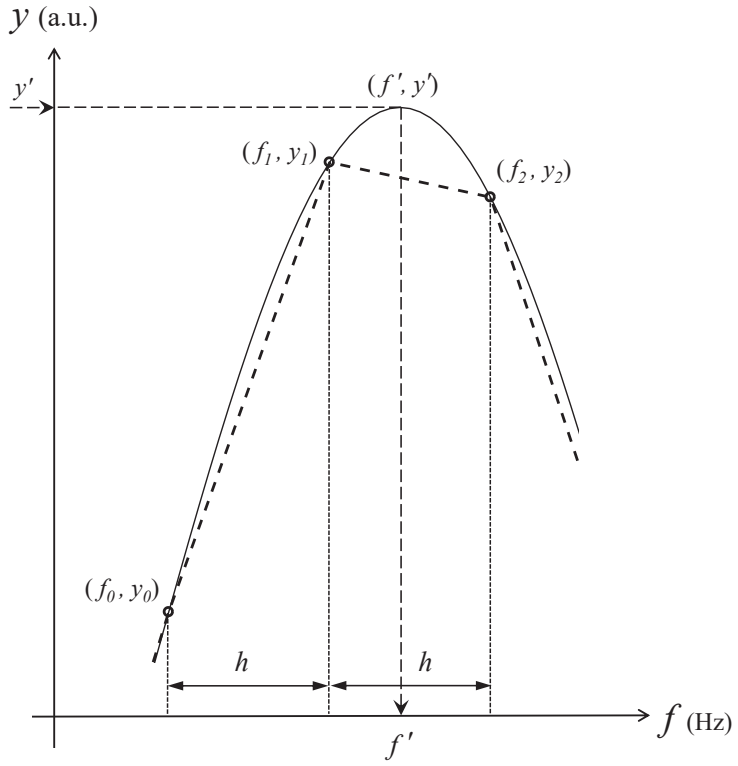

Figure 4.2: Estimation of the frequency by quadratic interpolation.

If the sampling rate is sufficiently high with respect to the frequency of the cross-correlation, the quadratic (parabolic) interpolation would give unbiased estimates (Céspedes *et al.*, 1995). Also, this method is fast and simple to implement. A parabolic curve between three adjacent points is placed in the quadratic interpolation method. Figure 4.2 illustrates the peak with its three closest neighbour samples (f_0, y_0), (f_1, y_1) and (f_2, y_2), from the Fourier spectrum of a smoothed signal and let the coordinate of the peak be (f', y'). Then, a quadratic polynomial (or parabola) for the peak can be expressed, namely (Chapra and Canale, 2015).

$$y = y_0 + \frac{(y_1 - y_0)}{(f_1 - f_0)}\left(\frac{f - f_0}{h}\right) + \frac{(y_2 - y_1)(f_1 - f_0) - (y_1 - y_0)(f_2 - f_1)}{2(f_2 - f_1)(f_1 - f_0)(f_2 - f_0)}\left(\frac{f - f_0}{h}\right)\left(\frac{f - f_1}{h}\right) \quad (4.2)$$

At the peak, it should satisfy,

$$\left.\frac{dy}{df}\right|_{(f', y')} = 0 \quad (4.3)$$

and gives

$$f' = f_0 + \frac{h}{2}\left(\frac{y_2 - 4y_1 + 3y_0}{y_2 - 2y_1 + y_0}\right). \tag{4.4}$$

Thus, the corresponding frequency of the ideal signal can be calculated from Equation 4.4. Note that if the sample rate does not properly match the signal frequencies then spectral leakage will occur in the Fourier spectrum of the signal. That is, spectral leakage results in a single-tone frequency bin spread among several frequencies in the Fourier domain and causes error in determining the ideal signal frequency. The magnitude of the error depends on the location of the actual peak of the cross-correlation function with respect to the location of the samples. Boucher and Hassab (1981) developed general expressions of the mean and variance of the time delay that is estimated using parabolic interpolation as a function of the spectral characteristics of the signal.

4.2.3 Amplitude Estimation for the Ideal Signal

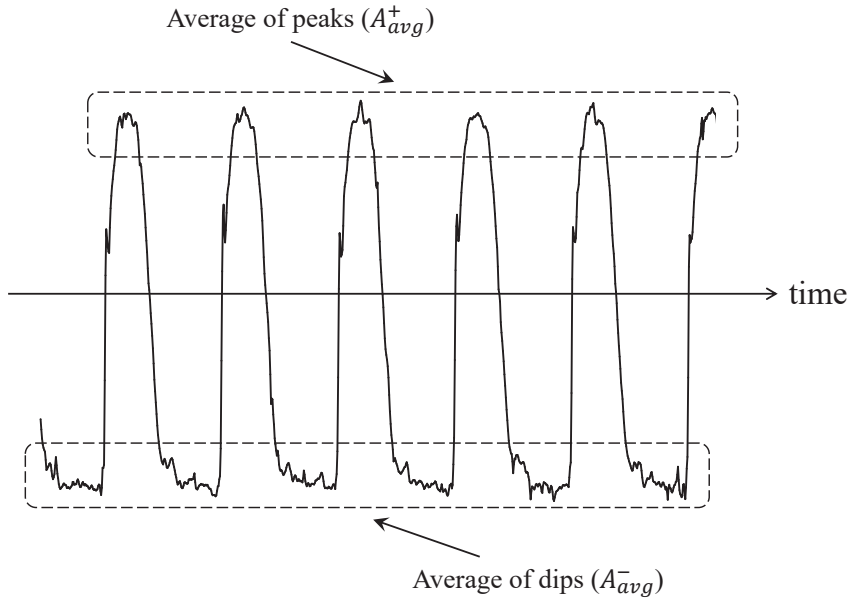

Figure 4.3: Estimation of the amplitude by averaging peaks and dips.

It is well known that the magnitude of the fundamental of the harmonic in the FFT can be used as an amplitude for the ideal signal. But we use a special technique since this special method involves the whole signal rather than the previous method. Both methods give approximately the same values. As an

example, let us consider a smoothed signal obtained from step ① as shown in Figure 4.3. In order to find the amplitude for the ideal signal A', we first take the averages of the peaks and dips within a threshold value, separately, namely

$$A^{+}_{avg} = \frac{1}{K_1}\sum_{k_1=1}^{K_1} A^{+}_{k_1}, \tag{4.5a}$$

$$A^{-}_{avg} = \frac{1}{K_2}\sum_{k_2=1}^{K_2} A^{-}_{k_2}, \qquad K_1, K_2 \in \mathbb{Z}^{+} \tag{4.5b}$$

then, take mean among them as

$$A' = \frac{A^{+}_{avg} + |A^{-}_{avg}|}{2}. \tag{4.6}$$

Therefore, the corresponding amplitude of the ideal signal can be calculated from Equation 4.6. Note that the accuracy of the signal's amplitude is not important since the zero crossings on the time axis are not dependent on the amplitude of the signal. However, this estimation can be used to compare the ideal and data signals visually.

Next, both signals (data and ideal) are aligned with respect to the first zero crossing point of either rising or falling edges as for step ③ in our proposed algorithm. We choose rising edges. In order to find the zero crossing points, we choose the two corresponding values that sit either side of the zero crossing for each cycle. The shape of the signal is very close to the straight line near the zero crossings. By using linear interpolation, the zero crossing points at rising edges for both signals are estimated, this being step ④. Also, this method provides faster results than other techniques (Maeland, 1988).

4.2.4 Identifying Zero Crossings

Figure 4.4 shows an example of the linear interpolation technique. Let the points (t_1, ν_1) and (t_2, ν_2) be the coordinates of the corresponding points that sit either side of the zero crossing for a cycle. Also, let (t', ν') be the relevant point of the zero crossing of that cycle (note that $\nu' = 0$). By considering the geometrical relation of the two triangles, it is not difficult to obtain

$$(\nu' - \nu_1)(t_2 - t_1) = (\nu_2 - \nu_1)(t' - t_1) \tag{4.7}$$

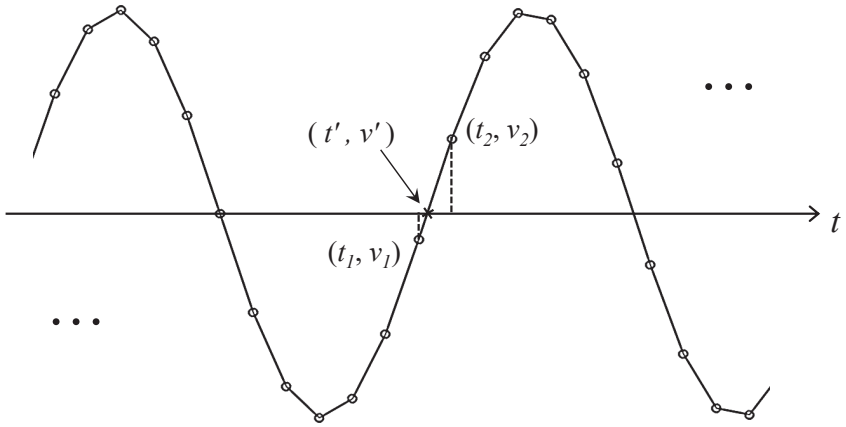

Figure 4.4: An example of linear interpolation technique.

and then, the corresponding zero crossing point at the rising edge can be computed by simplifying Equation 4.7 with $\nu' = 0$, thus,

$$t' = \frac{t_1\nu_2 - \nu_1 t_2}{\nu_2 - \nu_1}, \qquad \nu_2 \neq \nu_1. \tag{4.8}$$

We separately use Equation 4.8 to obtain more approximate zero crossings at rising edge for each signal.

In step ⑤, the jitter $\Delta t(t)$ of each rising edge of the signal is calculated at the time difference between the zero crossing points (obtained in step ④) of the data and ideal signals of the camera. For step ⑥, the frequency-domain spectrum is obtained by using the discrete Fourier transform (DFT) of the jitter signal. The number of cycles captured for the camera $N_{\Delta t}^{cal}$ depends on the modulation frequency f_m, the number of samples N_s in the acquired time-domain signal, and the sample rate of the acquisition F_s. This is

$$N_{\Delta t}^{cal} = \frac{f_m N_s}{F_s}. \tag{4.9}$$

Note that because the length of the signal is somewhat arbitrary there is no guarantee of complete sampled cycles of any periodic jitter present in the signal. The DFT assumes periodicity of the time-domain signal, which Equation 4.9 violates. Therefore, we take the nearest integer value $N_{\Delta t}$ by taking the floor of Equation 4.9 as

$$N_{\Delta t} = \text{floor}\left(N_{\Delta t}^{cal}\right) = \left\lfloor N_{\Delta t}^{cal} \right\rfloor, \tag{4.10}$$

and this is the corresponding total number of jitter samples for the experiment

(with respect to the acquisition setup used). The real problem is that a N-point DFT assumes the signal is repeated every N-points throughout all time. But for arbitrary $N_{\Delta t}$ and periodic jitter frequency, this assumption is violated. This discontinuity of the signal leads to spectral leakage in the spectrum, which is the phenomenon whereby the energy of a single sinusoidal signal (frequency) is spread out into neighbouring bins of the spectrum.

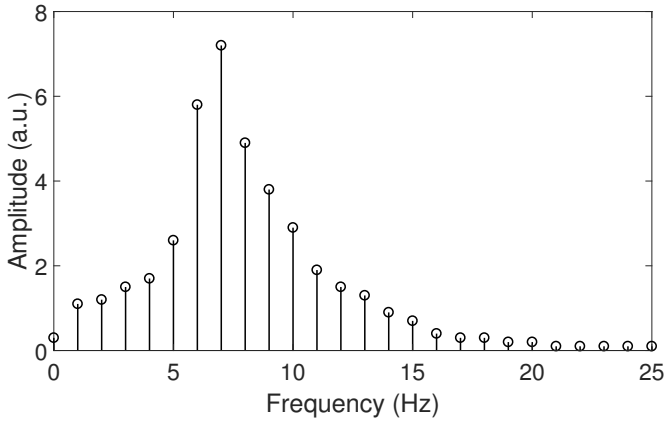

Figure 4.5: The effect of spectral leakage.

That is, the non-integral cycle frequency component of the signal does not correspond exactly to one of the spectra frequency lines as shown in Figure 4.5. Therefore, the obtained spectrum is not the actual spectrum of the original signal, but a spread version.

4.2.5 Minimization of the Spectral Leakage

The effects of spectral leakage can be minimized by a windowing function to smoothly attenuate both ends of the data towards zero. We use the Hann (sometimes referred to as Hanning) window which is more sophisticated for random and periodic analysis for Fourier spectra (Oppenheim *et al.*, 1999). The Hann window (Blackman and Tukey, 1958) is

$$w_{H}(n) = \sin^2\left(\frac{\pi n}{N-1}\right), \qquad n = 0, 1, \ldots, N-1. \tag{4.11}$$

Because the signal is windowed, less energy ends up in the spectrum which leads to a reduction of the signal amplitude, and this must be taken account of. Window correction factors are used to try and compensate for the effects of applying a window to data. There are both amplitude and energy correction factors. It is possible to correct both the amplitude and energy content of the windowed signal to equal the original signal.

The coherent gain of a window is defined as the sum of the coefficients of the window function over the interval (Lyons, 2011). Thus, the amplitude correction factor for the Hann window A_{H}^{cf}, is obtained by taking the reciprocal of the coherent gain, namely

$$\begin{aligned}\mathrm{A}_{H}^{cf} &= \left(\int_0^1 w_{H}(nt)\,dt\right)^{-1} \\ &= \left(\frac{1}{2}\left[t - \left(\frac{N-1}{2\pi n}\right)\sin\left(\frac{2\pi n\, t}{N-1}\right)\right]_0^1\right)^{-1} = 2.0. \end{aligned} \tag{4.12}$$

The incoherent gain is defined as the root of the sum of squares of the coefficients of the window function over the interval (Lyons, 2011). The energy correction factor for the Hann window E_{H}^{cf}, is obtained by the reciprocal of the incoherent gain as

$$\begin{aligned}\mathrm{E}_{H}^{cf} &= \left(\sqrt{\int_0^1 \Big(w_{H}(nt)\Big)^2 dt}\,\right)^{-1} \\ &= \left(\sqrt{\frac{1}{4}\left[\frac{3t}{2} - \left(\frac{N-1}{\pi n}\right)\sin\left(\frac{2\pi n\, t}{N-1}\right) + \left(\frac{N-1}{8\pi n}\right)\sin\left(\frac{4\pi n\, t}{N-1}\right)\right]_0^1}\right)^{-1} \\ &= \sqrt{8/3}. \end{aligned} \tag{4.13}$$

Then, each spectral line of the windowed frequency spectrum are multiplied by the above corresponding fixed factor. If the energy of the signal lands in a single bin (which is very unlikely to occur) then the periodic jitter can be computed by multiplying the corresponding peak with Equation 4.12.

But, if general, the energy of the signal is spread over multiple bins due to leakage and to correctly calculate the amplitude of the signal one must include the full energy of the signal. Therefore, in this case, Equation 4.13 must be used to correctly calculate the amplitude, hence the amount of jitter. The relevant portion of the peak (with neighbouring bins) can be obtained by choosing the interpolation level (see Figure 4.7) between the periodic and random jitter in the windowed spectrum. The interpolation level (IL) is computed by

$$\mathrm{IL} = \mu \pm \alpha\,\sigma, \qquad \alpha \in \mathbb{N} \tag{4.14}$$

where μ and σ are the mean and standard deviation of the windowed spectrum, respectively and α is chosen by visual inspection.

Finally, in the last step ⑦, the corresponding jitter parameters for the camera are extracted as described in Section 4.3.

4.3 Jitter Extraction Using the Spectrum

Since our ultimate goal is to extract the jitter in the light source signal of the AMCW ToF cameras, we focus on the random jitter and periodic jitter. Other types of jitter are not meaningful to the light source since they are data dependent. The first part of this section explains the extraction and calculation of the corresponding parameters of the random and periodic jitter from the jitter spectrum. The second part describes further analysis of the jitter spectrum by using the technique of curve fitting with the logarithmic scale.

4.3.1 Calculation of the Jitter Components

Figure 4.6 shows a sinusoidal signal (ideal) and its jittery signal. As previously described, the jitter amount for the nth cycle is given by $\Delta t_n = t_{n+1} - t_n + \Delta t_{n-1} - T$.

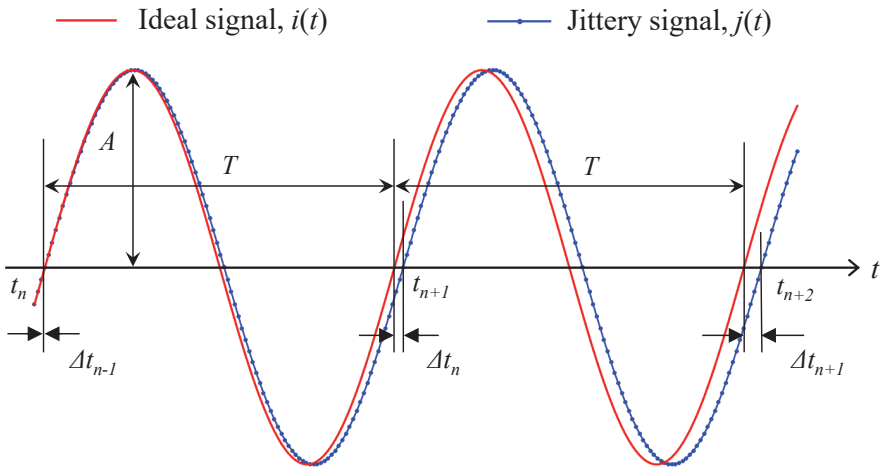

Figure 4.6: Ideal and jittery signals.

Let the ideal signal of frequency f and amplitude A be (see Equation 3.5)

$$i(t) = A \sin(2\pi f t). \tag{4.15}$$

It is assumed both the phase shift and background offset of the signal are zero.

The signal with jitter is

$$j(t) = A\sin\left(2\pi f(t + \Delta t^{RJ}(t) + \Delta t^{PJ}(t))\right) \tag{4.16}$$

where $\Delta t^{RJ}(t)$ and $\Delta t^{PJ}(t)$ are the random jitter (RJ) and periodic jitter (PJ), respectively. Once again, the phase shift and background offset of the signal are assumed zero. The RJ can be characterised with its RMS σ_{RJ}, thus,

$$\Delta t^{RJ}(t) = \varepsilon(t), \tag{4.17}$$

where $\varepsilon(t)$ is a random process which is a function of time and has a Gaussian distribution $\mathcal{N}$ with mean μ_{RJ} and variance σ^2_{RJ}, that is $\varepsilon \sim \mathcal{N}(\mu_{\text{RJ}}, \sigma^2_{\text{RJ}})$.

Periodic jitter is defined as the repetition of the jitter at a certain period in a signal. In a signal, there can be multiple PJs of various frequencies and these follow the superposition rule, thus (Li, 2007)

$$\Delta t^{PJ}(t) = \sum_{p=1}^{P} A^{(p)}_{\text{PJ}} \cos\left(2\pi f^{(p)}_{\text{PJ}}\, t\right), \qquad P \in \mathbb{Z}^+ \tag{4.18}$$

where $A^{(p)}_{\text{PJ}}$ and $f^{(p)}_{\text{PJ}}$ are the amplitude and frequency of the pth component of the PJ, respectively. From a signal perspective, periodic jitter is the same as any periodic signal in terms of frequency and phase, but its amplitude is jitter in units of timing. Then, from Equations 4.17 and 4.18, the total jitter $\Delta t(t)$ can be expressed as

$$\Delta t(t) = \varepsilon(t) + \sum_{p=1}^{P} A^{(p)}_{\text{PJ}} \cos\left(2\pi f^{(p)}_{\text{PJ}} t\right). \tag{4.19}$$

In the presence of both RJ and PJ, one first has to find the PJ by the DFT. The DFT spectrum measures the distribution of energy values as a function of frequency and each point represents the square root of energy of that corresponding frequency component. The DFT of the total jitter is

$$\mathscr{F}_k = \sum_{n,\,k\,=\,0}^{N-1} \Delta t_n\, e^{-i\frac{2\pi nk}{N}}, \tag{4.20}$$

where $\mathscr{F}_k$ is the DFT of the kth sample of the jitter signal. From the spectrum, we can easily identify the frequencies $f^{(p)}_{\text{PJ}}$ of each component of the PJ by peaks in the spectrum. Other jitter parameters $A^{(p)}_{\text{PJ}}$ of the PJ, and σ^2_{RJ} for RJ can

be computed by measuring the energy of the corresponding portions in the spectrum. As an example, Figure 4.7 shows the spectrum of the total jitter $\mathscr{F}_k$, against its frequency f, with the RJ and PJ at a single frequency. The PJ appears as a clear high peak at its frequency f_{PJ}. The RJ is spread evenly throughout the spectrum. The line $\widehat{\mathscr{F}}_k^{(1)}$ is the interpolated level of the RJ across that part of the spectrum that the PJ contributes to.

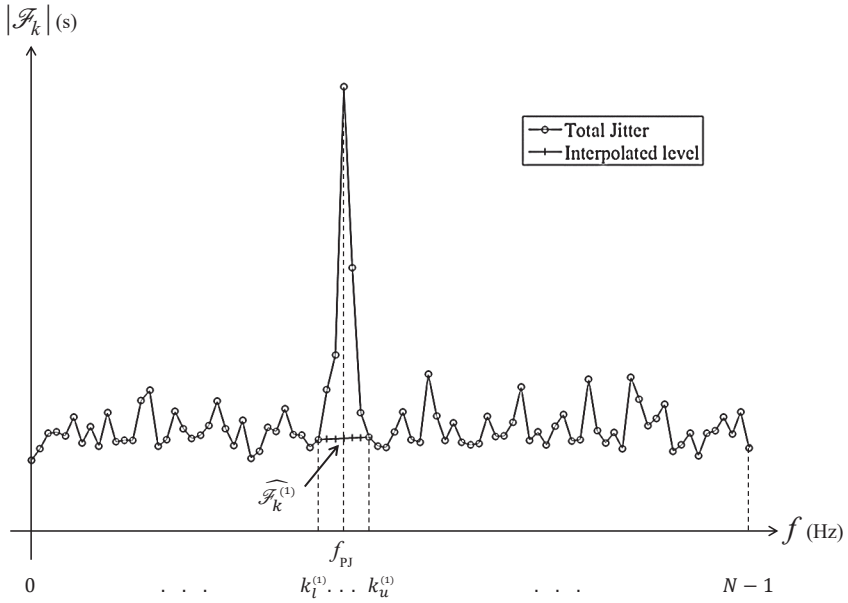

Figure 4.7: An example of a spectrum of the total jitter.

Each point of the spectrum is the square root of energy of that frequency component of the signal. In the frequency-domain, the power of a spectral line is calculated by taking the square of the DFT magnitude (Randall, 1987). Thus, the total energy in the spectrum shown in Figure 4.7, is obtained by

$$\mathrm{E}\left(\Delta t\right) = \mathrm{E}_H^{cf} \sum_{k=0}^{N-1} \left|\mathscr{F}_k\right|^2, \tag{4.21}$$

then, the amplitude of the total jitter of the signal is given by

$$\Delta t = \sqrt{2\,\mathrm{E}\left(\Delta t\right)}, \tag{4.22}$$

where the factor $\sqrt{2}$ is the conversion of the RMS of a sinusoid to its amplitude. The corresponding energy of the PJ is in its peak only, thus

$$\mathrm{E}\left(\Delta t^{PJ}\right) = \mathrm{E}_H^{cf} \sum_{p=1}^{P} \sum_{k\,=\,k_l^{(p)}}^{k_u^{(p)}} \left(\left|\mathscr{F}_k^{(p)}\right|^2 - \left|\widehat{\mathscr{F}}_k^{(p)}\right|^2 \right), \tag{4.23}$$

where $\mathscr{F}_k^{(p)}$ is the DFT of the kth sample of the pth component of the PJ and $\widehat{\mathscr{F}_k^{(p)}}$ is the interpolated level of the RJ across that part of the spectrum that pth component of the PJ contributes to. This part needs to be subtracted from the corresponding component of the PJ peak to be able to estimate the energy of the PJ. Terms $k_l^{(p)}$ and $k_u^{(p)}$ are the corresponding left (lower) and right (upper) indices of the interpolated level of the spectrum, respectively (see Figure 4.7 when $p = 1$). The amplitude of the PJ is

$$A_{\mathrm{PJ}} = \sqrt{2\,\mathrm{E}\,(\Delta t^{PJ})}. \tag{4.24}$$

Hence, by using Equations 4.21 and 4.23, the energy corresponding to the RJ is given by

$$\mathrm{E}\,(\Delta t^{RJ}) = \mathrm{E}\,(\Delta t) - \mathrm{E}\,(\Delta t^{PJ}) - \mathrm{E}\,(\widetilde{\Delta t^{PJ}}) \tag{4.25}$$

where $\mathrm{E}\,(\widetilde{\Delta t^{PJ}})$ is the corresponding energy of the other spikes of the spectrum. Thus, the RMS of the RJ is

$$\sigma_{_{RJ}} = \sqrt{\mathrm{E}\,(\Delta t^{RJ})}. \tag{4.26}$$

4.3.2 Curve Fitting Analysis for the Spectrum

Regression is a powerful tool for fitting non-linear data. Non-linear data can perform by transforming it into a straight line using the logarithmic scale and then applying the linear regression. Linear regression of the transformed data yields a slope and intercept that can be used to determine the parameters of interest (Chapra and Canale, 2015). As an example, Figure 4.8 shows the log-log scale of the jitter amplitude $\mathscr{F}$ against jitter frequency f. We define two linear models with different slopes and use the maximum among them as

$$\begin{aligned}\log \mathscr{F} = \max \big\{ & m_1(\log f - \log f') + \log \mathscr{F}', \\ & m_2(\log f - \log f') + \log \mathscr{F}' \big\},\end{aligned} \tag{4.27}$$

where m_1, m_2 are *slopes* of the two linear models. f' and $\mathscr{F}'$ are constants corresponding to the frequency and amplitude at the intersection point, respectively. By rearranging and taking the anti-logging of Equation 4.27 for either $i = 1$ or 2, gives

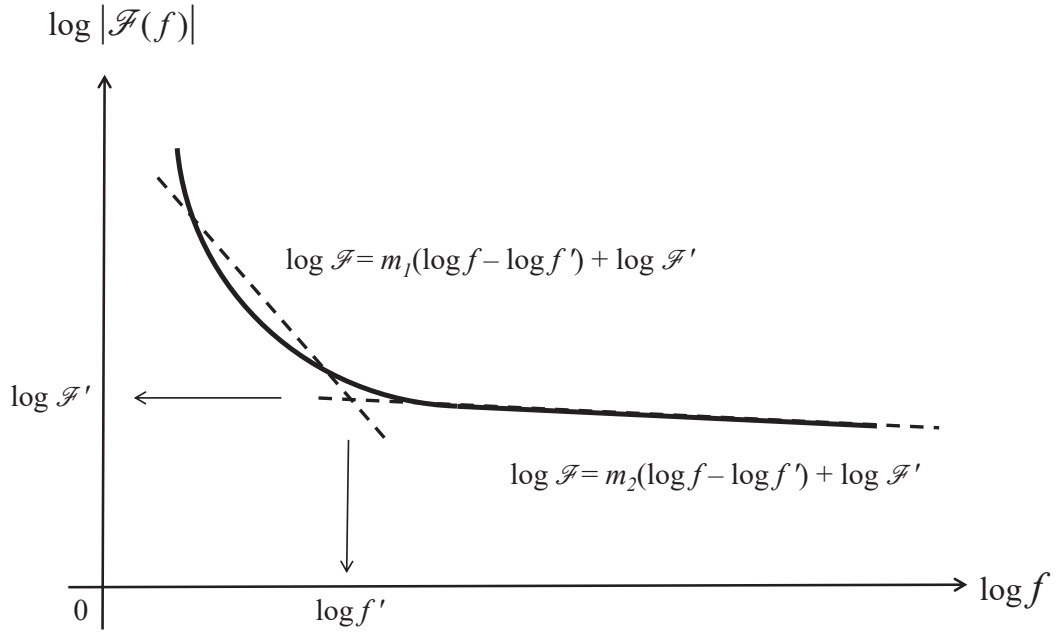

Figure 4.8: An example of the curve fitting for a jitter spectrum.

$$\mathscr{F} = \mathscr{F}' \left(\frac{f}{f'} \right)^{m_i}, \quad i = 1 \oplus 2, \tag{4.28}$$

and this is a power-law function of the form $\mathscr{F} \propto f^m$ (with $m = m_1 \oplus m_2$) that represents the straight line on a log-log graph. The power-law function for the jitter amount $\mathscr{F}$ against the frequency f, is given by

$$\mathscr{F} = \eta f^m \quad \text{with} \quad \eta = \frac{\mathscr{F}'}{(f')^m} \tag{4.29}$$

where η and m are the exponent and power of the power-law function, which represent the *intercept* and *slope* of the log-log graph, respectively.

4.4 Testing the Methodology with Simulated Data

Before experimentally testing the proposed methodology shown in Figure 4.1 on range measurement, we tested it on the simulation data first. We generated the ideal signal and jittery signal with the random and/or periodic jitter as described in Section 4.4.1. For each case, we used the same frequency for the two signals as in the homodyne operation of the AMCW ToF ranging cameras.

4.4.1 Simulation Setup

Five simulated signals with various frequencies (i.e., $f_i = i \times 10$ MHz, $i = 1, \ldots, 5$) and unit amplitude (i.e., $A = 1$) are considered throughout the simulation setup. Three types of setup including the numerate amount of random jitter, periodic jitter at a single frequency and both types are separately injected into each simulated signal corresponding to the frequency f_i are considered. The jitter amounts are chosen as two, four, six, eight and ten times the lowest value (5 ps) for each of σ_{RJ} and A_{PJ}, for the setup denoted as SET-*RJ* and SET-*PJ*, respectively as shown in Table 4.1.

Table 4.1: Three types of simulation setup

Simulation setup		**Frequency** f_i [MHz]	**No. of cycles** N_i^{cal}	**No. of cycles** N_i	**Injected jitter** $i = 1, \ldots, 5$
20 sets each	SET-*RJ*	10	81.92	81	$\sigma_{\text{RJ}} = \{5,\ i \times 10\}$ ps
	SET-*PJ*	20	163.84	163	$A_{\text{PJ}} = \{5,\ i \times 10\}$ ps
	SET-*Both*	30	245.76	245	$f_{\text{PJ}} = 4.37$ MHz
		40	327.68	327	
		50	409.60	409	

In addition, an arbitrarily chosen specific value for the frequency of the periodic jitter as $f_{\text{PJ}} = 4.37$ MHz is used throughout the simulations. The combination of these two types of jitter values are chosen for the setup denoted in SET-*Both*. Furthermore, by using Equations 4.9 and 4.10 with the parameters $f_m = f_i, N_s = 2^{16}$ and $F_s = 8$ GSa/s, the number of jitter samples for each signal frequency are also obtained in columns four and five, respectively. In order to control the uncertainties of the results, 20 sets for each simulation setup were used.

First, each simulation signal with jitter was constructed by injecting a known quantity of jitter amounts for the corresponding time domain signal (see Section C.1 in Appendix C for Matlab script). By using steps ① to ⑥ in Section 4.2, we obtained the jitter spectrum for each set of the relevant simulation setup, as for step ⑥. Finally, the mean spectrum of the total jitter along the 20 sets was obtained after taking the magnitude of spectra for the relevant simulation setup, and this mean spectrum is used to calculate the jitter components, as for step ⑦.

4.4.2 Results and Discussion

The spectrum of the total jitter when injecting the RJ (denoted as SET-*RJ*) for the values of RMS $\sigma_{\text{RJ}} = 5$ and 50 ps for the five simulated signals corresponding to the frequency f_i are shown in Figure 4.9. When the modulation frequency is relatively low (10 MHz and 20 MHz), some peaks are present in the spectra. These are due to the random fluctuation in simulation and the limited number of simulations (20 sets) used in the setup (see Table 4.1). In the limit of a very large number of simulations one would expect the spectra to tend to a flat line in Figure 4.9.

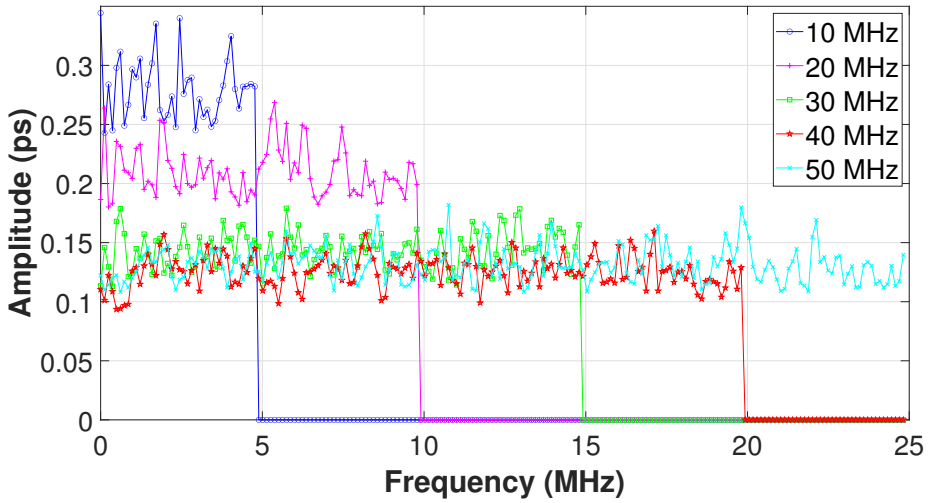

(a)

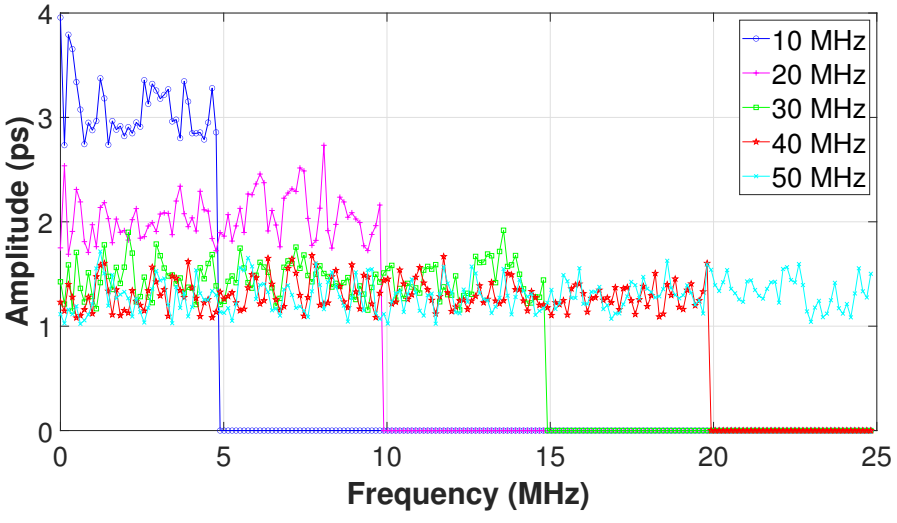

(b)

Figure 4.9: Spectrum of total jitter when injecting the random jitter as σ_{RJ} (a) 5 ps and (b) 50 ps, for setup denoted as SET-*RJ* in Table 4.1.

In order to illustrate the results in the same plot we padded the amplitude by zeros at the end of first four simulated signals (i.e., for the signal of $f_i = 10, \ldots, 40$ MHz), to the length of the number of bins of the spectrum of the 50 MHz signal, i.e., 409 (see Table 4.1). Similarly, when injecting the PJ (denoted as SET-*PJ*) and both RJ with PJ together (denoted as SET-*Both*) for the five simulated signals corresponding to the frequency f_i are shown in Figures 4.10 and 4.11, respectively.

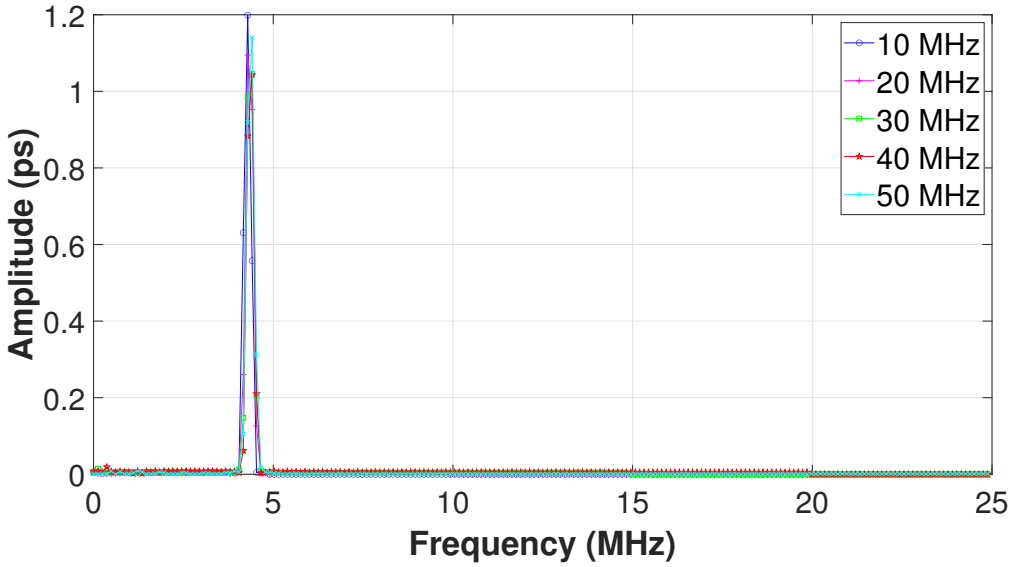

(a)

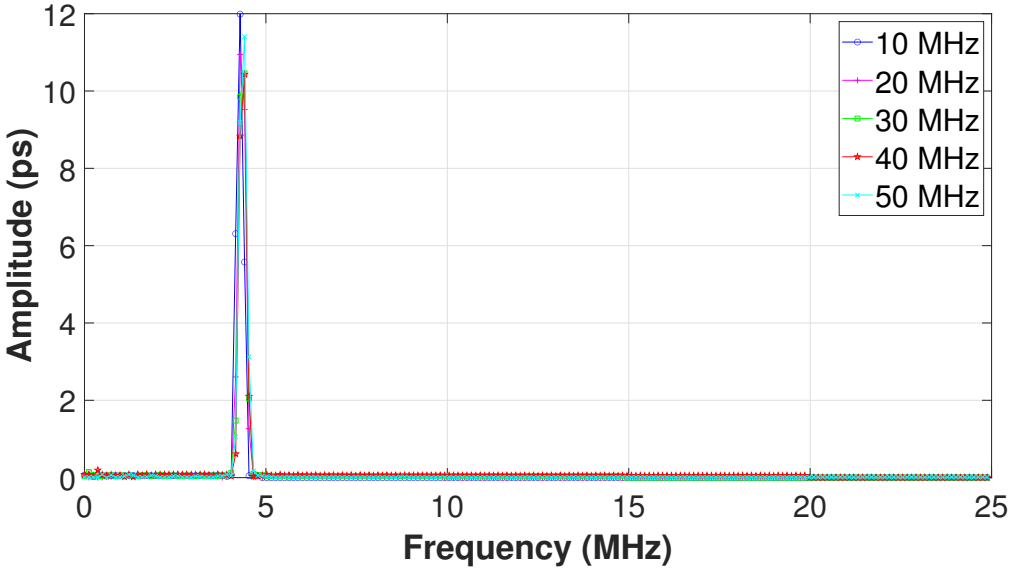

(b)

Figure 4.10: Spectrum of total jitter when injecting the periodic jitter as A_{PJ} (a) 5 ps and (b) 50 ps, at $f_{\mathrm{PJ}} = 4.37$ MHz for setup denoted as SET-*PJ*.

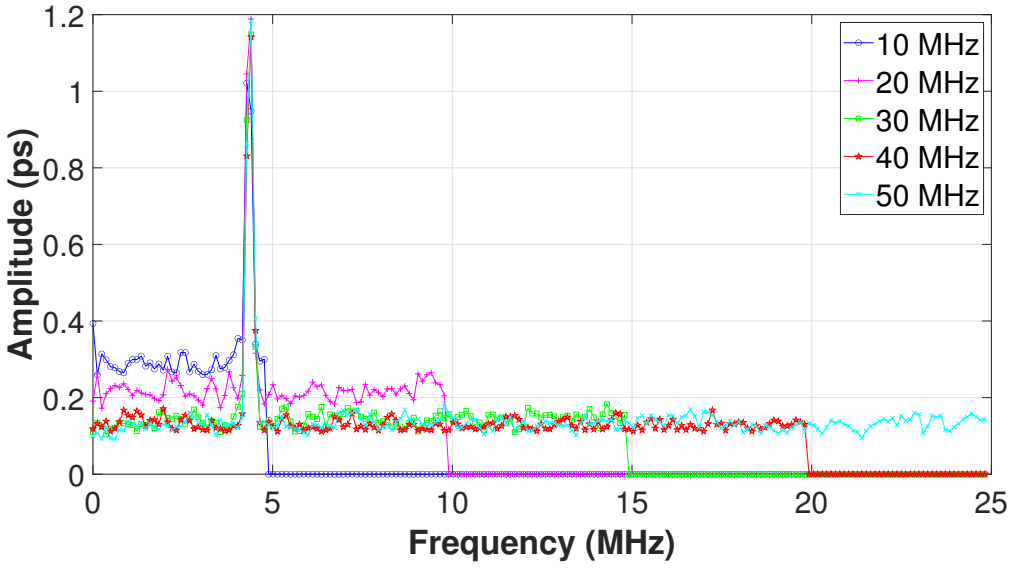

(a)

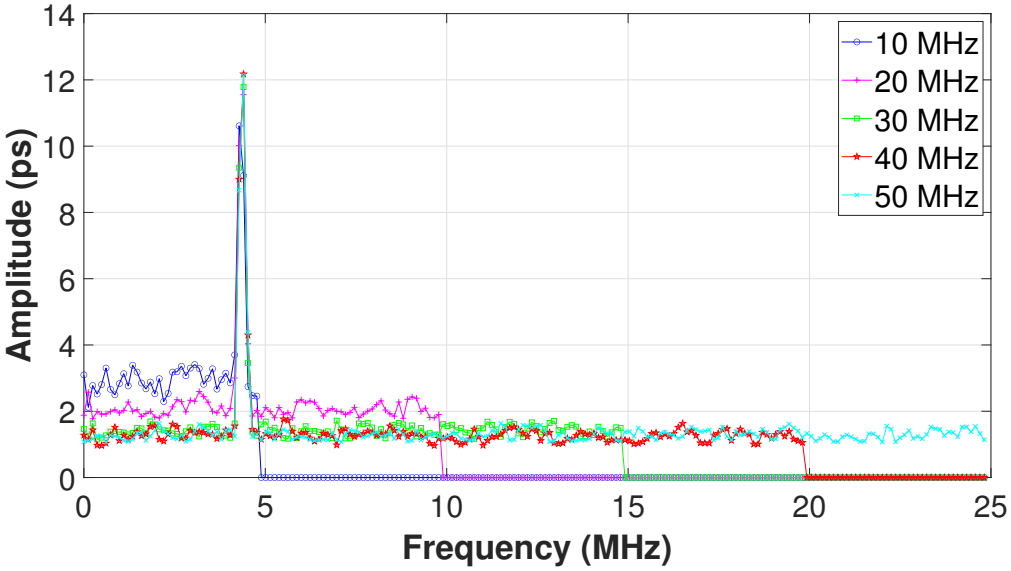

(b)

Figure 4.11: Spectrum of total jitter when injecting the RJ and PJ as (a) σ_{RJ} = 5 ps, A_{PJ} = 5 ps, f_{PJ} = 4.37 MHz and (b) σ_{RJ} = 50 ps, A_{PJ} = 50 ps, f_{PJ} = 4.37 MHz, for setup denoted as SET-*Both* in Table 4.1.

By comparison, we noted that the amplitude level of the spectrum in Figures 4.9(b), 4.10(b) and 4.11(b) is approximately 10 times that of Figures 4.9(a), 4.10(a) and 4.11(a), respectively. It clearly seems the high peak at the frequency of the PJ (at 4.37 MHz) in both Figures 4.10 and 4.11 has the value of (4.39 $\pm$ 0.02) MHz. Note that the interpolation level between the PJ and RJ for Figure 4.11 is obtained by visual inspection and using Equation 4.14.

Table 4.2 shows the corresponding results of the extracted jitter parameters for Figures 4.9 – 4.11.

Table 4.2: Extracted jitter amounts from Figures 4.9 – 4.11 by considering the five modulation frequencies

Simulation setup and injected jitter parameters		Computed jitter parameters		
		σ_{RJ} (ps)	$f_{\text{PJ}} = 4.37$ MHz	A_{PJ} (ps)
SET-*RJ*	5 ps	4.9 ± 0.2	—	—
	50 ps	45.7 ± 1.6	—	—
SET-*PJ*	5 ps	—	4.39 ± 0.02	4.8 ± 0.1
	50 ps	—		47.6 ± 0.7
SET-*Both*	$\sigma_{\text{RJ}} = 5$ ps, $A_{\text{PJ}} = 5$ ps	3.2 ± 0.1	4.39 ± 0.02	4.8 ± 0.1
	$\sigma_{\text{RJ}} = 50$ ps, $A_{\text{PJ}} = 50$ ps	31.6 ± 1.1		49.3 ± 1.2

We compare the actual and measured jitter amounts for each of three simulation setups, separately. Figures 4.12 and 4.13 show the comparison of the measured and actual jitter values with different amounts (see Table 4.1) for 10 and 50 MHz signals for simulations SET-*RJ* and SET-*PJ*, respectively. In addition, 1-to-1 curve and the fitted curve through the data points with the relevant linear regression for the measured jitter amounts are also included in each simulation result in the figure. The slope and intercept of this expression are good indicators for the accuracy and offset error, respectively, of the measured jitter parameters. When the values of slope and intercept are closer to one and zero, respectively that indicates the matching of the actual and measured amounts in each simulation. For SET-*RJ*, the deviation between the measured and actual values increases (see Figure 4.12) when the random jitter amount increases, and note that the offset errors are -0.3853 and 0.1850 for 10 MHz and 50 MHz signals, respectively. We believe this is due to the presence of more zero-crossings with a 50 MHz signal. Statistical uncertainty is reduced due to a larger sample size. For the case of PJ (SET-*PJ*), the jitter extraction in the absence of any other noise is accurate with very small measurement uncertainty for both f_{PJ} and A_{PJ}. The offset errors are 0.0004 and 0.0008 for 10 MHz and 50 MHz, respectively (see Figure 4.13).

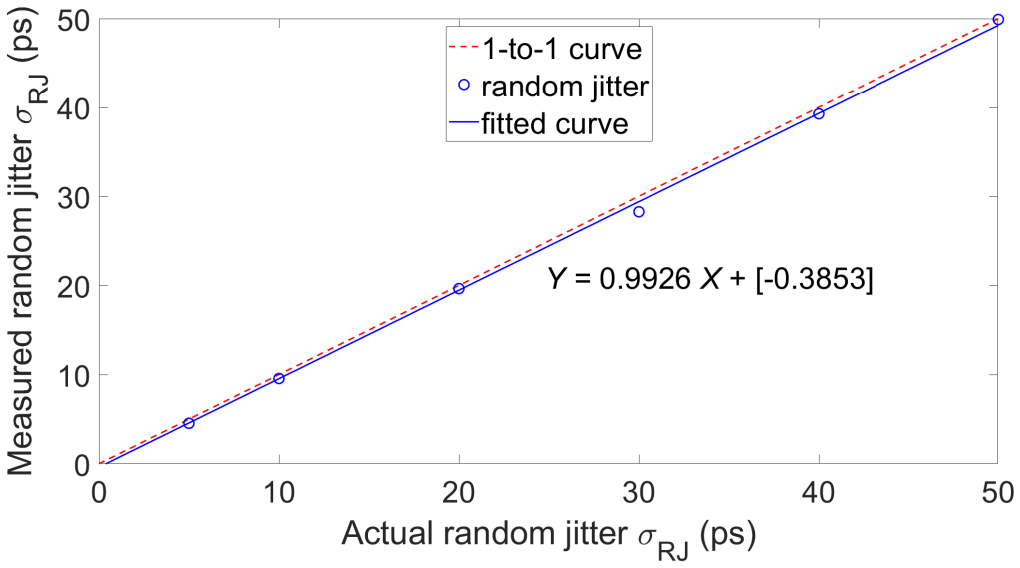

(a)

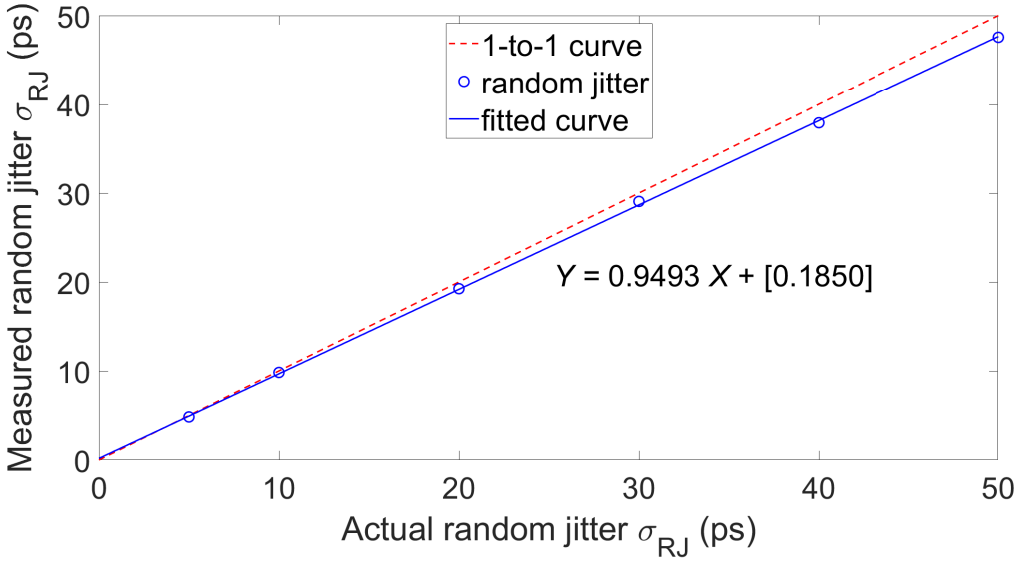

(b)

Figure 4.12: Comparison of the actual and measured random jitter in the signal of frequencies (a) 10 MHz and (b) 50 MHz, on the simulation setup denoted as SET-*RJ* in Table 4.1.

Similarly SET-*Both* on a 50 MHz signal is shown in Figure 4.14. Figure 4.14(a) compares the varies of the PJ with fixed $\sigma_{\text{RJ}} = 5$ ps while Figure 4.14(b) compares the varies of the RJ with fixed $A_{\text{PJ}} = 5$ ps at 4.37 MHz. Among these two plots, the offset error in Figure 4.14(a) is relatively larger [0.1252] than the same in Figure 4.14(b), [0.0737] that is, the amounts deviate from zero. We believe it is because the PJ affects a particular frequency while the

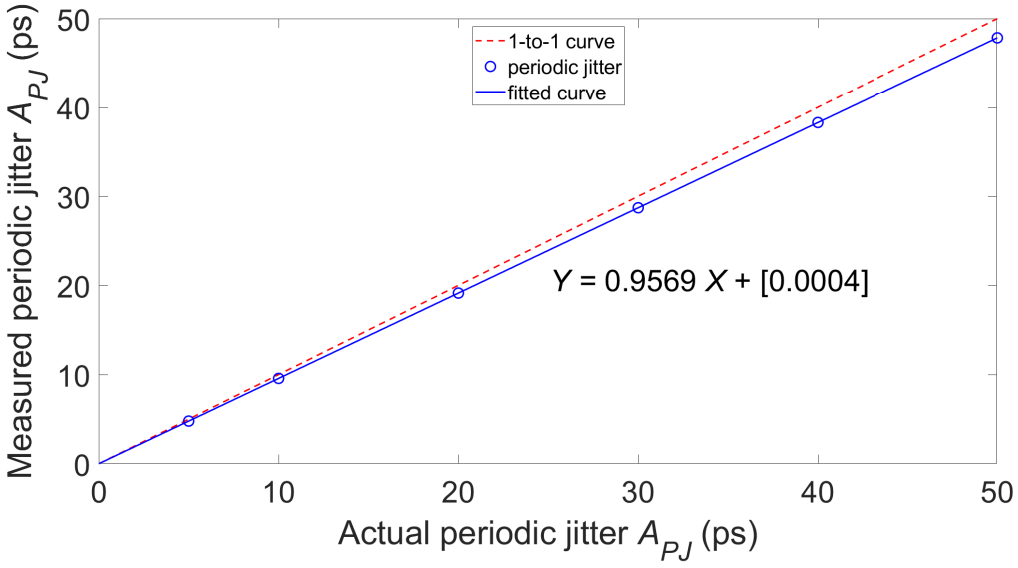

(a)

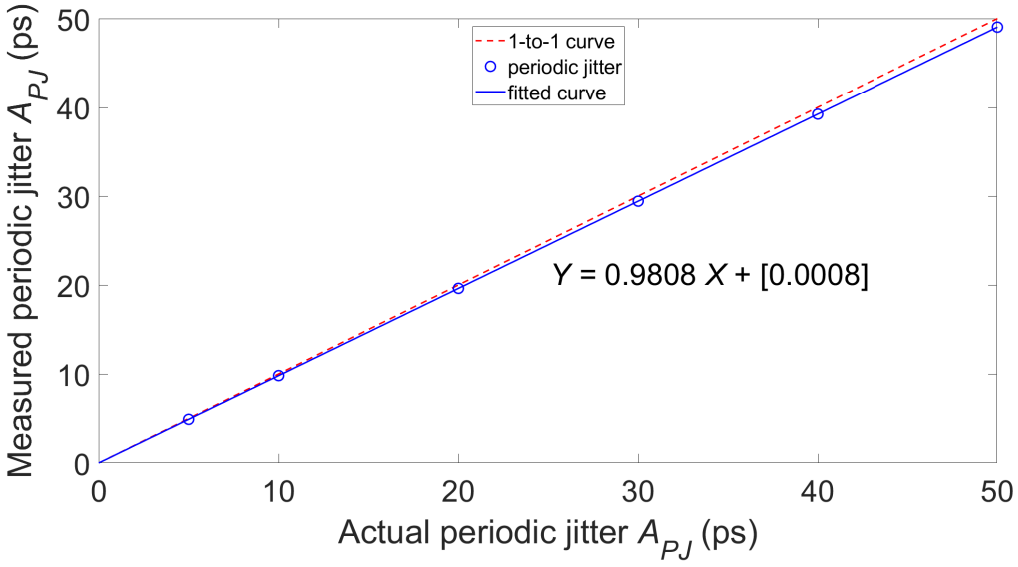

(b)

Figure 4.13: Comparison of the actual and measured periodic jitter at 4.37 MHz of the signal with modulation frequency f_i (a) 10 MHz and (b) 50 MHz, on the simulation setup denoted as SET-PJ in Table 4.1.

RJ affects all frequencies of the signal with spreading of the energy through the whole jitter signal. Therefore, the effect of the RJ on the calculation of PJ is less than the effect of the PJ on the calculation of RJ, when we inject the same amount of each. The measured and actual PJ with fixed RJ is closer (slope is 0.9849) than the measured and actual RJ with fixed PJ (slope is 0.8621), see Figure 4.14.

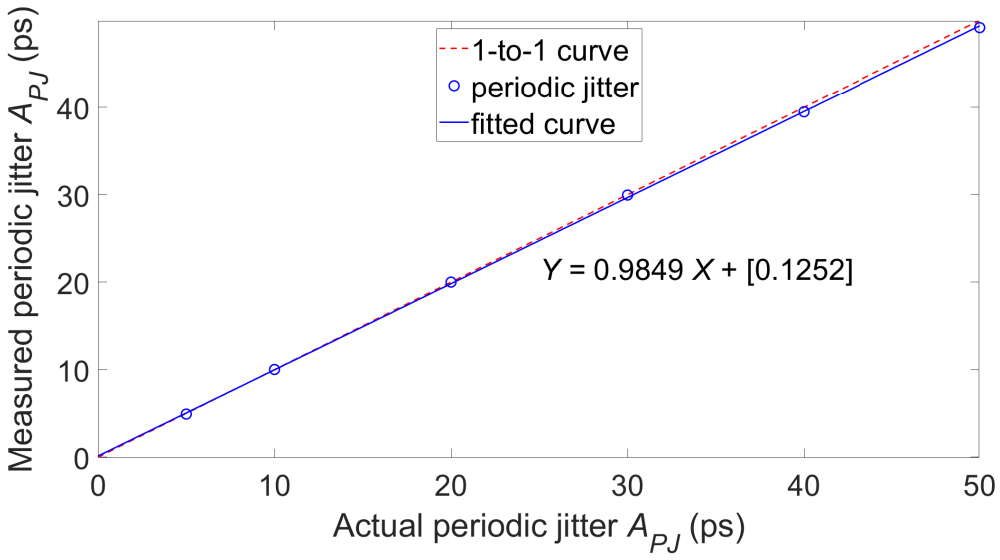

(a)

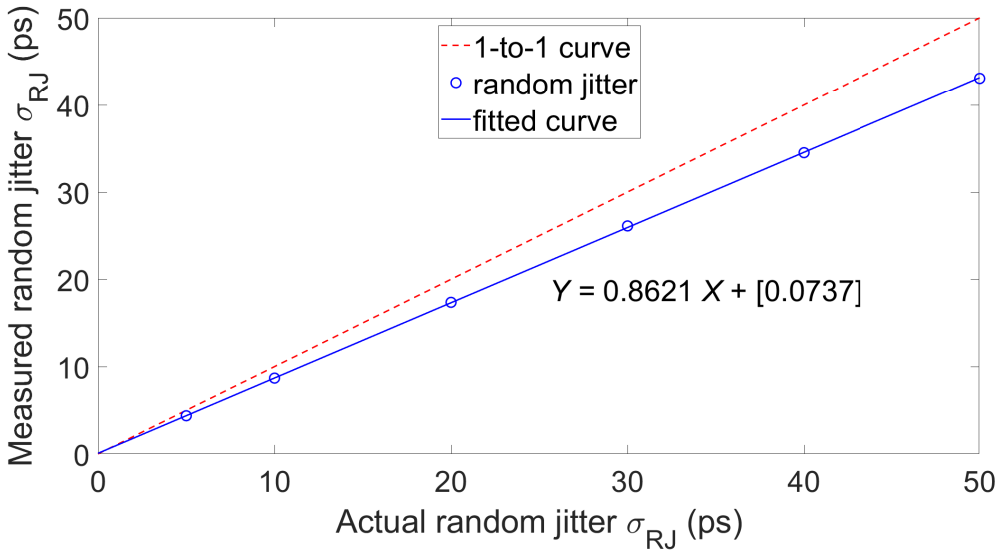

(b)

Figure 4.14: Comparison of the actual and measured of (a) periodic jitter with fixed $\sigma_{\text{RJ}} = 5$ ps and (b) random jitter with fixed $A_{\text{PJ}} = 5$ ps at 4.37 MHz, for the signal $f_i = 50$ MHz, separately, for setup denoted as SET-*Both*.

All the above simulations were performed using sinusoidal signals; now we need to clarify the proposed methodology for other standard shapes of signals, such as triangular and rectangular. We repeat the analysis for the triangular shape of signals with the same parameters used in Table 4.1. The spectra of the total jitter for the three simulation setup when injecting the jitter amounts of 5 ps and 50 ps for each corresponding modulation frequency f_i are shown in Figure 4.15, separately. The maximum jitter levels of each right sub-figures

are about ten times their corresponding left sub-figures. When the modulation frequency is relatively low (10 MHz and 20 MHz), some peaks are apparent in the spectra for SET-*RJ* because the number of cycles in those signals is relatively small.

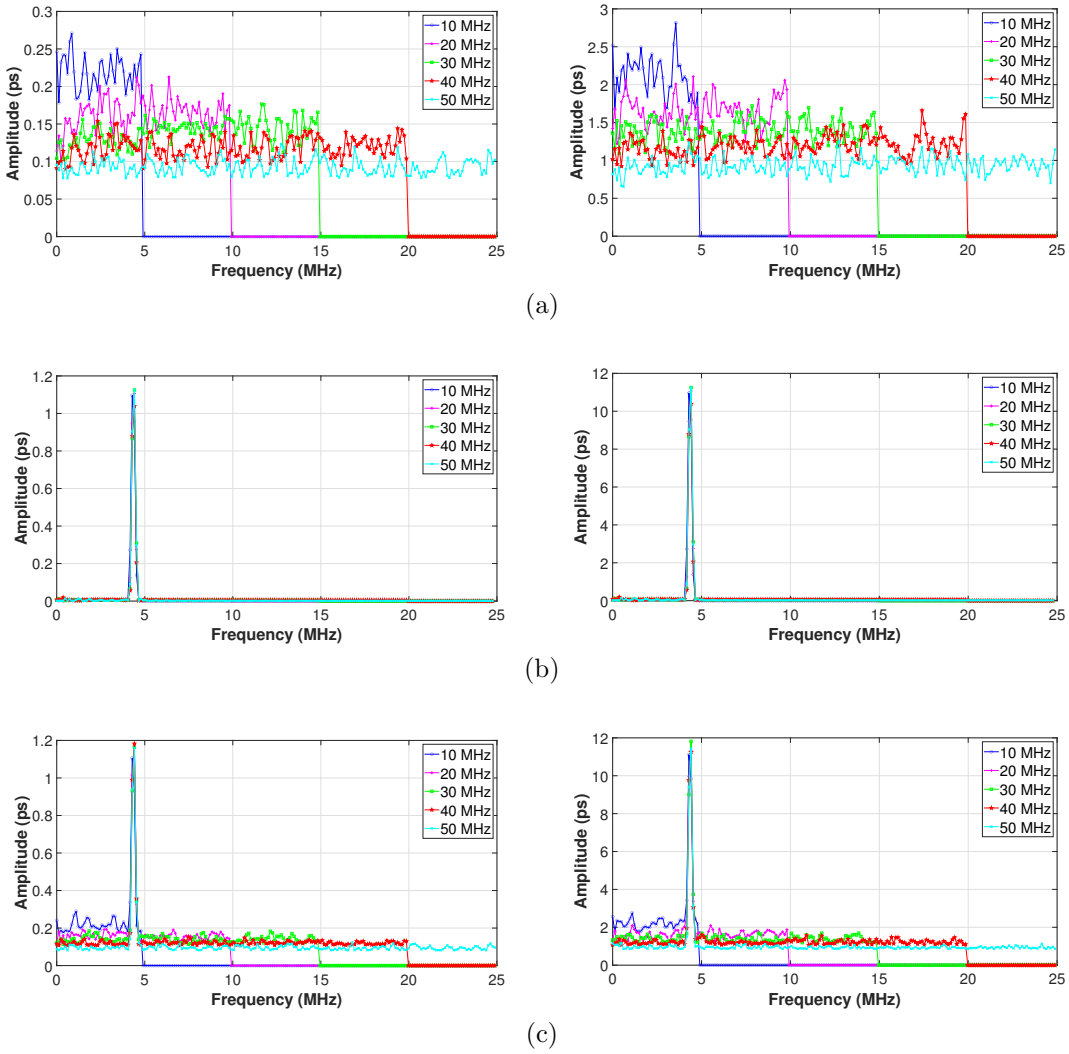

Figure 4.15: Spectrum of total jitter with the triangular signal for three simulation setup denoted as (a) SET-*RJ*, (b) SET-*PJ* and (c) SET-*Both*, for the jitter amounts (left) 5 ps and (right) 50 ps, separately shown in Table 4.1. Note that the PJ is injected at 4.37 MHz.

Now, let us consider the extracted jitter parameters corresponding to each simulation setup shown in Figure 4.15. When the injected RJ is $\sigma_{\text{RJ}} = 5$ ps and 50 ps, we have $\sigma_{\text{RJ}} = (4.76 \pm 0.13)$ ps and (47.5 ± 1.5) ps, respectively while for the injected PJ is $A_{\text{PJ}} = 5$ ps and 50 ps, we have $A_{\text{PJ}} = (4.76 \pm 0.07)$ ps and (47.6 ± 0.7) ps, respectively. In addition, when both jitter types are injected, we found $\sigma_{\text{RJ}} = (4.72 \pm 0.15)$ ps with $A_{\text{PJ}} = (4.98 \pm 0.08)$ ps and

$\sigma_{\mathrm{RJ}} = (47.61 \pm 1.31)$ ps with $A_{\mathrm{PJ}} = (49.44 \pm 0.40)$ ps when each jitter type is 5 ps and 50 ps, respectively. For each corresponding result, we found the PJ at $f_{\mathrm{PJ}} = (4.40 \pm 0.02)$ MHz when we injected it at $f_{\mathrm{PJ}} = 4.37$ MHz.

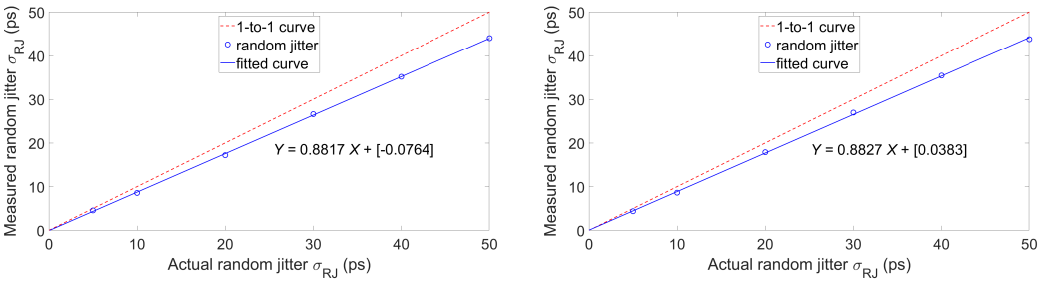

(a) (b)

Figure 4.16: Comparison of the actual and measured random jitter in the triangular signal of frequencies (a) 10 MHz and (b) 50 MHz, on the simulation setup denoted as SET-RJ in Table 4.1.

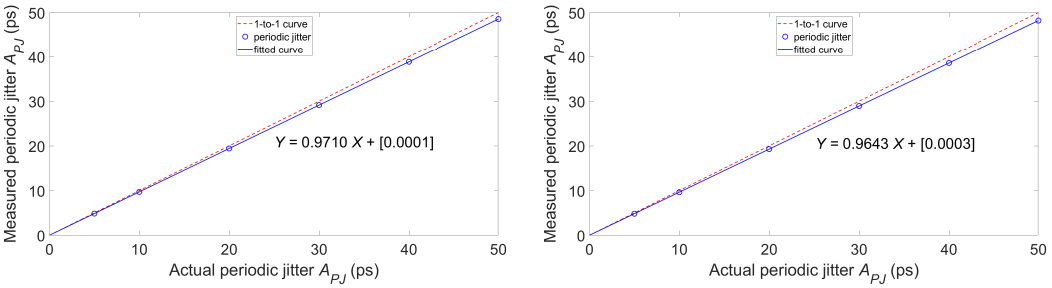

(a) (b)

Figure 4.17: Comparison of the actual and measured periodic jitter at 4.37 MHz of the triangular signal with modulation frequency f_i (a) 10 MHz and (b) 50 MHz, on the setup denoted as SET-PJ in Table 4.1.

One-to-one and fitted curves through the data points with the relevant linear regression for selected modulation frequencies corresponding to the simulation setup denoted by SET-RJ and SET-PJ are shown in Figures 4.16 and 4.17, respectively. As before, we include only the results corresponding to the chosen two modulation frequencies, 10 MHz and 50 MHz. By comparing the values of slopes and intercepts for each result (for 10 MHz and 50 MHz), we can verify that the presence of the periodic jitter gives accurate results (each slope of 0.97 and 0.96 are close to one while each intercept of [0.0001] and [0.0003] are essentially zero, see Figure 4.17) while the random jitter only is less accurately determined slopes of {0.88 and 0.88} are noticeably different from one, with intercepts nearly zero being {[-0.08] and [0.04]}, see Figure 4.16).

Figure 4.18 shows the corresponding results for the simulation setup denoted as SET-*Both*. The sub-figures (a) and (b) correspond to the modulation frequencies 10 MHz and 50 MHz, respectively, while left and right sub-figures correspond to the periodic jitter with fixed random jitter of RMS $\sigma_{\mathrm{RJ}} = 5$ ps and the random jitter with fixed periodic jitter of $A_{\mathrm{PJ}} = 5$ ps, respectively. We found the PJ at (4.40 ± 0.02) MHz each for the injected PJ (left sub-figures of Figure 4.18(a) and (b)). However, when the periodic jitter is relatively less than the random jitter the measurements are computed with less accuracy because of the difficulty to identify the interpolation level between the RJ and PJ. The slopes are {0.88 and 0.89} with intercepts of {[0.06] and [-0.05]} when the presence of RJ with fixed PJ for the signal with 10 MHz and 50 MHz, respectively (right sub-figures of Figure 4.18).

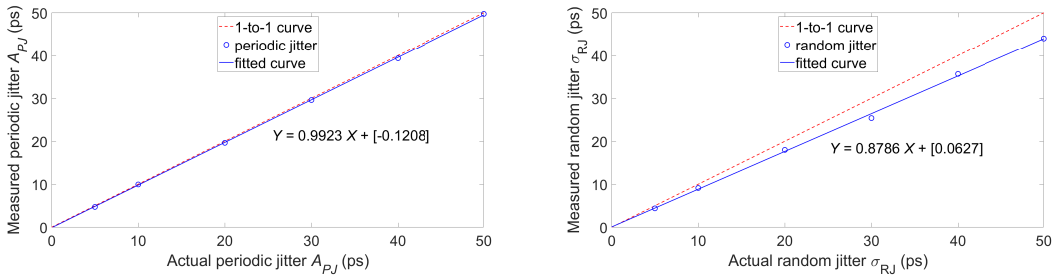

(a)

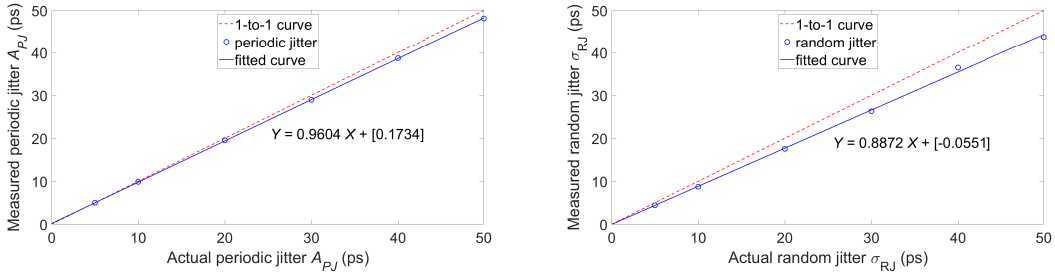

(b)

Figure 4.18: Comparison of the actual and measured of (left) the PJ with fixed RJ of $\sigma_{\mathrm{RJ}} = 5$ ps and (right) the RJ with fixed PJ of $A_{\mathrm{PJ}} = 5$ ps at 4.37 MHz, for the triangular signal with the modulation frequencies: (a) 10 MHz and (b) 50 MHz, separately, for setup denoted as SET-*Both*.

Table 4.3: Computed jitter amounts for the triangular signals by considering the five modulation frequencies

Simulation setup and parameter		Injected jitter amounts in picoseconds					
		5	10	20	30	40	50
SET-*RJ*	σ_{RJ} (ps)	4.8 ± 0.1	9.7 ± 0.4	18.95 ± 0.6	28.7 ± 0.8	38.3 ± 1.2	47.5 ± 1.5
SET-*PJ*	A_{PJ} (ps)	4.8 ± 0.1	9.5 ± 0.1	19.0 ± 0.3	28.5 ± 0.4	38.1 ± 0.5	47.6 ± 0.7
	f_{PJ} (MHz)	4.40 ± 0.02					
SET-*Both*		Fixed amount of the RJ with various amplitudes of the PJ at 4.37 MHz					
	$\sigma_{\mathrm{RJ}} = 5$ ps	4.7 ± 0.2	4.7 ± 0.2	4.9 ± 0.2	5.1 ± 0.2	5.3 ± 0.2	5.5 ± 0.3
	A_{PJ} (ps)	5.0 ± 0.1	9.9 ± 0.1	19.5 ± 0.2	29.1 ± 0.4	38.6 ± 0.6	48.2 ± 0.7
	f_{PJ} (MHz)	4.40 ± 0.02					
		Fixed amount of the PJ at 4.37 MHz with various amounts of the RJ					
	$A_{\mathrm{PJ}} = 5$ ps	5.0 ± 0.1	4.8 ± 0.1	4.9 ± 0.3	5.4 ± 0.8	5.9 ± 0.7	6.56 ± 0.97
	f_{PJ} (MHz)	4.40 ± 0.02	4.40 ± 0.02	4.40 ± 0.02	4.42 ± 0.01	4.32 ± 0.07	4.42 ± 0.07
	σ_{RJ} (ps)	4.7 ± 0.2	9.5 ± 0.3	18.8 ± 0.7	28.0 ± 1.1	38.06 ± 1.03	47.0 ± 1.6
	Large amounts of RJ and PJ	Computed $\sigma_{\mathrm{RJ}} = (47.6 \pm 1.3)$ ps, $A_{\mathrm{PJ}} = (49.4 \pm 0.4)$ ps and $f_{\mathrm{PJ}} = (4.40 \pm 0.02)$ MHz when injecting $\sigma_{\mathrm{RJ}} = 50$ ps, $A_{\mathrm{PJ}} = 50$ ps and $f_{\mathrm{PJ}} = 4.37$ MHz, respectively.					

The frequencies of the corresponding ideal signals are found by 10.002 MHz and 50.005 MHz for the generated signals of 10 MHz and 50 MHz, respectively. The extracted jitter amounts for the triangular signals computed by considering the chosen five modulation frequencies are tabulated in Table 4.3. The uncertainties are calculated by using the expressions in Section B.3. It is clear that the extracted jitter amounts for the setup SET-*RJ* are less accurate than the results from setup SET-*PJ*. The accuracy of the results from the setup SET-*Both* is even less accurate and worsens with relatively less fixed PJ (A_{PJ} = 5 ps) than the results with relatively less fixed RJ (σ_{RJ} = 5 ps). The frequencies of the periodic jitter for the setup SET-*PJ* and SET-*Both* are given almost similar amounts. However, either for fixed RJ or fixed PJ (5 ps each), the calculated amounts of the RJ and PJ are larger than 5 ps each, respectively (i.e., impossible) when the amount of the other type of jitter increases (from 30 ps each). When both PJ and RJ are relatively large then the results are relatively close to the injected jitter amounts (the last row of Table 4.3).

Next, we investigate the proposed methodology for rectangular shape signals for each simulation setup. Here, the amounts for periodic and random jitter are chosen to be ten times larger than the amounts in Table 4.1, that is, $\sigma_{\text{RJ}} = A_{\text{PJ}} = \{50, 100, \ldots, 500\}$ ps. Figure 4.19 shows the total spectrum when injecting the minimum and maximum amounts (among the chosen) for each modulation frequency for the three simulation setup shown in Table 4.1. As before, for the results corresponding to SET-*RJ*, see Figure 4.19(a), there are few peaks on the low modulation frequencies. In addition, for SET-*PJ*, there are medium peaks when the injected PJ is A_{PJ} = 50 ps (see, left sub-figure of Figure 4.19(b)), but the peaks are not present when the injected PJ is large A_{PJ} = 500 ps (see, right sub-figure of Figure 4.19(b)).

When the injected RJ is σ_{RJ} = 50 ps and 500 ps, we have $\sigma_{\text{RJ}} = (77 \pm 3)$ ps and (505 ± 7) ps, respectively while the injected PJ is A_{PJ} = 50 ps and 500 ps, we have $A_{\text{PJ}} = (71 \pm 5)$ ps and (463 ± 7) ps, respectively. When both jitter types are injected, we found $\sigma_{\text{RJ}} = (72.5 \pm 1.5)$ ps with $A_{\text{PJ}} = (510 \pm 1)$ ps and $\sigma_{\text{RJ}} = (645 \pm 16)$ ps with $A_{\text{PJ}} = (507 \pm 6)$ ps when each jitter type is 50 ps and 500 ps, respectively. For the setup SET-*Both*, the accuracies of the jitter amounts are relatively low because the computed jitter amounts are larger than the injected amounts and the corresponding uncertainty values are also large (i.e., $\pm$ 16 ps and $\pm$ 6 ps when the injected amounts of σ_{RJ} = 500 ps and A_{PJ} = 500, respectively). For each corresponding result, we found the PJ at $f_{\text{PJ}} = (4.39 \pm 0.02)$ MHz when we injected it at f_{PJ} = 4.37 MHz.

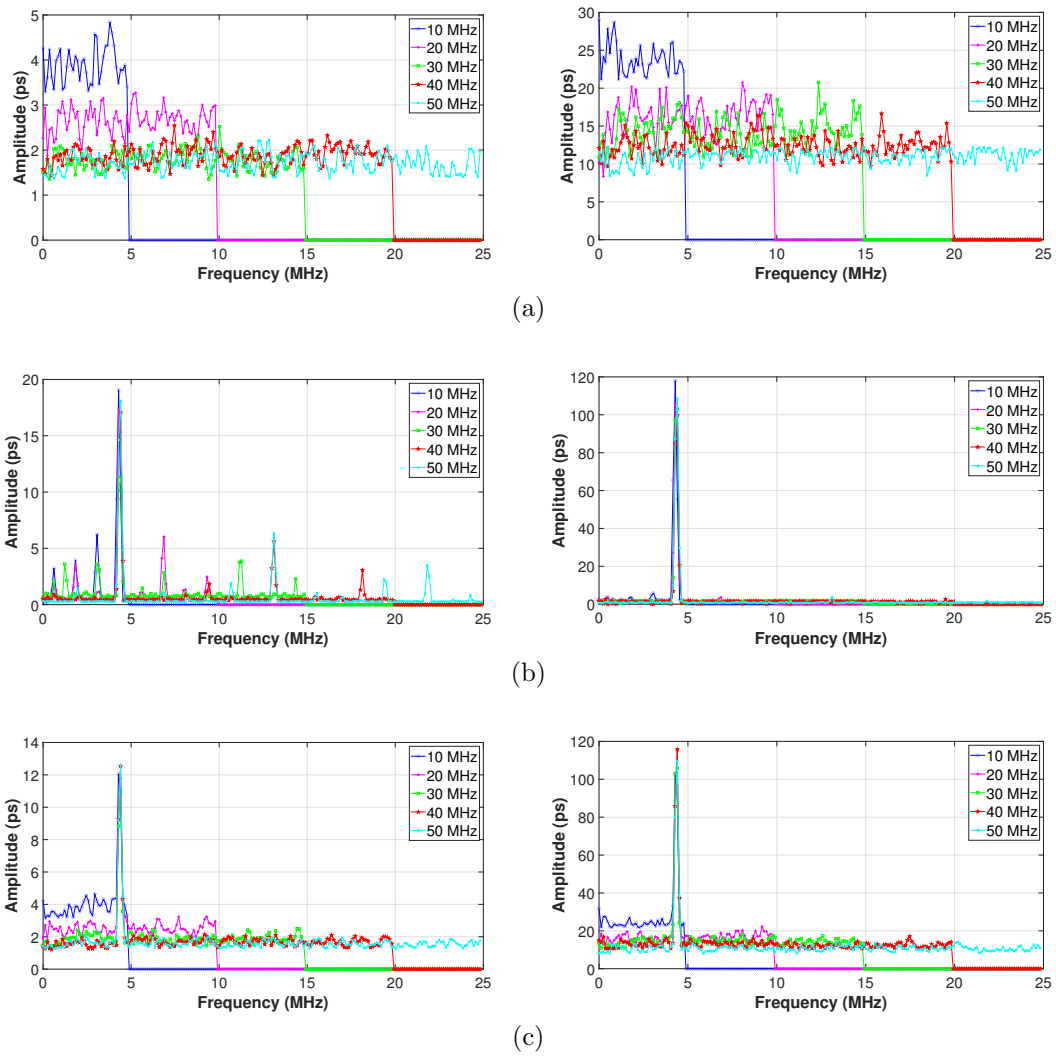

Figure 4.19: Spectrum of total jitter with the rectangular signal for three simulation setup denoted as (a) SET-*RJ*, (b) SET-*PJ* and (c) SET-*Both*, for the jitter amounts (left) 50 ps and (right) 500 ps, separately. Note that the injected PJ located at 4.37 MHz

One-to-one and fitted curves through the data points with the relevant linear regression for selected modulation frequencies corresponding to the simulation setup denoted by SET-*RJ* and SET-*PJ* are shown in Figures 4.20 and 4.21, respectively. As before, we include only the results corresponding to the chosen two modulation frequencies, 10 MHz and 50 MHz. We can verify, each slope is close to one while each intercept is far from zero and this deviation is very large when the presence of random jitter only (i.e., the intercepts are [22] and [20] for 10 MHz and 50 MHz, respectively, see Figure 4.20).

Figure 4.22 shows the corresponding results for the simulation setup denoted as SET-*Both*. Left and right sub-figures correspond to the PJ with fixed

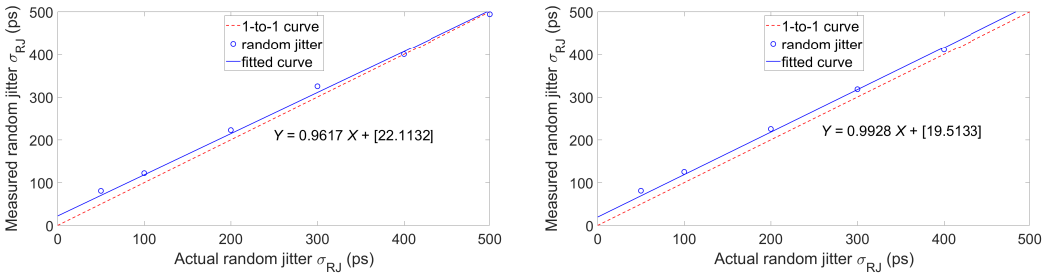

(a) (b)

Figure 4.20: Comparison of the actual and measured random jitter in the rectangular signal of frequencies (a) 10 MHz and (b) 50 MHz, on the simulation setup denoted as SET-*RJ* in Table 4.1.

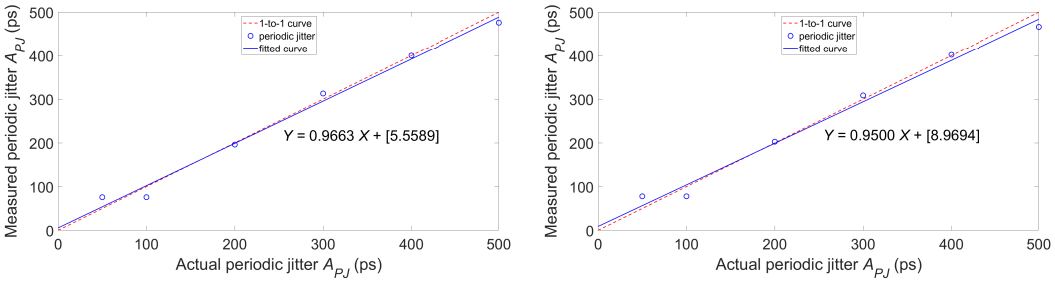

(a) (b)

Figure 4.21: Comparison of the actual and measured periodic jitter at 4.37 MHz of the triangular signal with modulation frequency f_i (a) 10 MHz and (b) 50 MHz, on the setup denoted as SET-*PJ* in Table 4.1.

random jitter of RMS $\sigma_{\mathrm{RJ}} = 50$ ps and the RJ with fixed periodic jitter of $A_{\mathrm{PJ}} = 50$ ps, respectively while the sub-figures (a) and (b) correspond to the modulation frequency 10 MHz and 50 MHz, respectively. We found the PJ at (4.39 ± 0.02) MHz each for the injected PJ (left sub-figures of Figure 4.22(a) and (b)). However, when the injected periodic jitter is fixed and relatively less than the random jitter, the frequency of the periodic jitter is difficult to locate in the spectrum. When the PJ is relatively less than the RJ this causes the measurements to be computed with less accuracy because of the difficulty to identify the interpolation level between the RJ and PJ. By considering each right sub-figures of Figure 4.22, the slopes are {0.96 and 0.95} and intercepts are {[20] and [22]} when the presence of RJ with fixed PJ for the signal with 10 MHz and 50 MHz, respectively. These large deviations (intercepts are far away from zero) are due to the amounts of first two measured random jitter, i.e., when the injected RJ of $\sigma_{\mathrm{RJ}} = 50$ ps and 100 ps. As before, the frequencies of the corresponding ideal signals are found by 10.002 MHz and 50.005 MHz.

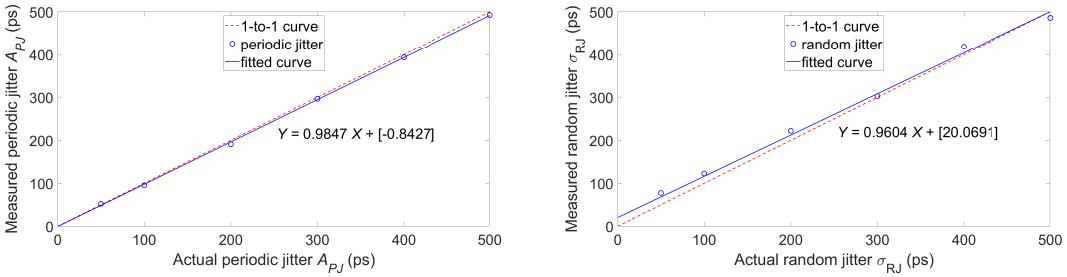

(a)

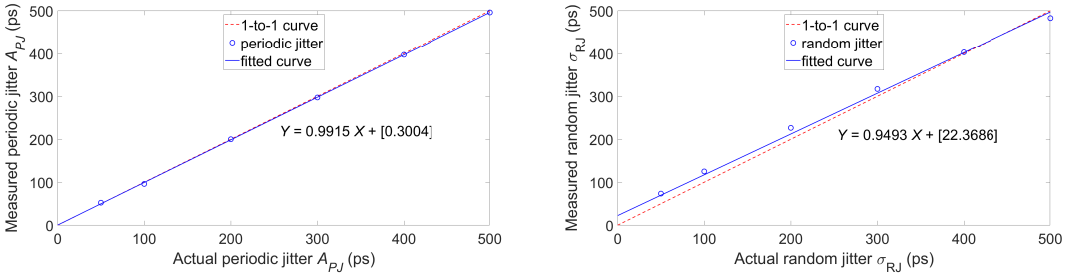

(b)

Figure 4.22: Comparison of the actual and measured of (left) the PJ with fixed RJ of $\sigma_{\mathrm{RJ}} = 50$ ps and (right) the RJ with fixed PJ of $A_{\mathrm{PJ}} = 50$ ps at 4.37 MHz, for the rectangular signal with the modulation frequencies: (a) 10 MHz and (b) 50 MHz, separately, for setup denoted as SET-*Both*.

The jitter amounts for the rectangular signals computed by considering the chosen five modulation frequencies are tabulated in Table 4.4. The results for the setup SET-*RJ* have less accuracy than the results from setup SET-*PJ*. The accuracy of the results from the setup SET-*Both* is much less than the other two types of simulation and is worse with relatively less fixed PJ ($A_{\mathrm{PJ}} = 50$ ps) than the results with relatively less fixed RJ ($\sigma_{\mathrm{RJ}} = 50$ ps). The frequencies of the periodic jitter for the setup SET-*PJ* and SET-*Both* are given almost similar amounts except when the presence of the maximum amount of RJ with a fixed amount of PJ is given $f_{\mathrm{PJ}} = 5.6 \pm 1.1$ (refer the last column and third row from the bottom of Table 4.4). However, either for fixed RJ or fixed PJ (50 ps each), the calculated amounts of the RJ and PJ are larger than 50 ps each, respectively (i.e., impossible) when the amount of the other type of jitter increases (from 300 ps each). If both PJ and RJ are relatively large then the measured RJ is given a larger value than the injected amount while the measured PJ are relatively close to the actual amount.

Table 4.4: Computed jitter amounts for the rectangular signals by considering the five modulation frequencies

Simulation setup and parameter		Injected jitter amounts in picoseconds					
		50	100	200	300	400	500
SET-*RJ*	σ_{RJ} (ps)	76.9 ± 2.7	119.2 ± 2.56	219.2 ± 4.4	315.3 ± 3.2	407.4 ± 2.7	505.4 ± 7.0
SET-*PJ*	A_{PJ} (ps)	71.0 ± 4.8	80.77 ± 4.02	193.1 ± 3.1	303.4 ± 4.5	393.1 ± 4.4	462.5 ± 6.7
	f_{PJ} (MHz)	4.39 ± 0.02					
SET-*Both*		Fixed amount of the RJ with various amplitudes of the PJ at 4.37 MHz					
	$\sigma_{\text{RJ}} = 50$ ps	72.5 ± 1.5	71.7 ± 1.2	72.5 ± 0.7	72.7 ± 0.7	75.2 ± 1.2	77.0 ± 0.8
	A_{PJ} (ps)	50.9 ± 1.0	94.9 ± 0.5	195.0 ± 1.8	292.9 ± 2.4	388.9 ± 4.4	485.5 ± 6.0
	f_{PJ} (MHz)	4.39 ± 0.02					
		Fixed amount of the PJ at 4.37 MHz with various amplitudes of the RJ					
	$A_{\text{PJ}} = 50$ ps	50.9 ± 1.0	48.2 ± 0.8	46.4 ± 1.9	64.2 ± 8.3	63.9 ± 9.2	69.8 ± 10.3
	f_{PJ} (MHz)	4.39 ± 0.02	4.39 ± 0.02	4.39 ± 0.02	4.41 ± 0.01	4.0 ± 0.4	5.6 ± 1.1
	σ_{RJ} (ps)	72.5 ± 1.5	119.7 ± 2.7	216.6 ± 4.0	311.1 ± 2.5	408.2 ± 3.6	493.9 ± 6.2
	Large amounts of RJ and PJ	Computed $\sigma_{\text{RJ}} = (645 \pm 16.1)$ ps, $\sigma_{\text{RJ}} = (507.5 \pm 6.1)$ ps and $f_{\text{PJ}} = (4.39 \pm 0.02)$ MHz when injecting $\sigma_{\text{RJ}} = 500$ ps, $A_{\text{PJ}} = 500$ ps and $f_{\text{PJ}} = 4.37$ MHz, respectively.					

4.4.3 Conclusion

The simulation results show reasonable accuracy in the jitter measurements. As examples, when we inject only a RJ of RMS values, 5 and 50 ps, our approach was given the values of (4.5 ± 0.3) ps and (45.2 ± 2.4) ps, respectively. Furthermore, if we inject only the PJ of 5 and 50 ps, separately, at the frequency 4.37 MHz, the calculated parameters were given as (4.93 ± 0.04) ps and (49.3 ± 0.5) ps, respectively, at the frequency of (4.40 ± 0.04) MHz when the generated signals are sinusoidal shape. If RJ is a large fraction of the total jitter then it can be difficult to separate the PJ accurately, on the simulation data. This phenomena is relatively further difficult in rectangular shape signals than the other two shapes. Now, we believe that the proposed methodology can apply for jitter extraction in real-time applications where we have no access to a reference clock signal.

4.5 Chapter Remarks

We proposed a method to extract periodic and random jitter in the light source signal of any AMCW ToF range imaging cameras. The most important advantage of this method is that it does not require a reference or sampling clock signal to measure jitter. Another dominant advantage is, this algorithm can be used for jitter extraction in any kind of signal (either analogue or digital) with any kind of shape (sinusoidal, triangular, rectangular) and where there is no access to the clock signal.

Before applying the proposed algorithm with the experiments on ToF ranging cameras, we first tested it on the generated simulation data. We considered only the random and periodic jitter in the simulation data since these are the two available types of jitter in the illumination source of ToF range imaging cameras which will be used in the next chapter. The random jitter (of known amount), periodic jitter (with known frequency and amount), and both together are separately injected to various modulation frequencies of sinusoidal signals. The approach is validated by several experiments with numerous values for the parameters of the signal and jitter. The significant accurate results are found for our proposed algorithm on generated simulation data. So, we have assured our proposed methodology for jitter measurement, and now it is needed to experiment the proposed algorithm using AMCW ToF range imaging cameras and this will be described in the next chapter.

Chapter 5

Testing the Methodology with AMCW ToF Range Imaging

This chapter verifies the proposed methodology in Chapter 4 by experimenting with commercial applications. First, we summarize the sub steps of the proposed methodology in point form as a flow chart. Then, the experimental setup using two AMCW depth cameras is separately investigated.

5.1 Methodology

We measure the jitter in modulated light sources of two AMCW ToF range imaging cameras, namely, the MESA Imaging SwissRanger 4000 and SoftKinetic DepthSense 325, separately. Since the emitted light source does not carry a data stream, we decompose the light signal into random jitter and periodic jitter. Other types of jitter (data dependent and bounded uncorrelated jitter) are only relevant to communication channels that transmit data. The light signal of each depth camera is captured by using a silicon biased photodetector, DET025A[1] and is measured by a medium speed real-time digital oscilloscope, namely, the Keysight Infiniium S-Series DSOS604A High-Definition[2] with 6 GHz bandwidth and 20 GSa/s sampling rate. The number of cycles in the signal will be large when the oscilloscope has a large waveform length (Equation 4.9). Figure 5.1 is a summary of the details of the sub steps in addition to the main steps of the methodology proposed in Section 4.2.

[1] https://www.thorlabs.com/thorproduct.cfm?partnumber=DET025A

[2] https://literature.cdn.keysight.com/litweb/pdf/5991-3904EN.pdf?id=2447379

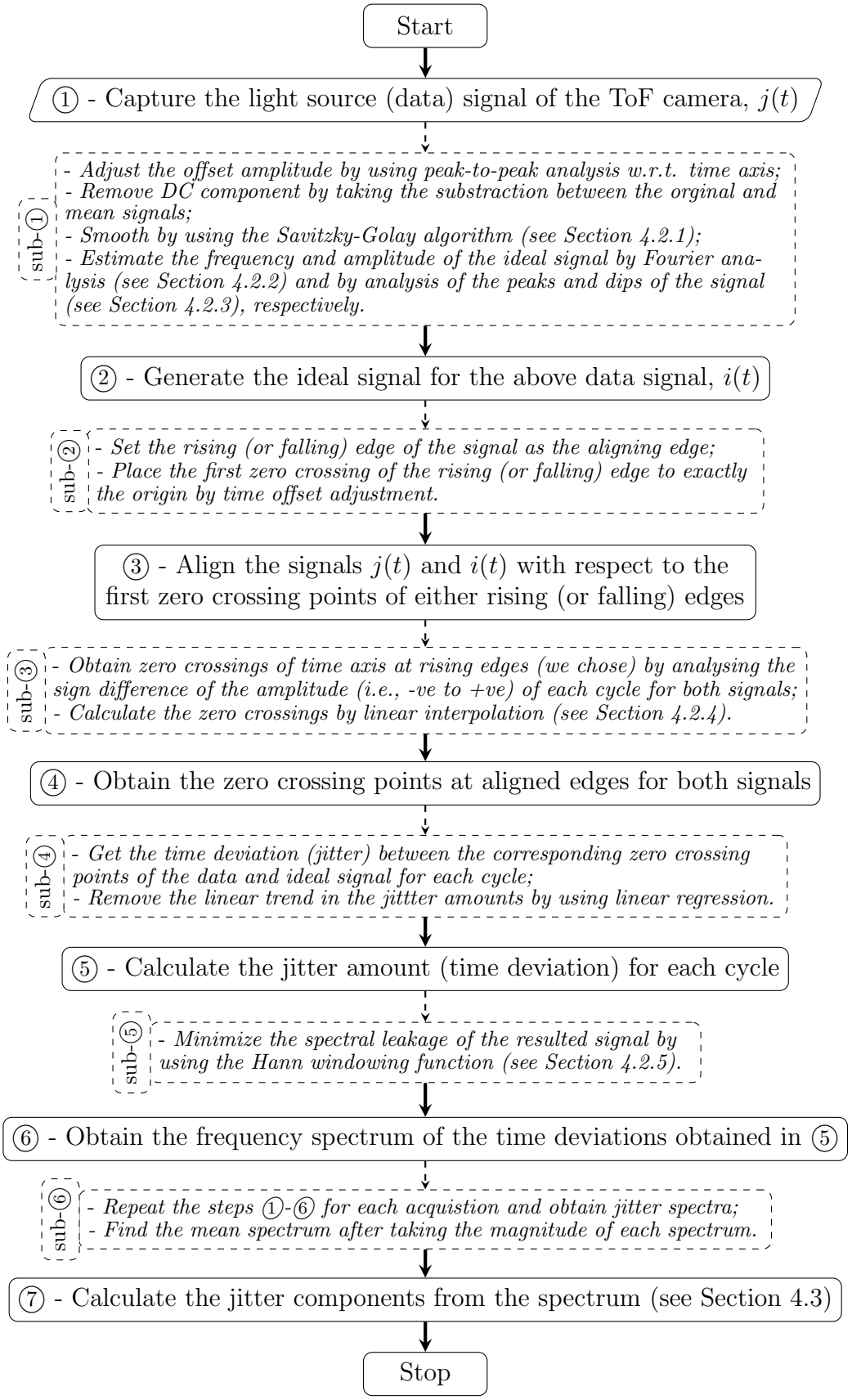

Figure 5.1: Summary of the sub steps with main steps of the methodology proposed in Section 4.2 for jitter extraction in ToF range imaging cameras.

5.2 MESA Imaging SwissRanger 4000

The MESA Imaging SwissRanger 4000 (SR4000) uses infrared LEDs for its illumination source. We choose its default modulation frequency (i.e., 30 MHz) with the frame rates of 50 fps for experimentation.

5.2.1 Experimental Setup for SR4000

We captured the light source signal of the SR4000 depth camera by using a silicon biased photodetector, DET025A. We used two coaxial cables as *'Medium'* (1.070 ± 0.005 m) and *'Long'* (1.790 ± 0.005 m) which are in different lengths measured from tip to tip of the BNC connectors for each experiment. For the control a 30 MHz pure sine wave (corresponding to the modulation frequency of SR4000) was generated with the HP Agilent 8648B[3] signal generator and measured with the oscilloscope. The specification of the components used is shown in Table 5.1.

Table 5.1: Specification of the components used with SwissRanger 4000

Component	**Specification used**		
ToF camera	Modulation frequency (f_m)	Frame rates	Illumination source
SwissRanger 4000	30 MHz	50 fps	Infrared LEDs 850 nm
Light detector	Detector	Bandwidth	Spectral range
Thorlabs DET025A	Silicon biased	2 GHz	400−1100 nm
Oscilloscope	Bandwidth	Sampling frequency (F_s)	Number of samples
S-Series DSOS604A	6 GHz	20 GSa/s	$N_s \approx 10^7$
Signal generator	Sinusoidal signal of the frequency		
HP Agilent 8648	30 MHz		
Cable	Length in meters		
Coaxial, (length from tip to tip of the BNC connectors)	*Medium (M)*	*Long (L)*	
	1.070 ± 0.005	1.790 ± 0.005	

[3] https://literature.cdn.keysight.com/litweb/pdf/5965-3432E.pdf?id=1000031128:epsg:dow

The experimental setup is illustrated in Figure 5.2 and the equipment parameters are given in Table 5.2. For the representation, we denote the corresponding experiment of SR4000 and signal generator as EXP. SR-{...} and EXP. SG30-{...}, respectively, with {...} representing the corresponding cable as either *Medium* or *Long*.

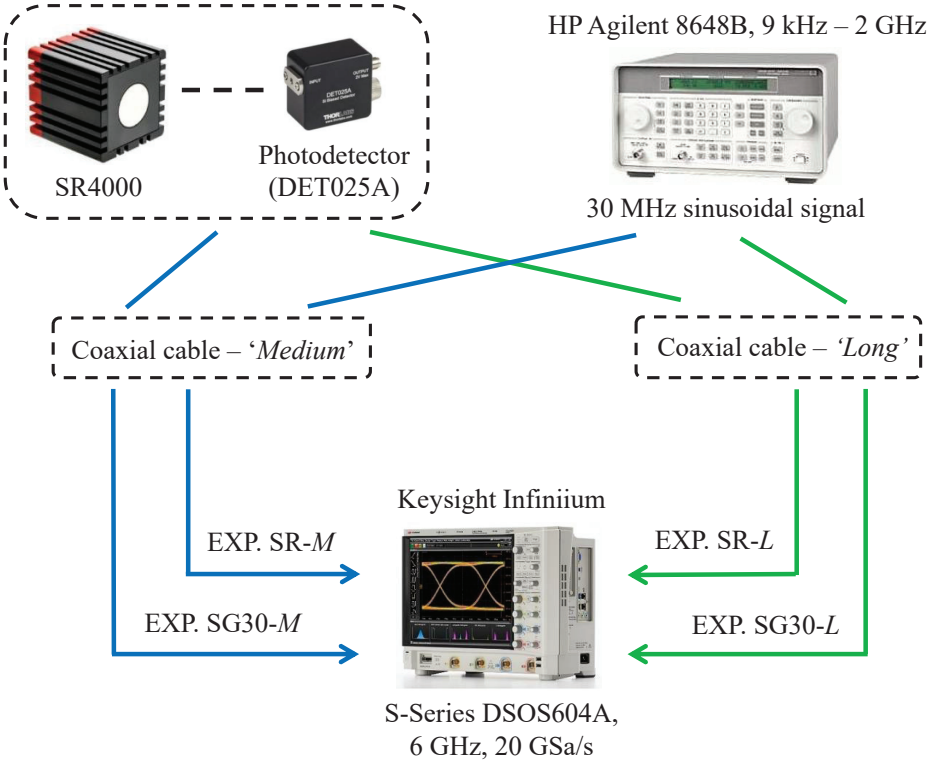

Figure 5.2: Experimental setup with MESA Imaging SwissRanger 4000.

Table 5.2: Parameters of the experimentation with SwissRanger 4000

Device	**Coaxial cable**	**No. of cycles**		**EXP. #**	
		$N_{\Delta t}^{cal}$	$N_{\Delta t}$		
MESA SR4000 with photodetector	*Medium*	15000	14998	SR-SG30	EXP. SR-*M*
					EXP. SG30-*M*
Signal Generator (30 MHz *sine* signal)	*Long*				EXP. SR-*L*
					EXP. SG30-*L*
Each experiment repeat 100 acquisitions					

5.2.2 Results and Discussion

For step ① of the proposed algorithm, the data signal from the light source of the camera and the 30 MHz sinusoidal signal from the signal generator were measured for each experimental setup separately. As an example, Figure 5.3 shows the corresponding results for the SR4000 and signal generator with the *Long* coaxial cable. By comparison, it is clear that the noise in the light source signal of SR4000 is relatively higher than from the signal generator.

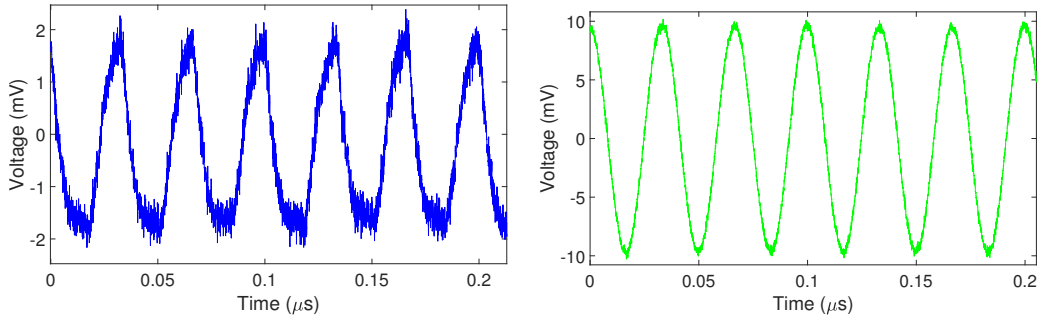

(a) (b)

Figure 5.3: Data signals as for step ① in proposed algorithm in Figure 5.1 for a single acquisition from (a) the light source signal of SR4000 and (b) signal generator (30 MHz signal), for the experiments denoted as EXP. SR-L and EXP. SG30-L in Table 5.2, respectively.

Before step ②, the DC component of each signal is removed by simply taking the subtraction of the original signal from its mean. Then, in order to obtain the smooth signal, it is important to optimise the parameters, such as the filter length and the order of polynomial of the Savitzky-Golay (SG) algorithm. Some various methods have been described in the literature (Persson and Strang, 2003; Vivó-Truyols and Schoenmakers, 2006; Krishnan and Seelamantula, 2012; Zhao *et al.*, 2014; Sadeghi and Behnia, 2018). When a signal is smoothed, it is impossible to obtain a method that eliminates all the noise without losing any valuable information. However, we used the trial and repetition method by visual inspection because it was quick and reliable.

Therefore, each signal is smoothed by the Savitzky-Golay filtering method (with third order polynomial and frame length $m = 55$ samples in Equation 4.1) with minimal impact on the zero crossings at the time axis (see sub-①). The resultant signals are shown in Figure 5.4. The corresponding reference (ideal) signal for each setup is generated by using the Fourier analysis as step ②. For that, the relevant frequency and the amplitude for the ideal signal are found as described in Sections 4.2.2 and 4.2.3, respectively.

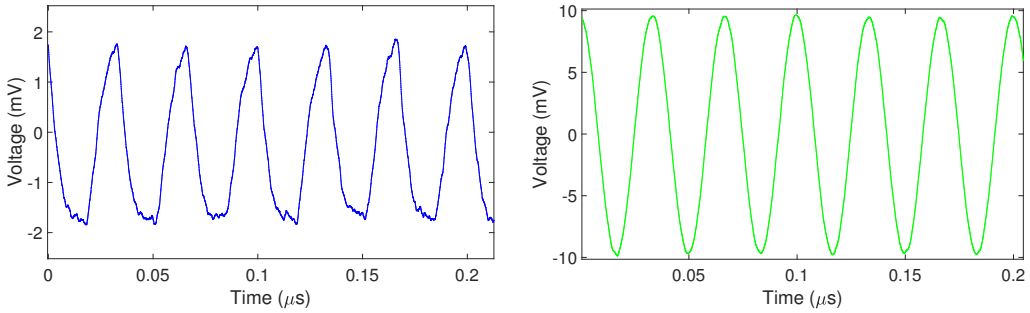

(a) (b)

Figure 5.4: Smoothed data signals (using Savitzky-Golay algorithm with third order polynomial and the length of 55 samples) for the same acquisition from (a) the light source of SR4000 and (b) signal generator, for the experiments denoted as EXP. SR-L and EXP. SG30-L in Table 5.2, respectively.

Next, the starting point of the signal at either rising or falling edge is set by removing the first full or partial cycles from the smoothed signal. We chose the rising edge as the aligning edge for all experiments in this chapter. Then, in order to align the smoothed signal with respect to the first zero crossing, the rising edge of the signal is placed exactly at the origin. For that, we use the corresponding time offset and linear interpolation technique. These sub-steps are illustrated in Figure 5.5 for the SR4000 (EXP. SR-L) and the signal generator (EXP. SG30-L).

For step ③, the data and ideal signals are aligned with respect to the first zero crossing point of rising edges as shown in Figure 5.6. Also, Figure 5.7 shows the corresponding zoomed-in portion around the origin of the aligned signals shown in Figure 5.6. Next, as sub-③, the zero crossings of the time axis at rising edges are obtained by analysing the sign difference of the amplitude (i.e., -*ve* to +*ve*) of each cycle for both signals.

By using linear interpolation (see Section 4.2.4), the zero crossing points at rising edges are estimated as for step ④. Then, the time deviation between the corresponding zero crossings of the data and ideal signals for each case is obtained as for step ⑤, as the jitter amount for each cycle of the signal. However, some of the resulted signals present with a linear trend because the ideal signal frequency is not exactly estimated. A *least-squared* linear regression (Chapra and Canale, 2015) is performed and subtracted off to detrend the signal as shown in Figure 5.8.

Next, before obtaining the jitter spectrum (as step ⑥) by DFT, the effect of spectral leakage is minimised by using the Hann window (see Section 4.2.5). Figure 5.9 shows the jitter amounts for each cycle with and without windowing

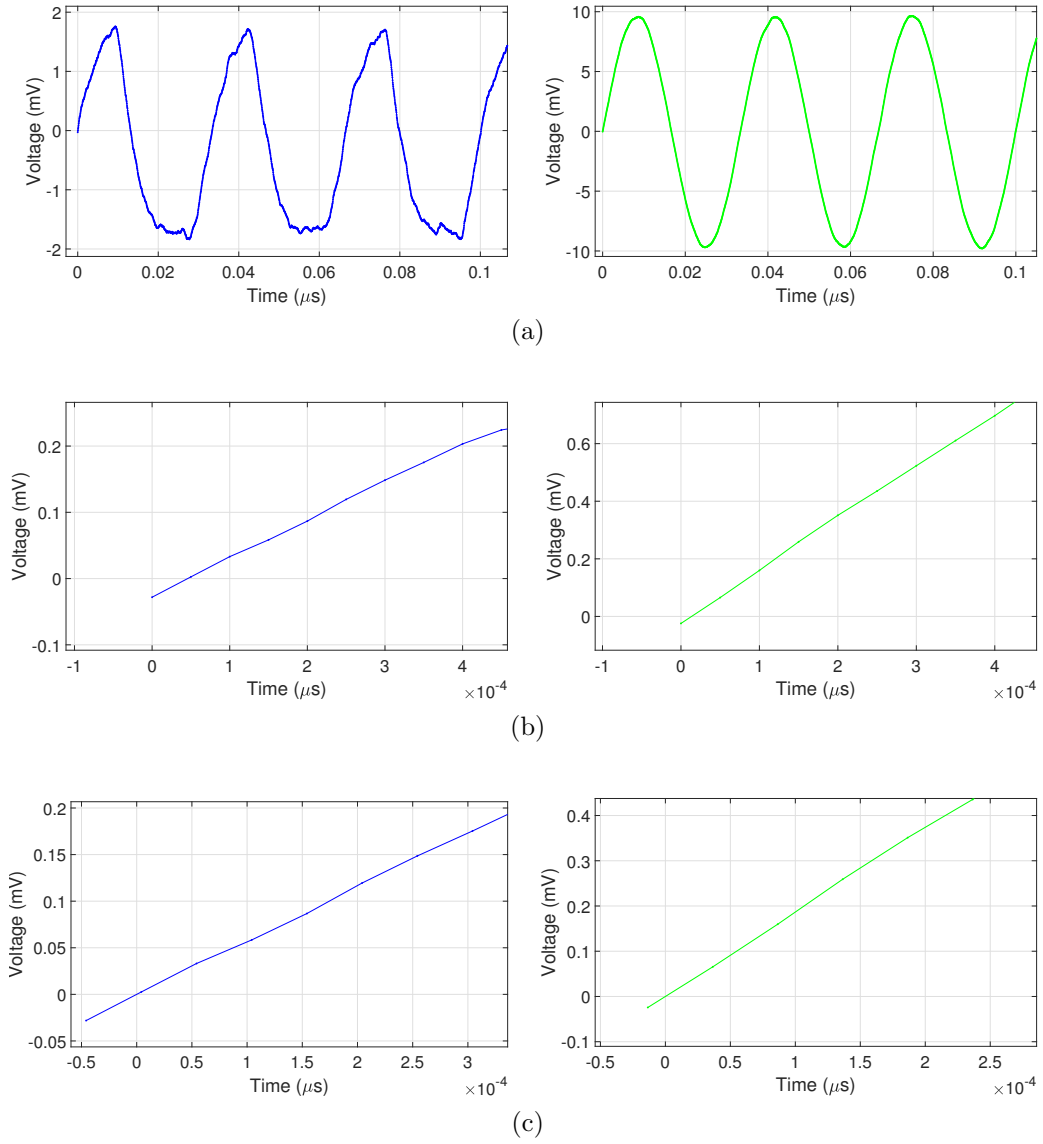

Figure 5.5: Sub steps (as sub-②) for the same acquisition shown in Figure 5.4 from (left) SR4000 and (right) signal generator, for the experiments denoted as EXP. SR-L and EXP. SG30-L in Table 5.2, respectively: (a) set the rising edge of smoothed signal as aligning edge (b) zoom-in the portion around origin of the aligned edge and (c) set the rising edge exactly at origin.

for the same acquisition for the experiments with SR4000 and signal generator, separately. The corresponding number of cycles is calculated by Equation 4.9 and its floor is included in column three and four, respectively, in Table 5.2.

In order to reduce the uncertainty of the result, we captured 100 acquisitions (by automating, see Section C.2 in Appendix C) for each experimental setup and obtained the jitter spectrum for each acquisition by using the steps ① to ⑥ in proposed algorithm as sub-⑥. Then, the total jitter spectrum

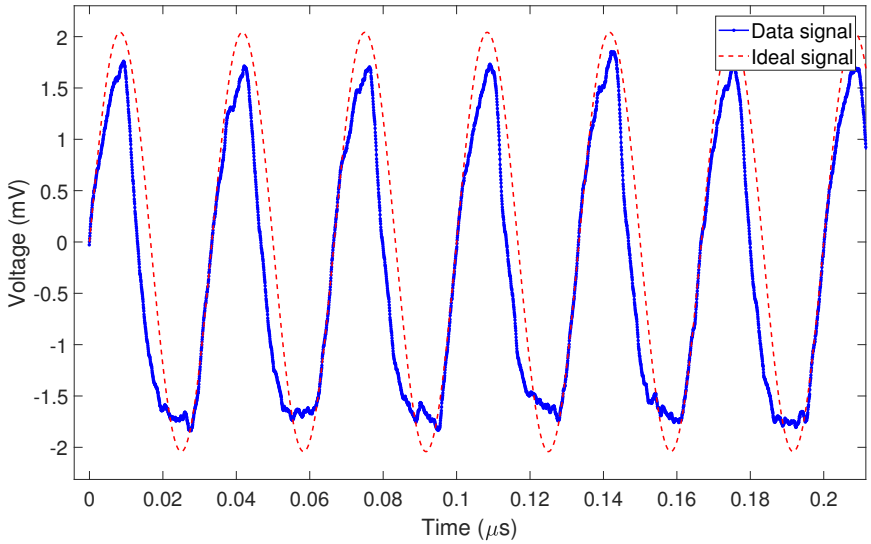

(a)

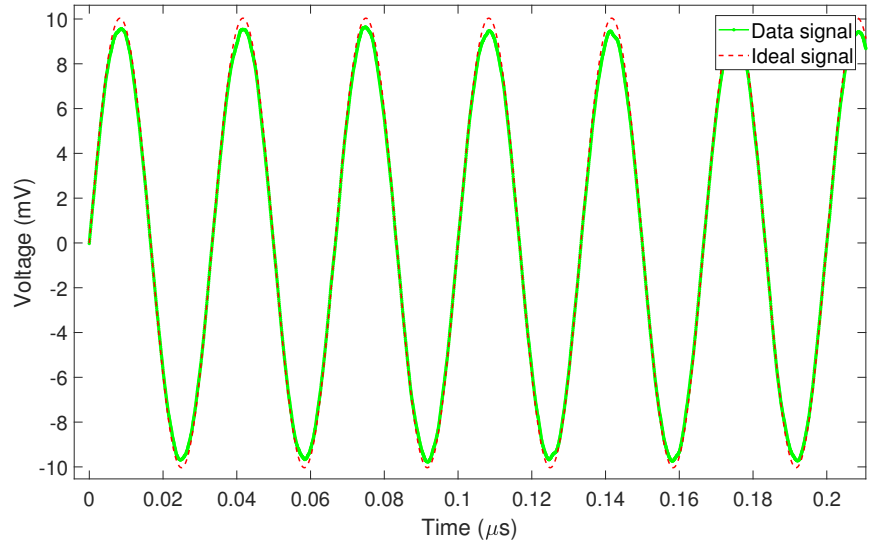

(b)

Figure 5.6: Aligned data and ideal signals (w.r.t first zero crossing at rising edge) as step ③ shown in Figure 5.1 for the same acquisition from (a) SR4000 and (b) signal generator, for the experiments denoted as EXP. SR-L and EXP. SG30-L in Table 5.2, respectively.

is formed by taking the mean spectrum among the multiple jitter spectra for each experiment. The jitter spectra for SR4000 and signal generator with the experiments using *Medium* and *Long* coaxial cables are illustrated in Figures 5.10 and 5.11, respectively. In addition, jitter components and the interpolated level between periodic and random jitter for each signal for both cases are marked in the figures.

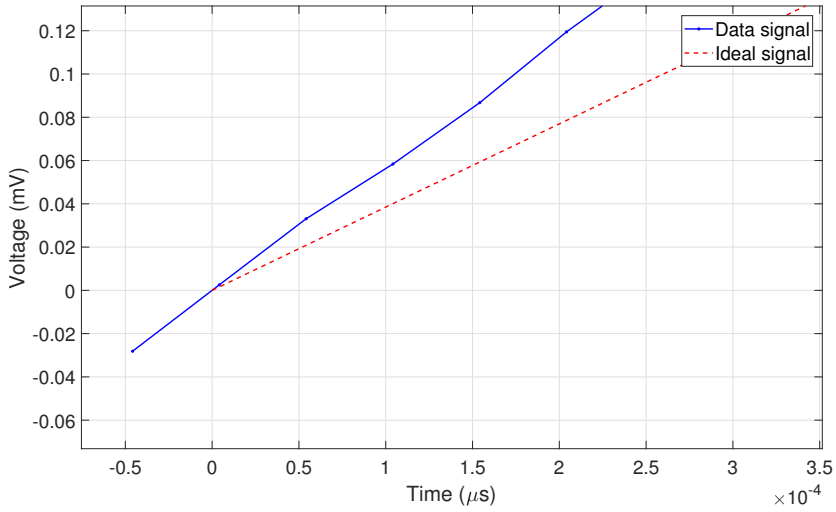

(a)

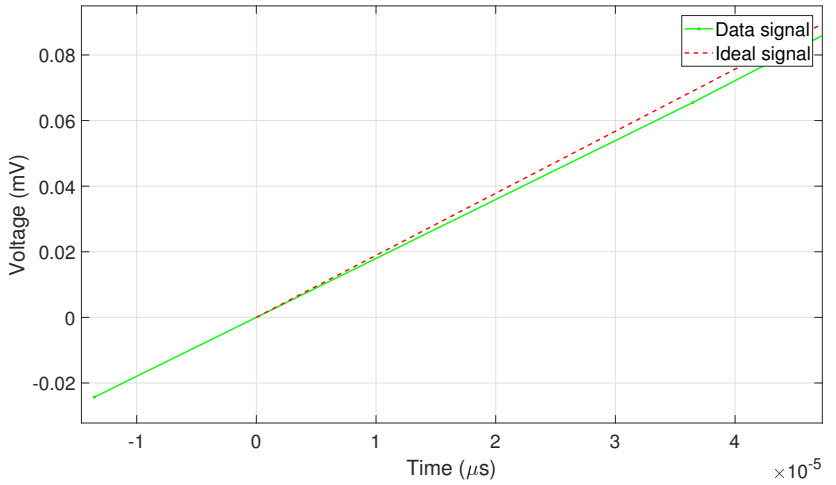

(b)

Figure 5.7: Zoomed-in portion around the origin of the aligned signals shown in Figure 5.6 for (a) SR4000 and (b) signal generator, for the experiments denoted as EXP. SR-L and EXP. SG30-L in Table 5.2, respectively.

By comparing two jitter signals (see Figures 5.10(b),(c) and 5.11(b),(c)) in each corresponding experiment, it is clear that there are two new high peaks at around 0 and 5 MHz on the jitter signal of SR4000 (i.e., both EXP. SR-M and EXP. SR-L) which are not present in the jitter signal of the signal generator (i.e., both EXP. SG30-M and EXP. SG30-L). There is also a broad and flat spectrum being the random jitter at the levels of approximately 1 and 0.3 ps for SR4000 and signal generator, respectively, in each case (see Figures 5.10(a) and 5.11(a)). Furthermore, there is a harmonic of the first PJ at around 0.12 MHz (see Figures 5.10(b) and 5.11(b)).

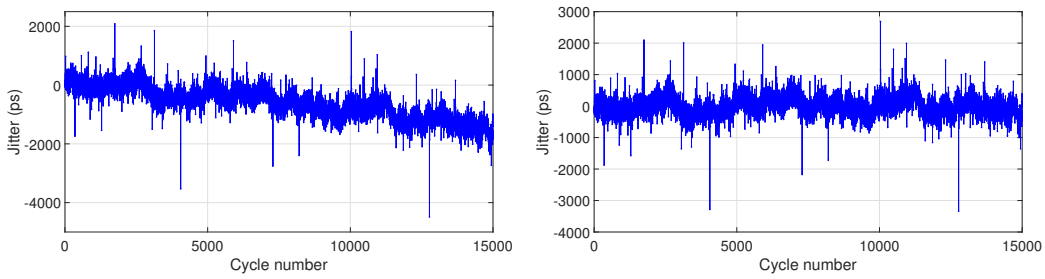

Figure 5.8: Jitter amounts (a) with linear trend and (b) without trend by using linear regression, for a particular acquisition of SR4000.

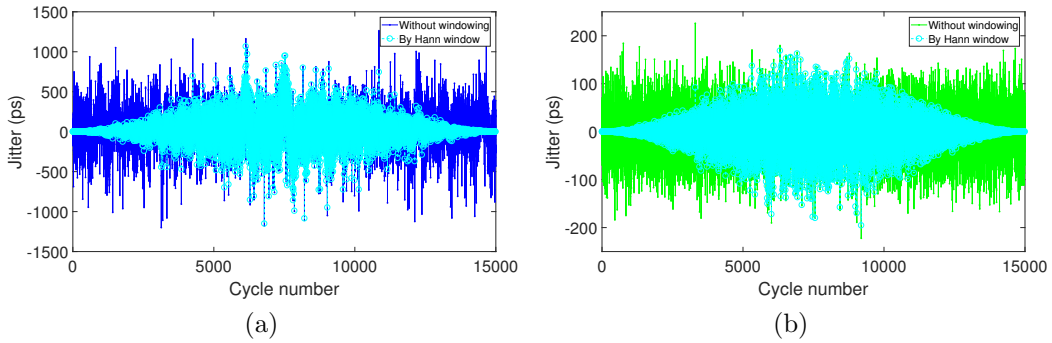

Figure 5.9: As step ⑤, jitter amount for each cycle (time deviation) with and without applying the Hann window for the same acquisition of (a) SR4000 and (b) signal generator, for the experiment denoted as EXP. SR-L and EXP. SG30-L in Table 5.2, respectively.

By using spectra of the total jitter (see Figures 5.10 and 5.11), it is straightforward to obtain the corresponding frequencies of the periodic jitter $f_{\mathrm{PJ}}^{(p)}$ in SR4000. The same value is given 0.064 MHz for the first frequency of PJ in both cases while they are bit different as 5.001 and 5.173 MHz for the second frequency of the PJ. Other jitter parameters are calculated by considering the energy of the spectrum as described in Section 4.3.1. The parameters, two amplitudes of periodic jitter $A_{\mathrm{PJ}}^{(p)}$ and the RMS of random jitter σ_{RJ} are calculated by using Equations 4.24 and 4.26, respectively. The calculated jitter parameters are tabulated in Table 5.3. The uncertainties are computed with the formulas shown in Section B.3.

The tabulated results are obtained by considering the full spectrum of the jitter signal for each relevant experiment. The corresponding frequency of the ideal signal for each experiment (a pure sine wave without jitter, extracted from the data) is included in column two. The standard error of the frequencies

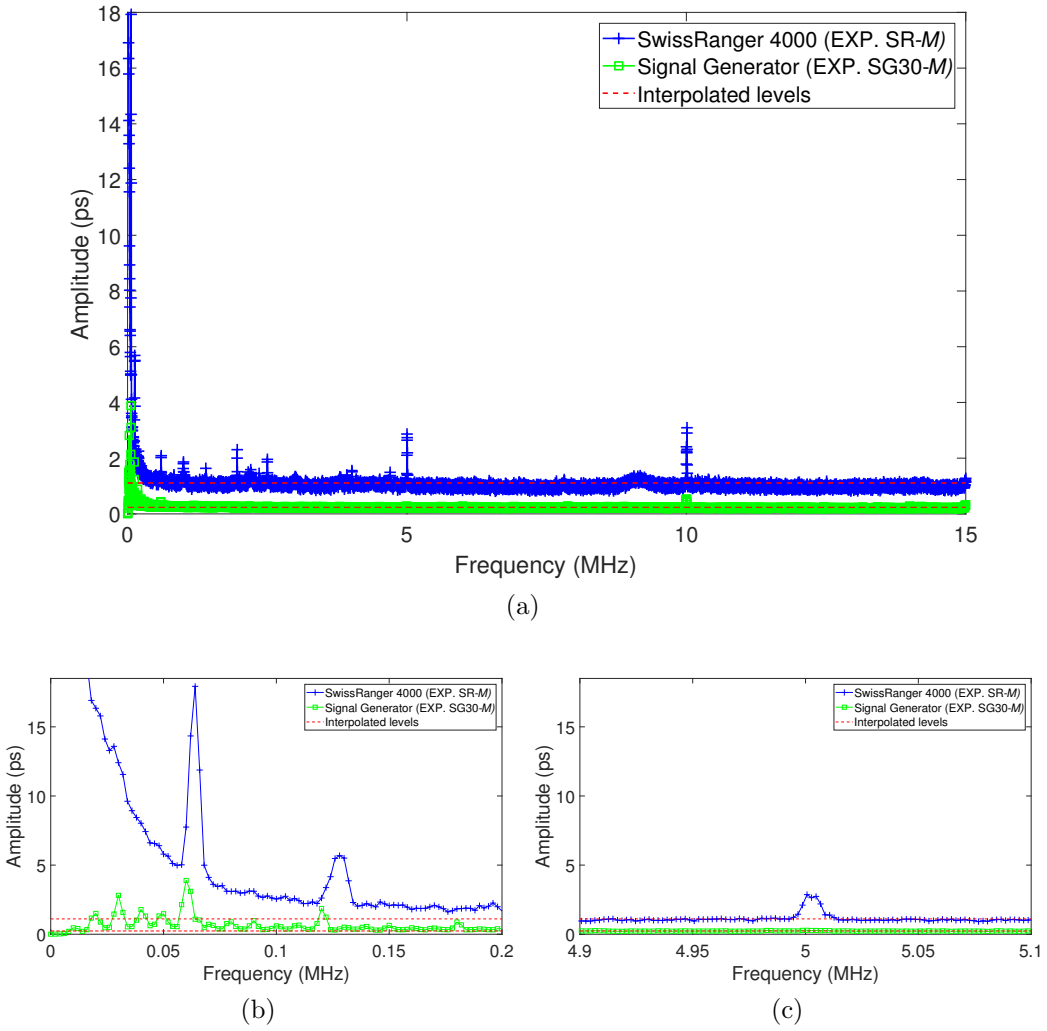

Figure 5.10: (a) Full spectrum, and its expansion portions at the two frequencies of PJ at the range (b) 0−0.2 MHz and (c) 4.9−5.1 MHz, for the SR4000 and signal generator for the experiment with *Medium* cable, denoted as EXP. SR-*M* and EXP. SG30-*M* in Table 5.2.

is also provided as a measure of precision. The SR4000 and signal generator frequencies are within one standard deviation of each other. The standard deviations are small compared to the ideal signal, with precision to six and seven significant digits for the SR4000 light source and signal generator, respectively. Therefore, we have measured the frequency to sufficient precision for our purposes. There is no detectable periodic jitter in the signal generator in both cases.

The lower frequency of the PJ is at 0.064 MHz with an amplitude of (71.5 ± 0.3) ps while the higher frequency is at (5.09 ± 0.06) MHz with an amplitude of (14.0 ± 1.4) ps. The RMS of the RJ in SR4000 is (173.6 ± 0.1) ps and

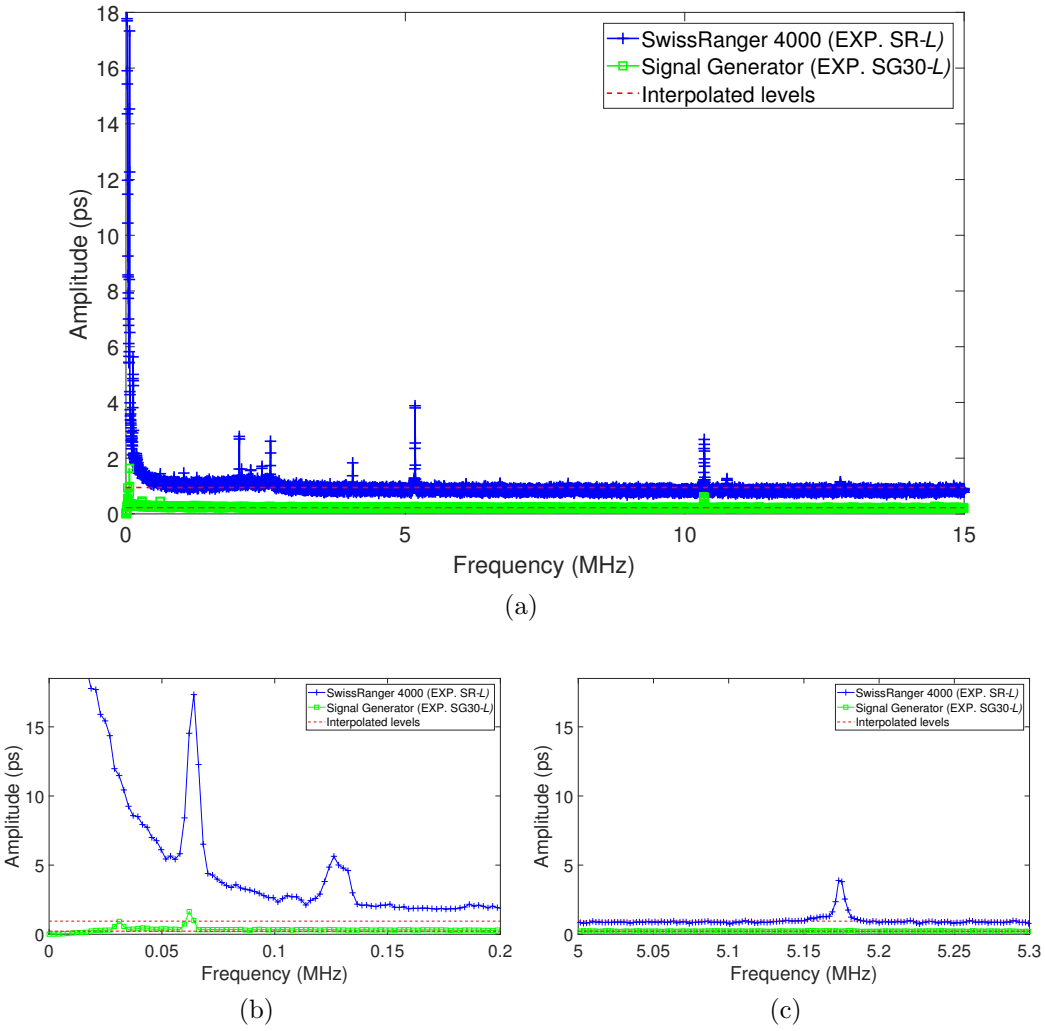

Figure 5.11: (a) Full spectrum, and its expansion portions at the two frequencies of PJ at the range (b) 0−0.2 MHz and (c) 5.0−5.3 MHz, for the SR4000 and signal generator for the experiment with *Long* cable, denoted as EXP. SR-*L* and EXP. SG30-*L* in Table 5.2.

(145.7 ± 0.1) ps while for the signal generator, it is (36.9 ± 0.1) and (34.3 ± 0.1) ps for the experiments with *Medium* and *Long* coaxial cables, respectively.

In addition, Table 5.4 shows previous experimental results that measured by using a low speed digital oscilloscope (HP Infiniium 54846B[4] with 2.25 GHz bandwidth, 8 GSa/s sampling rate and the maximum number of samples of 2^{16}, i.e., waveform length) for the same setup shown (with 1000 acquisitions) in the last column of Table 5.2. We found the random jitter of (35.4 ± 0.1) and (33.7 ± 0.2) ps for the signal generator experimented with *Medium* and

[4]`https://www.keysight.com/en/pd-1000004491%3Aepsg%3Apro-pn-54846B/infiniium-dso?cc=NZ&lc=eng#`

Table 5.3: Jitter parameters from the experiments with SwissRanger 4000

EXP. #	**Reference signal's frequency** (MHz)	**Periodic J.** $[f_{\mathrm{PJ}}^{(p)}$ (MHz), $A_{\mathrm{PJ}}^{(p)}$ (ps)]	**Random J.** σ_{RJ} (ps)
SR-*M*	29.999645 ± 0.000003	[0.064, 71] & [5.001, 12]	173.6 ± 0.1
SG30-*M*	30.00001 ± 0.00006	nil	36.9 ± 0.1
SR-*L*	29.999668 ± 0.000003	[0.064, 72] & [5.173, 16]	145.7 ± 0.1
SG30-*L*	30.00001 ± 0.00006	nil	34.3 ± 0.1

Long coaxial cables, respectively. This is strong evidence that the calculated random jitter corresponds to the signal generator itself only, not with including the oscilloscope.

On the other hand, it is found that for the SR4000 (see third column of Table 5.4), the frequencies of periodic jitter were at 0.12 and 5.04 MHz with amplitudes of (82.0 ± 14.8) and (32.0 ± 1.4) ps, respectively. It was unable to locate the frequency of 0.064 MHz from this low speed oscilloscope. With the waveform length, the bin width for the low speed oscilloscope (8 GSa/s ÷ 2^{16} = 122.11 kHz) is relatively larger than the medium speed oscilloscope (20 GSa/s ÷ 10^7 = 2 kHz), thus the low speed oscilloscope cannot resolve a low frequency periodic jitter. The intrinsic RMS jitter of the medium-speed and low-speed oscilloscopes are given as 100 fs and 8 ps ± 0.005% (delay setting) respectively, which are relatively very small compared to the measured jitter in the SR4000 camera.

Table 5.4: Jitter parameters for the same experiments shown in Table 5.2 with a low speed oscilloscope HP Infiniium 54846B

EXP. #	**Reference signal's frequency** (MHz)	**Periodic J.** $[f_{\mathrm{PJ}}^{(p)}$ (MHz), $A_{\mathrm{PJ}}^{(p)}$ (ps)]	**Random J.** σ_{RJ} (ps)
SR-*M*	30.00564 ± 0.00004	[0.12, 61] & [5.04, 34]	159.9 ± 0.3
SG30-*M*	30.00554 ± 0.00003	nil	35.4 ± 0.1
SR-*L*	30.00523 ± 0.00004	[0.12, 103] & [5.04, 30]	167.7 ± 0.5
SG30-*L*	30.00565 ± 0.00003	nil	33.7 ± 0.2

Since the jitter amplitudes at lower frequencies are very large, it is better to plot these figures in logarithmic scales. We analyse the data with curve fitting (see Section 4.3.2) and obtain the corresponding log-log graphs for total jitter.

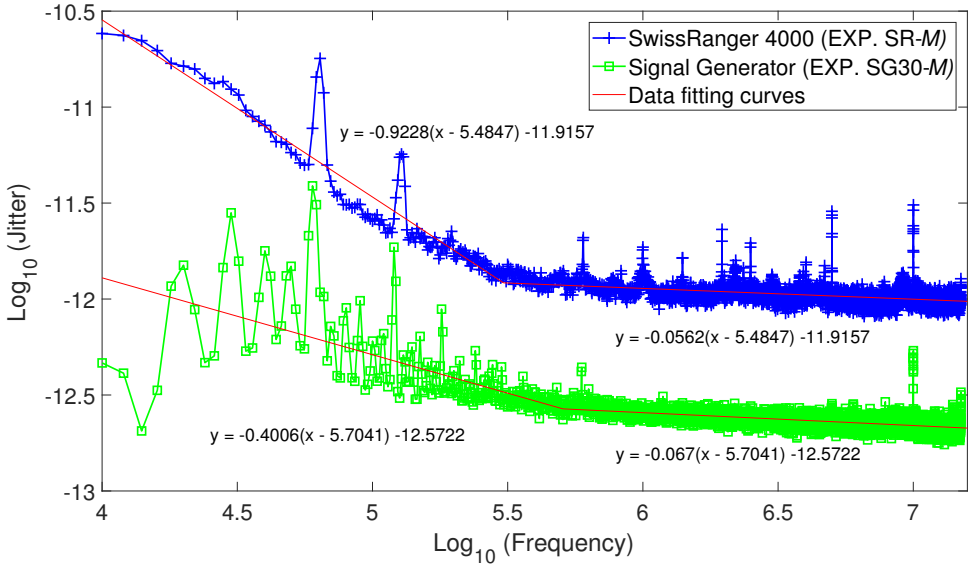

(a)

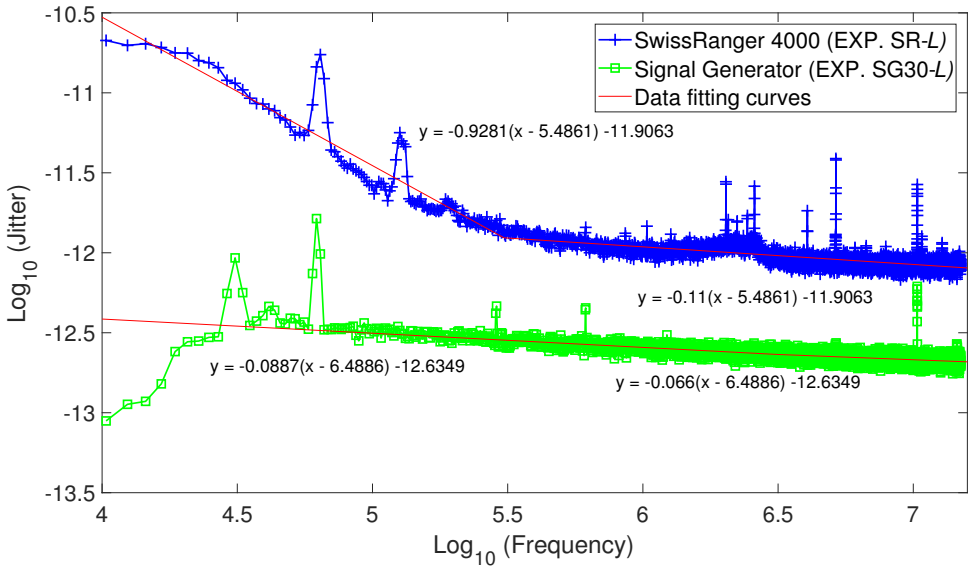

(b)

Figure 5.12: Log-log scale (base 10) with fitted curves for spectra shown in Figures 5.10 and 5.11 for the SR4000 and signal generator for the experiments with (a) *Medium* and (b) *Long* cables, denoted as EXP. SR-*L* and EXP. SG30-*L* in Table 5.2.

Figure 5.12 shows the log-log plots for the jitter spectra for the SR4000 and signal generator for both experimental setup (corresponding to Figures

5.10(a) and 5.11(a)). Note that the first few points from the data are not plotted because they are extremely large. In addition, the fitted curves (see Section 4.3.2) with their characteristic equations for each case are stated on the figures.

The slopes at low frequencies of the total jitter for the SR4000 are higher than at the rest of the frequencies (see Figures 5.10(b) and 5.11(b)) in each case. At the low frequencies of SR4000, the slope is -0.94 ± 0.02 while it is -0.3 ± 0.3 for the signal generator. This may be due to the flicker noise ($f^{-0.94\pm0.02} \approx 1/f$) in the camera. This trend is approximately similar in both cases for the SR4000 camera. In addition, there is a relatively larger slope at low frequencies for the *Medium* cable than *Long* cable for the signal generator (compare (a) and (b) of Figure 5.12). It is believed that these are due to cables and connectors.

5.3 SoftKinetic DepthSense 325

The illumination signal of the SoftKinetic DepthSense 325 (DS325) is captured by using the same photodetector, DET025A. The DS325 uses eye-safe near infrared laser light for its illumination source. Here we use its fixed modulation frequency (i.e., 50 MHz) with the frame rates of 25 fps throughout the experiments. The illumination source of this camera produces approximately square waves and all signals are measured with the same oscilloscope.

5.3.1 Experimental Setup for DS325

The same experimental setup used in Section 5.2.1 is used here, but additionally, a third coaxial cable which is shorter than the previous two cables was also used. Therefore, the three coaxial cables labelled as, *'Short', 'Medium'* and *'Long'* where length measured from tip to tip of the BNC connectors are listed in Table 5.5. For the control, the 50 MHz pure sine waves with the HP Agilent 8648B are generated and measured with the DSOS604A oscilloscope. The specification of the components used is presented in Table 5.5.

The experimental setup and its relevant parameters are shown in Figure 5.13 and Table 5.6, respectively. In order to verify our proposed algorithm for general cases, both square and sine waves are generated as for the ideal signals of the camera and both cases are analysed. These are denoted as EXP. DS_{sq}-{...} and EXP. DS_{sn}-{...}, in the figure and table.

Table 5.5: Specification of the components used with DepthSense 325

Component	**Specification used**		
ToF camera	Modulation frequency (f_m)	Frame rates	Illumination source
DepthSense 325	50 MHz	25 fps	Infrared laser
Light detector	Detector	Bandwidth	Spectral range
Thorlabs DET025A	Silicon biased	2 GHz	400 − 1100 nm
Oscilloscope	Bandwidth	Sampling frequency (F_s)	Number of samples
S-Series DSOS604A	6 GHz	20 GSa/s	$N_s \approx 5 \times 10^6$
Signal generator	Sinusoidal signal of the frequency		
HP Agilent 8648	50 MHz		
Cable	Length (m), from tip to tip of the BNC connectors		
	Short (S)	*Medium (M)*	*Long (L)*
Coaxial	0.490 ± 0.005	1.070 ± 0.005	1.790 ± 0.005

5.3.2 Results and Discussion

As before, we capture the data signal from the light source of the camera and directly from the signal generator, for each experimental setup. Figure 5.14 shows the square wave from the DS325 and a sine wave from the signal generator for a single acquisition of the experiments with *Long* coaxial cable, separately. These sub figures are adjusted by the offset amplitude. The noise in the DS325 is also relatively higher than the signal generator.

To generate the ideal signal, the procedure sub-① is used as shown in Figure 5.1 including the smoothing of the signal by Savitzky-Golay filtering method (with third order polynomial and frame length $m = 55$ samples in Equation 4.1). The resultant signal is shown in Figure 5.15 for both the camera and signal generator. The reference signal (ideal) for each setup is generated by using the Fourier analysis as step ②.

Next, the first couple of full or partial cycles from the smoothed signal are removed in order to start the signal at rising edge. Then, the first zero crossing at rising edge of the signal is placed exactly at the origin by using the

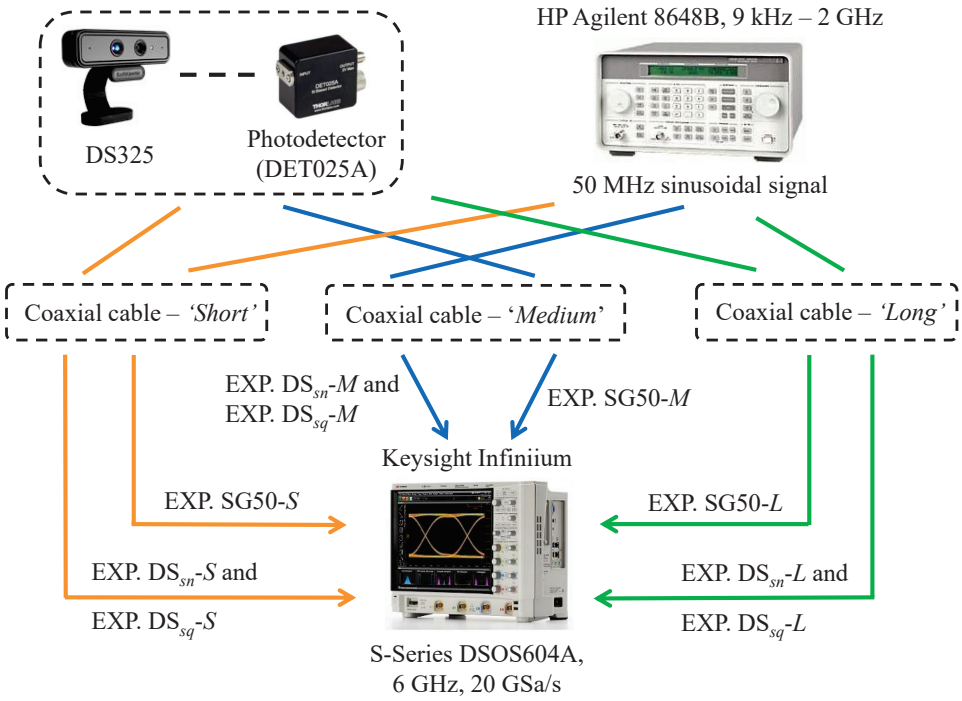

Figure 5.13: Experimental setup with SoftKinetic DepthSense 325.

Table 5.6: Parameters of the experimentation with DepthSense 325

Device	**Type of the ideal signal**	**Coaxial cable**	**Number of cycles ($N_{\Delta t}$)**	**EXP. #**	
DS325 with photodetector	*sine* / *square*	*Short*	12325	DS325	EXP. DS$_{sn}$-*S*
					EXP. DS$_{sq}$-*S*
	sine / *square*	*Medium*			EXP. DS$_{sn}$-*M*
					EXP. DS$_{sq}$-*M*
	sine / *square*	*Long*			EXP. DS$_{sn}$-*L*
					EXP. DS$_{sq}$-*L*
Signal Generator HP Agilent 8648 (50 MHz *sine* signal)		*Short*		SG50	EXP. SG50-*S*
		Medium			EXP. SG50-*M*
		Long			EXP. SG50-*L*

sub-steps denoted as sub-② and the results are illustrated in Figure 5.16 for DS325 (EXP. DS$_{sq}$-*L*) and signal generator (EXP. SG50-*L*), separately. For step ③, the data and ideal signals are aligned with respect to the first zero crossing point of rising edges as shown in Figure 5.17, for each case.

When we consider a sine wave ideal signal for the camera (denoted as EXP. DS$_{sn}$-{...}), we aligned the data and ideal signals as shown in Figure 5.18.

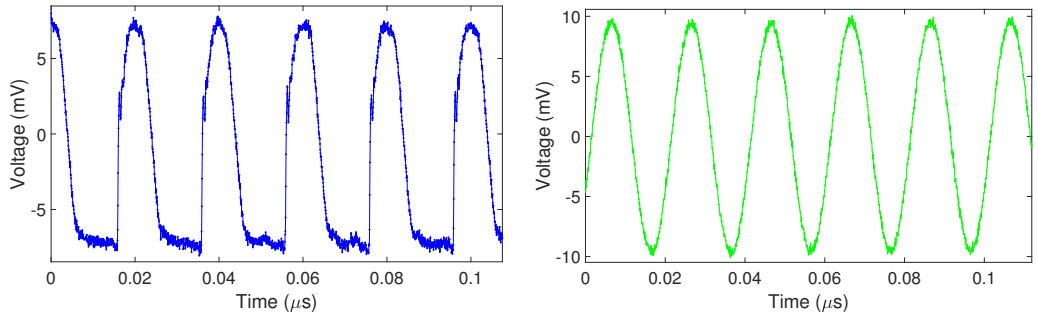

(a) (b)

Figure 5.14: Data signals as for step ① in proposed algorithm in Figure 5.1 for a single acquisition from (a) the light source signal of DS325 and (b) 50 MHz signal from signal generator, for the experiments denoted as EXP. DS$_{sq}$-L and EXP. SG50-L in Table 5.6, respectively.

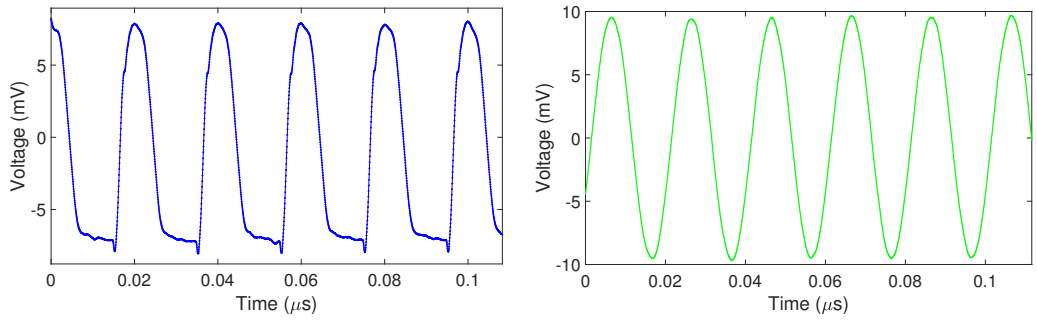

(a) (b)

Figure 5.15: Smoothed data signals (using Savitzky-Golay algorithm with third order polynomial and the length of 55 samples) for the same acquisition from (a) the light source of DS325 and (b) signal generator, for the experiments denoted as EXP. DS$_{sq}$-L and EXP. SG50-L in Table 5.6, respectively.

Next, as sub-③, the zero crossings of the time axis at rising edges are obtained by analysis of the sign difference of the magnitude (i.e., *-ve* to *+ve*) of each cycle for both signals. By using linear interpolation (see Section 4.2.4), the zero crossing points at rising edges are estimated as for step ④. Next, the time deviation between the corresponding zero crossings of the data and ideal signals for each case is obtained as for step ⑤. This gives the jitter signal.

The effect of spectral leakage is reduced by using the Hann window. Figure 5.19 shows the jitter signal for each cycle with and without windowing for the same acquisition for the experiments with DS325 when the shape of the ideal signal is in square wave and sine wave, separately. The calculated corresponding number of cycles for each case (by using Equation 4.9) and its floor are included in column three and four, respectively, in Table 5.6.

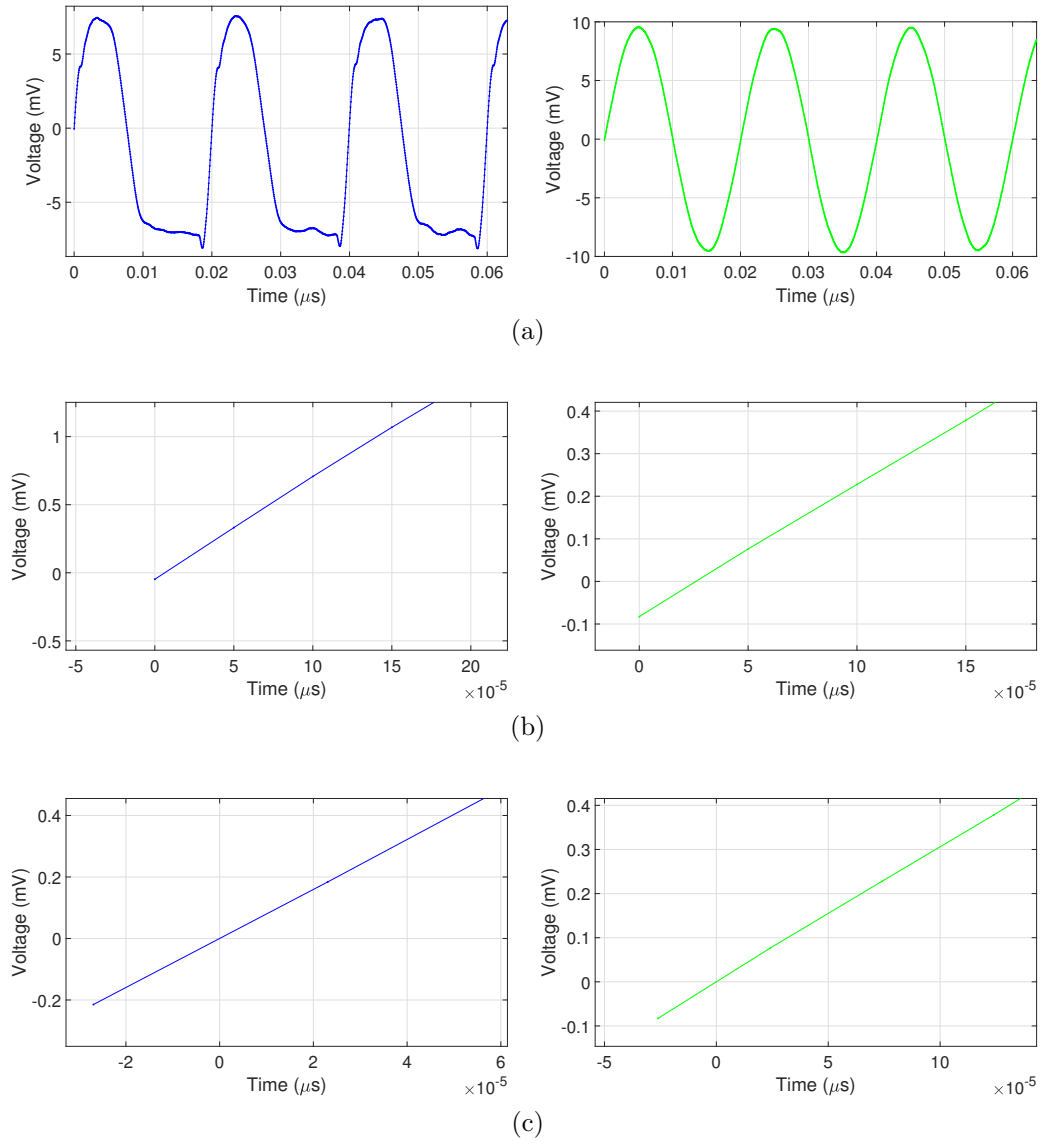

Figure 5.16: Sub-steps for the same acquisition shown in Figure 5.15 from (left) DS325 and (right) signal generator, for the experiments denoted as EXP. DS$_{sq}$-L and EXP. SG50-L in Table 5.6, respectively: (a) set the rising edge of smoothed signal as aligning edge (b) zoom-in the portion around origin of the aligned edge and (c) set the rising edge exactly at origin.

As before, in order to control the uncertainty of the results, 100 acquisitions were captured for each experimental setup and the jitter spectrum was formed for each acquisition by using steps ① to ⑥ of the proposed algorithm. Then, the total jitter spectrum is formed by taking the mean spectrum among the multiple jitter spectra for each experiment. The jitter spectra for DS325 and signal generator with the experiments using *Short* coaxial cable is illustrated in Figure 5.20. Each sub figure corresponds to the shape of the generated ideal

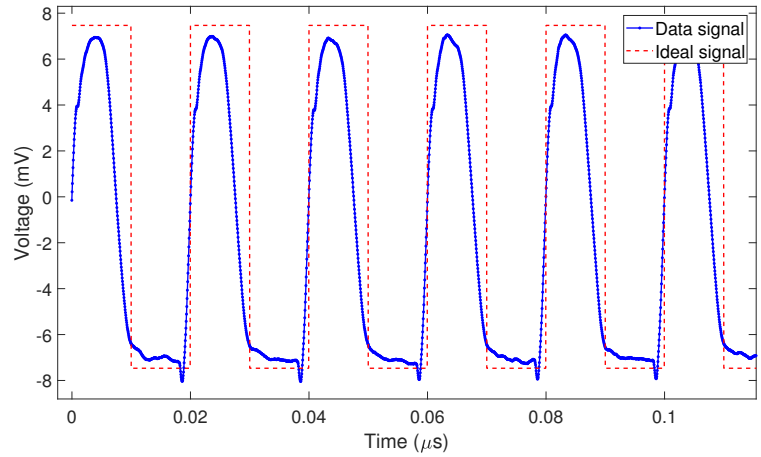

(a)

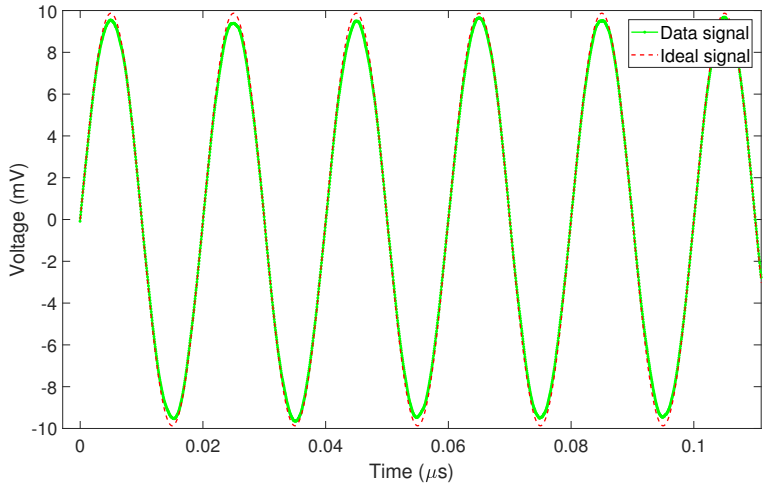

(b)

Figure 5.17: Aligned data and ideal signals (w.r.t first zero crossing at rising edge) as step ③ in Figure 5.1 for the same acquisition from (a) DS325 and (b) signal generator, for the experiments denoted as EXP. DS$_{sq}$-*L* and EXP. SG50-*L* in Table 5.6, respectively.

signal of the DS325 (i.e., sine wave as EXP. DS$_{sn}$-{...} and square wave as EXP. DS$_{sq}$-{...}), separately. In addition, jitter components for the DS325 and the interpolated level between periodic and random jitter for all cases are marked in the figures. Here also we can see there are two high peaks on the jitter signal of DS325 (both EXP. DS$_{sn}$-*S* and EXP. DS$_{sn}$-*S*) which are not present in the jitter signal of the signal generator. The expanded versions of these two peaks are illustrated in Figure 5.21. Similarly the results of the jitter spectra and their expanded versions from the experiments with *Medium* and *Long* coaxial cables are illustrated in Figures 5.22 – 5.25, respectively.

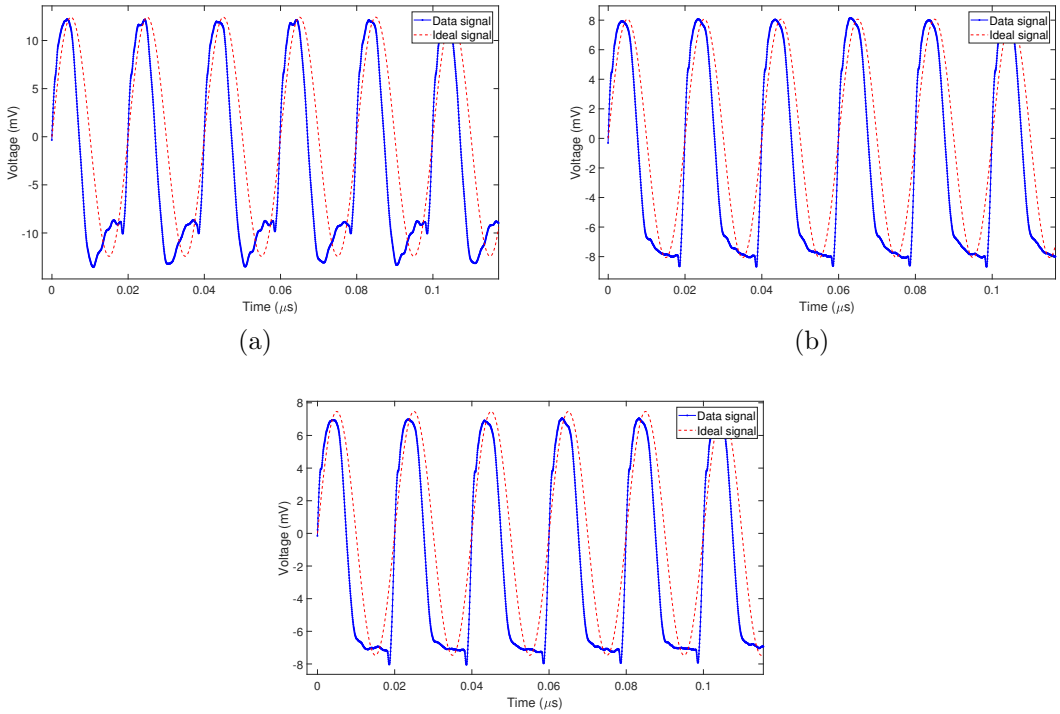

Figure 5.18: Aligned data and sine shape ideal signals (w.r.t first zero crossing at rising edge) as step ③ in Figure 5.1 for the acquisitions from DS325 for the experiments with (a) *Short* cable as EXP. DS$_{sn}$-*S* (b) *Medium* cable as EXP. DS$_{sn}$-*M* and (c) *Long* cable as EXP. DS$_{sn}$-*L* in Table 5.6.

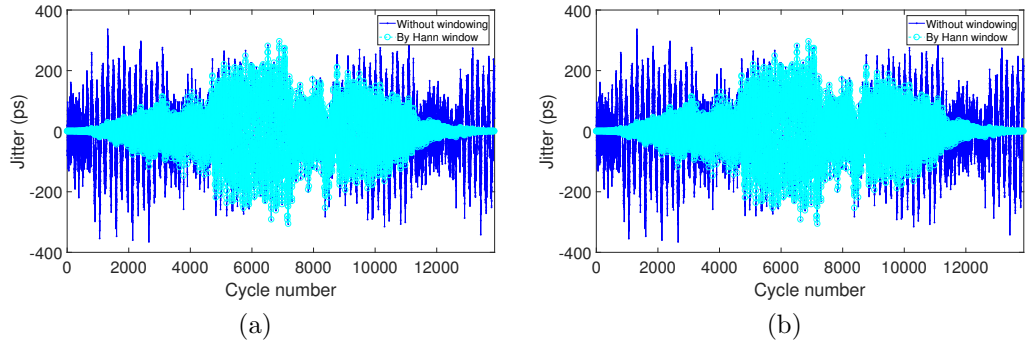

Figure 5.19: As for step ⑤, jitter amount for each cycle (time deviation) with and without applying Hann window for the same acquisition of DS325 when the shape of the generated ideal signal in (a) square wave and (b) sine wave, for the experiment denoted as EXP. DS$_{sq}$-*L* and EXP. DS$_{sn}$-*L* in Table 5.6, respectively.

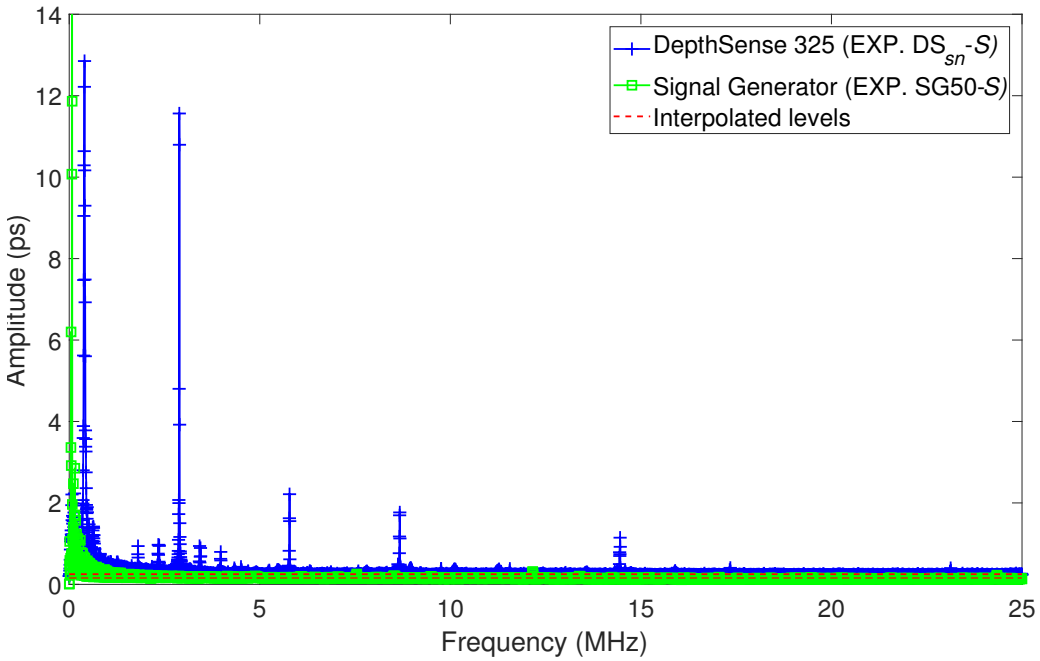

(a)

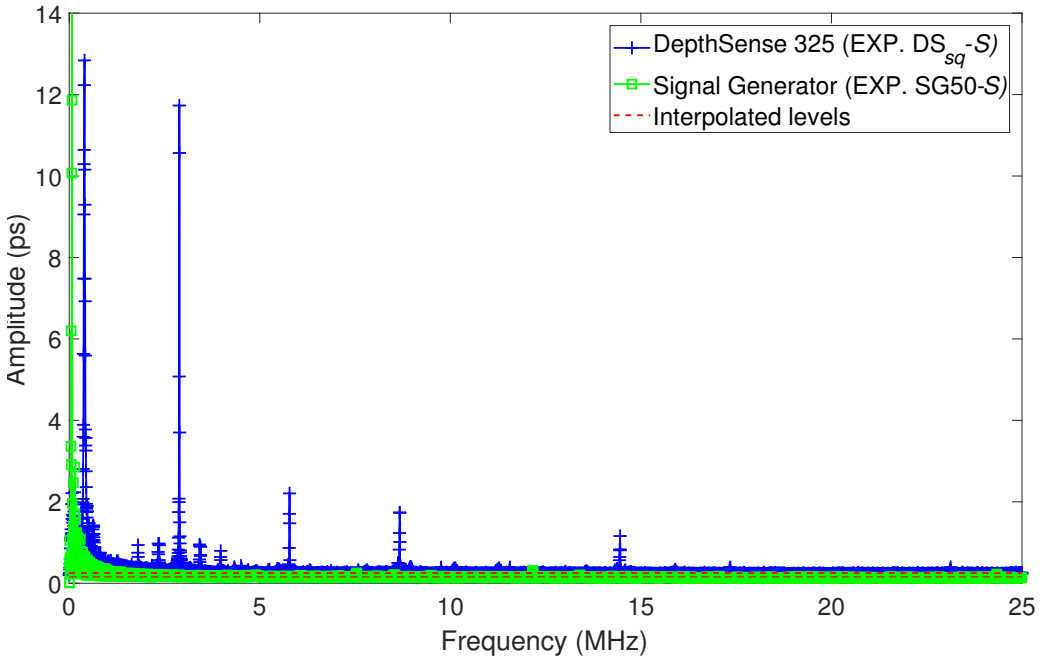

(b)

Figure 5.20: Jitter spectrum of the DS325 and signal generator for the experiment with *Short* cable when the generated ideal signal for the DS325 (a) sine wave and (b) square wave, denoted as EXP. DS$_{sn}$-*S* and EXP. DS$_{sq}$-*S* in Table 5.6, respectively.

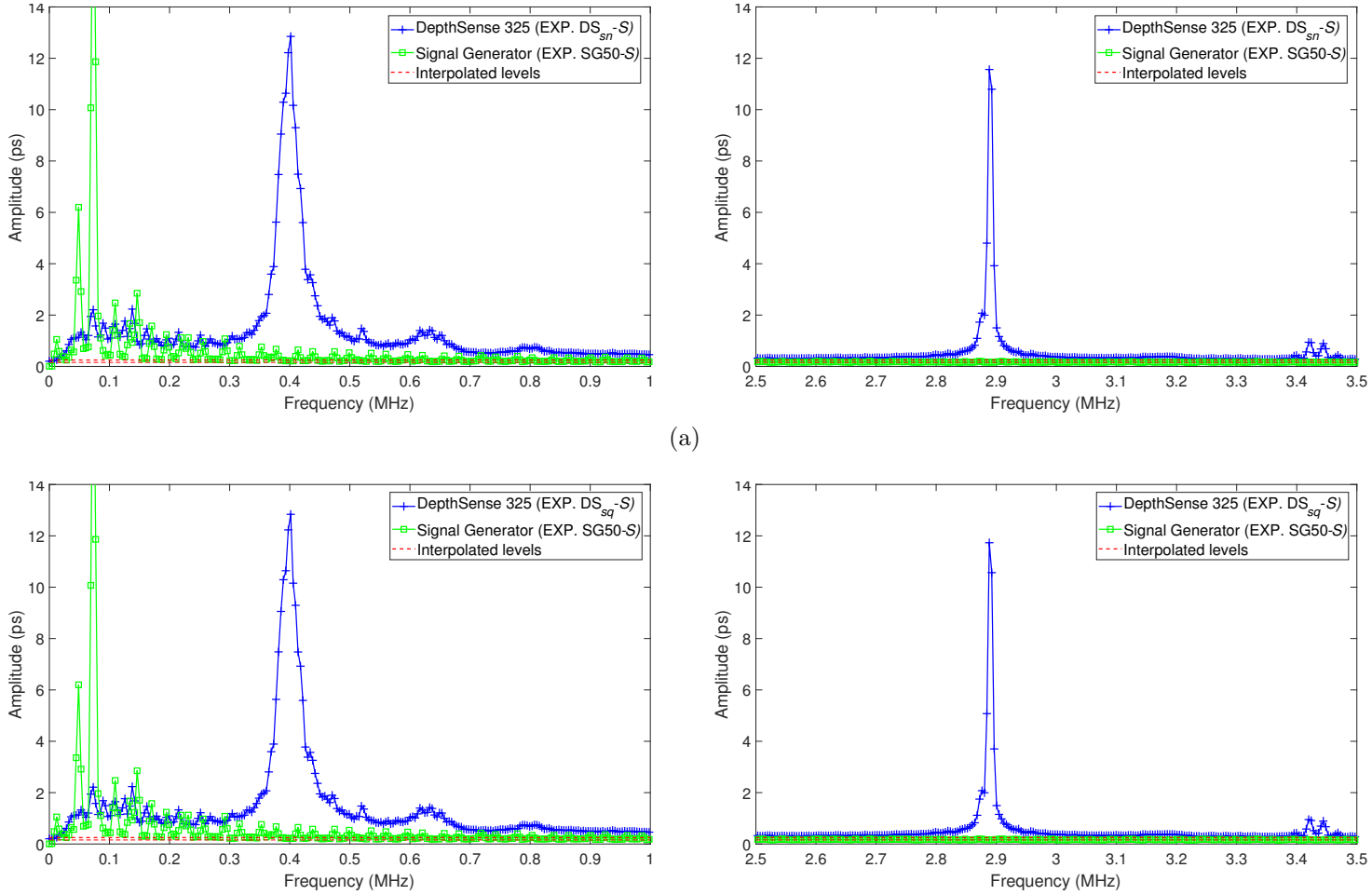

Figure 5.21: Expansion of the two frequencies (left and right) of the PJ of the jitter spectra for the DS325 and signal generator (corresponding to Figure 5.20), experimented with *Short* cable when the ideal signal of DS325 is (a) sine wave and (b) square wave.

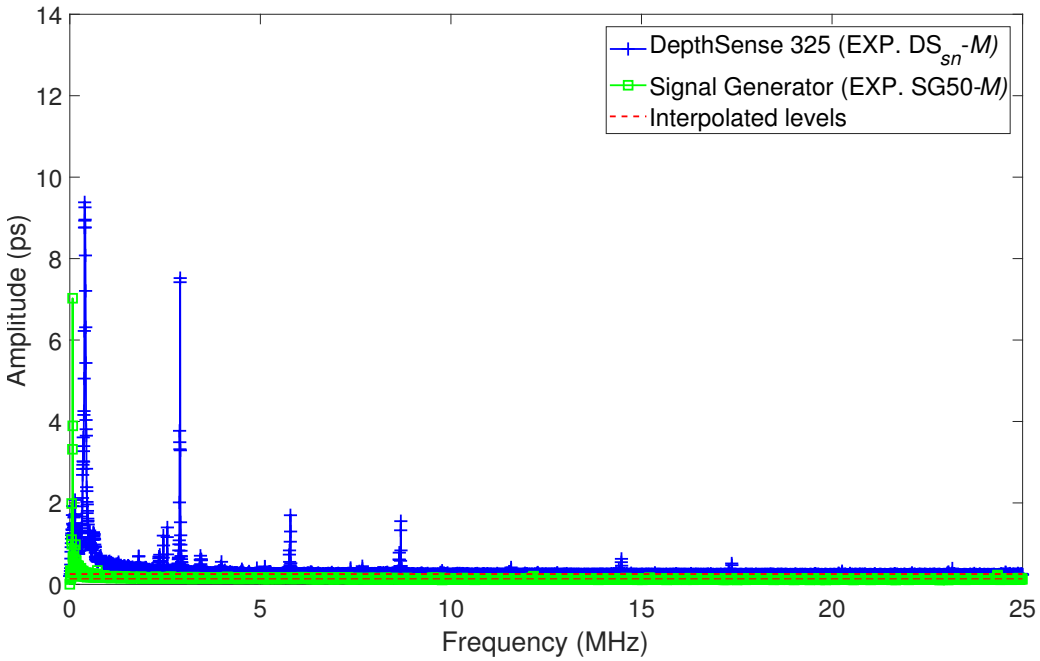

(a)

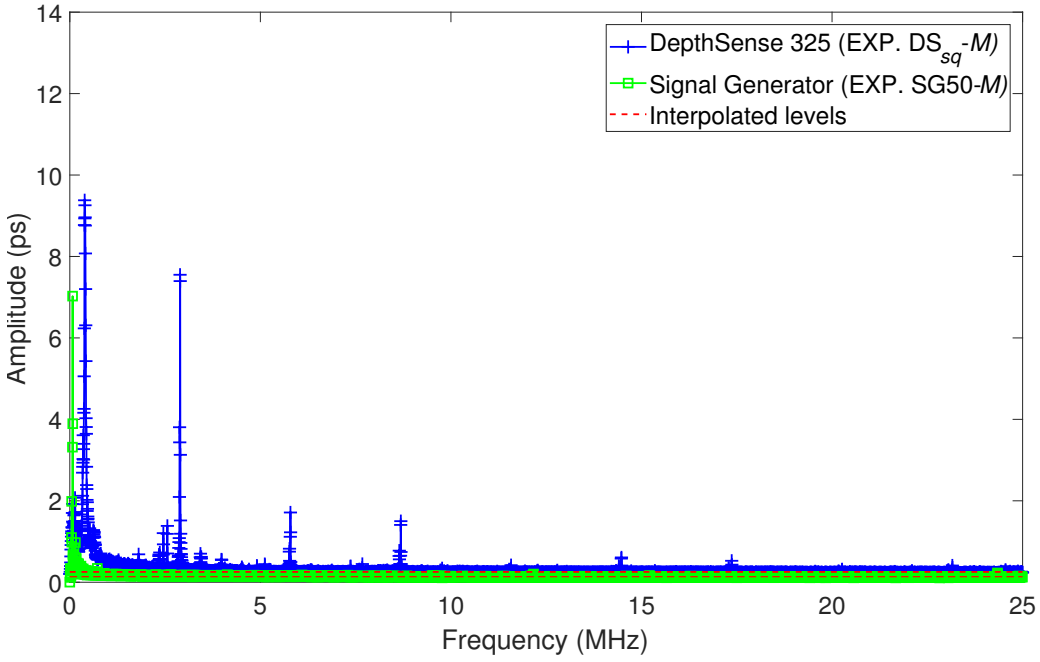

(b)

Figure 5.22: Jitter spectrum of the DS325 and signal generator for the experiment with *Medium* cable when the generated ideal signal for the DS325 (a) sine wave and (b) square wave, denoted as EXP. DS$_{sn}$-*M* and EXP. DS$_{sq}$-*M* in Table 5.6, respectively.

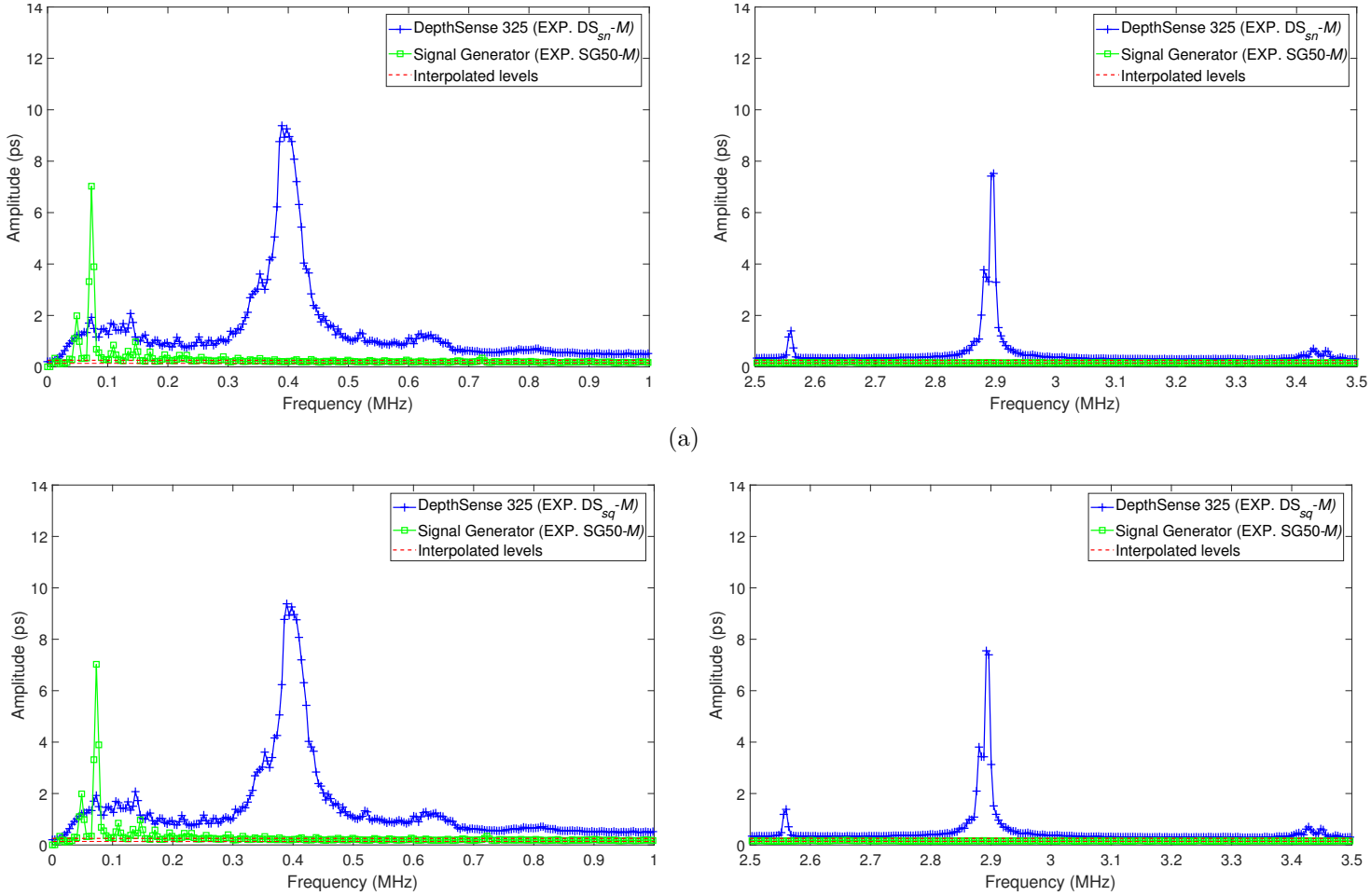

Figure 5.23: Expansion of the two frequencies (left and right) of the PJ of the jitter spectra for the DS325 and signal generator (corresponding to Figure 5.22), experimented with *Medium* cable for the ideal signal of DS325 is (a) sine wave and (b) square wave.

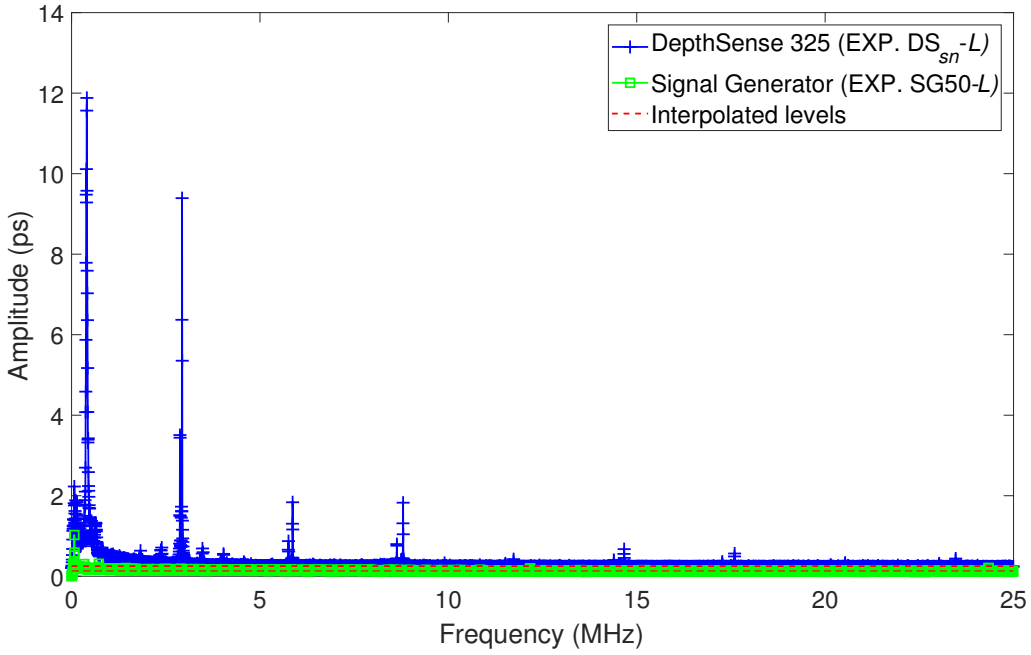

(a)

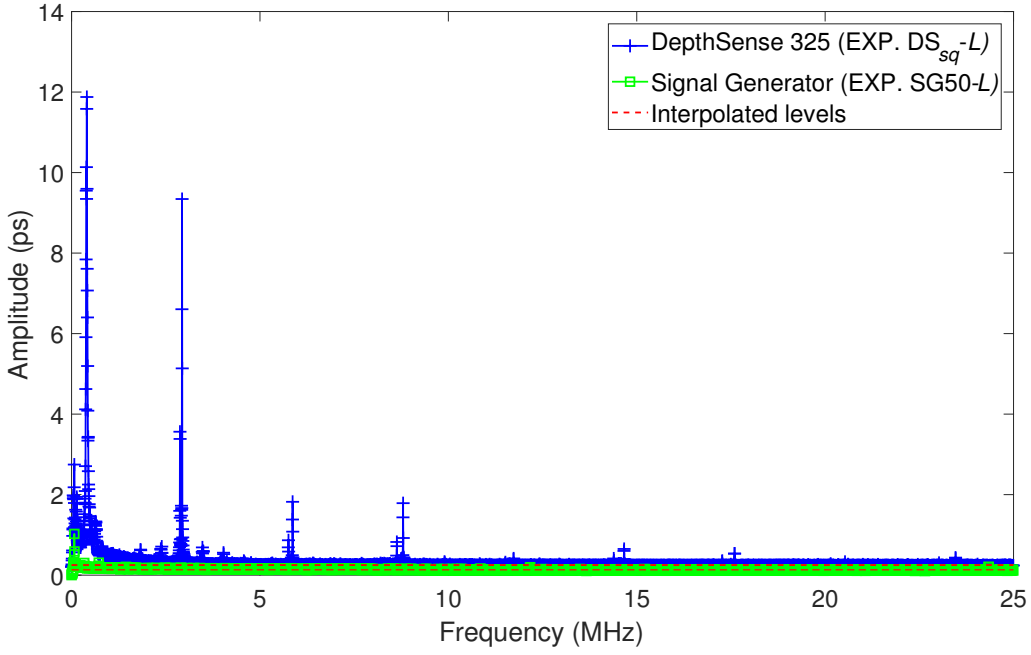

(b)

Figure 5.24: Jitter spectrum of the DS325 and signal generator for the experiment with *Long* cable when the generated ideal signal for the DS325 (a) sine wave and (b) square wave, denoted as EXP. DS$_{sn}$-L and EXP. DS$_{sq}$-L in Table 5.6, respectively.

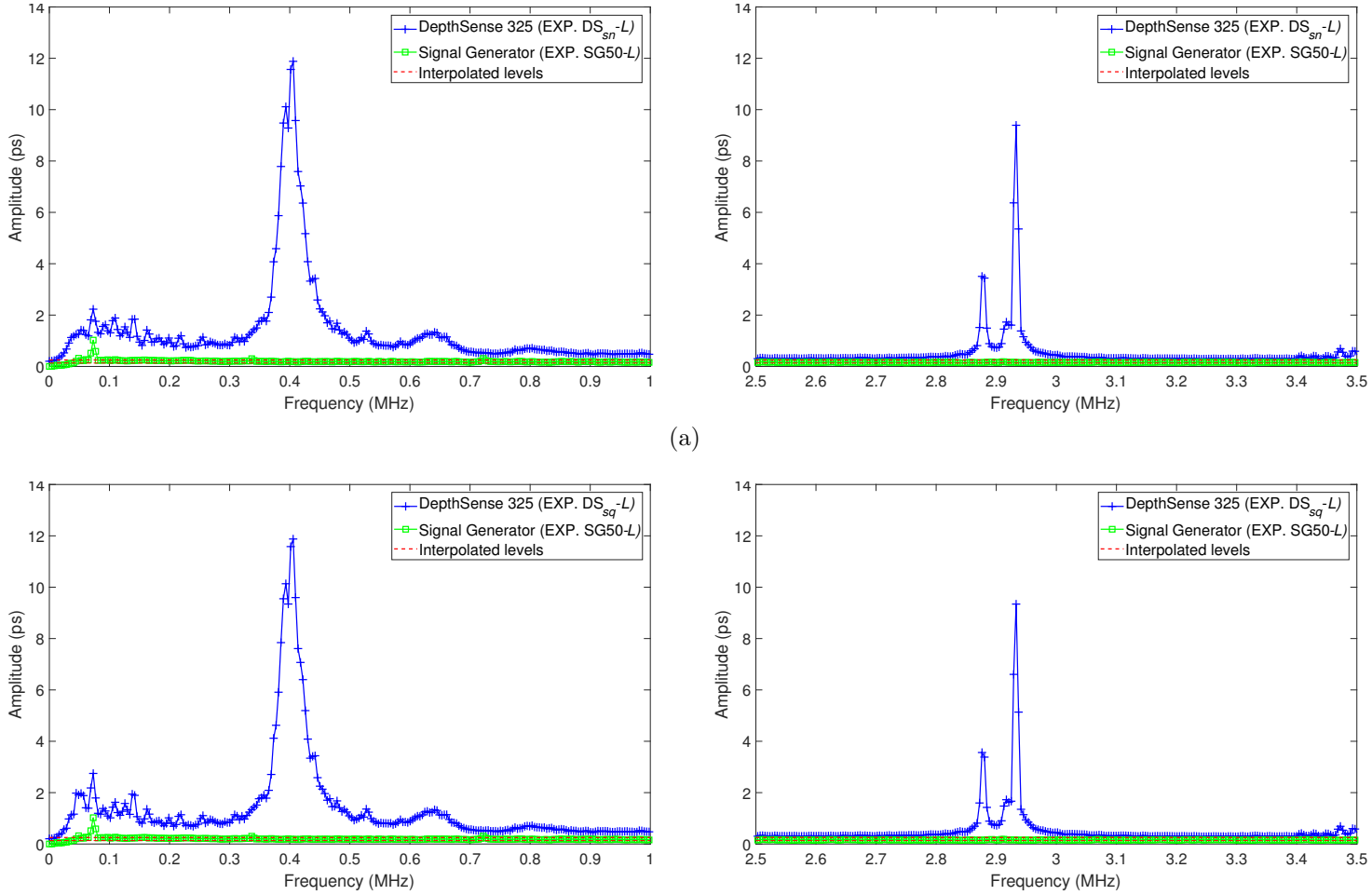

Figure 5.25: Expansion of the two frequencies (left and right) of the PJ of the jitter spectra for the DS325 and signal generator (corresponding to Figure 5.24), experimented with *Long* cable for the ideal signal of DS325 is (a) sine wave and (b) square wave.

By comparing the DS325 and signal generator two jitter signals in each corresponding experiment (see Figures 5.21, 5.23 and 5.25), it is clear that there are two new high peaks at around 0.4 and 2.9 MHz on the jitter signal of DS325 (i.e., EXP. DS$_{sn}$ and EXP. DS$_{sq}$) which are not present in the jitter signal of the signal generator (i.e., EXP. SG50). The corresponding sub-figures show that the jitter spectra are approximately similar regardless of the shape of the ideal signal generated for DS325. This is evidence that our proposed method can be used for any standard shape of the signal (i.e., sine, triangular and rectangular). The random jitter levels are approximately 0.5 and 0.13 ps for DS325 and signal generator, respectively, in each case.

By using the spectra of the total jitter, it is straightforward to obtain the corresponding frequencies of the periodic jitter $f_{\mathrm{PJ}}^{(p)}$ in DS325. Other jitter parameters are calculated by considering the energy of the spectrum as described in Section 4.3.1. The calculated jitter parameters are tabulated in Table 5.7.

Table 5.7: Jitter parameters from the experiments with DepthSense 325

EXP. #		**Reference signal's frequency** (MHz)	**Periodic Jitter** [$f_{PJ}^{(p)}$ (MHz), $A_{PJ}^{(p)}$ (ps)]	**RJ** σ_{RJ} (ps)
EXP. DS325	EXP. DS$_{sn}$-*S*	$50.000461 \pm 3 \times 10^{-6}$	[0.402, 69], [2.888, 44]	40.48 ± 0.04
	EXP. DS$_{sq}$-*S*	$50.000461 \pm 3 \times 10^{-6}$	[0.402, 69], [2.888, 44]	40.48 ± 0.04
	EXP. DS$_{sn}$-*M*	$50.000399 \pm 3 \times 10^{-6}$	[0.389, 51], [2.892, 32]	40.35 ± 0.04
	EXP. DS$_{sq}$-*M*	$50.000399 \pm 3 \times 10^{-6}$	[0.389, 51], [2.896, 32]	40.35 ± 0.04
	EXP. DS$_{sn}$-*L*	$50.000422 \pm 5 \times 10^{-6}$	[0.406, 63], [2.933, 33]	40.31 ± 0.04
	EXP. DS$_{sq}$-*L*	$50.000422 \pm 5 \times 10^{-6}$	[0.406, 63], [2.933, 33]	40.26 ± 0.04
EXP. SG50	EXP. SG50-*S*	$49.99997 \pm 6 \times 10^{-5}$	nil	22.21 ± 0.08
	EXP. SG50-*M*	$49.99998 \pm 6 \times 10^{-5}$	nil	19.31 ± 0.07
	EXP. SG50-*L*	$50.00004 \pm 6 \times 10^{-5}$	nil	18.75 ± 0.07

The tabulated results are obtained by considering the full spectrum of the jitter signal for each experiment. For each experiment, the corresponding frequency of the generated ideal signal indicates (third column of Table 5.7) the

good accuracy of both signals for the DS325 and signal generator. The standard error of the frequencies is relatively small values that provided a measure of precision to five and six significant digits for the DS325 light source and signal generator, respectively. Therefore, we have measured the frequency to sufficient precision for our purposes. The random jitter of the signal generator is (20.09 ± 0.07) ps. The DS325 camera has (40.37 ± 0.04) ps of random jitter and the PJ at two frequencies. The PJ occurs at (0.399 ± 0.003) MHz with the amplitude of (61.0 ± 5.2) ps and (2.905 ± 0.009) MHz with the amplitude of (36.3 ± 3.5) ps. Furthermore, the curvature at low frequencies of the total jitter for the DS325 (Figures 5.22 and 5.24) is lower than the same for the SR4000 (Figures 5.10 and 5.11), for *Medium* and *Long* cables, respectively.

After removing the first few points, the corresponding log-log scales of the total jitter spectra for the experiments from the three cables are shown in Figures 5.26 – 5.28, respectively. In addition, the fitted curves with their characteristic equations for each case are stated on the figures. For the same cable these relevant equations are almost similar for two types of the ideal signal (i.e., EXP. DS_{sn} and EXP. DS_{sq}).

As before, the slopes at low frequencies of the total jitter for the DS325 are higher than at the rest of the frequencies in each case. This trend is approximately similar in all cases for the DS325 camera while it is reasonably different for the signal generator with the experiments with *Long* cable than other two cables (compare the slope at low frequencies for the signal generator in Figures 5.26 – 5.28). At the low frequencies for the DS325, the slope is -0.504 ± 0.005 while it is -0.5 ± 0.3 for the signal generator.

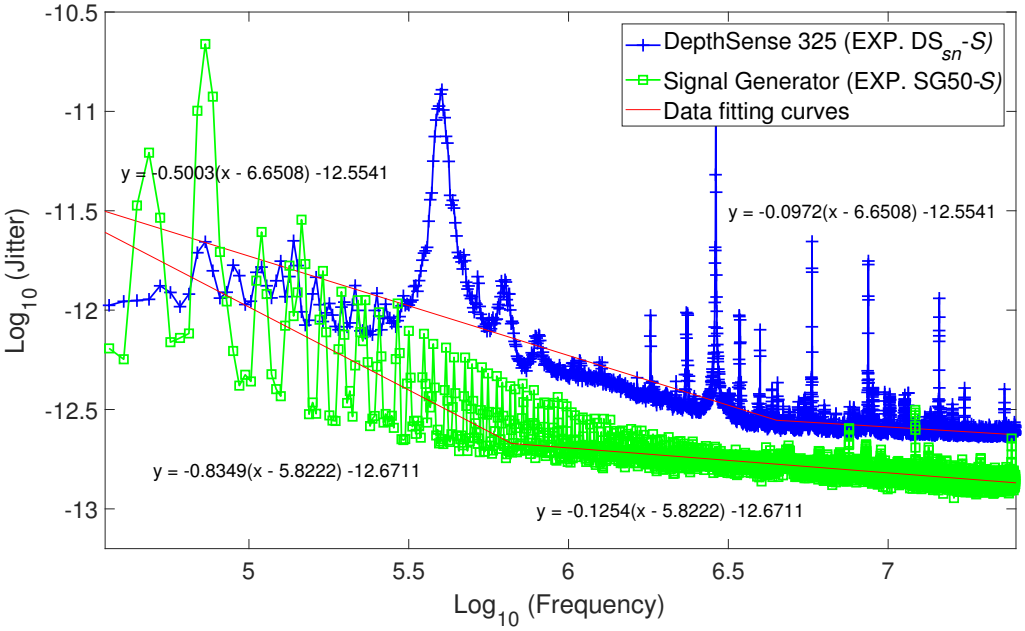

(a)

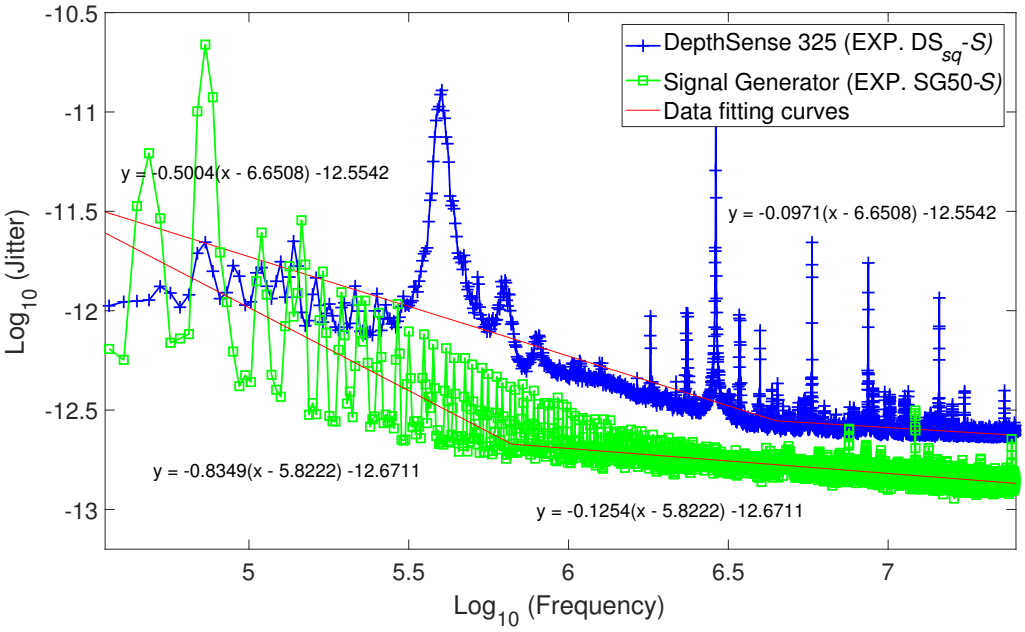

(b)

Figure 5.26: Log-log scale with fitted curves for spectra in Figure 5.20 for the DS325 and signal generator, separately, for the experiment with *Short* coaxial cable denoted as (a) EXP. DS$_{sn}$-*S* and (b) EXP. DS$_{sq}$-*S* in Table 5.6.

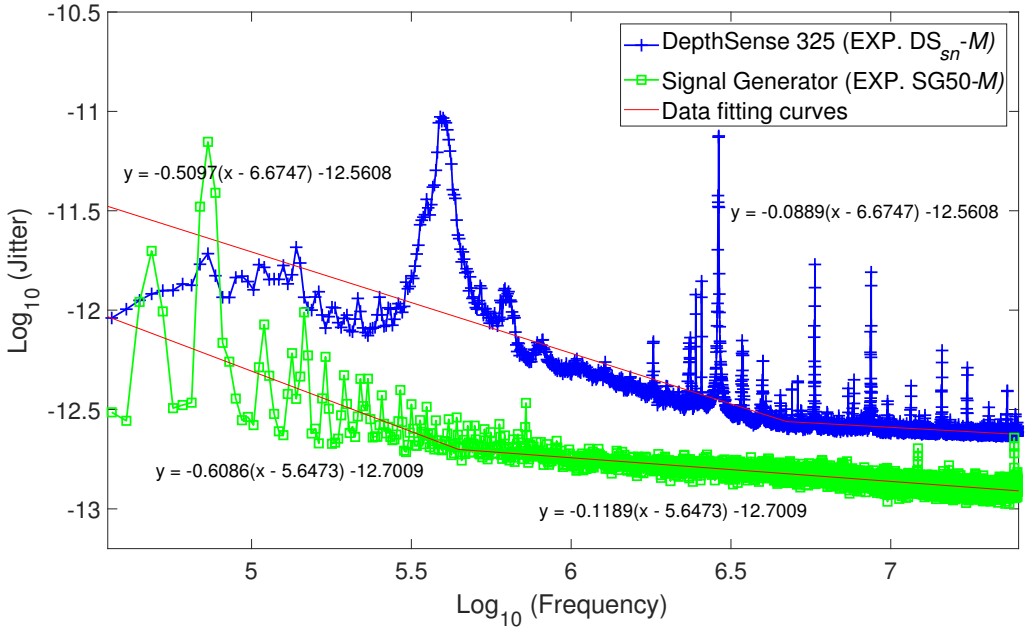

(a)

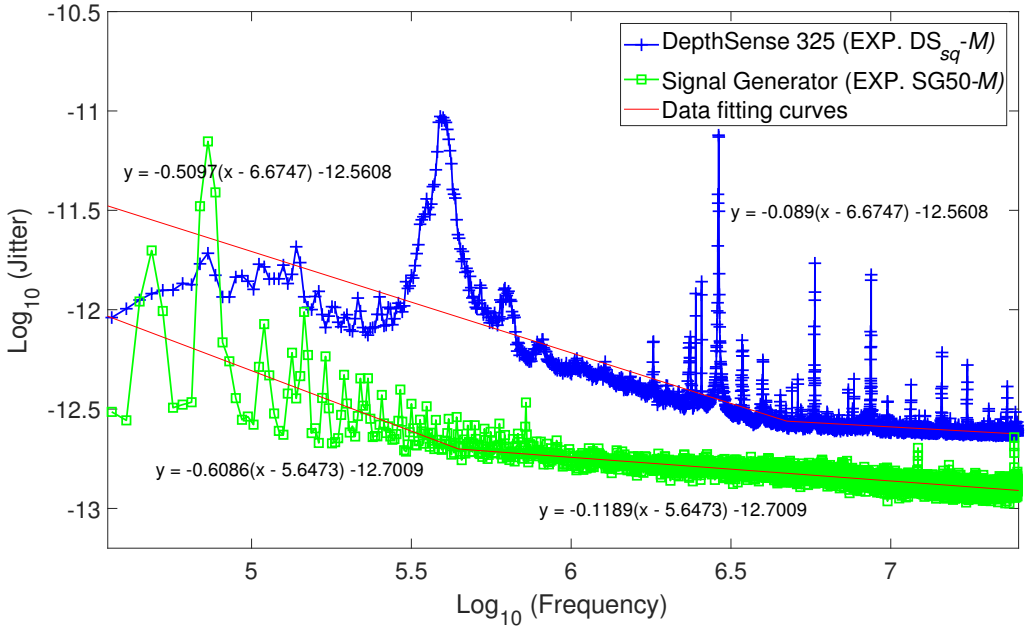

(b)

Figure 5.27: Log-log scale with fitted curves for spectra in Figure 5.22 for the DS325 and signal generator, separately, for the experiment with *Medium* coaxial cable denoted as (a) EXP. DS$_{sn}$-*M* and (b) EXP. DS$_{sq}$-*M* in Table 5.2.

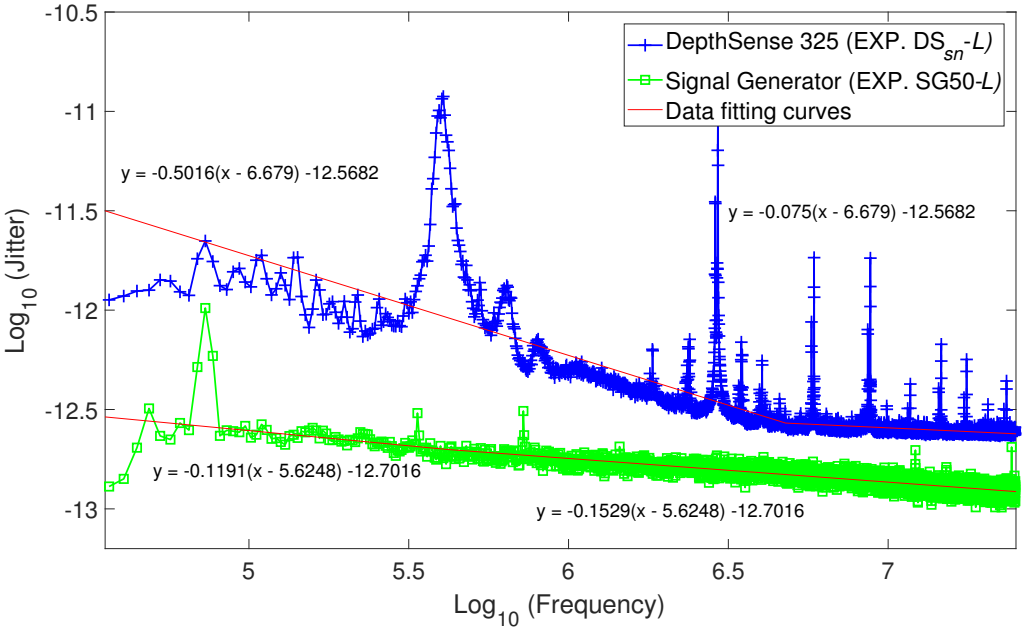

(a)

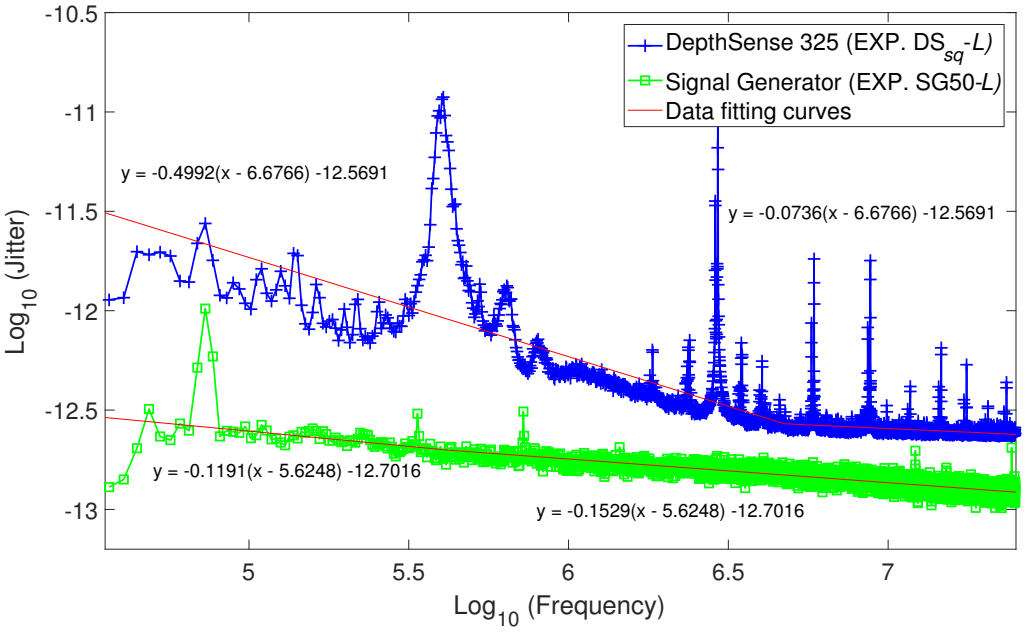

(b)

Figure 5.28: Log-log scale with fitted curves for spectra in Figure 5.24 for the DS325 and signal generator, separately, for the experiment with *Long* coaxial cable denoted as (a) EXP. DS$_{sn}$-*L* and (b) EXP. DS$_{sq}$-*L* in Table 5.2.

5.4 Chapter Remarks

In this chapter, the proposed method in Chapter 4 for jitter extraction in the light source of the ToF range imaging cameras is verified experimentally with two depth cameras, separately. In order to control the uncertainties, we captured 100 acquisitions for each experimental setup with a medium speed real-time oscilloscope while 1000 acquisitions were collected for low speed oscilloscope. From the methodology we used, the frequencies of the corresponding generated reference signals for each camera and the signal generator are found very accurately. They are (29.999656 ± 0.000003) and (50.000427 ± 0.000004) MHz for the MESA SR4000 and SoftKinetic DS325, respectively. For the signal generator they are (30.00001 ± 0.00006) and (49.999997 ± 0.000006) MHz for the corresponding signal of 30 and 50 MHz, respectively.

The periodic jitter at two frequencies are found in each camera. For SR4000, they are at 0.064 and (5.09 ± 0.06) MHz with the amplitudes of (71.5 ± 0.3) and (14.0 ± 1.4) ps, respectively. For DS325, they occurred at (0.399 ± 0.003) and (2.905 ± 0.009) MHz with the amplitudes of (61.0 ± 5.2) and (36.3 ± 3.5) ps, respectively. Among the two cameras, relatively large random jitter is available in SR4000 which is the RMS of (159.6 ± 0.1) ps and (40.37 ± 0.04) ps in DS325 camera. In contrast, we found evidence for an availability of the flicker noise in MESA SR4000 camera. On the other hand, for the signal generator, the RMS of RJ was found as (35.6 ± 0.1) and (20.09 ± 0.07) ps for the 30 and 50 MHz signals, respectively. As usual, there is no periodic jitter in the signal generator and we believe the oscilloscope measurements are well accurate.

Chapter 6

Jitter Extraction using Software Defined Radio Technology

In Chapter 5 we verified our proposed algorithm to extract jitter in the light source of two AMCW ToF range imaging cameras without the reference clock. There we measured the light source by a medium speed (6 GHz) real-time digital oscilloscope which is a very expensive instrument. Can we replace the oscilloscope by a much cheaper instrument? This chapter describes the possibility of re-purposing an emerging technology in current communication systems for jitter extraction in signals. We use the software defined radio (SDR) technology with our proposed method to extract the jitter on the light sources of the same two AMCW ToF cameras used in Chapter 5.

First, we briefly review the background and the operational principle of the receiver side of the SDR technology. Then, the experimental setup is described for the ToF cameras with a currently available SDR receiver connected to a computer, coupled with the methodology described in Section 5.1. Next, the emitted light source from the SwissRanger 4000 and DepthSense 325 with known jitter is used as the signal with jitter to be tested. Finally, the comparison of the result for the signal acquired with the SDR receiver to the same signal acquired by the oscilloscope described in Chapter 5 is also included.

6.1 Background

It was once traditional in radios to process the received radio signal entirely with analogue circuitry. Over the last couple of decades, computer technology has become sufficiently powerful to largely perform the signal demodulation and process by mathematical calculations in software. This has led to the

design of advanced radios to easily implement in software. In the late twentieth century, a new technology fusing software and digital radio called software defined radio (SDR) became the choice for wireless communication. SDR is a type of reconfigurable radio in which some or all of the physical layers of functionality are implemented in software and/or firmware (Tuttlebee, 2002). SDR consists of an analogue-digital converter (ADC) with an antenna on the receiver side and a digital-analogue converter (DAC) with an antenna on the transmitter side. The rest of the functionality is handled by reprogrammable processors (Mitola, 1993). The hardware components of SDR are now available at affordable consumer prices and software implementations are freely available. At present, the price of a SDR receiver can be less than US $40 in the market[1]. The SDR can be totally configured by software so that a common platform can be used in many areas such as in military applications in aviation (Lackey and Upmal, 1995; Tuttlebee, 2003), mobile communications (Davenport, 2005), smart antennas (Hall *et al.*, 2012), cognitive radio research (Jondral, 2005) and battery technologies (Tuttlebee, 1999) to name some of them. The advances in these emerging technologies are making SDR technically and commercially realistic (Laufer and Hoffman, 2016). In SDR technology, the signal from the antenna is directly converted to the digital domain and all the further processing is under software control.

6.2 Operational Principle of the SDR Receiver

SDR properly considered consists of a transmitter and a receiver. Since we need to capture the signals for jitter investigation, we are primarily interested in the operational principle of the receiver side of the SDR. In a SDR receiver, the signal from the antenna passes through wideband low-noise amplification, down-conversion to a lower frequency, before being digitally sampled.

6.2.1 SDR hardware

The basic structure of the SDR receiver is shown in Figure 6.1. We use a RTL-SDR USB receiver[2] (with 3.2 MSa/s) that consists of the Rafael R820T2[3] tuner which comprises the RF amp through to IF filter stages coupled to a

[1] https://www.rtl-sdr.com/buy-rtl-sdr-dvb-t-dongles/

[2] https://www.rtl-sdr.com/rtl-sdr-blog-v-3-dongles-user-guide/

[3] https://www.rtl-sdr.com/wp-content/uploads/2016/12/R820T2_Register_Description.pdf

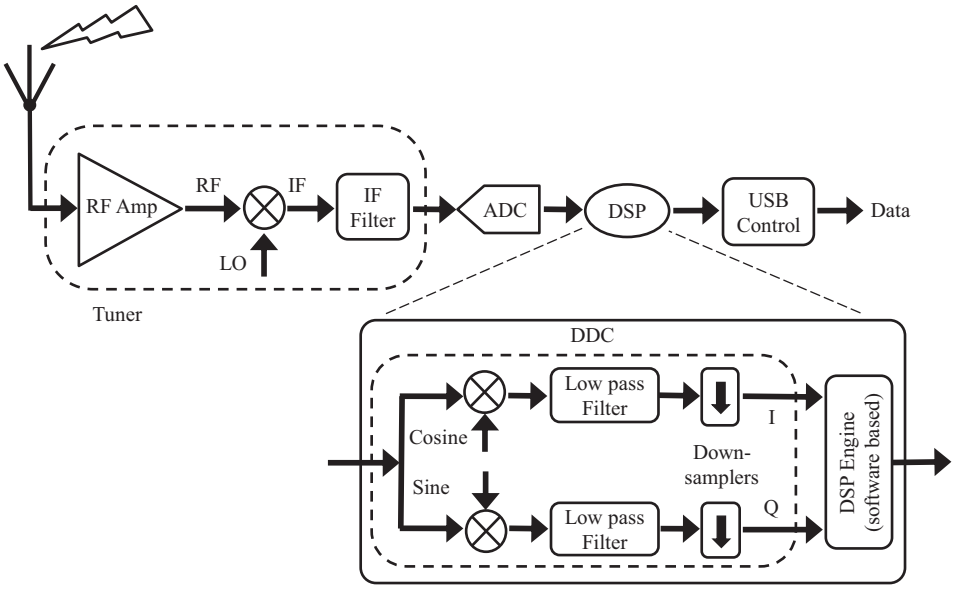

Figure 6.1: Structure of a SDR receiver side.

RTL2832U[4] demodulator which houses the ADC and digital signal processing (DSP) blocks. The DSP block consists of a digital down converter (DDC) block with DSP engine which is under software control. The DDC block includes in-phase (I) and quadrature (Q) mixers, digital low-pass filters and down samplers. This DSP block provides the connection to outside via the USB port.

The radio signal enters via the antenna and is amplified by a radio frequency (RF) tuner then is downshifted by mixing with the local oscillator (LO) frequency to the intermediate-frequency (IF). The IF signal is bandlimited (IF filter) before being sampled by the ADC at a fixed rate of 28.8 MHz, then passed through the DDC, a lowpass-filter and into a resampler (which then downsamples to the desired sample rate, 3.2 MHz at maximum). Therefore, from this SDR receiver, one can only measure frequencies below 1.6 MHz due to Nyquist, after down conversion. In addition, the effective frequency for aliasing is much higher than this value (i.e., the rate 14.4 MHz). Inside the DSP block, it uses separate ADC and low pass filter each for I and Q components. When the receiver uses a zero-IF tuner like the E4000[5] or a low-IF tuner like the R820T, then the DSP block uses both I and Q ADCs or only one of them, respectively[6].

[4] http://datasheetcafe.databank.netdna-cdn.com/wp-content/uploads/2015/09/RTL2832U.pdf

[5] https://www.nooelec.com/files/e4000datasheet.pdf

[6] https://www.reddit.com/r/RTLSDR/comments/1uazsw/rtl2832_datasheet_deep_info/

Therefore, the DDC only actives for low-IF tuners or the direct sampling mode, and it shifts and filters out the desired part of the spectrum, generating I/Q samples from real samples.

6.2.2 SDR Software

In order to operate the SDR receiver from a computer, it is necessary for complementary dedicated drivers and software to enable the interaction of the dongle as a software defined radio. Figure 6.2 shows the typical main screen of the RTL-SDR used in this chapter.

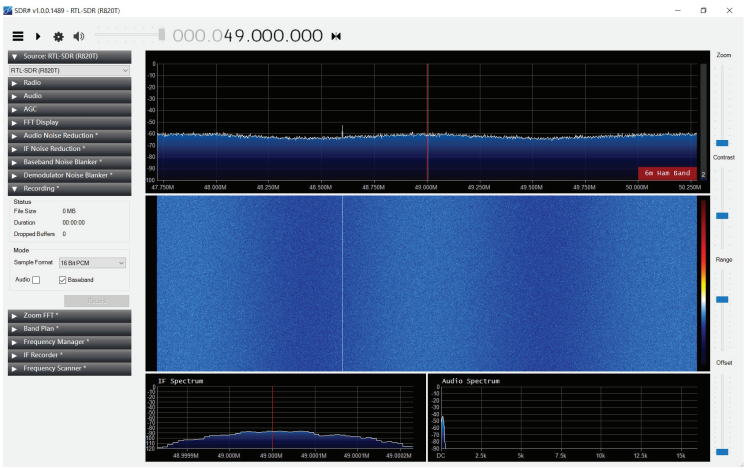

Figure 6.2: An example of the main menu of the RTL-SDR dongle.

In addition, one can set parameters such as the *Sampling Mode* and *Device sample rate* in the configuration window as shown in Figure 6.3. We use the quadrature sampling mode and maximum sample rate (3.2 MHz at the DDC) for all experiments from this dongle. In order to get the maximum performance from the device, the other parameters are chosen as follows. We set the 'Decimation' tab to *none* which results in the range of the visible spectrum as 2560 kHz, because, in practice, a good rule of thumb is to use the 80% relationship without significantly affecting the quality of the result (Hosking, 2016). Next, we amplify the signal while minimizing additional noise by setting the low-noise amplifier 'LNA Gain' to its maximum in the scale. The 'Mixer Gain' tab is set to approximately 2/3 of its maximum. Then, the variable-gain amplifier 'VGA Gain' is set to as much of a low value in the scale (Laufer and Hoffman, 2016). Finally, the corresponding signal of the light source is captured from this RTL-SDR receiver. The captured signal was recorded on the computer in the format of wave audio files with *.wav* extension.

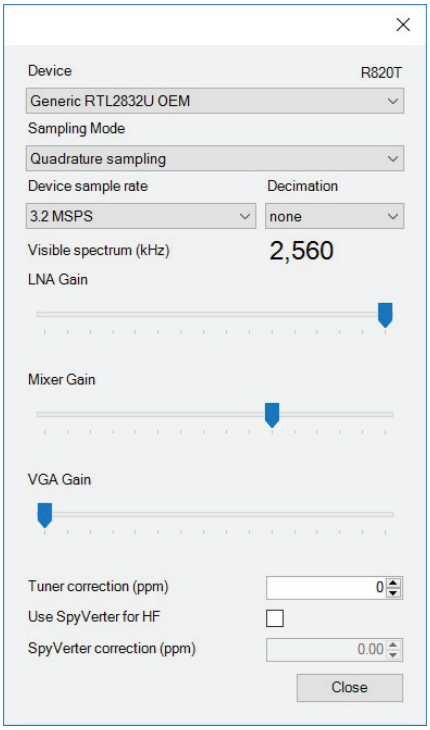

Figure 6.3: An example of the configure window of RTL-SDR dongle.

6.3 Experiment with MESA SR4000

As before, we captured the emitted light signal of the SR4000 camera using the same photodetector DET025A. Here, we used the SDR USB dongle, namely, RTL2832UR820T2 for the measurements. The range imaging camera was set to produce a 30 MHz modulated signal which was characterised in Section 5.2.1. For the control experiment, we generated 30 MHz sine waves with the same signal generator (HP Agilent 8648B). Both signal sources were analysed by the SDR USB dongle. We used the same two coaxial cables (as *Medium* and *Long*) that experimented in Section 5.2.1, for all experiments in here. In addition, the corresponding results from the previous experiment with the oscilloscope in Section 5.2.2 are also used. The corresponding experimental setup and the parameters of the components used are shown in Figure 6.4 and Table 6.1, respectively. The SDR dongle and the photodetector connect via SubMiniature version A (SMA) with the coaxial cable and BNC connectors. Also, the SDR dongle and the signal generator connect via SubMiniature version B (SMB) with the coaxial cable and BNC connectors.

From Chapter 5, we found that the first component of the PJ for SR4000 is at 0.12 MHz (see Table 5.4) and 0.064 MHz (see Table 5.3) by using low speed and medium speed oscilloscopes, respectively. However, at the time

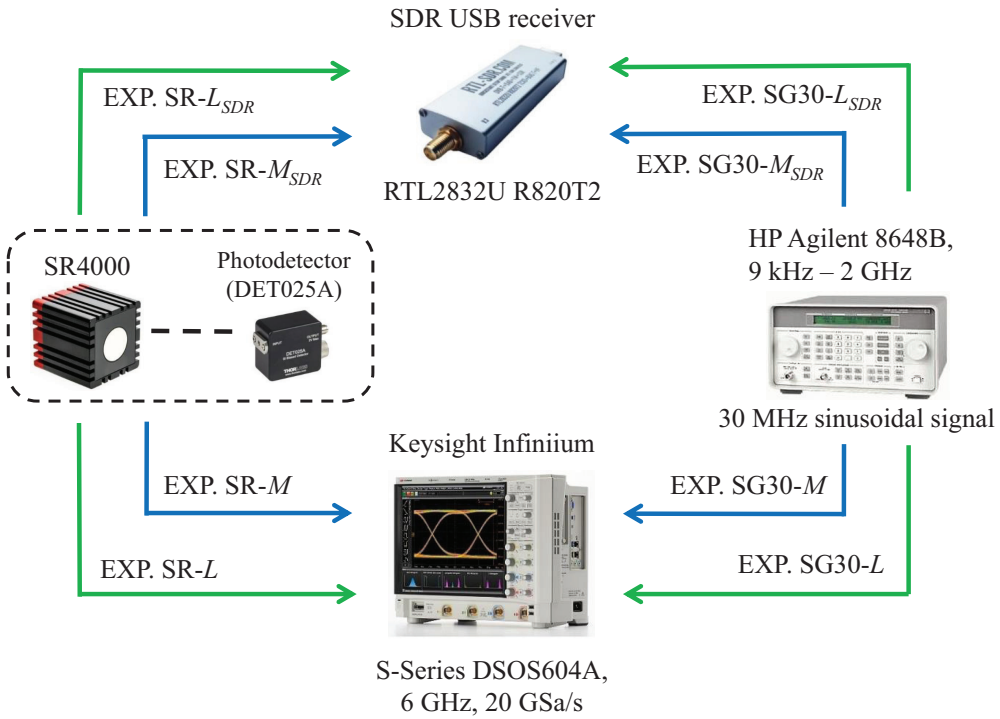

Figure 6.4: Experimental components and setup with RTL-SDR.

Table 6.1: Parameters of the components and setup with RTL-SDR

Device	**Measuring instrument**		**No. of cycles**		**EXP. #**	
			$N_{\Delta t}^{cal}$	$N_{\Delta t}$		
SR4000 with photodetector / Signal Generator (30 MHz signal)	SDR setup	SDR receiver 3.2 MSa/s (RTL2832U-R820T2)	1345	1344	*Medium* and *Long* cables	SR-M_{SDR}
						SR-L_{SDR}
						SG30-M_{SDR}
						SG30-L_{SDR}
SR4000 with photodetector / Signal Generator (30 MHz signal)	OSC setup	Oscilloscope 20 GSa/s (S-Series DSOS604A)	15000	14998		SR-M
						SR-L
						SG30-M
						SG30-L

of experiments with SDR, the medium speed oscilloscope was not available. Therefore, we selected 0.12 MHz as the first component of the PJ for SR4000. Then, for the full spectrum of the DFT, the upper limit of the frequency should be at least 0.24 MHz. However, with a safe margin, we chose 0.4 MHz as the IF for the SDR receiver. Therefore, for the SDR setup, the emitted light signal (30 MHz) of the camera was downmixed with 29.6 MHz as the RF

tuner LO frequency to give a 400 kHz IF signal at the ADC. The number of jitter samples $N_{\Delta t}^{cal}$ were found by using Equation 4.9 for the SDR with f_m = 400 kHz, $N_s \approx 10760$ and $F_s = 3.2$ MSa/s. In addition, $\lfloor N_{\Delta t}^{cal} \rfloor$ is calculated by using Equation 4.10 for each measurement setup. These are tabulated in column four and five of Table 6.1, respectively.

In order to reduce the uncertainty of the result, we captured 17000 data sets for each experiment with the SDR setup. However, about 1% of the data sets were found to contain errors and were discarded from the analysis. It appears that the SDR (or its device driver) occasionally drops samples (Laufer and Hoffman, 2016). For the comparison, the 100 acquisitions for each experiment with the oscilloscope from Chapter 5 are also used.

6.4 Results and Discussion

As before, for step ① of the proposed algorithm, we capture the data signal from the light source of the camera from the RTL-SDR receiver. Note that the SDR dongle captures the data in quadrature form (i.e., real and imaginary parts, separately) and here we concern the real portion of the light signal (imaginary portion also is given the same result) throughout the experiments. Figure 6.5 shows the real portion of the light signal of the SR4000 as step ①.

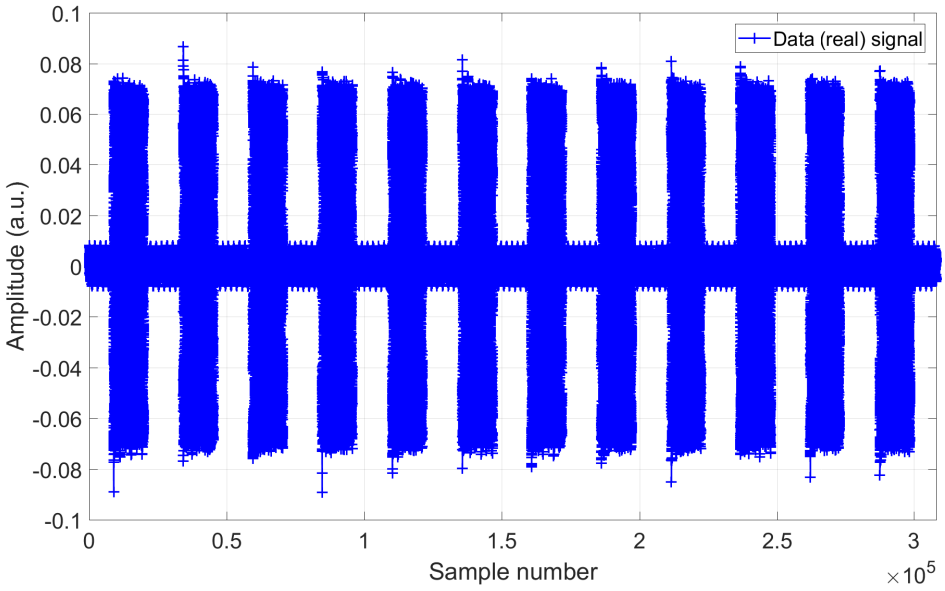

Figure 6.5: Real portion of the data signal captured from the SDR setup for a single acquisition of the light source of SR4000, experiment with *Medium* cable denoted as SR-M_{SDR} in Table 6.1.

It shows the set of pulses since the camera shutter is at 'on' and 'off' stages during the integration period. Now, we need to separate each section as follows. By comparison the threshold value (here it is chosen as 0.01 a.u.) with the amplitude, we obtain the first sample positions that increase the amplitude of sections by adding fixed amount greater than the number of samples N_s of the section (i.e., we choose 11000 since $N_s \approx 10700$) to each section. So, now, the starting position (leftmost) of each section is known. Then in order to find the last position (rightmost) of the section, the same value N_s is adding to the left most position of each section. Finally, a couple of cycles at the end of the section are removed. In addition, Figures 6.6 show the corresponding expansion versions of the real portion of the data signals of the SR4000 and signal generator (30 MHz signal), separately, in the experiment with *Medium* cable.

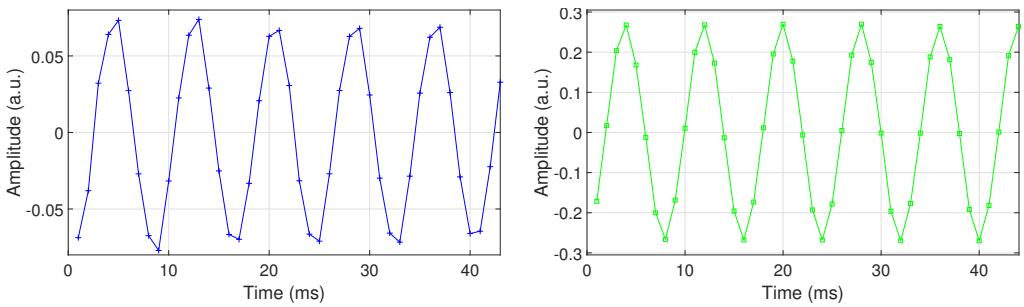

Figure 6.6: Data signals from the SDR setup for a single acquistion from (a) the light source of SR4000 and (b) signal generator, with the *Medium* cable denoted as SR-M_{SDR} and SG30-M_{SDR} in Table 6.1, respectively.

Then, by applying the process of sub-① in Figure 5.1, we generate the corresponding ideal signal for each case (for step ②). Table 6.2 tabulates the experimental parameters for each setup and the fourth column represents the number of samples per cycle. The last column is the corresponding frequency with the standard deviation (STD) of the ideal (reference) signal which is extracted from the data, for each experimental setup. Each of these STDs is based on a large number of data sets (i.e., 100 sets with $\approx 10^7$ samples each for OSC setup and 17000 sets with $\approx 10^4$ samples each for SDR setup). The frequencies of the signals are listed in Table 6.2 and are determined very accurately. This is used to generate the reference signal.

Figure 6.7 shows the corresponding result for step ③ for the same acquisition of SR4000 and the signal generator from the SDR setup, separately. The data and ideal signals are aligned with respect to the first zero crossing point

Table 6.2: Experimental parameters for setup with SDR and oscilloscope

EXP. #		Sampling time $1/F_s$	No. of Sa/cycle	Reference signal's frequency
SDR	SR-M_{SDR}	312.5 ns	8	399.566 ± 0.003 kHz
	SG30-M_{SDR}			399.504 ± 0.007 kHz
	SR-L_{SDR}			399.546 ± 0.001 kHz
	SG30-L_{SDR}			399.508 ± 0.008 kHz
OSC	SR-M	50 ps	2000/3	29.999645 ± 0.000003 MHz
	SG30-M			30.00001 ± 0.00006 MHz
	SR-L			29.999668 ± 0.000003 MHz
	SG30-L			30.00001 ± 0.00006 MHz

in each case. For the SDR setup the number of samples per cycle 8 can be verified from Figure 6.7(a) as well. This value is relatively very small, the representation of the signal is not a great view (i.e. the number of samples per cycle is low). This likely increases the error in determining the zero crossings. By using the number of samples per cycle (8 Sa/cycle) and the sampling rate of the dongle (3.2 MSa/s), we can compute the frequency of the ideal signal as 400 kHz. This can be verified from the last column of Table 6.2.

The jitter spectrum for each acquisition is obtained by using steps ① to ⑥ in the proposed methodology shown in Figure 5.1. After step ⑥, we obtained jitter spectra for MESA SR4000 and 30 MHz signal for each cable, separately, as shown in Figure 6.8. The jitter components and the interpolated level between periodic and random jitter for each signal is marked in the figure. The frequency range for the SDR setup and oscilloscope setup are 0 – 200 kHz (since the IF signal is 400 kHz) and 0 – 15 MHz, respectively. In order to compare the results from the two instruments, we focus on the expansion version of the first 200 kHz from the oscilloscope results that were previously obtained as shown in Figures 5.10(b) and 5.11(b) in Chapter 5. So, these figures are rescaled as shown in Figure 6.9.

The curvature at low frequencies of the spectra obtained from SDR setup is higher than the same from oscilloscope (compare Figures 6.8 and 6.9). We expect this may be due to the noise in the SDR USB dongle. Then this may significantly leak the energy to adjacent bins of the spectra. Note that we compensated the results from SDR setup by the ratio $1 : 250/3$ (see the fourth

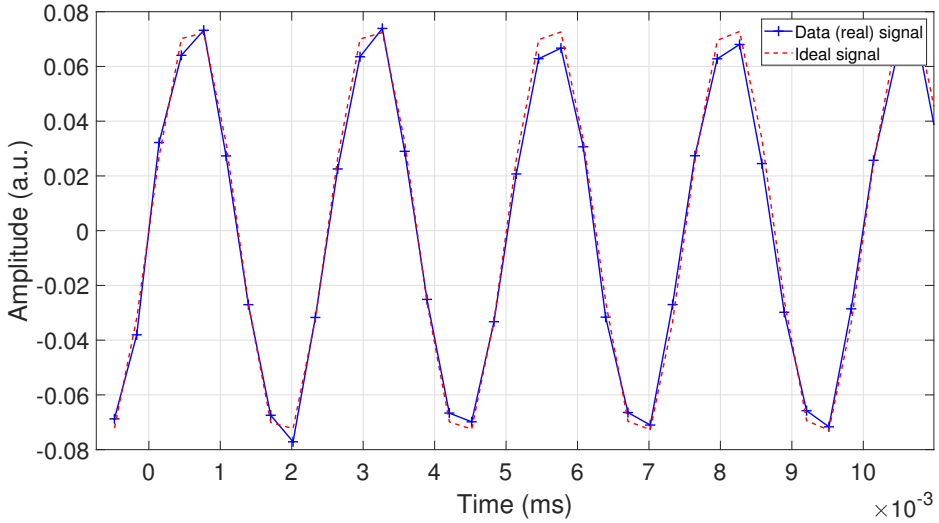

(a)

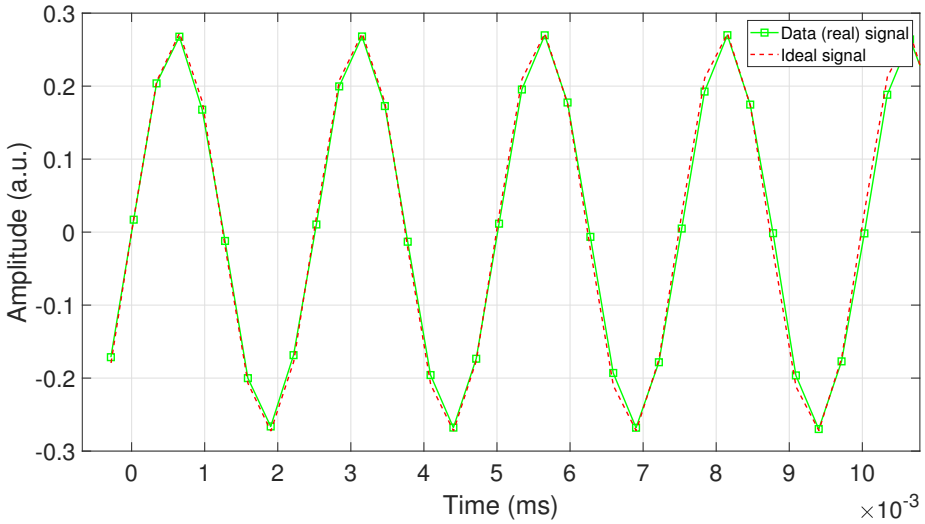

(b)

Figure 6.7: Aligned the same data signal and ideal signal for a single acquisition from (a) the SR4000 and (b) signal generator, using the SDR setup.

column of Table 6.2) since the number of samples per cycle is influenced on the energy of the signal. As before, from Figure 6.8, it is straightforward to identify the high peak on the jitter signal of SR4000 from the experiments with two cables, separately. They are at 61 and 64 kHz with the amplitudes 61 and 66 ps, respectively, for the experiment with *Medium* and *Long* cables. In addition, we compute the jitter parameters for the first harmonic of this periodic jitter for each case. They are 122 and 127 kHz with the amplitudes 22 and 29 ps, respectively, for the two cables. There is no PJ in the signal generator for both cases.

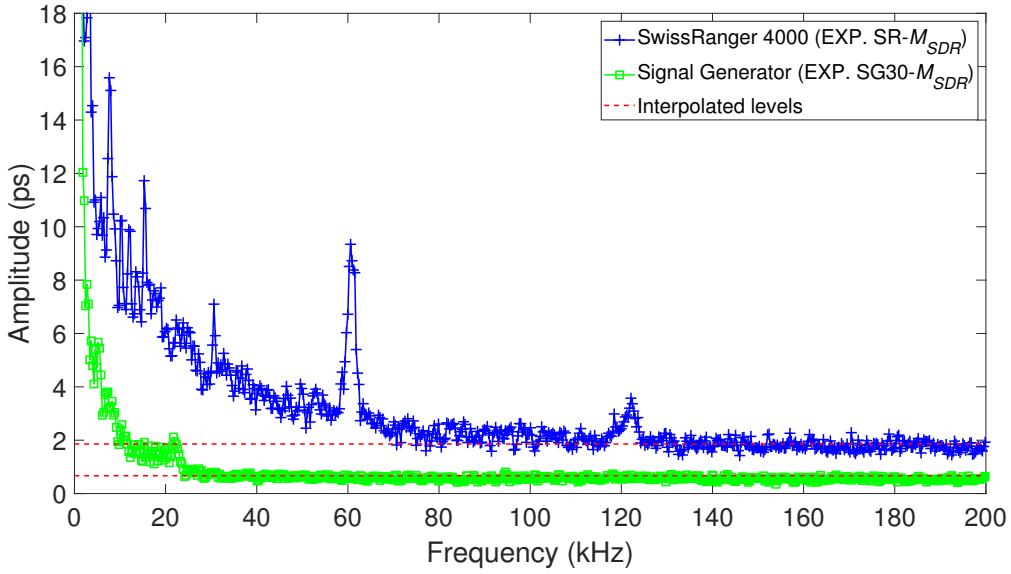

(a)

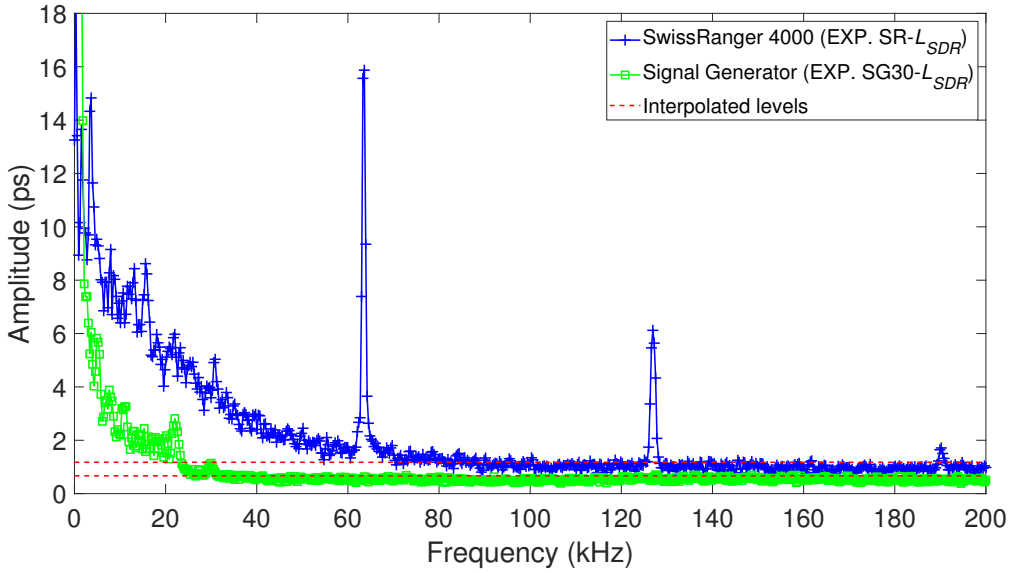

(b)

Figure 6.8: Jitter components for the SR4000 and signal generator from the experiments with the SDR receiver for (a) *Medium* (b) *Long* coaxial cables denoted as SDR setup in Table 6.1.

Furthermore, the previous result from the oscilloscope (in Chapter 5), the frequencies are as 64 and 64 kHz with the amplitudes 71 and 72 ps, respectively, for the two cables. In addition, the parameters for the first harmonic of the PJ are 128 and 126 kHz with 29 and 28 ps amplitudes, respectively, for the two cables. There is a broad and flat spectrum being the RJ in the camera.

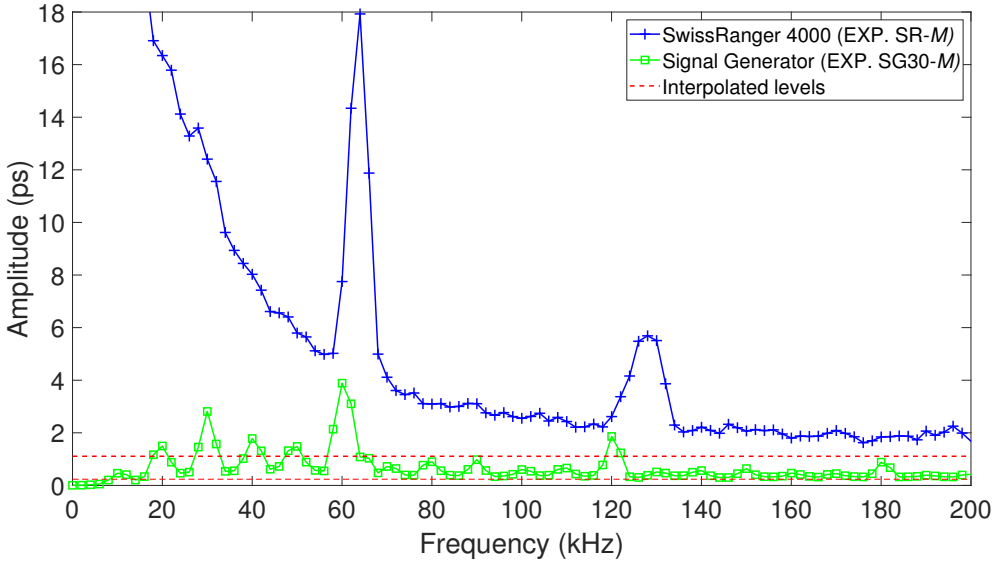

(a)

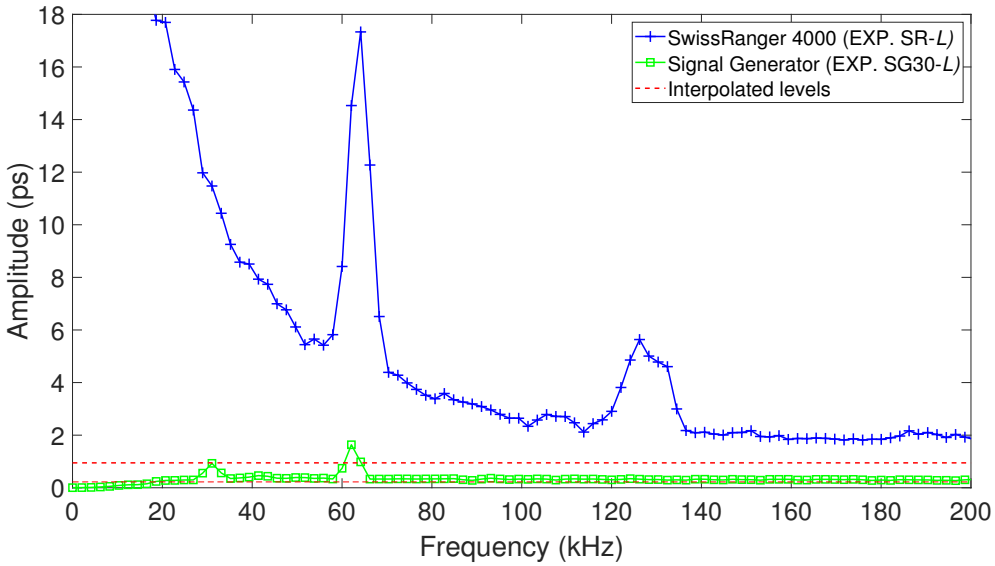

(b)

Figure 6.9: Expansion version of the first 200 kHz of the jiter components for the SR4000 and signal generator from the oscilloscope setup (corresponding to the Figures 5.10(b) and 5.11(b) in Chapter 5) that experimented with (a) *Medium* and (b) *Long* coaxial cables, denoted as OSC setup in Table 6.1.

Table 6.3: Extracted results from measurements

EXP. setup		Periodic jitter $[f_{PJ}^{(p)}$ (MHz), $A_{PJ}^{(p)}$ (ps)]	Random jitter σ_{RJ} (ps)
SDR	SR-M_{SDR}	[0.061, 61], [0.122, 22] ‡	85.8 ± 0.2
	SG30-M_{SDR}	nil	30.8 ± 0.2
	SR-L_{SDR}	[0.064, 66], [0.127, 29] ‡	54.3 ± 0.3
	SG30-L_{SDR}	nil	30.8 ± 0.1
OSC	SR-M	[0.064, 71], [0.128, 29] ‡ and [5.001, 12]	173.6 ± 0.1
	SG30-M	nil	36.9 ± 0.1
	SR-L	[0.064, 72], [0.126, 28] ‡ and [5.173, 16]	145.7 ± 0.1
	SG30-L	nil	34.3 ± 0.1

By considering the full spectrum for each experiment, jitter parameters are calculated as shown in Table 6.3. The PJ at (62.5 ± 1.1) kHz with the amplitude (63.5 ± 1.8) ps is represented by the SDR receiver while it is 64 kHz from the oscilloscope. In addition, for the first harmonic of this PJ, they are (124.5 ± 1.8) kHz with the amplitude (25.5 ± 2.5) ps for the SDR setup while (127.0 ± 0.7) kHz with (28.5 ± 0.3) ps for the OSC setup. The RJ with RMS of (70.0 ± 0.2) ps and (159.6 ± 0.1) ps are obtained from SDR and OSC setup, respectively. The measurements of the RJ in signal generator from the SDR and OSC setup are found as (30.8 ± 0.1) ps and (35.6 ± 0.1) ps, respectively.

Note that the RJ amounts for both camera and signal generator from the SDR setup are relatively less than the same from the oscilloscope setup. This is because the SDR receiver can measure only up to half of the IF (i.e., 200 kHz). There are relatively larger slopes at low frequencies with both *Medium* and *Long* cables for the signal generator from the SDR setup than with OSC setup (compare the signal generator curves of Figures 6.8 and 6.9). This may be due to the lower quality of the SDR receiver.

As discussed in Section 4.3.2, the corresponding log-log plots for the jitter spectra for the SR4000 and signal generator for both experimental setup (relevant to Figure 6.8) is shown in Figure 6.10. In addition, the fitted curves with their characteristic equations for each case are stated on the figures. The slopes at low frequencies of the total jitter for the SR4000 are higher than at the rest of the frequencies (see Figure 6.10) in each case. At low frequencies of

‡first harmonic of the PJ.

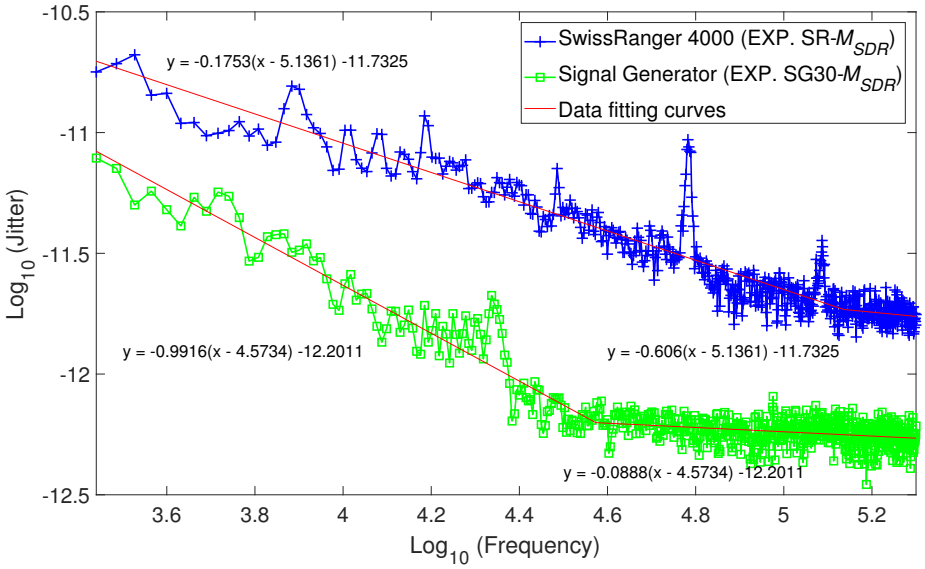

(a)

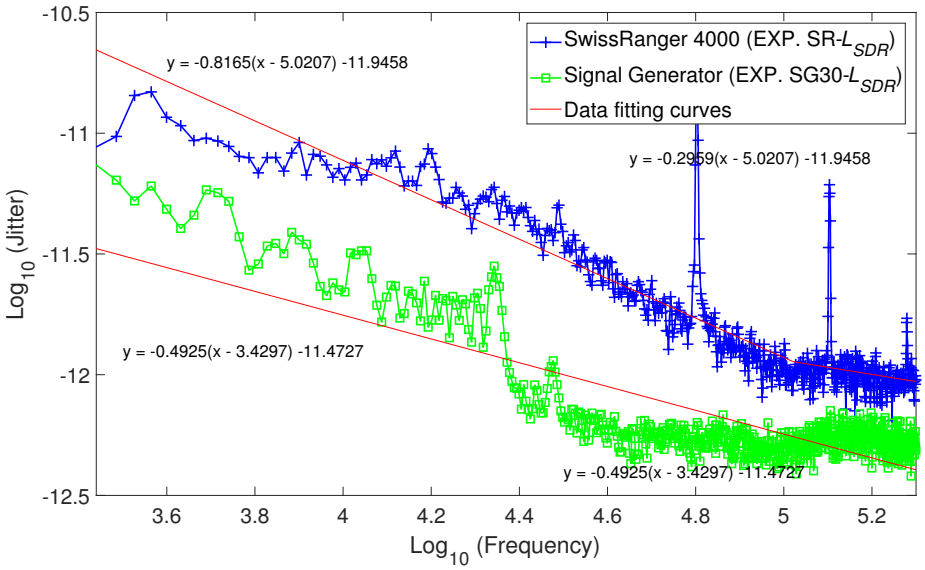

(b)

Figure 6.10: Log-log scale with fitted curves for jitter spectra shown in Figure 6.8 for the SR4000 and signal generator for the experiments with (a) *Medium* and (b) *Long* cables, denoted as SDR setup in Table 6.1.

SR4000, the experiment with *Long* cable (see Figure 6.10(b)) shows the slope $f^{-0.8165}$ while from the *Medium* cable (see Figure 6.10(a)) it is $f^{-0.1753}$. This is because in the later case the PJ is more spread out for neighbour bins than the experiments with *Long* cable.

6.5 Experiment with SoftKinetic DS325

We repeat the experiment with the DS325 camera which has first component of the PJ at (0.399 ± 0.003) MHz using the SDR USB dongle, for the measurements. For the full spectrum of the DFT, the upper limit of the frequency should be at least 0.8 MHz. However, with a safe margin, we chose 1 MHz as the IF for the SDR receiver. Therefore, we down mixed the emitted light signal (50 MHz) of the camera with 49 MHz as the RF tuner LO frequency to give a 1 MHz IF signal at the ADC. Figure 6.11 shows the captured signal of the light signal of the DS325 with *Long* cable.

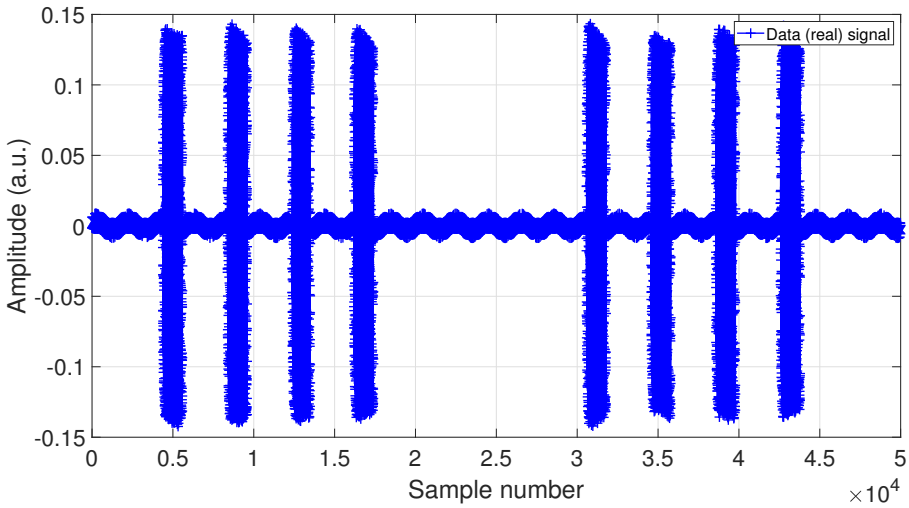

(a)

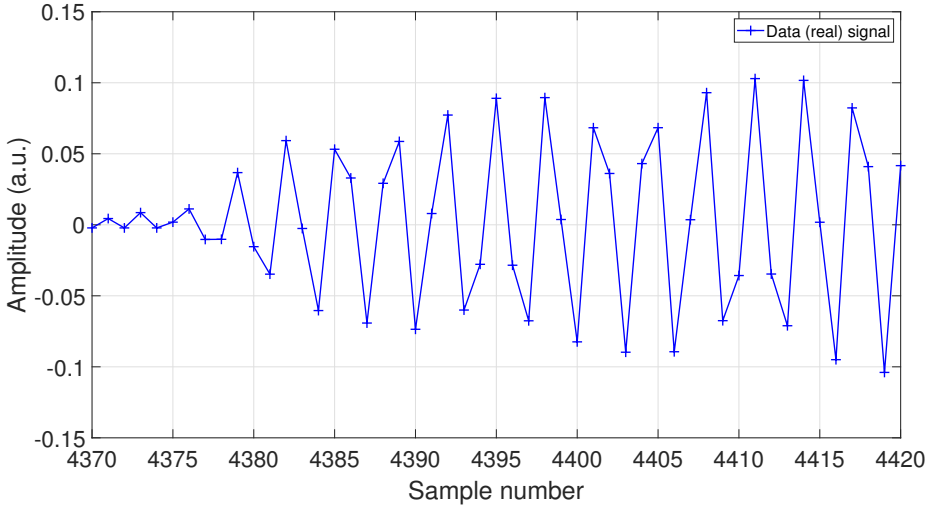

(b)

Figure 6.11: Data (real part) signal from the SDR setup for a single acquisition of (a) the light source of DS325 and (b) its expansion, with the *Long* cable.

Since the DS325 camera uses four phase-step in its correlation, Figure 6.11(a) shows the corresponding portions for $0, \pi/2, \pi$ and $3\pi/2$. Figure 6.11(b) indicates the number of samples per cycle is a very low value (3 or 4). Therefore the representation of the signal is poor and it will give incorrect jitter amounts, hence we do not further investigate the analysis of jitter of the light signal of the DS325 camera using this RTL-SDR dongle.

Both the oscilloscopes and SDR dongles have inherent frequency errors however, the reasonable uncertainty of the measurements occurs from 200 MHz (about 0.2%) in oscilloscopes[7]. Since the modulation frequency of each camera is much less than 200 MHz, we believe the inherent frequency errors in the oscilloscope has not affected jitter measurement. We were unable to find any references about the inherent frequency errors in SDR dongles and there may be errors that effect the jitter measurement.

6.6 Chapter Remarks

The main aim of this chapter was to use the SDR technology (as an alternative measurement instrument for oscilloscope) to measure the jitter in signals. We experimented with a cheap SDR USB dongle with the proposed method to measure jitter on the emitted light signal of MESA SR4000 and SoftKinetic DS325 depth cameras. For SR4000, we downshifted the signal to a low frequency (400 kHz) and were able to find the periodic jitter at lower frequencies (less than 1.6 MHz which is the Nyquist frequency of this particular dongle). By performing the proposed algorithm in Chapter 4, we extracted some of the jitter parameters for the camera SR4000.

We believe the high sample rates and high quality of SDRs can be used to explore periodic jitter at least at lower frequencies in a RF signal. We need to know the ratio of the number of samples per cycle between the two instruments: oscilloscope and SDR receiver for the correction of the amplitude calculations of the periodic and random jitter. However, from our proposed method, it is straight forward to find the corresponding frequency (only for less than the Nyquist frequency of the dongle) of the periodic jitter in the light source of the camera. However, jitter extraction was not a success for the other camera DS325, since the number of samples per cycle from the SDR receiver is very less causes the representation of the signal is incorrect.

[7] `https://us.flukecal.com/literature/articles-and-education/electrical-calibration/white-paper/understanding-and-dealing-high-`

Hence, we conclude the SDR USB dongle which is a much cheaper instrument (respect to the oscilloscope) can be used to measure jitter in a signal, but there are limitations: (1) the periodic and random jitter only up to half of the intermediate-frequency obtaining from the down shift of the amplified radio frequency with the local oscillator which is less than the Nyquist frequency of the dongle and (2) when the sampling frequency is less (i.e., if the number of sample points is not sufficient in a cycle), then this SDR dongle cannot be used for jitter measurement since the signal is not properly (smoothly) represented. Therefore, it has given incorrect jitter amounts. From the experiments with this SDR dongle, for MESA SR4000, the PJ at (62.5 $\pm$ 1.1) kHz with the amplitude (63.5 $\pm$ 1.8) ps and the RJ with RMS of (70.0 $\pm$ 0.2) ps are found. For the DS325, further experimentation was not carried out since the captured light signal of the camera from this SDR dongle was not properly represented in the signal.

From this chapter and Chapter 5 we clearly found the periodic and random jitter in the light signals of the two AMCW ToF ranging cameras and successfully measured by using a proposed algorithm which can be used for any type of illumination signal of ranging systems. In addition, the use of the SDR technology for measuring the jitter in signals was successful. Even though we measured those two types of jitter, will it be important to the user and will it influence the range measurements? This interesting investigation will be inspected in the next two chapters which is the third section of this thesis.

Chapter 7

Influence of Periodic Jitter on Range Measurements

This chapter presents a theoretical investigation of the influence of periodic jitter in AMCW ToF range imaging cameras. We develop an analytical model with the help of Fourier analysis and standard mathematical functions. First, the standard mathematical expressions with relevant properties of the Fourier transform are introduced. Then, the operation principle without the jitter in the emitted light source and shutter signals in AMCW lidar systems is explored by using Fourier analysis. Next, the analytical model is extended to predict the effect of periodic jitter on range measurements in AMCW ToF cameras. Both homodyne and heterodyne operations of the camera are considered. In addition, two known numerical approaches: trapezoidal and Romberg integrations are also included. For the numerical approaches, the four phase-step computation is considered. The results and discussion from both analytical and numerical approaches on simulation data with various parameters in AMCW lidar systems are presented. Furthermore, the approximate computation time for each setup with each model is pointed out.

7.1 Background

As stated in Chapter 2, current modulation frequencies of AMCW ToF cameras are less than 100 MHz. However, due to improvements of the technologies in camera sensors, it is not surprising, the modulation frequencies of those cameras will be in GHz levels with the high frame rate in the future. In general, the use of higher modulation frequencies guarantees higher range resolution yields on the higher noise and jitter levels as well. Therefore, with the improvement

of the technologies, it is important to consider the accuracy and precision of the depth measurements in AMCW ToF cameras.

Chapters 5 and 6 have demonstrated that periodic and random jitter are present in commercial AMCW ToF range imaging cameras, at least, in the emitted light signal. However, to date, there is no prior investigation of the impact of periodic jitter on range measurements in AMCW lidar systems. The investigation of jitter influence on the depth data is important because this time deviation causes errors on the phase difference (which is the ToF principle), hence on the range measurement. Once a model of jitter influence on the ToF cameras is developed, such a model can be used to correct for these effects on range imaging data. Not only that, the result of this investigation can be used in AMCW ToF camera manufacturing industries in future because the precision and accuracy are important for many applications.

7.2 Notation and Definitions

In this section, we review the standard mathematical functions and Fourier analysis used in this chapter. Let i be the imaginary unit, and $g(t)$ and $h(t)$ be square-integrable functions. For complex $z = u + iv$, let $\Re[z]$ be the real part of z, that is $\Re[z] = u$. Let a and b be are non zero real constant and a real constant, respectively, $*$ be the convolution operator and f be the frequency conjugate to t.

7.2.1 Definition of Fourier Transform and its Inverse

The Fourier transform of $g(t)$ is given by (Oppenheim *et al.*, 1999)

$$G(f) = \mathscr{F}[g(t)] = \int_{-\infty}^{\infty} g(t)e^{-i2\pi ft}\,dt, \tag{7.1}$$

with inverse Fourier transform,

$$\begin{aligned} g(t) &= \mathscr{F}^{-1}[G(f)], && (7.2)\\ &= \mathscr{F}[g(-t)], && (7.3)\\ &= \mathscr{F}^{-1}[G(-f)], && (7.4)\\ &= \int_{-\infty}^{\infty} G(f)e^{i2\pi ft}\,df. && (7.5) \end{aligned}$$

7.2.2 Identities of Fourier Transform and its Inverse

The Fourier transform and its inverse satisfy the following well-known identities:

$$\mathscr{F}[g(at)] = \frac{1}{|a|} G\left(\frac{f}{a}\right), \tag{7.6}$$

$$\mathscr{F}[g(t \pm a)] = e^{\pm i2\pi af} G(f), \tag{7.7}$$

$$\mathscr{F}^{-1}[G(f \pm a)] = e^{\mp i2\pi at} g(t), \tag{7.8}$$

$$\begin{aligned} \mathscr{F}[gh] &= \mathscr{F}[g] * \mathscr{F}[h] \\ &= G(f) * H(f), \end{aligned} \tag{7.9}$$

$$\begin{aligned} \mathscr{F}^{-1}[G * H] &= \mathscr{F}^{-1}[G] * \mathscr{F}^{-1}[H] \\ &= gh, \end{aligned} \tag{7.10}$$

where $H(f)$ and $\mathscr{F}^{-1}[H]$ are the Fourier transform of $h(t)$ and inverse Fourier transform of $H(f)$, respectively.

7.2.3 Mathematical Functions

Let $\delta(t)$ be the conventional Dirac delta function and its scaling property is,

$$\delta(at) = \frac{\delta(t)}{|a|}. \tag{7.11}$$

Since the delta function is an even distribution, we have,

$$\delta(-\alpha) = \delta(\alpha). \tag{7.12}$$

Let $\mathrm{rect}_T(t)$ be the rectangular function of width T given by,

$$\mathrm{rect}_T(t) = \begin{cases} 1 & |t| < T/2 \\ 0 & \text{otherwise}, \end{cases} \tag{7.13}$$

and the sinc function be given by

$$\mathrm{sinc}(t) = \frac{\sin(t)}{t}, \tag{7.14}$$

with

$$\lim_{t \to 0} \frac{\sin(t)}{t} = 1. \tag{7.15}$$

7.2.4 Fourier Transforms of Some Functions

We make use of the following Fourier transforms:

$$\mathscr{F}[a] = a\,\delta(f), \tag{7.16}$$

$$\mathscr{F}[\mathrm{rect}_T(t)] = T\,\mathrm{sinc}(\pi f T), \tag{7.17}$$

$$\mathscr{F}[\cos(t)] = \frac{1}{2}\left[\delta\left(f - \frac{1}{2\pi}\right) + \delta\left(f + \frac{1}{2\pi}\right)\right], \tag{7.18}$$

$$\mathscr{F}[\cos(at+b)] = e^{i2\pi\frac{b}{a}f}\,\mathscr{F}[\cos(at)]. \tag{7.19}$$

7.2.5 Relationships of Some Functions

The sinc function for any argument $\alpha \in \mathbb{C}$ has the relation when $T \to \infty$ (Balakrishnan, 2003)

$$\lim_{T\to\infty} T\,\mathrm{sinc}(\alpha T) = \pi\,\delta(\alpha). \tag{7.20}$$

Let $J_m(x)$ be the Bessel function of the first kind of order m given by (Abramowitz and Stegun, 1965)

$$J_m(x) = \frac{1}{2\pi}\int_{-\pi}^{\pi} e^{i(x\sin\theta - m\theta)}\,d\theta. \tag{7.21}$$

Note the expansion (Haykin and Moher, 2007)

$$e^{ix\sin(\theta)} = \sum_{m=-\infty}^{\infty} J_m(x)\,e^{im\theta}, \tag{7.22}$$

and since the summation is linear (Haykin and Moher, 2007)

$$\Re\left[\sum_{m=-\infty}^{\infty} J_m(x)\,e^{im\theta}\right] = \sum_{m=-\infty}^{\infty} J_m(x)\,\cos(m\theta). \tag{7.23}$$

7.3 ToF Operation in Frequency Domain

Most of the results and implications of this section are well known (Lange and Seitz, 2001; Horaud *et al.*, 2016) and are described in Section 2.2, however, this section provides a clear exposition and outlines the approach that we generalise in Section 7.4 to include the presence of periodic jitter. The ToF is measured indirectly by correlating the reflected signal with a reference signal of the illumination and determining the phase shift ϕ due to the time of flight.

Consider the light and shutter relationship as shown in Figure 2.2 and set the shutter signal with zero offset. Then, let the modulated light reflected back by the scene and received at the camera be,

$$l(t, \phi) = A \cos(2\pi f_l t - \phi) + B, \tag{7.24}$$

where A is the amplitude of the illumination signal, B is any offset due to background illumination, f_l is the light modulation frequency and ϕ is the ToF phase delay. Let $s(t, \theta)$ be the shutter signal given by

$$s(t, \theta) = \cos(2\pi f_s t + \theta), \tag{7.25}$$

where f_s and θ are the modulation frequency of the shutter signal and an adjustable phase delay introduced to the shutter (the *phase-step*, which is controlled by the camera), respectively. We assume the offset background of the shutter signal to zero and its amplitude is embedded in A and B of the reflected light. Note that both the ToF phase shift and phase-step are in units of radians by convention.

The camera integrates a frame capture over an integration period of T for a specific phase-step θ, hence the received signal $I(\theta)$ is given by,

$$I(\theta) = \int_{-T/2}^{T/2} s(t, \theta)\, l(t, \phi)\, dt. \tag{7.26}$$

In practice, it is typical to adjust θ stepwise between captures, but here we take the phase-step θ to be continuous so that we can take the Fourier transform with respect to θ, namely let

$$\widehat{I}(\vartheta) = \mathscr{F}[I(\theta)]_{\theta \to \vartheta} = \int_{-T/2}^{T/2} \mathscr{F}[s(t, \theta)]\, l(t, \phi)\, dt. \tag{7.27}$$

where ϑ is the angular frequency conjugate to θ in units of per radian (i.e., rad^{-1}). The Fourier transform of the shutter signal (Equation 7.25) is found by application of the Fourier shift theorem (Equation 7.7) and the Fourier transform of the cosine (Equation 7.18), we have

$$\begin{aligned} \mathscr{F}[s(t, \theta)]_{\theta \to \vartheta} &= \mathscr{F}[\cos(2\pi f_s t + \theta)]_{\theta \to \vartheta} = e^{i2\pi(2\pi f_s t)\vartheta} \mathscr{F}[\cos(\theta)] \\ &= \frac{e^{i(2\pi)^2 f_s t \vartheta}}{2} \left[\delta\left(\vartheta - \frac{1}{2\pi}\right) + \delta\left(\vartheta + \frac{1}{2\pi}\right) \right]. \end{aligned} \tag{7.28}$$

Now, let $\Theta = 2\pi\vartheta$ be the 'frequency' conjugate to θ, and with the scaling property of delta function (Equation 7.11), we have

$$\begin{aligned}\mathscr{F}[s(t,\theta)] &= \frac{e^{i2\pi f_s\Theta t}}{2}\left[\delta\left(\frac{\Theta-1}{2\pi}\right)+\delta\left(\frac{\Theta+1}{2\pi}\right)\right] \\ &= \frac{e^{i2\pi f_s\Theta t}}{2}\left[\frac{\delta(\Theta-1)}{|1/2\pi|}+\frac{\delta(\Theta+1)}{|1/2\pi|}\right] \qquad (\because \text{Equation 7.11}) \\ &= \pi e^{i2\pi f_s\Theta t}\left[\delta(\Theta-1)+\delta(\Theta+1)\right], \end{aligned} \tag{7.29}$$

hence Equation 7.27 becomes,

$$\widehat{I}(\Theta) = \pi\big[\delta(\Theta-1)+\delta(\Theta+1)\big]\left\{A\int_{-T/2}^{T/2}\cos\left(2\pi f_l t-\phi\right)\, e^{i2\pi f_s\Theta t}\,dt + B\int_{-T/2}^{T/2} e^{i2\pi f_s\Theta t}\,dt\right\}. \tag{7.30}$$

Now, let us simplify the two integrals in Equation 7.30, separately. Consider the first integral, which is found by

$$\begin{aligned}&\int_{-T/2}^{T/2}\cos\left(2\pi f_l t-\phi\right)e^{i2\pi f_s\Theta t}\,dt \\ &\quad= \int_{-\infty}^{\infty}\mathrm{rect}_T(t)\cos(2\pi f_l t-\phi)\, e^{i2\pi f_s\Theta t}\,dt \\ &\quad= \mathscr{F}^{-1}\big[\,\mathrm{rect}_T(t)\cos(2\pi f_l t-\phi)\big]_{t\to f_s\Theta} \\ &\quad= \mathscr{F}^{-1}\big[\,\mathrm{rect}_T(t)\big] * \mathscr{F}^{-1}\big[\cos(2\pi f_l t-\phi)\big] \\ &\quad= T\,\mathrm{sinc}(\pi f_s\Theta T) * \exp\left(\frac{i2\pi f_s\Theta\phi}{2\pi f_l}\right)\mathscr{F}^{-1}\big[\cos(2\pi f_l t)\big] \quad (\because \text{Equation 7.8}) \\ &\quad= \frac{T}{2}\,\mathrm{sinc}(\pi f_s\Theta T) * \exp\left(\frac{if_s\Theta\phi}{f_l}\right)\left[\delta\left(f_s\Theta-\frac{2\pi f_l}{2\pi}\right)+\delta\left(f_s\Theta+\frac{2\pi f_l}{2\pi}\right)\right] \\ &\quad= \frac{T}{2}\exp\left(\frac{if_s\Theta\phi}{f_l}\right)\Big(\,\mathrm{sinc}\left(\pi f_s\Theta T\right) * \left[\delta(f_s\Theta-f_l)+\delta(f_s\Theta+f_l)\right]\Big) \\ &\quad= \frac{T}{2}\exp\left(i\frac{f_s\Theta}{f_l}\phi\right)\left[\mathrm{sinc}\left(\pi(f_s\Theta-f_l)T\right)+\mathrm{sinc}\left(\pi(f_s\Theta+f_l)T\right)\right], \end{aligned} \tag{7.31}$$

where we have used the fact that the sinc and delta functions are both even, thus there is no difference between the forward and inverse transforms. We used inverse Fourier shift theorem (Equation 7.8) and the Fourier transform of the cosine (Equation 7.18).

Note that the phase shift ϕ in Equation 7.31 due to ToF appears as the phase of the signal scaled by f_s/f_l at the $|\Theta| = f_l/f_s$ frequency. It is therefore typical to operate a camera in homodyne ($f_l = f_s$) and capture a sequence of N frames with $\theta = j/N$ for $j = 0, \ldots, N-1$, then the phase can be recovered from the fundamental frequency of an N-point DFT of the captured frames. The second integral in Equation 7.30, is

$$\begin{aligned}\int_{-T/2}^{T/2} e^{i2\pi f_s \Theta t}\, dt &= \int_{-\infty}^{\infty} \mathrm{rect}_T(t)\; e^{i2\pi f_s \Theta t}\, dt \\ &= \mathscr{F}^{-1}\big[\,\mathrm{rect}_T(t)\big]_{t \to f_s\Theta} = T\,\mathrm{sinc}\,(\pi f_s \Theta T). \end{aligned} \tag{7.32}$$

The background lighting B appears at the DC component of the DFT as Equation 7.32 thus does not (in principle) affect the measurement of the ToF phase (in practice it degrades SNR because it reduces dynamic range at the sensor (Lange and Seitz, 2001)). Now, substituting Equations 7.31 and 7.32 in Equation 7.30 gives

$$\begin{aligned}\widehat{I}(\Theta) = \pi T\big[\delta(\Theta-1) + \delta(\Theta+1)\big] \Bigg\{ \frac{A}{2} \exp\left(i\frac{f_s\Theta}{f_l}\phi\right) \big[\mathrm{sinc}\left(\pi(f_s\Theta - f_l)T\right) \\ + \mathrm{sinc}\left(\pi(f_s\Theta + f_l)T\right)\big] + B\,\mathrm{sinc}\,(\pi f_s \Theta T) \Bigg\}. \end{aligned} \tag{7.33}$$

And on applying the delta functions and considering the fundamental ($\Theta = 1$) frequency in Equation 7.33,

$$\begin{aligned}\widehat{I}(1) = \frac{\pi T A}{2}\, e^{i\left(\frac{f_s}{f_l}\right)\phi} \left[\mathrm{sinc}(\pi T(f_s - f_l)) + \mathrm{sinc}(\pi T(f_s + f_l))\right] \\ + \pi B T\,\mathrm{sinc}(\pi f_s T). \end{aligned} \tag{7.34}$$

In current implementations the integration period of the frame capture is very long compared to the period of the modulation cycle, thus consider the limit of T large, which with application of Equations 7.20 and 7.11 is found to be,

$$\lim_{T\to\infty} \widehat{I}(1) = \frac{\pi A}{2}\; e^{i\left(\frac{f_s}{f_l}\right)\phi}\big[\delta(f_s - f_l) + \delta(f_s + f_l)\big]. \tag{7.35}$$

That is, the so-called correlation integral becomes a true correlation and only frequencies that are present in *both* the illumination and shutter modulation signals contribute to the measurement of the ToF phase. This is standard wisdom in AMCW lidar but we note that, while accurate for current hard-

ware, as modulation frequencies increase and frame capture times decrease the assumption will eventually be violated in hardware.

It is normal to operate a system in homodyne, that is $f = f_s = f_l$. Returning to a finite integration time, Equation 7.34 is then,

$$\widehat{I}(1) = \frac{\pi T A}{2} e^{i\phi} \left[1 + \operatorname{sinc}(2\pi f T)\right] + \pi B T \operatorname{sinc}(\pi f T). \tag{7.36}$$

The term 1 in the brackets is the integration across a whole number of modulation cycles and the term $\operatorname{sinc}(2\pi f T)$ is due to the integration of the remaining fraction of a cycle. For sufficiently large T the sinc term is very small compared to 1 thus taking the phase of the fundamental frequency of the DFT of a sequence of frame captures gives the ToF phase. It is instructive to ask when the sinc term might be significant. Note that it only affects the measured magnitude of $\widehat{I}(1)$, not the ToF phase, unlike the final sinc term due to the background lighting. If B is sufficiently large and T sufficiently small then the background light not cancelled out in the final part cycle of frame integration may introduce an error to the measurement of the ToF phase.

Returning to the general solution (Equation 7.34) note that if the modulation signals are not pure and the integration period is not sufficiently large, then it is possible that the side-lobes of the sinc functions for modulation frequencies $|f_s| \neq |f_l|$ may contribute to the result, and if they do, then the ToF phase is distorted because of the f_s/f_l multiplier in the argument of the exponential. Retrieving the ToF phase by DFT will return a value with some error. That harmonic content on the modulation signals leads to measurement error is well known (Dorrington *et al.*, 2011) and many effective mitigation methods have been proposed (Kahlmann *et al.*, 2006; Lindner and Kolb, 2006; Streeter and Dorrington, 2015). The importance for us is in realising that PJ on the modulation signals introduces new frequencies that potentially can interact together via the sinc functions to contaminate the phase of the cosine. The question of whether the contamination is sufficiently significant to be of concern is what we consider in Section 7.4.

7.4 Correlation Model with Periodic Jitter

In this section, we introduce periodic jitter as a form of deterministic jitter into both the light and shutter sources and investigate its effect on reconstructing range. Periodic jitter is defined as the repetition of the jitter at a certain

period in a signal (Li, 2007). We now introduce periodic jitter of amplitude A_{PJ} and frequency f_{PJ} into both the light and shutter sources. The modulated light signal with a unity amplitude and periodic jitter is given by

$$l(t,\phi) = \cos\left(2\pi f_l(t + A_{\mathrm{PJ}}\sin\left(2\pi f_{\mathrm{PJ}}t\right)) - \phi\right). \tag{7.37}$$

The shutter signal is given by

$$s(t,\theta) = \cos\left(2\pi f_s(t + A_{\mathrm{PJ}}\sin\left(2\pi f_{\mathrm{PJ}}t + \phi^s_{\mathrm{PJ}}\right)\right) + \theta), \tag{7.38}$$

where ϕ^s_{PJ} is the phase difference of the periodic jitter in shutter signal with respect to the light signal where it is now assumed that the offset coefficient and noise in the signals are zero because background offset is not contributed to the correlation model.

Now, let see how the correlation model with jitter can be solved numerically and analytically.

7.4.1 Numerical Approaches

In general, for computing an integral, most numerical methods split up the original integral into a sum of several integrals, each covering a small part of the original integration interval. We use two types of integration methods, the trapezoidal and Romberg for the approximate calculation of the definite integral (Garcia, 2000). Then, the integral can be found by

$$I(t) = \int_{-T/2}^{T/2} c(t)\,dt = \int_{-T/2}^{T/2} s(t,\theta)\,l(t,\phi)\,dt. \tag{7.39}$$

We repeat this integration in Equation 7.39 for four phase frames $\theta = 0, \pi/2, \pi$ and $3\pi/2$ to find the phase ϕ, and this will be used with the range measurement relation (Equation 2.1) to find the corresponding distance to the scene.

7.4.1.1 Trapezoidal Integration

Lets consider the function $c(t)$ on the interval $[t_l\ t_u]$ as shown in Figure 7.1. The integration in Equation 7.39 can be represented as the area between the t-axis and the curve $c(t)$ of the integrand on the given interval. This is approximated with the sum of the areas of a series of parallel trapezoids as

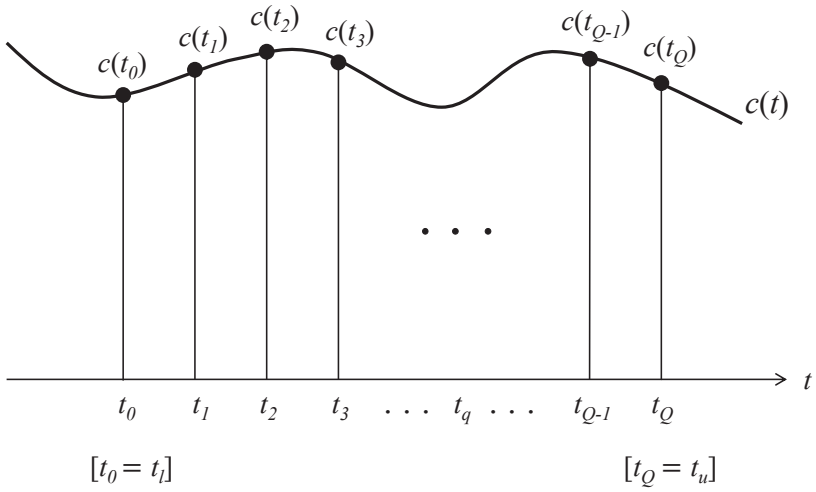

Figure 7.1: Illustration of the trapezoidal integration for multiple segments on the function $c(t)$.

$$I_{\text{trapz}} \approx \frac{1}{2}\sum_{q=0}^{Q-1}(t_{q+1}-t_q)\,(c(t_{q+1})+c(t_q)), \quad Q \in \mathbb{Z}^+ \tag{7.40}$$

where Q is the number of intervals, t_q are the integration points that are distributed on the given interval $[t_0 = t_l \;\; t_Q = t_u]$. These points may, or may not, be evenly distributed. An even distribution simplifies the computation and is often sufficient. Then Equation 7.40 becomes (Chapra and Canale, 2015)

$$I_{\text{trapz}} \approx \frac{(t_u - t_l)}{2\,Q}\sum_{q=0}^{Q-1}\big(c(t_q)+c(t_{q+1})\big), \quad [t_l \; t_u] \tag{7.41}$$

where $(t_u - t_l)/Q$ is the gap on the t-axis between consecutive integration points. In here, the integration is computed under a straight-line segment to approximate the integral under a curve, it is obvious that a substantial error can be incurred. If the function of the segment has a positive second derivative then the integrand is concave up, thus the error is negative and the trapezoidal method overestimates the actual value.

A concave-down function yields an underestimate since the area is unaccounted for under the curve. Both of these situations are not considered in Equation 7.41. Therefore, as usual, the error occurs in the trapezoidal method. It is clear that the number of intervals Q increases then the error decreases. Therefore, high accuracy can be attained by choosing sufficiently large value for Q. But the computational work involved is roughly proportional to the number of points where $c(t)$ must be computed (Dahlquist and Bjorck, 2008).

7.4.1.2 Romberg Integration

When the interval size use in trapezoidal rule is set to half by taking the number of sub-intervals to the power of two, these are called panels as shown in Figure 7.2.

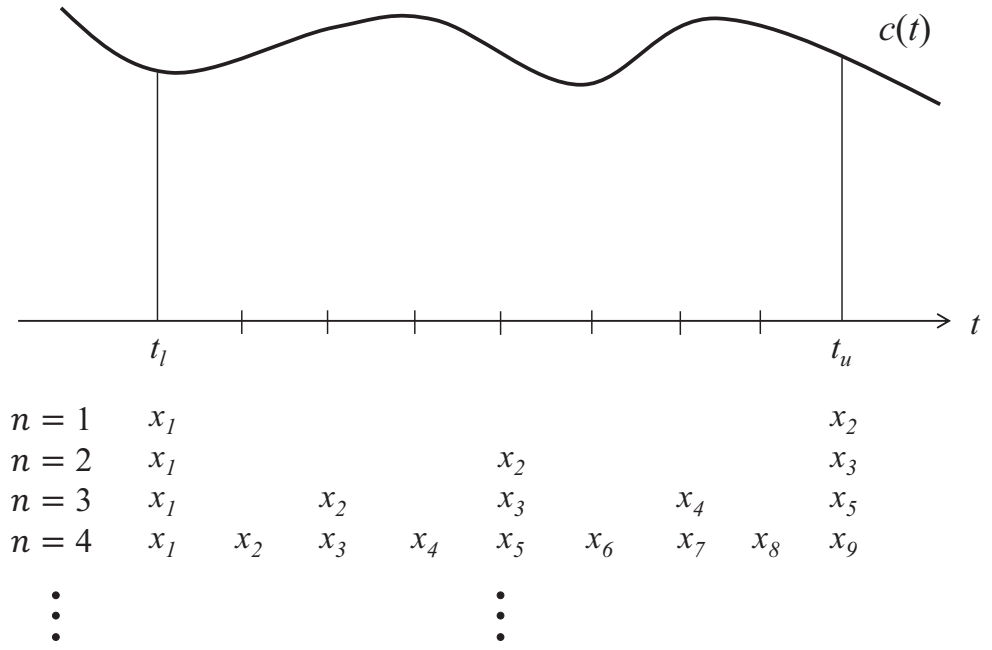

Figure 7.2: Illustration of the recursive trapezoidal integration panels on the function $c(t)$.

Then by the recursive method, we can add the panels until the answer begins to converge. This builds a form of a lower triangular matrix. The successive columns are computed by the Richardson's extrapolation method which is given by (Garcia, 2000)

$$\mathcal{R}_{n+1,m+1} = \mathcal{R}_{n+1,m} + \frac{1}{4^m - 1}\left(\mathcal{R}_{n+1,m} - \mathcal{R}_{n,m}\right), \tag{7.42}$$

where (n, m) is the nth row and mth column of the table.

The first two columns are represented by the recursive trapezoidal and Simpson's rules, respectively. The success of repeated Richardson extrapolations is related to the behaviour in the integration limit of the higher derivatives of the integrand. The most accurate estimate for the integrals is the value at the bottom right corner of the matrix as in Equation 7.43.

$$[\mathcal{R}]_{M\times M} = \begin{pmatrix} \mathcal{R}_{1,1} & - & - & - & - \\ \mathcal{R}_{2,1} & \mathcal{R}_{2,2} & - & - & - \\ \mathcal{R}_{3,1} & \mathcal{R}_{3,2} & \mathcal{R}_{3,3} & - & - \\ \mathcal{R}_{4,1} & R_{4,2} & \mathcal{R}_{4,3} & \mathcal{R}_{4,4} & \dots \\ \vdots & \vdots & \vdots & & \ddots \end{pmatrix}, \quad M \in \mathbb{Z}^+. \tag{7.43}$$

7.4.2 Analytical Approach

With Equations 7.37 and 7.38, let us consider the correlation function in Equation 7.26 taking the Fourier transform with respect to $\theta \to \vartheta$. As before, by application of the Fourier theorems in Equations 7.7, 7.18 and 7.11 with $\Theta = 2\pi\vartheta$, the Fourier transform of the shutter signal can be obtained, namely

$$\begin{aligned} \mathscr{F}[s(t,\theta)] &= \mathscr{F}\left[\cos\left(2\pi f_s(t + A_{\mathrm{PJ}}\sin\left(2\pi f_{\mathrm{PJ}}t + \phi^s_{\mathrm{PJ}}\right)\right) + \theta\right)\right]_{\theta\to\vartheta} \\ &= e^{i(2\pi)^2 f_s\left(t + A_{PJ}\sin\left(2\pi f_{PJ}t + \phi^s_{PJ}\right)\right)\vartheta}\mathscr{F}[\cos(\theta)] \\ &= \frac{1}{2}e^{i(2\pi)^2 f_s\left(t + A_{PJ}\sin\left(2\pi f_{PJ}t + \phi^s_{PJ}\right)\right)\vartheta}\left[\delta\left(\vartheta - \frac{1}{2\pi}\right) + \delta\left(\vartheta + \frac{1}{2\pi}\right)\right] \\ &= \pi e^{i2\pi f_s\left(t + A_{PJ}\sin\left(2\pi f_{PJ}t + \phi^s_{PJ}\right)\right)\Theta}\left[\delta(\Theta - 1) + \delta(\Theta + 1)\right]. \end{aligned} \tag{7.44}$$

Substituting Equation 7.44 into Equation 7.26, with rearrangement gives,

$$\widehat{I}(\Theta) = \pi[\delta(\Theta - 1) + \delta(\Theta + 1)]\int_{-T/2}^{T/2} e^{i2\pi f_s\Theta\left(t + A_{\mathrm{PJ}}\sin(2\pi f_{\mathrm{PJ}}t + \phi^s_{\mathrm{PJ}})\right)} l(t,\phi)\, dt. \tag{7.45}$$

Letting $\beta_s = 2\pi f_s A_{\mathrm{PJ}}$ and $\beta_l = 2\pi f_l A_{\mathrm{PJ}}$, and substituting Equation 7.37, gives

$$\begin{aligned} \widehat{I}(\Theta) = \pi[\delta(\Theta - 1) + \delta(\Theta + 1)]\int_{-T/2}^{T/2} & e^{i2\pi f_s\Theta t}\, e^{i\beta_s\Theta\sin(2\pi f_{\mathrm{PJ}}t + \phi^s_{\mathrm{PJ}})} \\ & \times \Re\left[e^{i(2\pi f_l t - \phi)}\, e^{i\beta_l\sin(2\pi f_{\mathrm{PJ}}t)}\right] dt. \end{aligned} \tag{7.46}$$

With Equation 7.22 substituted into Equation 7.46, and rearrangement gives

$$\begin{aligned} \widehat{I}(\Theta) = \pi[\delta(\Theta - 1) + \delta(\Theta + 1)]\int_{-T/2}^{T/2} & \sum_{m=-\infty}^{\infty} e^{im\phi^s_{\mathrm{PJ}}} J_m(\beta_s\Theta) \\ & \times e^{i2\pi(f_s\Theta + mf_{\mathrm{PJ}})t}\,\Re\left[\sum_{n=-\infty}^{\infty} J_n(\beta_l)\, e^{i(2\pi(f_l + nf_{\mathrm{PJ}})t - \phi)}\right] dt. \end{aligned} \tag{7.47}$$

Evaluating the real function by substituting Equation 7.23 and separating time dependent terms gives

$$\begin{aligned}\widehat{I}(\Theta) = \pi[\delta(\Theta-1)+\delta(\Theta+1)] \sum_{m=-\infty}^{\infty} e^{im\phi_{\mathrm{PJ}}^{s}}\, J_m(\beta_s\Theta) \sum_{n=-\infty}^{\infty} J_n(\beta_l) \\ \times \int_{-T/2}^{T/2} e^{i2\pi(f_s\Theta+mf_{\mathrm{PJ}})t} \cos\big(2\pi(f_l+nf_{\mathrm{PJ}})t-\phi\big)dt.\end{aligned} \tag{7.48}$$

The integral in Equation 7.48 is found by

$$\begin{aligned}&\int_{-T/2}^{T/2} e^{i2\pi(f_s\Theta+mf_{\mathrm{PJ}})t} \cos\big(2\pi(f_l+nf_{\mathrm{PJ}})t-\phi\big)dt \\ &\quad= \int_{-\infty}^{\infty} \mathrm{rect}_T(t) \cos\big(2\pi(f_l+nf_{\mathrm{PJ}})t-\phi\big)\, e^{i2\pi(f_s\Theta+mf_{\mathrm{PJ}})t}\, dt \\ &\quad= \mathscr{F}^{-1}\left[\mathrm{rect}_T(t)\, \cos\big(2\pi(f_l+nf_{\mathrm{PJ}})t-\phi\big)\right]_{t\to f_s\Theta+mf_{\mathrm{PJ}}} \\ &\quad= \mathscr{F}^{-1}\left[\mathrm{rect}_T(t)\right] * \mathscr{F}^{-1}\left[\cos\big(2\pi(f_l+nf_{\mathrm{PJ}})t-\phi\big)\right] \\ &\quad= T\ \mathrm{sinc}(\pi(f_s\Theta+mf_{\mathrm{PJ}})T) * \left(\exp\left(\frac{i2\pi(f_s\Theta+mf_{\mathrm{PJ}})\,\phi}{2\pi(f_l+nf_{\mathrm{PJ}})}\right) \right. \\ &\qquad\qquad \left. \times\, \mathscr{F}^{-1}\big[\cos\big(2\pi(f_l+nf_{\mathrm{PJ}})t\big)\big] \right) \\ &\quad= T\ \mathrm{sinc}(\pi(f_s\Theta+mf_{\mathrm{PJ}})T) * \left(\exp\left(\frac{i2\pi(f_s\Theta+mf_{\mathrm{PJ}})\,\phi}{2\pi(f_l+nf_{\mathrm{PJ}})}\right) \right. \\ &\qquad \left. \times\, \frac{1}{2}\big[\delta(f_s\Theta+mf_{\mathrm{PJ}}-f_l-nf_{\mathrm{PJ}})+\delta(f_s\Theta+mf_{\mathrm{PJ}}+f_l+nf_{\mathrm{PJ}})\big] \right) \\ &\quad= \frac{T}{2}\exp\left(i\left(\frac{f_s\Theta+mf_{\mathrm{PJ}}}{f_l+nf_{\mathrm{PJ}}}\right)\phi\right)\Big[\mathrm{sinc}(\pi(f_s\Theta+mf_{\mathrm{PJ}}-f_l-nf_{\mathrm{PJ}})T) \\ &\qquad\qquad + \mathrm{sinc}(\pi(f_s\Theta+mf_{\mathrm{PJ}}+f_l+nf_{\mathrm{PJ}})T)\Big].\end{aligned} \tag{7.49}$$

Hence

$$\begin{aligned}\widehat{I}(\Theta) = \frac{\pi T}{2}\left[\delta(\Theta-1)+\delta(\Theta+1)\right] \sum_{m=-\infty}^{\infty}\sum_{n=-\infty}^{\infty} J_m(\beta_s\Theta)\, J_n(\beta_l) \\ \times \exp\left(i\left\{\left(\frac{f_s\Theta+mf_{\mathrm{PJ}}}{f_l+nf_{\mathrm{PJ}}}\right)\phi + m\phi_{\mathrm{PJ}}^{s}\right\}\right) \\ \times \big[\mathrm{sinc}(\pi T(f_s\Theta+mf_{\mathrm{PJ}}-f_l-nf_{\mathrm{PJ}})) \\ + \mathrm{sinc}(\pi T(f_s\Theta+mf_{\mathrm{PJ}}+f_l+nf_{\mathrm{PJ}}))\big].\end{aligned} \tag{7.50}$$

The fundamental frequency is

$$\widehat{I}(1) = \frac{\pi T}{2} \sum_{m=-\infty}^{\infty} \sum_{n=-\infty}^{\infty} J_m(\beta_s) J_n(\beta_l) \exp\left(i \left\{ \left(\frac{f_s + m f_{\mathrm{PJ}}}{f_l + n f_{\mathrm{PJ}}} \right) \phi + m \phi^s_{\mathrm{PJ}} \right\} \right) \times \left[\mathrm{sinc}(\pi T (f_s - f_l + (m-n) f_{\mathrm{PJ}})) + \mathrm{sinc}(\pi T (f_s + f_l + (m+n) f_{\mathrm{PJ}})) \right]. \tag{7.51}$$

In the limit of long integration time ($T \gg f_s, f_l$), by using Equations 7.20 and 7.11, gives

$$\lim_{T\to\infty} \widehat{I}(1) = \frac{\pi}{2} \sum_{m=-\infty}^{\infty} \sum_{n=-\infty}^{\infty} J_m(\beta_s) J_n(\beta_l) \exp\left(i \left\{ \left(\frac{f_s + m f_{\mathrm{PJ}}}{f_l + n f_{\mathrm{PJ}}} \right) \phi + m \phi^s_{\mathrm{PJ}} \right\} \right) \times \left[\delta(f_s - f_l + (m-n) f_{\mathrm{PJ}}) + \delta(f_s + f_l + (m+n) f_{\mathrm{PJ}}) \right]. \tag{7.52}$$

If f_{PJ} is not a factor of $f_s - f_l$ then the first delta function is only non-zero if both $f_s = f_l = f$ and $m = n$. The second delta function is only ever potentially non-zero for large (and negative) m and n at which point the Bessel functions are effectively zero. In this case, let $\beta = \beta_s = \beta_l$ then, Equation 7.52 gives

$$\begin{aligned} \lim_{T\to\infty} \widehat{I}(1) &= \frac{\pi}{2} \sum_{n=-\infty}^{\infty} J_n^2(\beta)\, e^{i\left(\phi + n\phi^s_{\mathrm{PJ}}\right)}, \\ &= \frac{\pi}{2} e^{i\phi} \left[J_0^2(\beta) + \sum_{n=1}^{\infty} \left(J_n^2(\beta)\, e^{in\phi^s_{\mathrm{PJ}}} + J_{-n}^2(\beta)\, e^{-in\phi^s_{\mathrm{PJ}}} \right) \right] \\ &= \frac{\pi}{2} e^{i\phi} \left[J_0^2(\beta) + 2 \sum_{n=1}^{\infty} J_n^2(\beta) \cos(n\phi^s_{\mathrm{PJ}}) \right], \end{aligned} \tag{7.53}$$

where we have used a property of the Bessel's function $J_{-n}(\beta) = (-1)^n J_n(\beta)$. The last line shows that while there may be distortions in received amplitude (assuming sufficiently large β) there is nevertheless no error in the ToF phase.

If on the other hand f_{PJ} is a factor of $f_s - f_l$ then the first delta function of Equation 7.52 can be non-zero when $m \neq n$. That will lead to phases of the form $((f_s + m f_{\mathrm{PJ}})/(f_l + n f_{\mathrm{PJ}}))\phi$ appearing in the exponentials in the summation, thus distorting the phase from the ToF phase. Whether these terms make a significant contribution depends on the value of β. Table 7.1 shows first five terms of $J_n(\beta)$ when $A_{\mathrm{PJ}} = 100$ ps with $f = 2^k \times 50$ MHz, $k = 0, 1, 2, 3$. It seems that the first three values: $J_0(\beta), J_1(\beta), J_2(\beta)$ for each β are reasonable amounts. Thus, it is conceivable that particular combinations of f_s, f_l and f_{PJ} might lead to detectable error in measuring the ToF phase.

Table 7.1: First five values of Bessel function of the first kind of argument β when $f = \{50, 100, 200, 400\}$ MHz and $A_{\mathrm{PJ}} = 100$ ps

Order n	$J_n(\beta)$	Argument $\beta = 2\pi f A_{\mathrm{PJ}}$ with four values of f			
		0.0314	0.0628	0.1257	0.2513
0	$J_0(\beta)$	9.997×10^{-1}	9.990×10^{-1}	9.960×10^{-1}	9.843×10^{-1}
1	$J_1(\beta)$	1.571×10^{-2}	3.140×10^{-2}	6.271×10^{-2}	1.247×10^{-1}
2	$J_2(\beta)$	1.233×10^{-4}	4.933×10^{-4}	1.971×10^{-3}	7.854×10^{-3}
3	$J_3(\beta)$	6.459×10^{-7}	5.166×10^{-6}	4.130×10^{-5}	3.294×10^{-4}
4	$J_4(\beta)$	2.536×10^{-9}	4.058×10^{-8}	6.489×10^{-7}	1.036×10^{-5}

With the system in homodyne operation (then $\beta = 2\pi f A_{\mathrm{PJ}} = \beta_s = \beta_l$) and finite integration time, the fundamental frequency in Equation 7.51 becomes

$$\widehat{I}(1) = \frac{\pi T}{2} \sum_{m=-\infty}^{\infty} \sum_{n=-\infty}^{\infty} J_m(\beta) J_n(\beta) \exp\left(i \left\{ \left(\frac{f + m f_{\mathrm{PJ}}}{f + n f_{\mathrm{PJ}}} \right) \phi + m \phi^s_{\mathrm{PJ}} \right\} \right) \times \left[\mathrm{sinc}(\pi T (m-n) f_{\mathrm{PJ}}) + \mathrm{sinc}(\pi T (2f + (m+n) f_{\mathrm{PJ}})) \right]. \quad (7.54)$$

Multiples of the phase relationship of the jitter ϕ and ϕ^s_{PJ} appear in the summation and can contaminate the overall phase of the result. The amount of contamination depends on the modulation frequency and frame integration time of the camera, the amplitude and the frequency of the periodic jitter. It is not a straight forward relationship but we can immediately note that the limit of no jitter ($A_{\mathrm{PJ}} = 0$) results in Equation 7.36 with $A = 1$ and $B = 0$ as expected. Even without the phase difference of the periodic jitter between the shutter and light signals (i.e., $\phi^s_{\mathrm{PJ}} = 0$ in Equation 7.54), the periodic jitter influences range measurements. The double summation consists of two complex series with the product of common Bessel functions and two sinc terms $\mathrm{sinc}(\pi((\Theta - 1)f + (m-n)f_{\mathrm{PJ}})T)$ and $\mathrm{sinc}(\pi((\Theta + 1)f + (m+n)f_{\mathrm{PJ}})T)$.

7.4.3 The Phase Error due to the Periodic Jitter

The phase error ϕ_{err} due to the periodic jitter of the analytical model obtained in Equation 7.51 can be computed by

$$\phi_{\mathrm{err}} = \left|\phi\right| - \left|\angle \widehat{I}(1)\right|, \quad (7.55)$$

where $\angle$ is the angle of the resulted function.

Note that the scalar factor $\frac{\pi T}{2}$ in the analytical model does not affect the phase. It is clear that the ToF phase shift ϕ is always added to the double summation in the analytical model obtained (Equation 7.51), therefore, some portion of the phase shift contributes to the phase error in the system. For the fundamental frequency, when the indices are same (i.e., $m = n$), the ϕ is independent from the double summation and hence the phase error is independent from ϕ. However, when the indices are $m \neq n \neq 0$, then the phase error is dependent on ϕ for those terms.

7.5 Simulation Setup

The homodyne operation is considered for various modulation frequencies (201 values) span in $f = 0$ to 1000 MHz by 5 MHz steps. For jitter frequency f_{PJ}, the two fixed values are chosen for the simulations, one is 5 MHz that exactly divide the modulation frequencies used (i.e., 10^6 times of the greatest common divisor (GCD) among f). The second value is 4.9261 MHz (less than and closer to the above GCD) that does not exactly divide modulation frequencies. For jitter amplitude, 101 values that span in $A_{\mathrm{PJ}} = 0$ to 1000 ps by 10 ps steps are selected throughout the simulations. In addition, for the phase difference of the jitter in shutter with respect to the light signal, we use multiple phases that non-integer factor of each other such as $\phi^s_{\mathrm{PJ}} = 0$ to π by $\pi/19$ rad steps, for each evaluation and then select the maximum phase error (worst) among them. Table 7.2 shows all corresponding parameters of the simulation setup.

Table 7.2: Parameters of the simulation setup

ToF camera	**Periodic jitter**
Modulation frequency (MHz) $f = 5(k-1), \quad k = 1, \ldots, 201$	Frequency (MHz) $f_{\mathrm{PJ}} = 4.9261$ and 5
Integration period (ms) $T = 0.01, 0.1, 1$	Amplitude (ps) $A_{\mathrm{PJ}} = 10(k-1), \quad k = 1, \ldots, 101$
Phase frame (rad) $\theta_k = \frac{\pi}{2}k, \quad k = 0, \ldots, 3$	Phase shift (rad) $\phi^s_{\mathrm{PJ}} = 0$ to π by $\pi/19$ rad steps
ToF phase shift (rad) $\phi = 0$ to $5\pi/6$ by $\pi/6$ steps	Argument of Bessel function β $\beta = 2\pi f A_{\mathrm{PJ}} = 0$ to 2π
For the analysis, choose three phase errors $\phi_{\mathrm{err}} = 0.1$, 0.01, 0.001 rad and select the maximum phase error (worst) among the above 20 phase shifts	

In particular, for the numerical approaches, the traditional four phase frames method is performed in order to calculate the phase errors. The three precisions (i.e., phase errors, $\phi_{\text{err}} = 0.1$, 0.01 and 0.001 rad) of range measurements on simulated signals from both analytical and numerical approaches are evaluated. These values are the corresponding phase errors for depth errors of approximately $d_{\text{err}} = 100$, 10 and 1 mm, respectively, for the MESA SR4000 when $f = 30$ MHz with non-ambiguity range of 5.0 meters (but actual calculated phase errors are approximately $\phi_{\text{err}} = 0.12566$, 0.012566 and 0.0012566 rad). In addition, three different integration periods ($T = 0.01$, 0.1 and 1 ms) on the phase error are also performed for each evaluation. These values are chosen to investigate the influence of PJ on range measurements in current AMCW ToF cameras and predicting for the future AMCW ToF cameras. As an example, the integration period in the MESA Imaging SR4000[1] can be selectable in the range of 0.3 to 25.8 ms by 0.1 ms steps.

7.6 Results and Discussion

In order to use the analytical model (Equation 7.55), first, we need to find the optimal value of the order that converge the Bessel functions. With the maximum amounts of f and A_{PJ} (see Table 7.2), the corresponding maximum argument of Bessel functions is given by $\beta = 2\pi f A_{\text{PJ}} = 2\pi$. But, for consistency of the optimal value, we choose $\beta = 0$ to 2.5π and $n = \{10, 20, 30, 40, 50\}$ for the evaluation purpose. Then, the behaviour of the analytical model is performed when the frequency of the periodic jitter $f_{\text{PJ}} = 4.9261$ and 5 MHz, separately, as in the following two sections.

7.6.1 Jitter Frequency as a Non-factor of Modulation Frequency

Tables 7.3 and 7.4 show the corresponding phase error with fifteen significant digits due to periodic jitter at the frequency $f_{\text{PJ}} = 4.9261$ MHz, for a selected ToF phase shift (i.e., $\phi = \pi/6$) with different order values of the Bessel function with two integration periods $T = 0.01$ and 1 ms, respectively. For $T = 0.1$ ms, this similar analysis is also valid. The twenty first row of both tables corresponds to the maximum argument $\beta = 2\pi$ for the Bessel function with the parameters chosen ($f = 1000$ MHz and $A_{\text{PJ}} = 1000$ ps).

[1] `https://www.adept.net.au/cameras/Mesa/pdf/SR4000.pdf`

Table 7.3: Calculated maximum phase error (worst) with five different order n of Bessel functions: $f = 1000$ MHz, $\phi = \pi/6$, $f_{\mathrm{PJ}} = 4.9261$ MHz, $A_{\mathrm{PJ}} = 1000$ ps, $\beta = (0 : \pi/10 : 2.5\pi)$ and $T = 0.01$ ms in Equation 7.55

#	β	$n = 10$	$n = 20$	$n = 30$	$n = 40$	$n = 50$
1	0	0.0000000000000001	0.0000000000000001	0.0000000000000001	0.0000000000000001	0.0000000000000001
2	0.3142	0.0000081829684362	0.0000081829684362	0.0000081829684362	0.0000081829684362	0.0000081829684362
3	0.6283	0.0000206259312883	0.0000206259312882	0.0000206259312882	0.0000206259312882	0.0000206259312882
4	0.9425	0.0000560729116991	0.0000560729116996	0.0000560729116996	0.0000560729116996	0.0000560729116996
5	1.2566	0.0000000004246901	0.0000000004246903	0.0000000004246903	0.0000000004246903	0.0000000004246903
6	1.5708	0.0000000006273826	0.0000000006273850	0.0000000006273850	0.0000000006273850	0.0000000006273850
7	1.8850	0.0000000008305953	0.0000000008306148	0.0000000008306148	0.0000000008306148	0.0000000008306148
8	2.1991	0.0000000009965212	0.0000000009966277	0.0000000009966277	0.0000000009966277	0.0000000009966277
9	2.5133	0.0000000010914115	0.0000000010918552	0.0000000010918552	0.0000000010918552	0.0000000010918552
10	2.8274	0.0531755820274713	0.0531756100658393	0.0531756100658393	0.0531756100658393	0.0531756100658393
11	3.1416	0.0239644980212721	0.0239645495492085	0.0239645495492085	0.0239645495492085	0.0239645495492085
12	3.4558	0.0257644840843909	0.0257646632065283	0.0257646632065283	0.0257646632065283	0.0257646632065283
13	3.7699	0.0135056893253362	0.0135058017014605	0.0135058017014605	0.0135058017014605	0.0135058017014605
14	4.0841	0.0135848613801971	0.0135846288449853	0.0135846288449849	0.0135846288449849	0.0135846288449849
15	4.3982	0.0305724295279469	0.0305726764352811	0.0305726764352844	0.0305726764352844	0.0305726764352844
16	4.7124	0.0060254980739001	0.0060257444297759	0.0060257444297791	0.0060257444297791	0.0060257444297791
17	5.0265	0.0197648817408274	0.0197680045987675	0.0197680045987587	0.0197680045987587	0.0197680045987587
18	5.3407	0.0061645317187871	0.0061680836624408	0.0061680836624293	0.0061680836624293	0.0061680836624293
19	5.6549	0.0472959336417237	0.0472824746265259	0.0472824746266738	0.0472824746266738	0.0472824746266738
20	5.9690	0.0122612272154266	0.0122569362027165	0.0122569362028634	0.0122569362028634	0.0122569362028634
21	6.2832	0.0053079181287907	0.0053070491478532	0.0053070491481236	0.0053070491481236	0.0053070491481236
22	6.5973	0.1403387891786890	0.1404537135815630	0.1404537135804180	0.1404537135804180	0.1404537135804180
23	6.9115	0.0228852430059199	0.0228420785554446	0.0228420785532450	0.0228420785532450	0.0228420785532450
24	7.2257	0.1023726722866610	0.1021057589777790	0.1021057590747610	0.1021057590747610	0.1021057590747610
25	7.5398	0.0390394633352832	0.0376703386724775	0.0376703389620549	0.0376703389620549	0.0376703389620549
26	7.8540	0.0196258882535562	0.0188022254089634	0.0188022251842409	0.0188022251842409	0.0188022251842409

Table 7.4: Calculated maximum phase error (worst) with five different order n of Bessel functions: $f = 1000$ MHz, $\phi = \pi/6$, $f_{\mathrm{PJ}} = 4.9261$ MHz, $A_{\mathrm{PJ}} = 1000$ ps, $\beta = (0 : \pi/10 : 2.5\pi)$ and $T = 1$ ms in Equation 7.55

#	β	$n = 10$	$n = 20$	$n = 30$	$n = 40$	$n = 50$
1	0	0.0000000000000001	0.0000000000000001	0.0000000000000001	0.0000000000000001	0.0000000000000001
2	0.3142	0.0000064682518306	0.0000064682518306	0.0000064682518306	0.0000064682518306	0.0000064682518306
3	0.6283	0.0000147023101312	0.0000147023101312	0.0000147023101312	0.0000147023101312	0.0000147023101312
4	0.9425	0.0000322877504456	0.0000322877504456	0.0000322877504456	0.0000322877504456	0.0000322877504456
5	1.2566	0.0005888899926361	0.0005888899925994	0.0005888899925994	0.0005888899925994	0.0005888899925994
6	1.5708	0.0001986135251906	0.0001986135252273	0.0001986135252273	0.0001986135252273	0.0001986135252273
7	1.8850	0.0001493112970540	0.0001493112970485	0.0001493112970485	0.0001493112970485	0.0001493112970485
8	2.1991	0.0001726359422258	0.0001726359445675	0.0001726359445675	0.0001726359445675	0.0001726359445675
9	2.5133	0.0001253098182393	0.0001253098252459	0.0001253098252459	0.0001253098252459	0.0001253098252459
10	2.8274	0.0021918009236132	0.0021918013802154	0.0021918013802154	0.0021918013802154	0.0021918013802154
11	3.1416	0.0001516529011097	0.0001516526841262	0.0001516526841262	0.0001516526841262	0.0001516526841262
12	3.4558	0.0007725830968844	0.0007725861399759	0.0007725861399759	0.0007725861399759	0.0007725861399759
13	3.7699	0.0000775324198746	0.0000775330568149	0.0000775330568149	0.0000775330568149	0.0000775330568149
14	4.0841	0.0001160108862120	0.0001160131420389	0.0001160131420389	0.0001160131420389	0.0001160131420389
15	4.3982	0.0002469018992108	0.0002469122819047	0.0002469122819047	0.0002469122819047	0.0002469122819047
16	4.7124	0.0000467516379190	0.0000467553739710	0.0000467553739710	0.0000467553739710	0.0000467553739710
17	5.0265	0.0000541974838414	0.0000542057150575	0.0000542057150575	0.0000542057150575	0.0000542057150575
18	5.3407	0.0000640469514056	0.0000640643568566	0.0000640643568561	0.0000640643568561	0.0000640643568561
19	5.6549	0.0000780832671327	0.0000781190914602	0.0000781190914586	0.0000781190914586	0.0000781190914586
20	5.9690	0.0001004314701792	0.0001005051200799	0.0001005051200738	0.0001005051200738	0.0001005051200738
21	6.2832	0.0001774825035497	0.0001909819540751	0.0001909819535894	0.0001909819535894	0.0001909819535894
22	6.5973	0.0002656864234740	0.0002661914060932	0.0002661914059647	0.0002661914059647	0.0002661914059647
23	6.9115	0.0060779921624553	0.0063240295918506	0.0063240295835633	0.0063240295835633	0.0063240295835633
24	7.2257	0.0001384999258035	0.0001439867585732	0.0001439867587878	0.0001439867587878	0.0001439867587878
25	7.5398	0.0090304186628690	0.0071669080698577	0.0071669080234683	0.0071669080234683	0.0071669080234683
26	7.8540	0.0001106578928241	0.0001265011200378	0.0001265011134433	0.0001265011134433	0.0001265011134433

The thick border line indicates the corresponding last row for each order n that satisfies the precision level of seventeen significant digits. Thus, in order to get seventeen significant digits, it is sufficient that of selecting the order n = 30 for those chosen parameters. But, to be safe, the order of the Bessel function has been selected to be 40. Thus, the summation of Equation 7.55 is truncated for both m and n to be -40 to 40 each, which is well sufficient for the fundamental frequency. Then, there are $81 \times 81 = 6561$ terms in the double summation in Equation 7.55. Now consider an analysis when the modulation frequency of $f = 30$ and 1000 MHz before the main results from the analytical model. Figure 7.3 shows the corresponding phase error for the ToF phase shift $\phi = 0$, due to the periodic jitter at $f_{\text{PJ}} = 4.9261$ MHz for the range of the argument $\beta = 0$ to 0.7 (this range is chosen for this particular case) with three integration periods for the two modulation frequencies in Equation 7.55, separately. These two subplots are approximately similar, therefore the changes of the values cannot be visualized for the naked eyes.

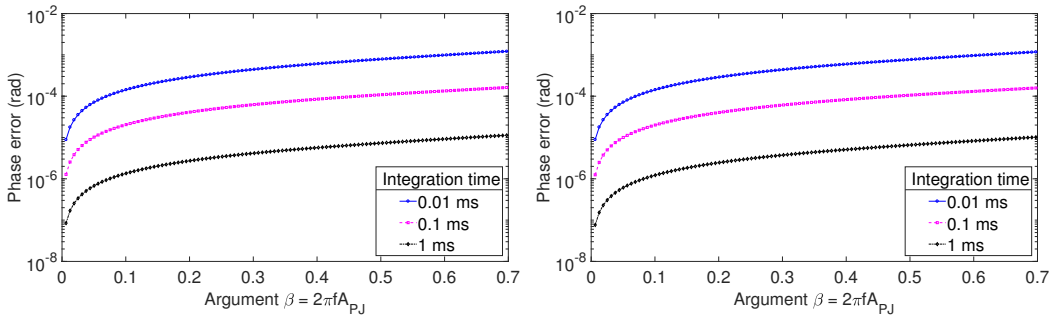

Figure 7.3: Phase error for the ToF phase shift $\phi = 0$ due to the periodic jitter at $f_{\text{PJ}} = 4.9261$ MHz, when the modulation frequency (a) $f = 30$ MHz and (b) $f = 1000$ MHz, for the three integration periods with $m, n = -40{:}40$ each using the analytical model in Equation 7.55.

If the amplitude of the jitter $A_{\text{PJ}} = 100$ ps each for $f = 30$ and 1000 MHz then $\beta = 0.006\pi$ and 0.2π, respectively. From Figure 7.3, for the three integration periods, the corresponding phase errors for $f = 30$ and 1000 MHz can be obtained as $\phi_{\text{err}} = \{2.661\times10^{-5}, 3.830\times10^{-6}, 2.535\times10^{-7}\}$ and $\{1.018\times 10^{-3}, 1.381 \times 10^{-4}, 8.794 \times 10^{-6}\}$ rad, respectively. It is clear that the phase error increases when the integration period T is shorter and this error is further worst when the modulation frequency f increases. Note that here we fixed the amount of periodic jitter $A_{\text{PJ}} = 100$ ps and considered only a single ToF phase shift $\phi = 0$.

Now, let us consider the worst behaviours of the model with other parameters. Figure 7.4 shows the maximum phase error (worst) due to the periodic jitter at the frequency $f_{\mathrm{PJ}} = 4.9261$ MHz for six ToF phase shifts $\phi = 0$ to $5\pi/6$ by $\pi/6$ steps, separately, for the three integration periods with the argument range of $\beta = 0$ to 0.2 for each evaluation. This range is chosen for analysing the phase error when the modulation frequency $f = 30$ MHz and this analysis is valid for rest of the modulation frequencies as well.

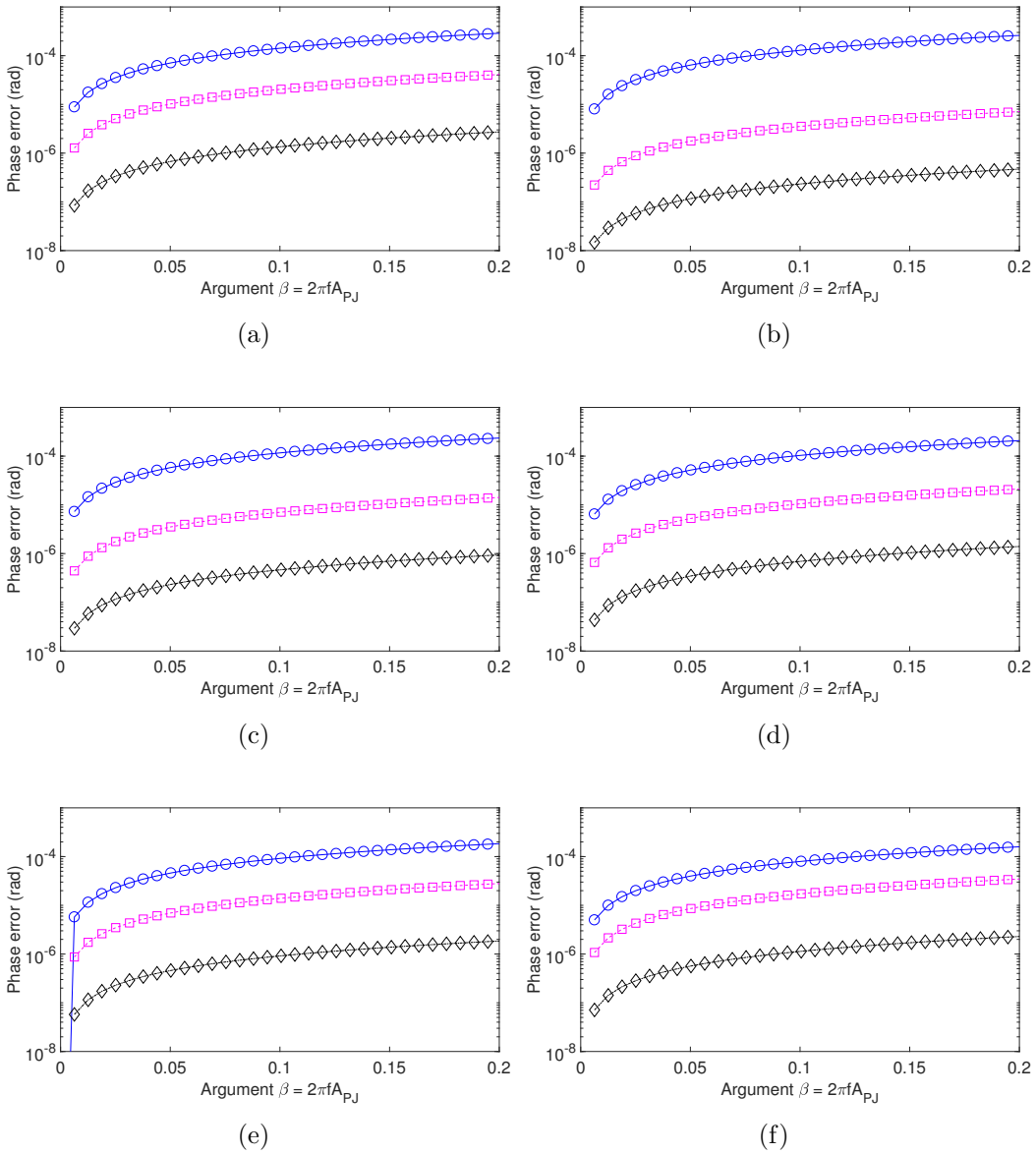

Figure 7.4: Phase error (a) to (f) for the ToF phase shift $\phi = 0$ to $5\pi/6$ by $\pi/6$ steps, respectively, due to the PJ at $f_{\mathrm{PJ}} = 4.9261$ MHz, when $f = 30$ MHz for the integration periods: 0.01 ms (—o—), 0.1 ms (—□—) and 1 ms (—◇—) with $m, n = -40{:}40$ each using the analytical model in Equation 7.55.

Among the six ToF phase shifts with the maximum argument of $\beta = 0.2011$, the phase errors are approximately in the ranges of $(1.60 - 2.90)\times10^{-4}$, $(3.48 - 4.13)\times10^{-5}$ and $(2.31 - 2.74)\times10^{-6}$ rad for the integration periods $T = 0.01$, 0.1 and 1 ms, respectively. This seems, when $T = 1$ ms, phase error is relatively very small (in microradians) which is insignificant to depth measurements. As examples, from Equation 2.1 with $f = 30$ MHz, the corresponding range errors due to phase errors $\phi_{\text{err}} = 10^{-4}, 10^{-5}$ and 10^{-6} rad are given by $d_{\text{err}} = 0.25/\pi, 0.025/\pi$ and $0.0025/\pi$ mm, respectively. These values are more insignificant when the modulation frequency f increases. It is clear that the phase error increases when the integration period decreases. That is, the frame rates of the camera increases. Furthermore, for both fixed integration time and argument of Bessel function, the phase error decreases when the ToF phase shift increases (see Figure 7.4). As examples, for $\beta = 0.1005$ and $T = 0.01$ ms, the phase errors are $\phi_{\text{err}} = 0.1295$, 0.1039 and 0.0798 mrad when $\phi = \pi/6, \pi/2$ and $5\pi/6$, respectively.

Next, the evaluation is extended on the multiple set of characteristic parameters (see Table 7.2) such as a set of phase error with various modulation frequencies f and periodic jitter amplitudes A_{PJ} for different integration periods. Figures 7.5, 7.6 and 7.7 show the contour diagrams for the aforementioned phase errors against the modulation frequency and jitter amplitude at the frequency $f_{\text{PJ}} = 4.9261$ MHz when the periods $T = 0.01$, 0.1 and 1 ms, respectively, for the two ToF phase shifts (i.e., $\phi = \pi/6$ and $\pi/3$) by the analytical model in Equation 7.55. Each of the figures is seen to be approximately symmetric along the diagonal line from (0, 0) to (1000, 1000) because the model obtained is almost a reciprocal. Interestingly the three chosen contours (phase errors of 0.001, 0.01, and 0.1 radian) land very close together indicating that there is a catastrophic decrease in accuracy when the periodic jitter exceeds a certain amount. In addition, there are phase error curves around 5 MHz modulation frequency throughout all amplitude amounts in each analytical result.

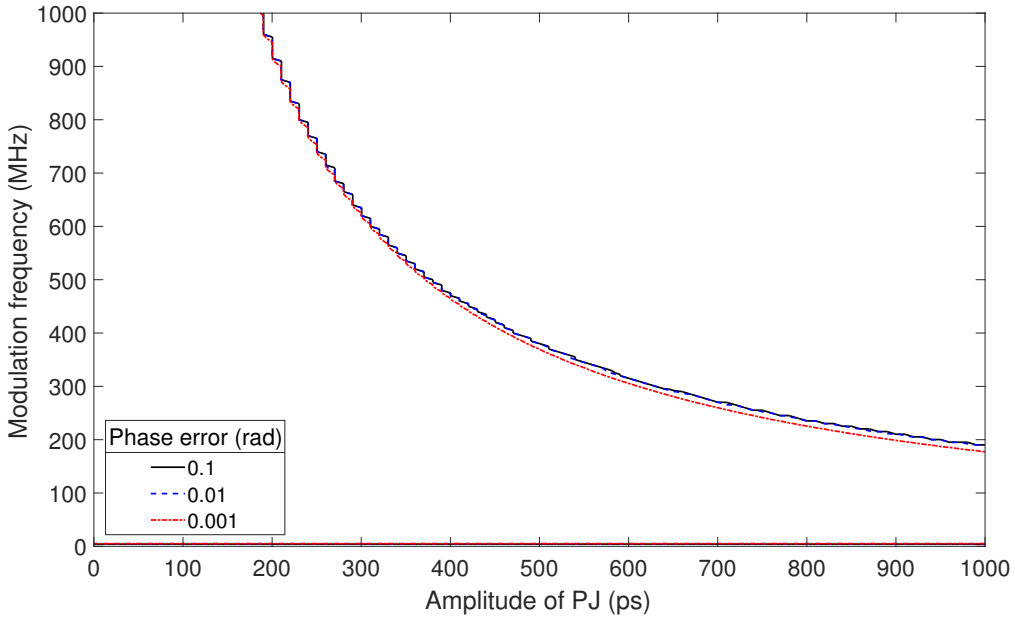

(a)

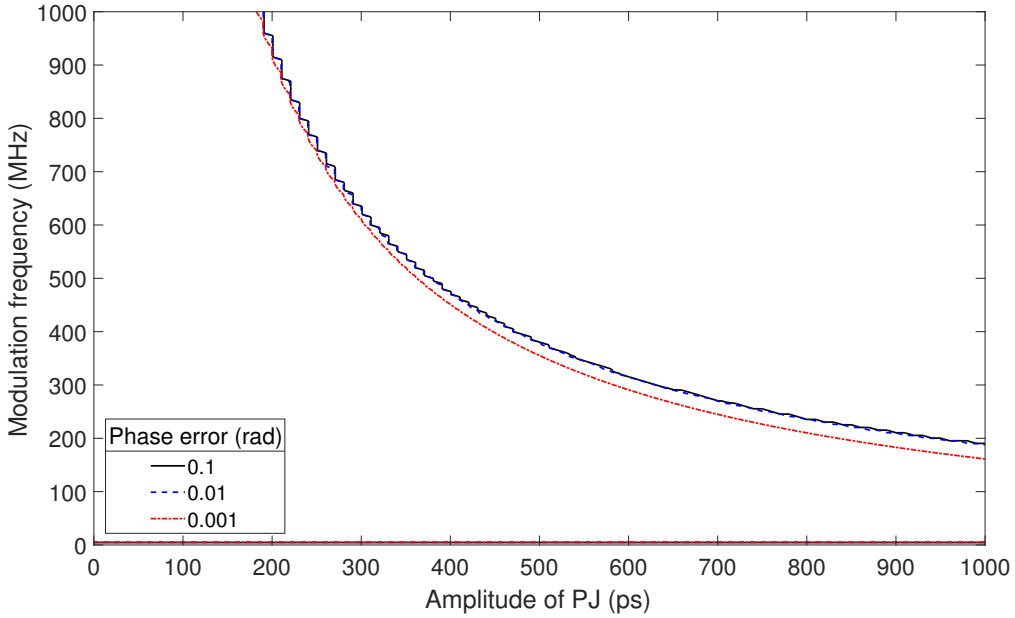

(b)

Figure 7.5: Phase error due to the periodic jitter at the frequency $f_{\mathrm{PJ}} = 4.9261$ MHz with various modulation frequencies against various jitter amplitudes by the analytical model with order $m, n = -40{:}40$ in Equation 7.55, for ToF phase shifts: (a) $\phi = \pi/6$ and (b) $\phi = \pi/3$, when the period $T = 0.01$ ms.

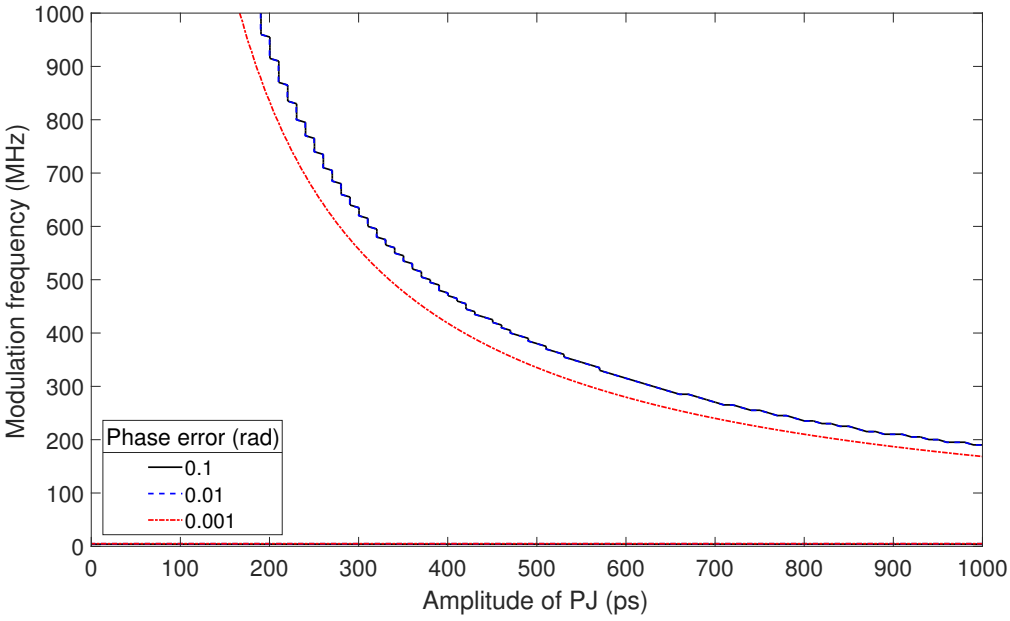

(a)

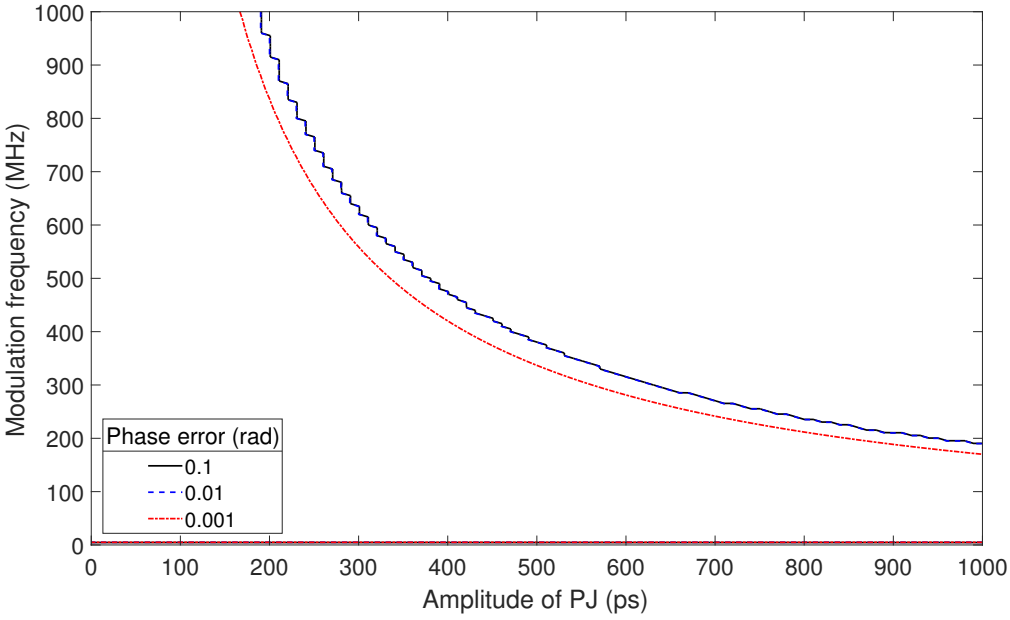

(b)

Figure 7.6: Phase error due to the periodic jitter at the frequency $f_{\mathrm{PJ}} = 4.9261$ MHz with various modulation frequencies against various jitter amplitudes by the analytical model with order $m, n = -40{:}40$ in Equation 7.55, for ToF phase shifts: (a) $\phi = \pi/6$ and (b) $\phi = \pi/3$, when $T = 0.1$ ms.

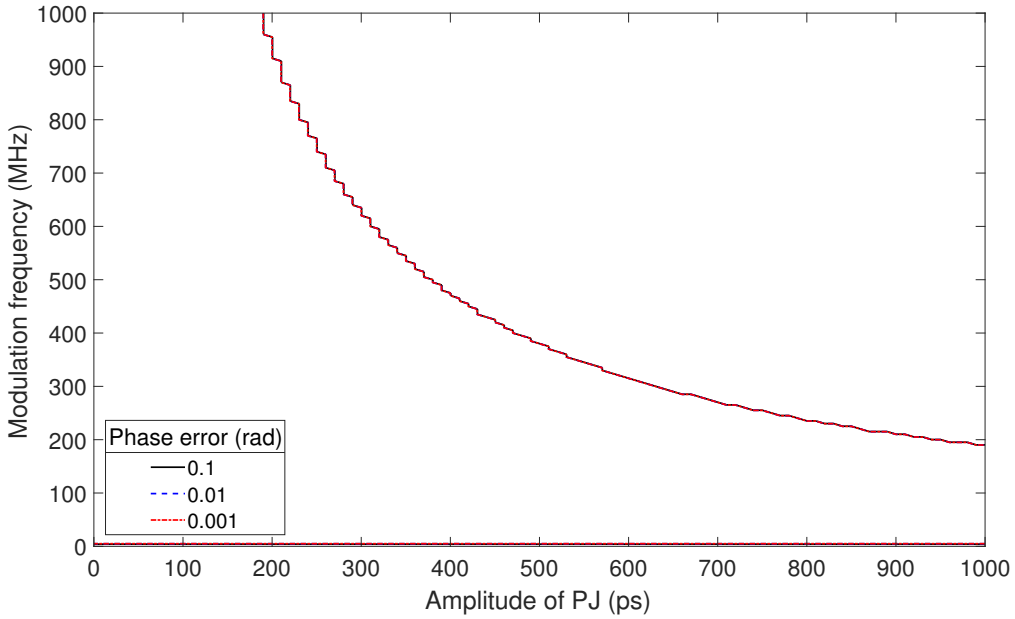

(a)

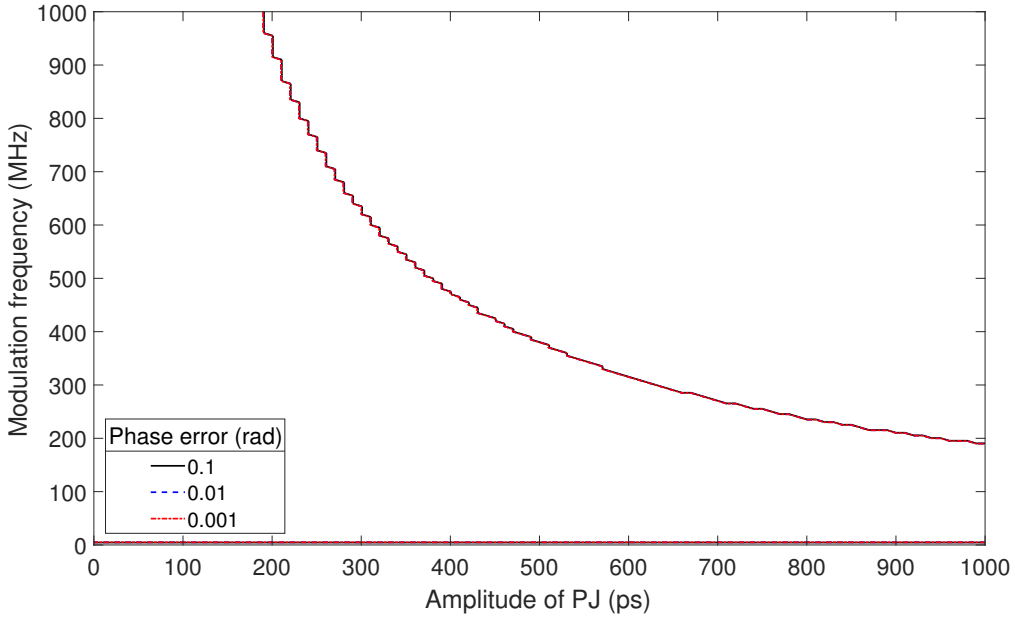

(b)

Figure 7.7: Phase error due to the periodic jitter at the frequency $f_{\mathrm{PJ}} = 4.9261$ MHz with various modulation frequencies against various jitter amplitudes by the analytical model with order $m, n = -40{:}40$ in Equation 7.55, for ToF phase shifts: (a) $\phi = \pi/6$ and (b) $\phi = \pi/3$, when $T = 1$ ms.

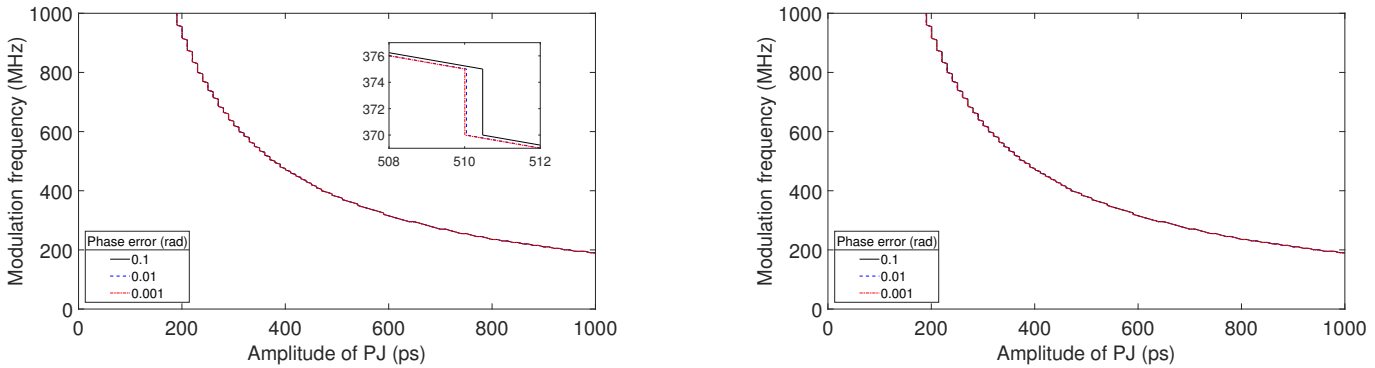

(a)

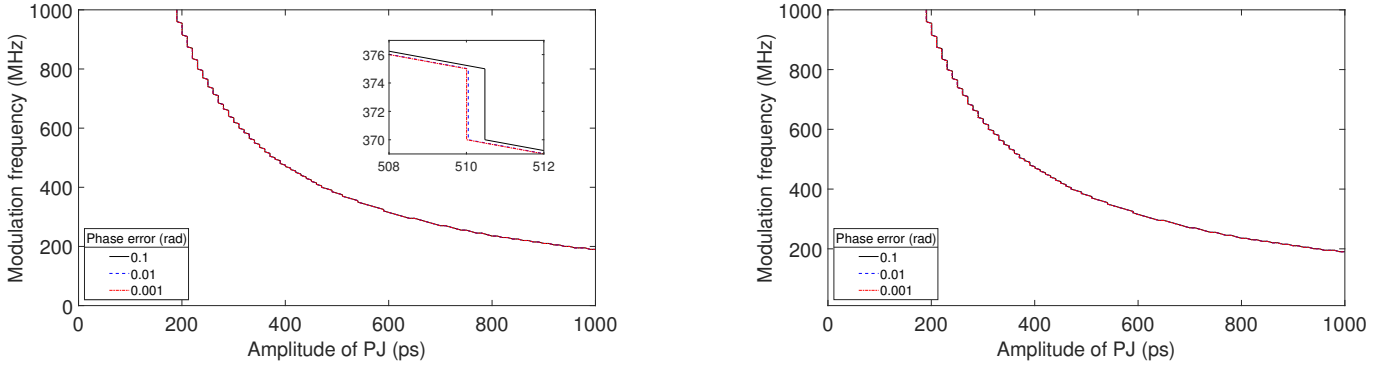

(b)

Figure 7.8: Phase error due to the PJ at the frequency $f_{\mathrm{PJ}} = 4.9261$ MHz for various modulation frequencies against various jitter amplitudes by two numerical approaches: (a) trapezoidal integration with 21000 intervals in Equation 7.41 and (b) Romberg integration with $2^{19} = 524288$ panels in Equation 7.43, for ToF phase shifts: (left) $\phi = \pi/6$ and (right) $\phi = \pi/3$, when $T = 0.01$ ms.

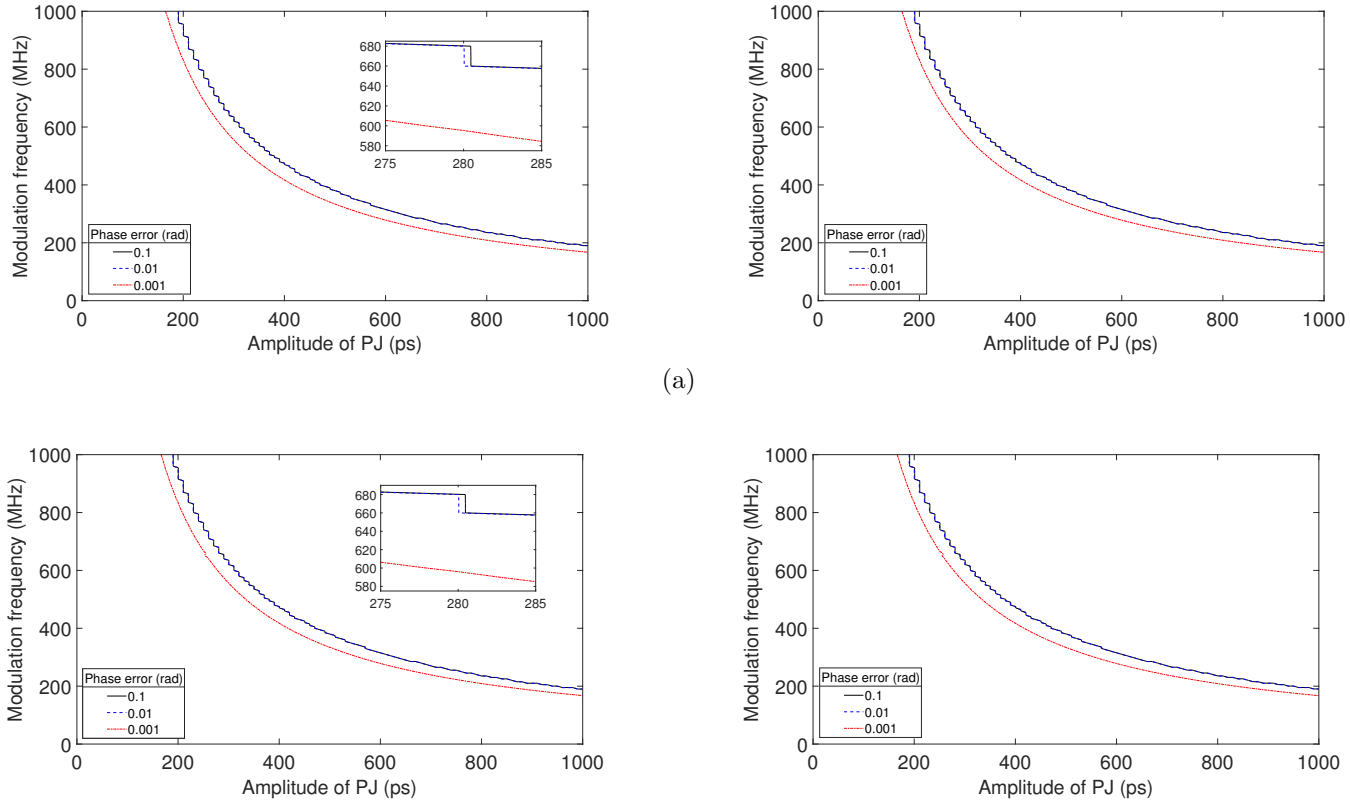

Figure 7.9: Phase error due to the PJ at the frequency $f_{\mathrm{PJ}} = 4.9261$ MHz for various modulation frequencies against various jitter amplitudes by two numerical approaches: (a) trapezoidal integration with 220000 intervals in Equation 7.41 and (b) Romberg integration with $2^{19} = 524288$ panels in Equation 7.43, for ToF phase shifts: (left) $\phi = \pi/6$ and (right) $\phi = \pi/3$, when $T = 0.1$ ms.

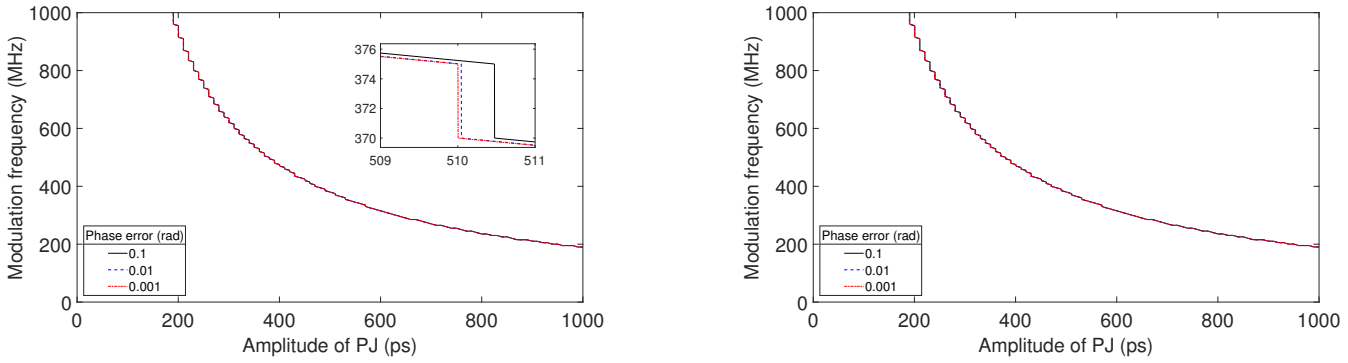

(a)

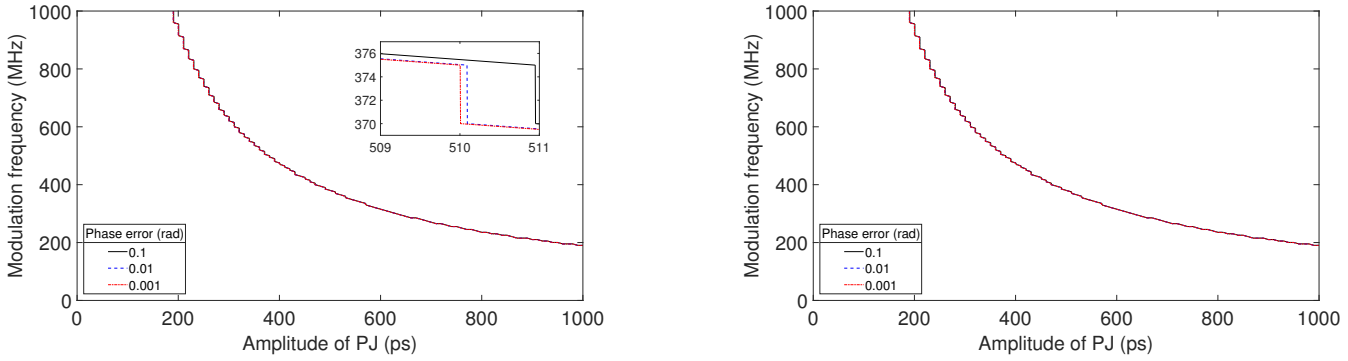

(b)

Figure 7.10: Phase error due to the PJ at the frequency $f_{\mathrm{PJ}} = 4.9261$ MHz for various modulation frequencies against various jitter amplitudes by two numerical approaches: (a) trapezoidal integration with 220000 intervals in Equation 7.41 and (b) Romberg integration with $2^{19} = 524288$ panels in Equation 7.43, for ToF phase shifts: (left) $\phi = \pi/6$ and (right) $\phi = \pi/3$, when $T = 1$ ms.

In addition, Figures 7.8, 7.9 and 7.10 show the corresponding contour diagrams of the phase error for the two ToF phase shifts $\phi = \pi/6$ and $\phi = \pi/3$ when the integration periods $T = 0.01$, 0.1 and 1 ms, respectively, from the two numerical approaches, the trapezoidal and Romberg integrations, separately. For the trapezoidal integration, the number of intervals $Q = \{21000, 220000, 220000\}$ are sufficient in Equation 7.41 for the integration periods $T = \{0.01, 0.1, 1\}$ ms, respectively, while for the Romberg integration, the matrix in Equation 7.43 is truncated to the size of $M \times M = 20$ by 20 (i.e., 2^{19} = 524288 panels) for each integration period. By comparison the sub figures in Figures 7.8, 7.9 and 7.10, the corresponding curves from both numerical integrations are given approximately similar results for each integration period (the difference is dificult to see in the graphs by eye). However, for the phase error $\phi_{\text{err}} = 0.001$ rad is more deviated when the $T = 0.1$ ms (see Figure 7.9) than the other two periods (see Figures 7.8 and 7.10) and these situations are matched with the corresponding analytical results (see Figure 7.6).

The results demonstrate the analytical and numerical approaches give very similar results. However, from the analytical approach, it is seen the phase error curves around 5 MHz modulation frequency for each integration period (see Figures 7.5 – 7.7), but in numerical approach those curves are not visible.

7.6.2 Jitter Frequency as a Factor of Modulation Frequency

Now the above analysis is repeated when the f_{PJ} is a factor of the modulation frequency by selecting $f_{\text{PJ}} = 5$ MHz in the model. Tables 7.5 and 7.6 show the corresponding phase error with fifteen significant digits due to periodic jitter at an arbitrary chosen of the frequency $f_{\text{PJ}} = 5$ MHz, for a selected ToF phase shift (i.e., $\phi = \pi/6$) with different order values of the Bessel function with two integration periods $T = 0.01$ and 1 ms, respectively. As before, the maximum argument $\beta = 2\pi$ for the Bessel function with the parameters chosen (f = 1000 MHz and $A_{\text{PJ}} = 1000$ ps) is located at the twenty first row of each table.

Table 7.5: Calculated maximum phase error (worst) with five different order n of Bessel functions: $f = 1000$ MHz, $\phi = \pi/6$, $f_{\mathrm{PJ}} = 5$ MHz, $A_{\mathrm{PJ}} = 1000$ ps, $\beta = (0 : \pi/10 : 2.5\pi)$ and $T = 0.01$ ms in Equation 7.55

#	β	$n = 10$	$n = 20$	$n = 30$	$n = 40$	$n = 50$
1	0	0.0000000000000001	0.0000000000000001	0.0000000000000001	0.0000000000000001	0.0000000000000001
2	0.3142	0.0000000000000001	0.0000000000000001	0.0000000000000001	0.0000000000000001	0.0000000000000001
3	0.6283	0.0000000000000001	0.0000000000000001	0.0000000000000001	0.0000000000000001	0.0000000000000001
4	0.9425	0.0000000000000003	0.0000000000000003	0.0000000000000003	0.0000000000000003	0.0000000000000003
5	1.2566	0.0000000000000041	0.0000000000000041	0.0000000000000041	0.0000000000000041	0.0000000000000041
6	1.5708	0.0000000000000013	0.0000000000000013	0.0000000000000013	0.0000000000000013	0.0000000000000013
7	1.8850	0.0000000000000006	0.0000000000000006	0.0000000000000006	0.0000000000000006	0.0000000000000006
8	2.1991	0.0000000000000013	0.0000000000000013	0.0000000000000013	0.0000000000000013	0.0000000000000013
9	2.5133	0.0000000000000004	0.0000000000000007	0.0000000000000007	0.0000000000000007	0.0000000000000007
10	2.8274	0.0000000000000208	0.0000000000000219	0.0000000000000219	0.0000000000000219	0.0000000000000219
11	3.1416	0.0000000000000017	0.0000000000000017	0.0000000000000017	0.0000000000000017	0.0000000000000017
12	3.4558	0.0000000000000109	0.0000000000000113	0.0000000000000113	0.0000000000000113	0.0000000000000113
13	3.7699	0.0000000000000011	0.0000000000000011	0.0000000000000011	0.0000000000000011	0.0000000000000011
14	4.0841	0.0000000000000019	0.0000000000000018	0.0000000000000018	0.0000000000000018	0.0000000000000018
15	4.3982	0.0000000000000036	0.0000000000000039	0.0000000000000039	0.0000000000000039	0.0000000000000039
16	4.7124	0.0000000000000097	0.0000000000000093	0.0000000000000093	0.0000000000000093	0.0000000000000093
17	5.0265	0.0000000000000009	0.0000000000000009	0.0000000000000009	0.0000000000000009	0.0000000000000009
18	5.3407	0.0000000000000022	0.0000000000000021	0.0000000000000021	0.0000000000000021	0.0000000000000021
19	5.6549	0.0000000000000010	0.0000000000000010	0.0000000000000010	0.0000000000000010	0.0000000000000010
20	5.9690	0.0000000000000039	0.0000000000000038	0.0000000000000038	0.0000000000000038	0.0000000000000038
21	6.2832	0.0000000000000016	0.0000000000000016	0.0000000000000016	0.0000000000000016	0.0000000000000016
22	6.5973	0.0000000000000059	0.0000000000000063	0.0000000000000063	0.0000000000000063	0.0000000000000063
23	6.9115	0.0000000000000413	0.0000000000000266	0.0000000000000286	0.0000000000000286	0.0000000000000286
24	7.2257	0.0000000000000020	0.0000000000000022	0.0000000000000020	0.0000000000000020	0.0000000000000020
25	7.5398	0.0000000000002510	0.0000000000001795	0.0000000000001836	0.0000000000001836	0.0000000000001836
26	7.8540	0.0000000000000046	0.0000000000000049	0.0000000000000047	0.0000000000000047	0.0000000000000047

Table 7.6: Calculated maximum phase error (worst) with five different order n of Bessel functions: $f = 1000$ MHz, $\phi = \pi/6$, $f_{\mathrm{PJ}} = 5$ MHz, $A_{\mathrm{PJ}} = 1000$ ps, $\beta = (0 : \pi/10 : 2.5\pi)$ and $T = 1$ ms in Equation 7.55

#	β	$n = 10$	$n = 20$	$n = 30$	$n = 40$	$n = 50$
1	0	0.0000000000000001	0.0000000000000001	0.0000000000000001	0.0000000000000001	0.0000000000000001
2	0.3142	0.0000000000000001	0.0000000000000001	0.0000000000000001	0.0000000000000001	0.0000000000000001
3	0.6283	0.0000000000000000	0.0000000000000000	0.0000000000000000	0.0000000000000000	0.0000000000000000
4	0.9425	0.0000000000000003	0.0000000000000003	0.0000000000000003	0.0000000000000003	0.0000000000000003
5	1.2566	0.0000000000000010	0.0000000000000010	0.0000000000000010	0.0000000000000010	0.0000000000000010
6	1.5708	0.0000000000000002	0.0000000000000002	0.0000000000000002	0.0000000000000002	0.0000000000000002
7	1.8850	0.0000000000000004	0.0000000000000003	0.0000000000000003	0.0000000000000003	0.0000000000000003
8	2.1991	0.0000000000000007	0.0000000000000008	0.0000000000000008	0.0000000000000008	0.0000000000000008
9	2.5133	0.0000000000000001	0.0000000000000001	0.0000000000000001	0.0000000000000001	0.0000000000000001
10	2.8274	0.0000000000000066	0.0000000000000068	0.0000000000000068	0.0000000000000068	0.0000000000000068
11	3.1416	0.0000000000000012	0.0000000000000011	0.0000000000000011	0.0000000000000011	0.0000000000000011
12	3.4558	0.0000000000000042	0.0000000000000026	0.0000000000000026	0.0000000000000026	0.0000000000000026
13	3.7699	0.0000000000000021	0.0000000000000019	0.0000000000000019	0.0000000000000019	0.0000000000000019
14	4.0841	0.0000000000000019	0.0000000000000019	0.0000000000000019	0.0000000000000019	0.0000000000000019
15	4.3982	0.0000000000000029	0.0000000000000030	0.0000000000000030	0.0000000000000030	0.0000000000000030
16	4.7124	0.0000000000000069	0.0000000000000069	0.0000000000000069	0.0000000000000069	0.0000000000000069
17	5.0265	0.0000000000000026	0.0000000000000027	0.0000000000000027	0.0000000000000027	0.0000000000000027
18	5.3407	0.0000000000000022	0.0000000000000023	0.0000000000000023	0.0000000000000023	0.0000000000000023
19	5.6549	0.0000000000000057	0.0000000000000059	0.0000000000000059	0.0000000000000059	0.0000000000000059
20	5.9690	0.0000000000000037	0.0000000000000033	0.0000000000000033	0.0000000000000033	0.0000000000000033
21	6.2832	0.0000000000000246	0.0000000000000220	0.0000000000000220	0.0000000000000220	0.0000000000000220
22	6.5973	0.0000000000000104	0.0000000000000105	0.0000000000000105	0.0000000000000105	0.0000000000000105
23	6.9115	0.0000000000000017	0.0000000000000017	0.0000000000000017	0.0000000000000017	0.0000000000000017
24	7.2257	0.0000000000000042	0.0000000000000039	0.0000000000000060	0.0000000000000060	0.0000000000000060
25	7.5398	0.0000000000001632	0.0000000000001165	0.0000000000001205	0.0000000000001205	0.0000000000001205
26	7.8540	0.0000000000000026	0.0000000000000028	0.0000000000000026	0.0000000000000026	0.0000000000000026

The precision level of seventeen significant digits for each order n is indicated by the thick border line. Then, it is clear that even $n = 30$ is good enough to obtain the seventeen significant digits, but for safely, we choose the order of the Bessel function to be 40 which summed up the 6561 terms in Equation 7.55. As before, let us consider the behaviour of the phase error due to the PJ at $f_{\mathrm{PJ}} = 5$ MHz for a single ToF phase shift. Figure 7.11 shows the corresponding phase error for the ToF phase shift $\phi = \pi/6$ when the modulation frequency of $f = 30$ and 1000 MHz, for the range of argument $\beta = 0$ to 0.7 with three integration periods in Equation 7.55, separately. By comparison with the results when $f_{\mathrm{PJ}} = 4.9261$ MHz (see Figure 7.3), it is clear that these two sub plots in Figure 7.11 are given relatively less amounts of phase errors at each corresponding integration period. As an example, the relevant phase errors for $f = 1000$ MHz with three $T = 0.01$, 0.1 and 1 ms, when the periodic jitter at $f_{\mathrm{PJ}} = 4.9261$ and 5 MHz, respectively, are in the ranges of $\phi_{\mathrm{err}} = \{10^{-3}, 10^{-4}, 10^{-5}\}$ and $\{10^{-4}, 10^{-4}, 10^{-6}\}$ rad, for the chosen maximum argument $\beta = 0.7$.

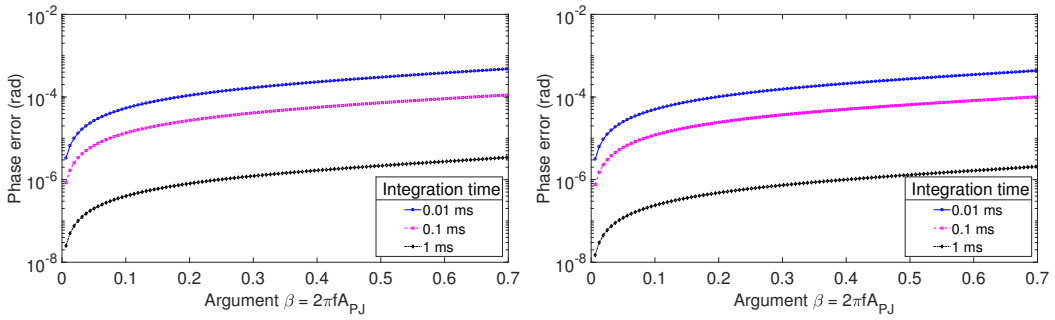

Figure 7.11: Phase error for the ToF phase shift $\phi = 0$ due to the periodic jitter at $f_{\mathrm{PJ}} = 5$ MHz, when the modulation frequency (a) $f = 30$ MHz and (b) $f = 1000$ MHz, for the three integration periods with $m, n = -40{:}40$ each using the analytical model in Equation 7.55.

Now, the evaluation is performed with the various parameters in the system. Figure 7.12 shows the maximum phase error (worst) due to the periodic jitter at the frequency $f_{\mathrm{PJ}} = 5$ MHz for the same six ToF phase shifts ϕ, separately, for the three integration periods with the values from 0 to 0.2 of the argument β for each evaluation. With the maximum argument chosen for $\beta = 0.2011$ with the integration periods $T = 0.01$, 0.1 and 1 ms, the phase errors are approximately in the ranges of $(0.96 - 1.09)\times10^{-4}$, $(1.50 - 2.73)\times10^{-5}$, and $(0.70 - 0.81)\times10^{-6}$ rad, respectively.

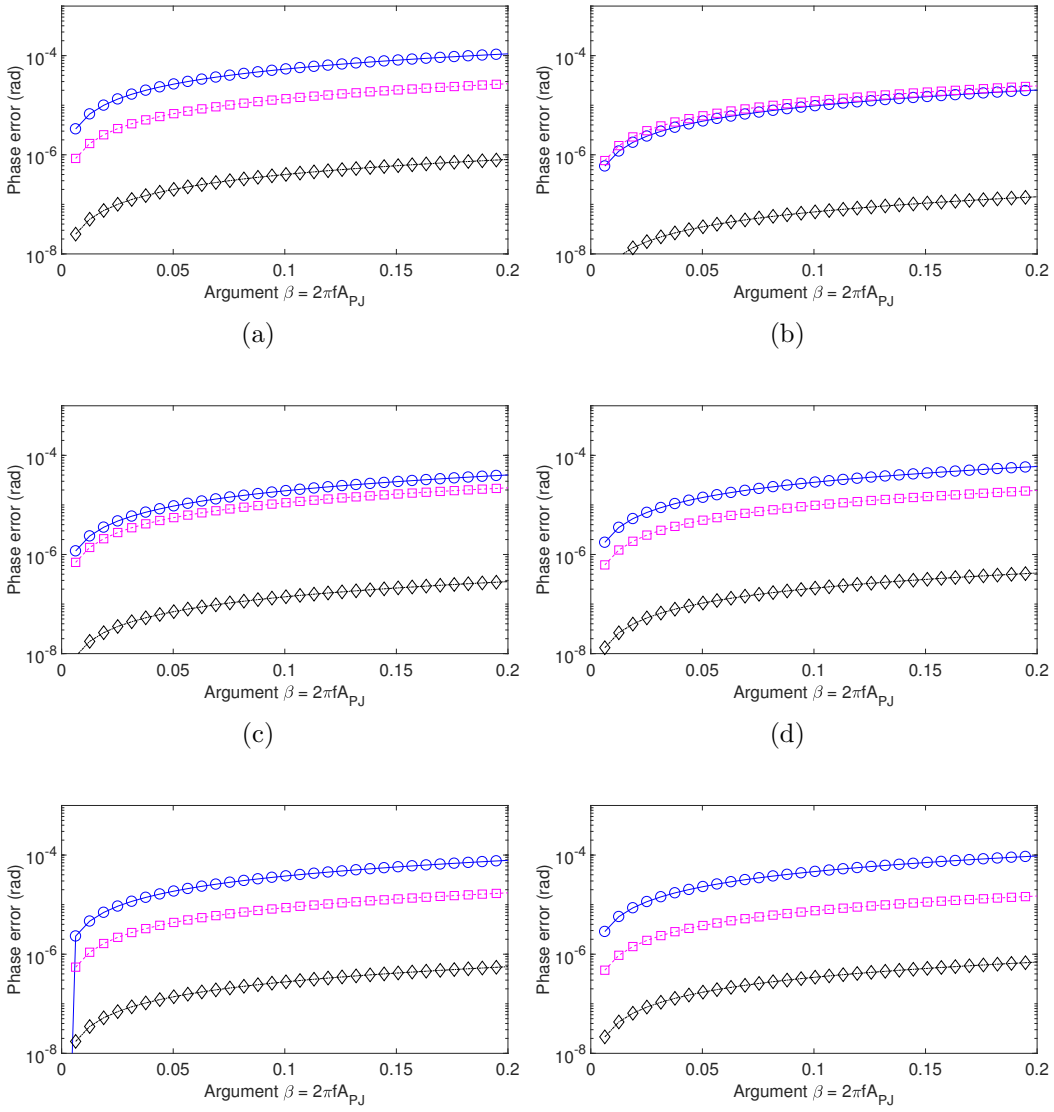

Figure 7.12: Phase error (a) to (f) for the ToF phase shift $\phi = 0$ to $5\pi/6$ by $\pi/6$ steps, respectively, due to the PJ at $f_{\text{PJ}} = 5$ MHz, when $f = 30$ MHz for the integration periods: 0.01 ms (—o—), 0.1 ms (—□—) and 1 ms (—◇—) with $m, n = -40{:}40$ each using the analytical model in Equation 7.55.

By comparison with the phase errors when $f_{\text{PJ}} = 4.9261$ MHz (see Figures 7.4 and 7.12), these are extremely small (less than a microradian) when $T = 1$ ms (among these three integration periods), which is more insignificant to depth measurements. It is clear that the phase error increases when the T decreases. That is, the frame rates of the camera increases. Furthermore, for both fixed T and β, the phase error decreases when the ToF phase shift increases. For examples, with $\beta = 0.1005$ and $T = 0.01$ ms, the phase errors

are $\phi_{\text{err}} = 9.71$, 28.72 and 46.55 microradians when $\phi = \pi/6, \pi/2$ and $5\pi/6$, respectively.

Next, Figures 7.13 – 7.15 show contour diagrams for the aforementioned phase error against the f and A_{PJ} when the frequency $f_{\text{PJ}} = 5$ MHz with three integration periods $T = 0.01$, 0.1 and 1 ms, respectively, for $\phi = \pi/6$ and $\pi/3$ separately, by the analytical model in Equation 7.55. From the three figures, it can be verified the corresponding phase errors are given the similar results for each integration period. In addition, as in Section 7.6.1, the three phase error curves around 5 MHz modulation frequency are visible in each analytical result. If we compare these three figures with the results when f_{PJ} is a non factor of f (see Figures 7.5 – 7.7, respectively), in here, all three phase errors are almost aligned with each other when $T = 0.1$ ms (see Figure 7.14), but it is not same in Figure 7.6.

Now, let us consider the results from the two numerical approaches. Figures 7.16 – 7.18 show the corresponding contour diagrams for the phase error when the integration periods $T = 0.01$, 0.1 and 1 ms, respectively, by using trapezoidal and Romberg integrations, separately. Here, for each T, same number of intervals $Q = 3000$ in Equation 7.41 and same number of panels $2^{M-1} = 2^{17} = 131072$ panels in Equation 7.43 are well sufficient while they were different and relatively large in trapezoidal integration when the $f_{\text{PJ}} = 4.9261$ MHz. However, in here, for the Romberg integration, one-fourth of the number of panels when $f_{\text{PJ}} = 4.9261$ MHz, was well sufficient (i.e., $2^{17} : 2^{19}$) for each T. As before, in each case, both numerical approaches are given similar results for different T as well as for all three phase errors ϕ_{err}. However, they were different for $T = 0.1$ ms than other two periods when $f_{\text{PJ}} = 4.9261$ MHz (see Figure 7.9).

By comparison the results among the two numerical approaches (compare each (a) and (b) of Figures 7.16 – 7.18), the corresponding curves from both numerical integrations are given almost similar results (the difference is unseen to the naked eye). Now, by comparing the results of the two approaches, as before, the numerical methods also given the same corresponding analytical results for each chosen integration period as shown in Figures 7.13 – 7.15. Thus, again, we can verify the correctness of our developed analytical model.

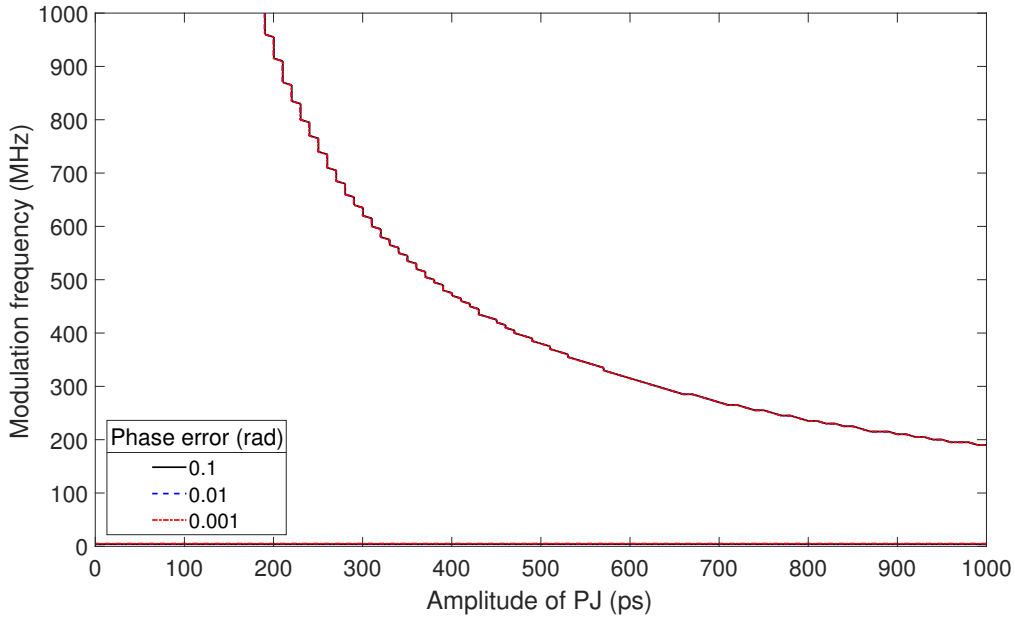

(a)

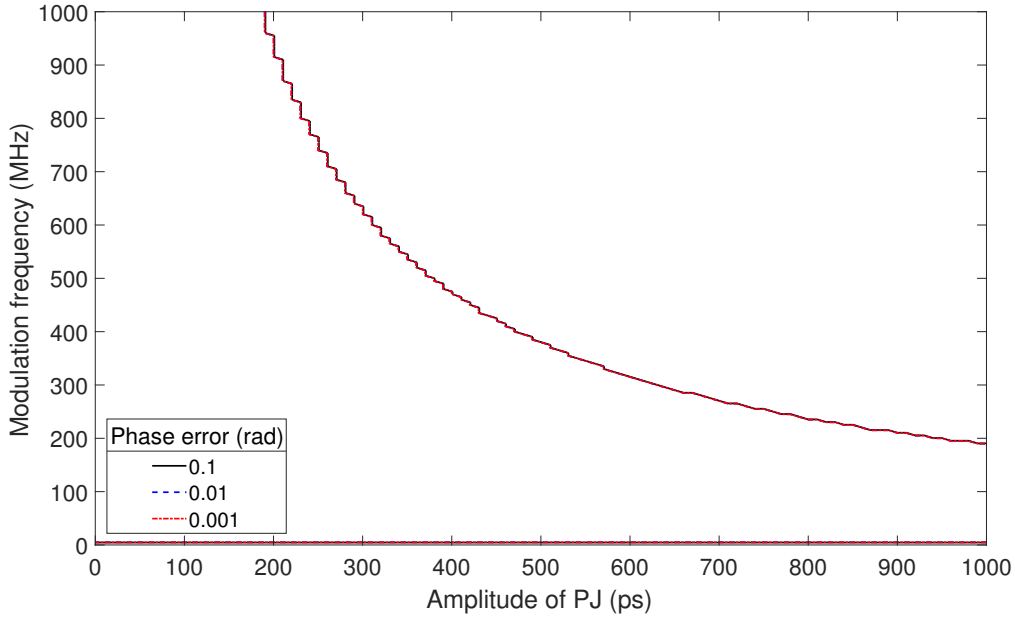

(b)

Figure 7.13: Phase error due to the PJ at the frequency $f_{\mathrm{PJ}} = 5$ MHz with various modulation frequencies against various jitter amplitudes by the analytical model with order $m, n = -40{:}40$ in Equation 7.55, for ToF phase shifts: (a) $\phi = \pi/6$ and (b) $\phi = \pi/3$, when the integration period $T = 0.01$ ms.

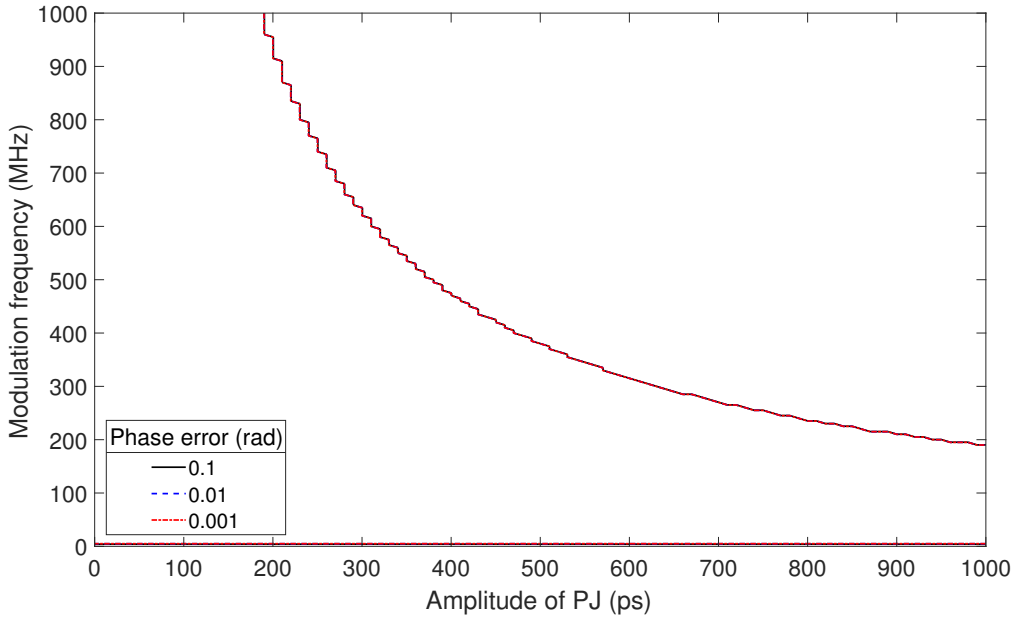

(a)

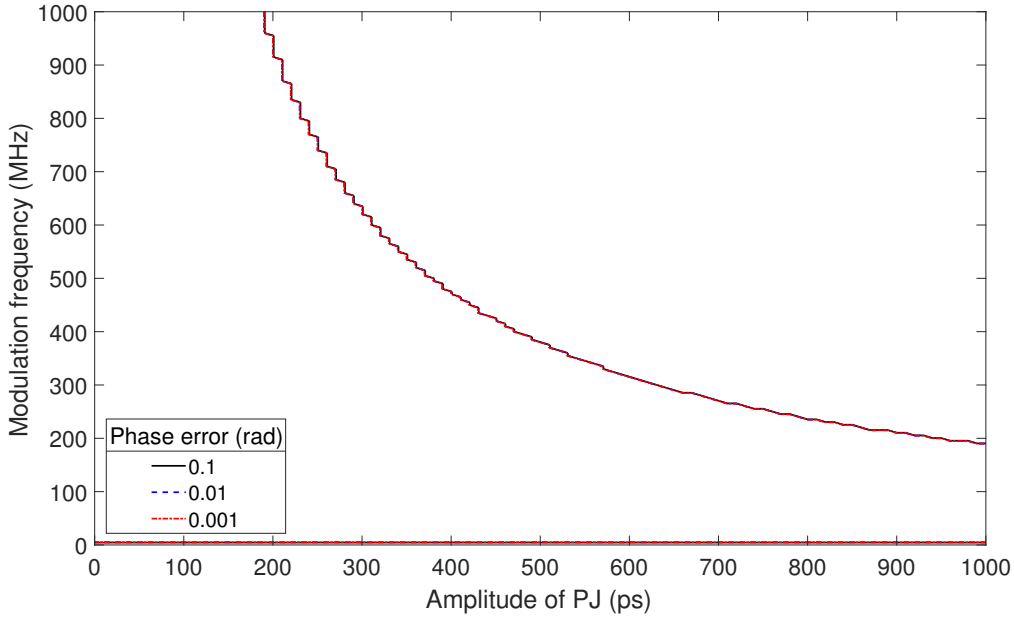

(b)

Figure 7.14: Phase error due to the PJ at the frequency $f_{\mathrm{PJ}} = 5$ MHz with various modulation frequencies against various jitter amplitudes by the analytical model with order $m, n = -40{:}40$ in Equation 7.55, for ToF phase shifts: (a) $\phi = \pi/6$ and (b) $\phi = \pi/3$, when the integration period $T = 0.1$ ms.

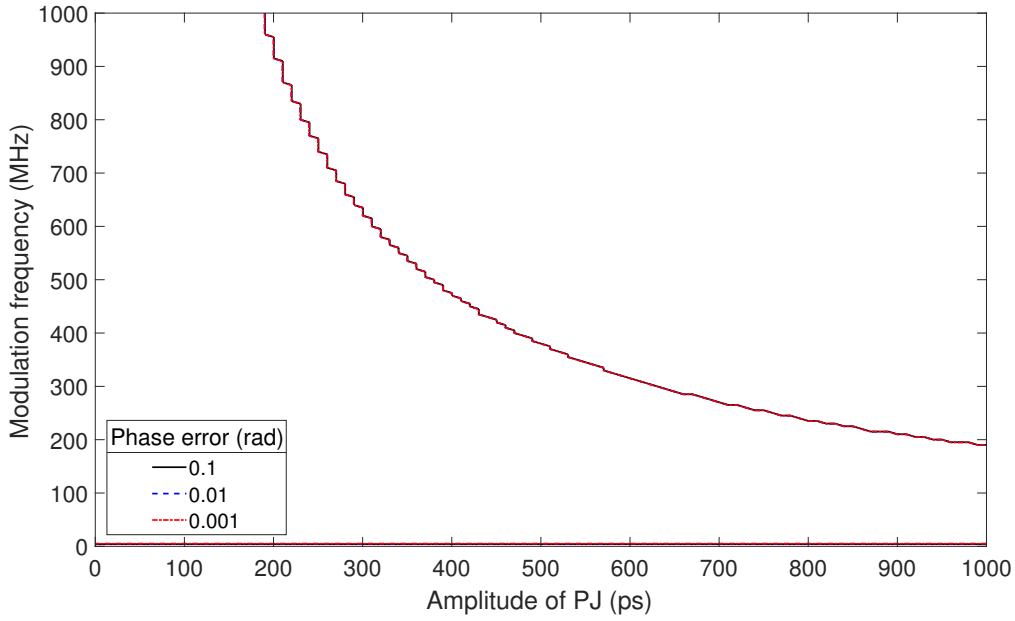

(a)

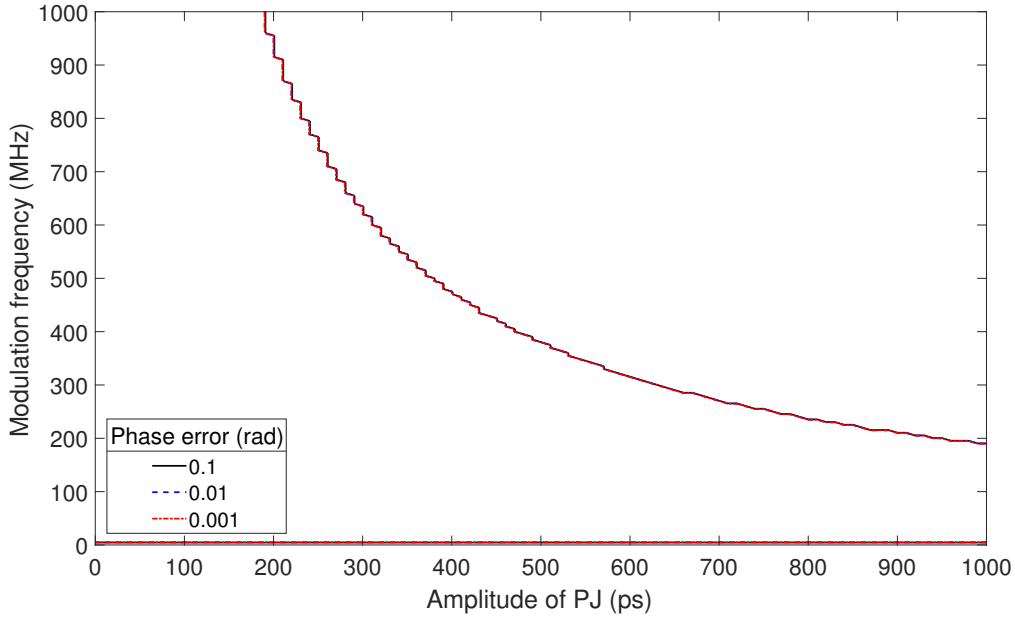

(b)

Figure 7.15: Phase error due to the PJ at the frequency $f_{\mathrm{PJ}} = 5$ MHz with various modulation frequencies against various jitter amplitudes by the analytical model with order $m, n = -40{:}40$ in Equation 7.55, for ToF phase shifts: (a) $\phi = \pi/6$ and (b) $\phi = \pi/3$, when $T = 1$ ms.

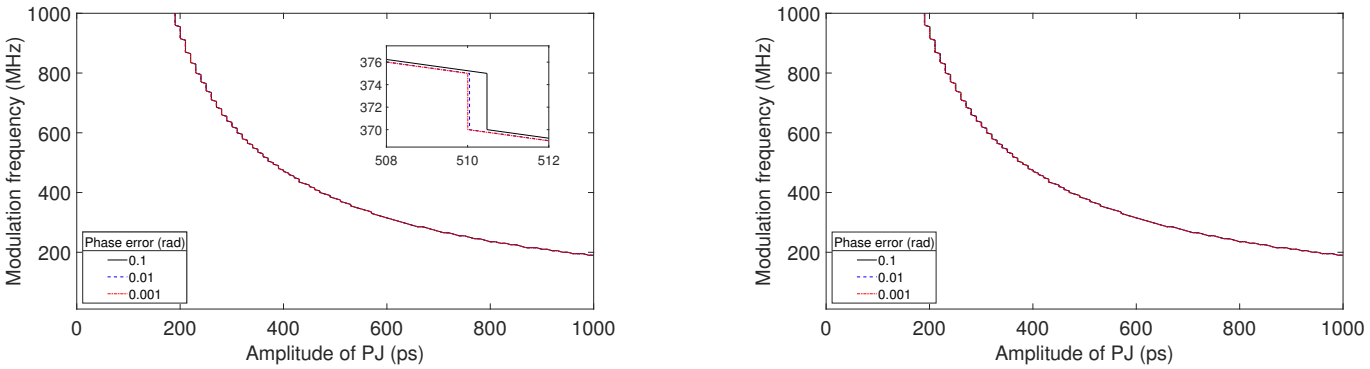

(a)

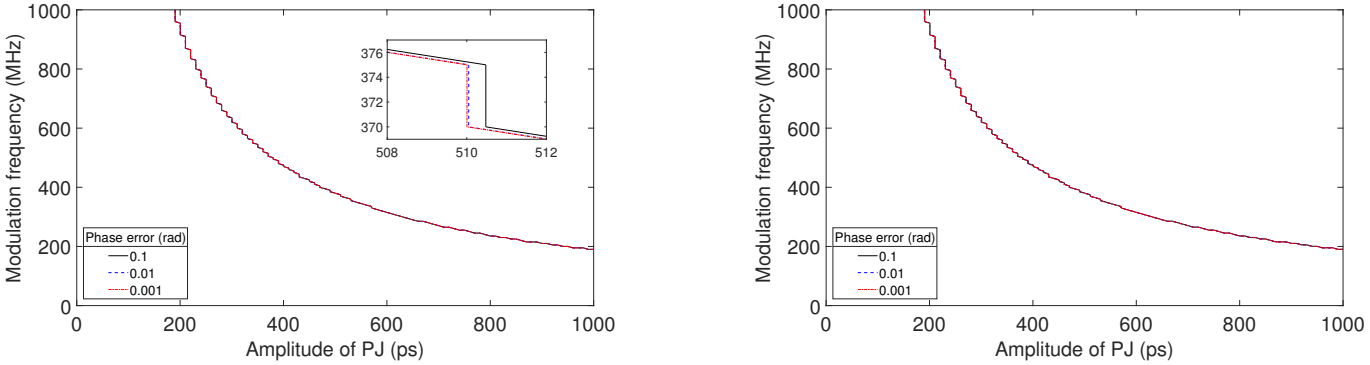

(b)

Figure 7.16: Phase error due to the PJ at frequency $f_{\mathrm{PJ}} = 5$ MHz with various modulation frequencies against various jitter amplitudes by two numerical approaches: (a) trapezoidal integration with 3000 intervals in Equation 7.41 and (b) Romberg integration with $2^{17} = 131072$ panels in Equation 7.43, for ToF phase shifts: (left) $\phi = \pi/6$ and (right) $\phi = \pi/3$, when $T = 0.01$ ms.

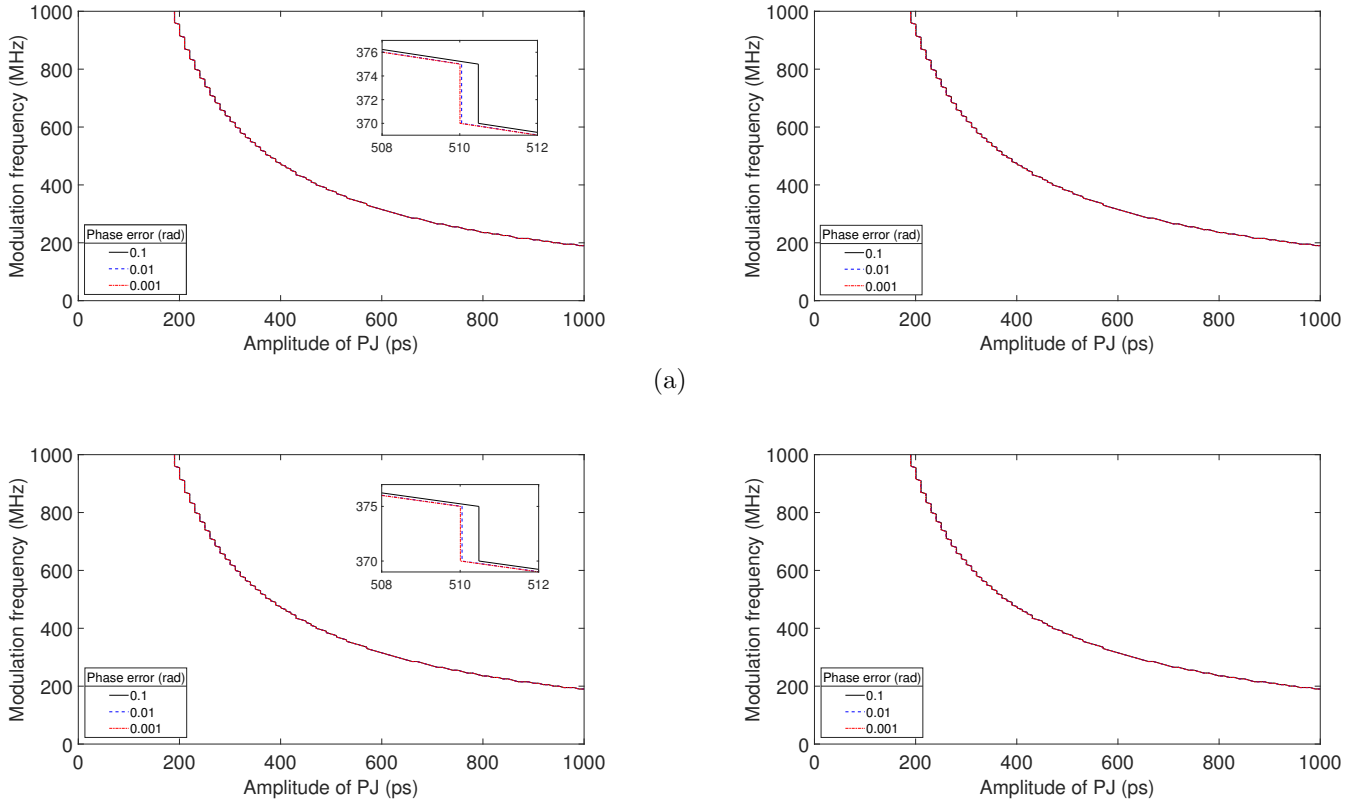

Figure 7.17: Phase error due to the PJ at frequency $f_{\mathrm{PJ}} = 5$ MHz with various modulation frequencies against various jitter amplitudes by two numerical approaches: (a) trapezoidal integration with 3000 intervals in Equation 7.41 and (b) Romberg integration with $2^{17} = 131072$ panels in Equation 7.43, for ToF phase shifts: (left) $\phi = \pi/6$ and (right) $\phi = \pi/3$, when $T = 0.1$ ms.

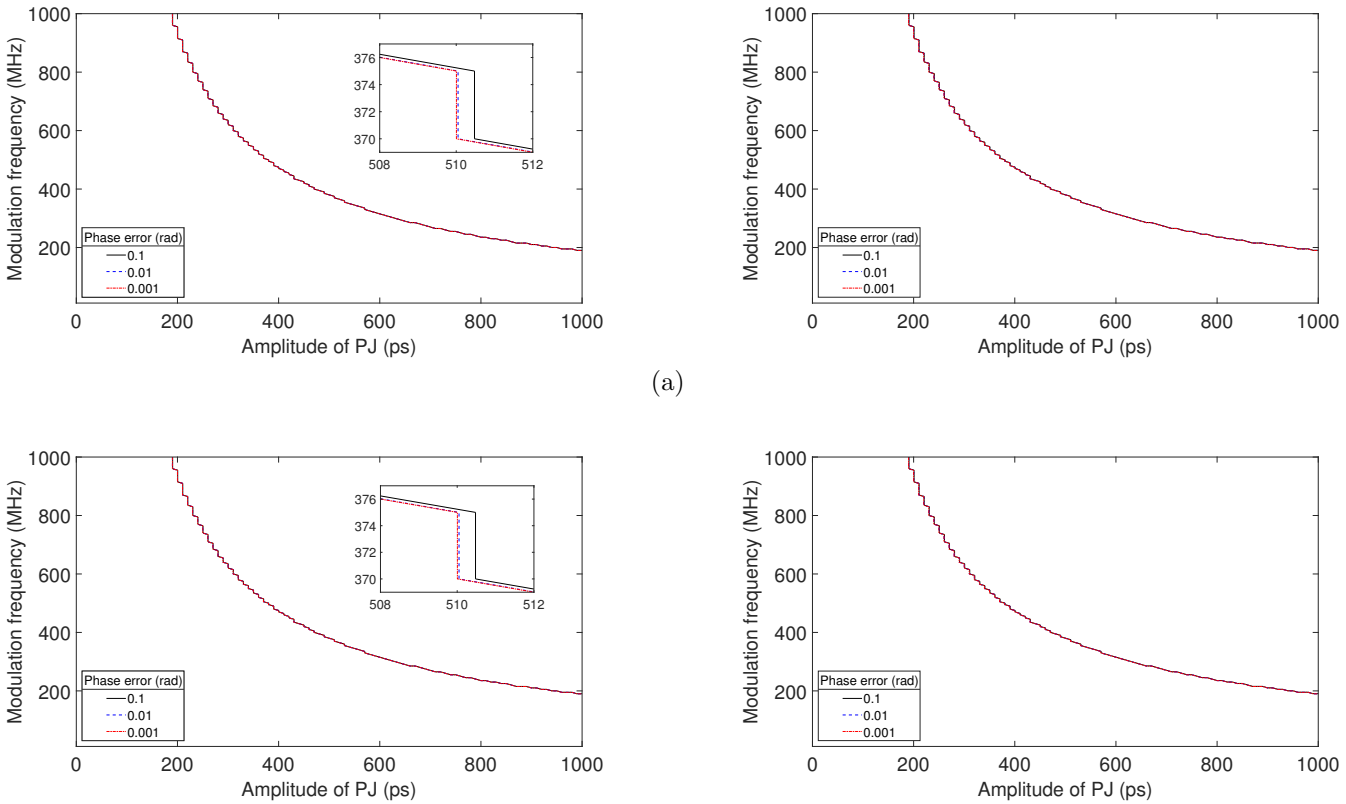

Figure 7.18: Phase error due to the PJ at frequency $f_{\mathrm{PJ}} = 5$ MHz with various modulation frequencies against various jitter amplitudes by two numerical approaches: (a) trapezoidal integration with 3000 intervals in Equation 7.41 and (b) Romberg integration with $2^{17} = 131072$ panels in Equation 7.43, for ToF phase shifts: (left) $\phi = \pi/6$ and (right) $\phi = \pi/3$, when $T = 1$ ms.

7.6.3 Execution Time for the Simulation

Table 7.7 shows the approximate execution time for the corresponding results from analytical and numerical approaches used in this chapter. For each result, the corresponding model is performed four times with their parameters (since four phase-step computation) for each numerical approach while it is a single step for the analytical model. The average execution time is calculated by taking the mean time among the two phase shifts $\phi = \pi/6$ and $\pi/3$ for each corresponding result of the simulation setup. Note that these amounts (last column) are rounded up to the nearest one decimal place.

All simulation are implemented with MATLAB R2017a, The MathWorks, Inc., and are executed using a desktop computer consisting a Intel Core™ i5-7500 CPU @ 3.40 GHz, 4 Cores with 16.0 GB RAM on 64-bit Windows 10 Enterprise 2016 LTBS, 2016 Microsoft Corporation. In order to minimise the execution time, all cores are used for each simulation.

Table 7.7: Approximate execution time for the simulation setup

f_{PJ} (MHz)	Approach with the parameter used			T (ms)	Average time (in minutes)
4.9261	Analytical model in Equation 7.55, with orders m, n	$-40 \leq \{m, n\} \leq 40$ 6561×2 terms		0.01	443.4
				0.1	599.8
				1.0	523.8
	Trapezoidal model in Equation 7.41, with intervals Q	21000	four times	0.01	84.6
		220000		0.1	369.1
		220000		1.0	271.4
	Romberg model in Equation 7.43, with panels 2^{M-1}	$2^{19} = 524288$		0.01	2279.3
				0.1	2293.2
				1.0	2320.7
5	Analytical model in Equation 7.55, with orders m, n	$-40 \leq \{m, n\} \leq 40$ 6561×2 terms		0.01	514.8
				0.1	644.9
				1.0	530.2
	Trapezoidal model in Equation 7.41, with intervals Q	3000	four times	0.01	97.6
				0.1	108.3
				1.0	110.2
	Romberg model in Equation 7.43, with panels 2^{M-1}	$2^{17} = 131072$		0.01	401.4
				0.1	418.6
				1.0	432.5

As usual, for a greater number of terms, it takes more execution time, i.e., for 2^{19} terms (with four times) in Romberg model, it has taken an average of $\approx$ 2300 minutes while for 3000 terms (with four times) in trapezoidal model has taken an average of 100 minutes. However, the execution time is relatively less at the short integration period $T = 0.01$ ms for all approaches. Note that these average times may slightly change due to the execution of other concurrent processes in the computer.

7.7 Chapter Remarks

The range sensor manufacturing industries are attempting to increase the performance of the cameras and in the near future one expects to see ToF cameras with high modulation frequencies so they are introducing relevant electronic components to build these cameras. As a result of that, it may effect time deviation of the signal generated inside which causes an increase in the jitter in the signals of the camera. At the same time, they are focusing on the accuracy of the camera as well since the accuracy and precision of ToF range cameras are important for many applications. Then, we cannot ignore the effect of the jitter on the range measurement. In this chapter, we proposed an analytical model to clarify the influence of the periodic jitter by using the Fourier analysis on the correlation function of the ToF camera. Even though we presented the influence of the periodic jitter on three phase errors (0.1, 0.01 and 0.001 rad), our model is able to identify the phase error in the range of 0 to 2π rad. Another advantage of our model is the capability of the usage in heterodyne operation in ToF cameras. We chose the range of $\beta = 0$ to 2π which is the product of angular modulation frequency (upto $f_{\mathrm{PJ}} = 1000$ MHz) and the periodic jitter amplitude (upto $A_{\mathrm{PJ}} = 1000$ ps) of the camera.

We proved and found evidence that the phase difference of the periodic jitter between the emitted light and shutter signals of the camera, the modulation frequency, the integration period, the amplitude of the periodic jitter and the relationship of the periodic jitter frequency to the modulation frequency are the parameters that influence the periodic jitter on range measurement. Besides, whether the frequency of the periodic jitter is a factor of the modulation frequency or not, it is caused by different behaviour in the system. However, this influence can be compensated by adjusting the integration period of the camera since this phenomenon also depends on the integration period. When the integration period is $T = 0.01$ ms (the shortest period among the chosen)

then the periodic jitter influences the range measurement for all chosen three phase errors for certain amplitudes of periodic jitter A_{PJ} and modulation frequencies f. When the periodic jitter is a non factor of modulation frequency $f_{\mathrm{PJ}} = 4.9261$ MHz, they are in the range of $[A_{\mathrm{PJ}}, f_{\mathrm{PJ}}]$ = [(200 ps, 1000 MHz) – (1000 ps, 200 MHz)] for the phase errors $\phi_{\mathrm{err}} = 0.01$ and 0.001 rad while for $\phi_{\mathrm{err}} = 0.1$ rad, they are in the range of $[A_{\mathrm{PJ}}, f_{\mathrm{PJ}}]$ = [450 ps, 1000 MHz] to [1000 ps, 450 MHz]. With the increase of the integration period, the corresponding range of the $[A_{\mathrm{PJ}}, f_{\mathrm{PJ}}]$ due to the PJ is systematically increased. This similar behaviour was presented when the $f_{\mathrm{PJ}} = 5$ MHz, but in slightly different amounts. However, in both cases, the starting influence range of the corresponding A_{PJ} and f_{PJ} are similar (i.e., (200 ps, 1000 MHz) – (1000 ps, 200 MHz)) for the phase errors $\phi_{\mathrm{err}} = 0.01$ and 0.001 rad.

At present, AMCW ToF cameras use relatively low modulation frequencies and low frame rates. Therefore, the range measurement is not affected by the PJ from current AMCW ToF cameras such as MESA Imaging SwissRanger 4000 (with 30 MHz) and SoftKinetic DepthSense 325 (with 50 MHz) which we used in the experiments in Chapters 5 and 6. In future, the depth sensor manufacturers increase the resolution range of ToF cameras by using high modulation frequencies and very high frame rates which are the factors that affect integration periods of the cameras. Thus, in order to minimise the influence of the periodic jitter on range measurement, we are recommending when the integration period $T = 0.01$ ms and the modulation frequency of the camera $f = 200$ MHz then amplitude of the PJ is should be $A_{\mathrm{PJ}} < 700$ ps while when $f = 1000$ MHz it should be $A_{\mathrm{PJ}} < 180$ ps. Also, in order to prevent the phase errors of $\phi_{\mathrm{err}} = 0.001$ and 0.01 rad, the parameters should be satisfied when $A_{\mathrm{PJ}} < 400$ ps for $f = 400$ MHz. In addition, these recommended values of A_{PJ} and f should be further reduced when the integration period of the camera is reduced. Thus, the PJ is significantly affected to range measurements apart from the above recommended amounts of the three parameters: the integration period, jitter amplitude and modulation frequency.

Finally, we clearly found that the periodic jitter in the light signals is influenced by the range measurements in AMCW ToF ranging cameras. By referring to Chapters 5 and 6, we concluded by experimenting that the random jitter is relatively larger than the periodic jitter in the illumination signals of two commercial AMCW ToF cameras. So, it is important and more interesting to check whether the random jitter has an influence on the range measurements in AMCW ToF ranging cameras. This is the focus of the next chapter.

Chapter 8

Influence of Random Jitter on Range Measurements

As described in Chapters 5 and 6, random jitter was shown to be relatively larger than the periodic jitter in commercial AMCW ToF range imaging cameras. The random effects have an influence on every stage of the correlation process of the camera and finally on the range measurement as well. This chapter describes a benchmark analytical model based on stochastic calculus to investigate the behaviour of random jitter on range measurements. The model is developed with the help of fundamental statistical concepts and Fourier analysis. It is assumed that the random jitter follows the Gaussian distribution. The model applies for both heterodyne and homodyne operations in the AMCW ToF range imaging cameras. First, a brief introduction of the standard mathematical expressions with the fundamental concepts in statistics for the main theorems is described. Next, the correlation function with random jitter in both the illumination and shutter signals is considered and a stochastic model is developed. The Monte Carlo simulation is used to analyse the model since this is the best technique to understand the impact of possibility and significant uncertainty in the prediction quantitative model due to the intervention of random variables. The simulation is performed by two non-parametric estimations for the simulated data. The various parameters such as modulation frequency f and amount of random jitter σ_{RJ} with fixed integration time are evaluated throughout the simulations. Finally, very interesting results for what corresponding amounts of σ_{RJ} and f that influence range measurements are pointed out. In addition, the uncertainty analysis of the results and execution time for the simulation are examined.

8.1 Notation and Definitions

Random jitter is often modelled as a Gaussian distribution (Li, 2007) and we need the help of some statistical techniques to investigate the influence of the random jitter in AMCW ToF range imaging systems. This section is focused on the standard statistical expressions used in this chapter, namely, the means and variances of a continuous random variable and a linear combination of random variables, the Gaussian probability distribution, the central limit theorem, Monte Carlo method and two types of density estimates for non-parametric variables: the histogram and kernel density estimations. The definitions and some theorems of Fourier transforms described in Section 7.2 are also employed.

8.1.1 Mean and Variance of a Continuous Random Variable

Let X be a continuous random variable, and the expected value of X be given by (Blitzstein and Hwang, 2014)

$$\mathbb{E}[X] \triangleq \int_{-\infty}^{\infty} x f_X(x)\, dx \tag{8.1a}$$

where $f_X(x)$ is the probability density function (PDF) of X. Then, the variance of the variable X is given by

$$\mathbb{V}[X] = \mathbb{E}\left[(X - \mathbb{E}[X])^2\right] = \mathbb{E}[X^2] - (\mathbb{E}[X])^2 \tag{8.1b}$$

where $\mathbb{E}[X^2]$ is the second moment of X (or expectation of X^2) which can be obtained by using the LOTUS theorem (see Appendix B.1.1). The mean and variance of a real constant variable α is (Blitzstein and Hwang, 2014)

$$\mathbb{E}[\alpha] = \alpha, \tag{8.2a}$$

$$\mathbb{V}[\alpha] = 0. \tag{8.2b}$$

8.1.2 Mean and Variance of a Linear Combination of Random Variables

Let $Y = \sum_{k=1}^{K} \alpha_k X_k$ be the linear combination of K independent random variables X_k with α_k the real constants. Then, the mean μ_Y and variance σ_Y^2 of

the linear combination Y is given by (Rohatgi and Saleh, 2015),

$$\mu_Y = \sum_{k=1}^{K} \alpha_k \mu_k, \tag{8.3a}$$

$$\sigma_Y^2 = \sum_{k=1}^{K} \alpha_k^2 \sigma_k^2, \tag{8.3b}$$

where μ_k and σ_k^2 are the mean and variance of the kth random variable X_k.

8.1.3 Gaussian (Normal) Probability Distribution

Random jitter that is not bounded is usefully modelled by a Gaussian (normal) probability distribution. The normal distribution is a probability distribution that associates the random variable X with a cumulative probability (see Appendix B.1.2) and is defined by

$$f_X(x) = \frac{1}{\sigma\sqrt{2\pi}} \exp\left\{ -\frac{1}{2}\left(\frac{x-\mu}{\sigma}\right)^2 \right\}, \tag{8.4}$$

where $x \in X$ with μ and σ^2 are the mean and variance of the variable X, respectively. Figure 8.1 shows a normal distribution with the shaded area in the interval $\mu \pm \sigma$ that contains 68.27% of the distribution.

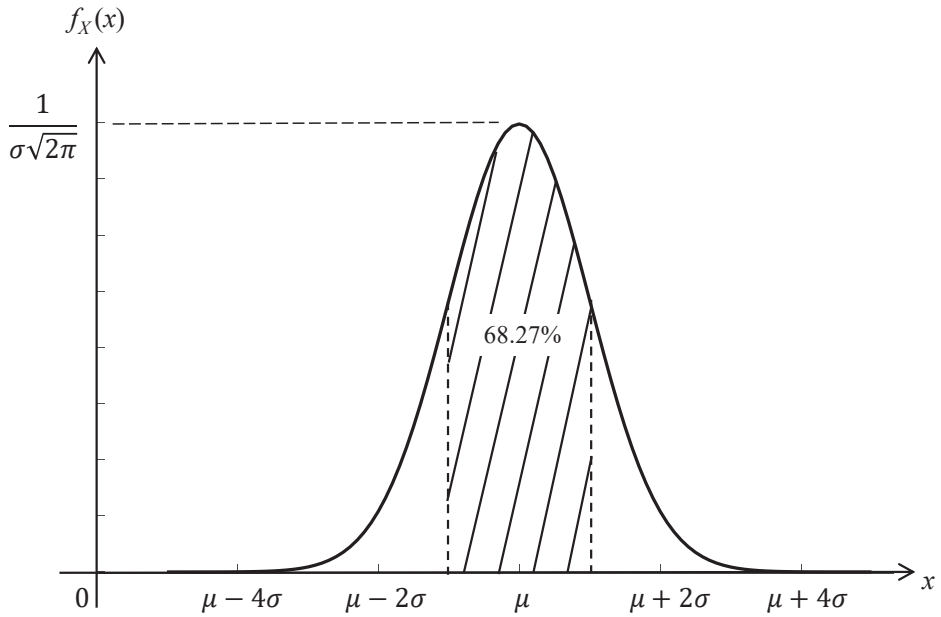

Figure 8.1: The normal distribution with the shaded area of 68.27% from its total, in the interval $\mu \pm \sigma$.

In other words, this figure indicates there is approximately a 68.27% possibility that any particular x falls within one standard deviation of the mean. In addition, the possibilities that x falls within two and three standard deviations of the mean are approximately 95.45% and 99.73%, respectively (see Appendix B.2.2).

8.1.4 Central Limit Theorem

The central limit theorem states that when there are sufficiently large numbers of random samples from the population with mean μ and standard deviation σ, then the distribution of the sample means will be approximately normally (Gaussian) distributed. Therefore, we can use the normal probability model to quantify uncertainty when making inferences about a population mean based on the sample mean $\bar{x}$. Thus, the uncertainty or standard error (SE) of the sample means is defined by (Taylor, 1997)

$$\mathrm{SE}(\bar{x}) = \pm\frac{s}{\sqrt{K}}, \tag{8.5}$$

where s and K are the standard deviation of the samples and the number of samples, respectively.

However, the mean of any finite set of measurements is not to be exactly equal to the actual value of the quantity since the random errors are not likely to perfectly cancel when the number of measurements is relatively small or the distribution is not normal. In that case, the Student's t-factor is introduced to compensate for the uncertainty in s, thus, Equation 8.5 is modified to

$$\mathrm{SE}(\bar{x}) = \pm\, t_{K-1}\frac{s}{\sqrt{K}}, \tag{8.6}$$

where t_{K-1} is a constant called the Student's t-factor for given confidence interval (e.g., 5%, 2%, 1% etc.) with $K-1$ *degrees of freedom*, which can be obtained from standard t distribution (Bennett *et al.*, 1954).

8.1.5 Monte Carlo Method

The Monte Carlo method is a technique used to understand the impact of uncertainty in prediction and forecasting models. These are used to model the probability of different outcomes in a process that cannot easily be predicted due to the intervention of random variables (Robert and Casella, 2013). Monte Carlo simulation (MCS) performs random sampling and conducts a large num-

ber of experiments on the computer, then the statistical characteristics of the experiments are observed, and conclusions on these results are drawn based on the statistical process. Thus, when faced with significant uncertainty in the process of making an estimation, rather than just replacing the uncertain variable with a single average number, the Monte Carlo simulation might prove to be a better solution.

8.1.6 Non-parametric Density Estimates

In order to estimate the density function from the observed data, there are two approaches: parametric and non-parametric estimations. In the parametric approach, the data is drawn from a known distribution while for the other, it is assumed that the distribution has an unknown probability density, then the data are used to estimate its density function. The width of one standard deviation of the probability density function is the corresponding measurement for the parameter. In this chapter, we are focusing on two types of non-parametric density estimations: histogram and kernel density (Silverman, 1998). All estimates of the density function satisfying relatively strong conditions are shown to be biased (Rosenblatt, 1956).

Let $\{x_1, \ldots, x_n\}$ be univariate independent and identically distributed n samples drawn from some distribution with an unknown density function $f(x)$. Let $\widehat{f}(x)$ be an estimate of $f(x)$. Now, let us see how the density function can be estimated from these two methods.

8.1.6.1 Histogram Estimation

Histogram estimation is the most widely used density estimator for the distribution of numerical data. To construct the histogram, both an origin x_0 and width of the bin h are chosen. The bins of the histogram are defined as the intervals $[x_0 + nh, x_0 + (n+1)h)]$ for $n \in \mathbb{Z}^*$. The histogram is then defined by

$$\widehat{f}(x) = \frac{\text{number of } x_j \text{ in the same bin as } x}{nh}, \quad j = 1, \ldots, n \in \mathbb{Z}^+. \tag{8.7}$$

In order to obtain an unbiased estimation of the PDF, the optimal width of the bin can be found by the Freedman-Diaconis rule, given by (Freedman and Diaconis, 1981)

$$h_{opt}^{hist} = 2\,\frac{\text{IQR}}{\sqrt[3]{n}}, \tag{8.8}$$

where IQR is the interquartile range of the data which is calculated by the difference between the third and first interquartile ($Q_3 - Q_1$).

The histogram is an extremely useful class of density estimate, particularly in the univariate case for the presentation and exploration of data. However, the histogram has some drawbacks. As it is not continuous, it is very difficult to find the derivatives. Also, the histogram is not smooth, as the result interpretation depends on the width of the bins and end points of the bins (each of the bins start). The representation of bivariate and trivariate data by histogram is difficult (Silverman, 1998).

8.1.6.2 Kernel Density Estimation

Kernel functions are typically smooth functions with a single mode at $x = 0$. In addition, to remove the dependence on the end points of the bins, kernel estimators centre a kernel function at each data point. Here, it uses a simple technique: to make a prediction for any point x, just sum, for all points x_j in the sample, all the kernel functions of the difference between x_j and x are used. Therefore, the shape of the function $f(x)$ can be formulated by its kernel density estimator, defined by (Silverman, 1998)

$$\widehat{f}(x) = \frac{1}{nh} \sum_{j=1}^{n} \mathcal{K}\left(\frac{x - x_j}{h}\right), \qquad n \in \mathbb{Z}^+ \tag{8.9}$$

where $h > 0$ is the smoothing parameter called the *bandwidth* and $\mathcal{K}(.)$ is the *kernel* function which is non-negative and satisfies the condition,

$$\int_{-\infty}^{\infty} \mathcal{K}(x)\, dx = 1. \tag{8.10}$$

Usually, $\mathcal{K}(.)$ will be a symmetric PDF. There are a range of commonly used kernel functions including Gaussian, uniform, triangular, biweight, triweight and Epanechnikov.

We focus on the Gaussian kernel function. The optimal bandwidth for this function according to Silverman's *rule of thumb* (Silverman, 1998) is

$$h_{opt}^{kde} = \frac{1.06}{\sqrt[5]{n}} \times \min\left(\sigma, \frac{\text{IQR}}{1.34}\right), \tag{8.11}$$

where σ is the sample standard deviation and constant 1.34 is the interquartile range of the standard normal distribution. That is, for the Gaussian data samples, IQR $\approx 1.34\,\sigma$ (Härdle *et al.*, 1991).

8.2 Random Jitter in the Correlation Model

Random jitter is non-deterministic jitter due to random processes and it often follows a Gaussian (normal) distribution $\mathcal{N}$. Therefore, random jitter can be characterised with its root-mean-square (RMS) σ, thus, (Li, 2007)

$$\Delta t = \varepsilon(t) \sim \mathcal{N}(\mu, \sigma^2) \tag{8.12}$$

where $\varepsilon(t)$ is a random process which is a function of time and has a Gaussian distribution $\mathcal{N}$ with mean μ and variance σ^2. For the heterodyne operation in the camera, we use separate Gaussian random processes for light and shutter signals, respectively, namely

$$l(t, \phi) = \cos(2\pi f_l(t + \varepsilon_l(t)) - \phi), \tag{8.13}$$

and

$$s(t, \theta) = \cos(2\pi f_s(t + \varepsilon_s(t)) + \theta), \tag{8.14}$$

where f_l and f_s are the modulation frequencies of the light and shutter signals, respectively. ϕ is the ToF phase shift and θ is the phase-step which is controlled by the camera. The parameters $\varepsilon_l(t) \sim \mathcal{N}(\mu_l, \sigma_l^2)$ and $\varepsilon_s(t) \sim \mathcal{N}(\mu_s, \sigma_s^2)$ are Gaussian random variables for the random jitter in the light and shutter signals, respectively. Note that both signals are assumed to have an unity amplitude with zero offset coefficient due to the background illumination because background offset is not contributed to the correlation model.

Since the camera integrates a frame capture over an integration period of T for a specific phase-step θ, the correlation function $I(\theta)$ with the random jitter is given by

$$I(\theta) = \int_{-T/2}^{T/2} s(t, \theta)\, l(t, \phi)\, dt. \tag{8.15}$$

As before, we take the phase-step θ to be continuous, so by taking the Fourier transform of Equation 8.15 with respect to θ, namely let

$$\widehat{I}(\vartheta) = \mathscr{F}[I(\theta)]_{\theta \to \vartheta} = \int_{-T/2}^{T/2} \mathscr{F}[s(t, \theta)]\, l(t, \phi)\, dt, \tag{8.16}$$

where ϑ is the angular frequency conjugate to θ in units of per radian.

The Fourier transform of the shutter signal can be obtained by application of the Fourier shift theorem (Equation 7.7) and Fourier transform of cosine (Equation 7.18) as

$$\begin{aligned}\mathscr{F}[s(t,\theta)] &= \mathscr{F}\left[\cos\left(2\pi f_s(t+\varepsilon_s(t))+\theta\right)\right]_{\theta\to\vartheta} \\ &= \mathscr{F}\left[\cos\left(\theta+2\pi f_s(t+\varepsilon_s(t))\right)\right]_{\theta\to\vartheta} \\ &= e^{i2\pi(2\pi f_s(t+\varepsilon_s(t)))\vartheta}\mathscr{F}[\cos(\theta)] \\ &= \frac{1}{2}e^{i(2\pi)^2 f_s(t+\varepsilon_s(t))\vartheta}\left[\delta\left(\vartheta-\frac{1}{2\pi}\right)+\delta\left(\vartheta+\frac{1}{2\pi}\right)\right]. \end{aligned} \tag{8.17}$$

Let $\Theta = 2\pi\vartheta$ be the 'frequency' conjugate to θ, and with the scaling property of delta function (Equation 7.11), then Equation 8.17 becomes

$$\mathscr{F}[s(t,\theta)] = \pi e^{i2\pi f_s(t+\varepsilon_s(t))\,\Theta}\left[\delta(\Theta-1)+\delta(\Theta+1)\right] \tag{8.18}$$

Thus Equation 8.16 becomes

$$\begin{aligned}\widehat{I}(\Theta) = \pi\big[\delta(\Theta-1)+\delta(\Theta+1)\big]\int_{-T/2}^{T/2} & e^{i2\pi f_s(t+\varepsilon_s(t))\,\Theta} \\ & \times\cos\left(2\pi f_l(t+\varepsilon_l(t))-\phi\right)dt. \end{aligned} \tag{8.19}$$

Considering the fundamental frequency ($\Theta = 1$) only

$$\widehat{I}(1) = \pi\int_{-T/2}^{T/2} e^{i2\pi f_s(t+\varepsilon_s(t))}\cos\left(2\pi f_l(t+\varepsilon_l(t))-\phi\right)dt. \tag{8.20}$$

Then, the phase error ϕ_{err} of the correlation model obtained in Equation 8.20 can be computed by

$$\phi_{\text{err}} = |\phi| - \left|\angle\left\{\pi\int_{-T/2}^{T/2} e^{i2\pi f_s(t+\varepsilon_s(t))}\cos\left(2\pi f_l(t+\varepsilon_l(t))-\phi\right)dt\right\}\right|. \tag{8.21}$$

Now, by using the non-parametric estimation, a corresponding estimator (mean or variance) for the parameter ϕ_{err} can be obtained. In here, the variance σ^2 (or standard deviation σ) is more important since the mean μ of the parameter can be controlled with an offset adjustment in the system. Thus, the standard deviation of the phase error $\sigma_{\phi_{\text{err}}}$ which is the characteristic parameter (since by setting $\mu = 0$) for the estimation of Equation 8.21 can be obtained by using the histogram (or KDE, see Section 8.1.6), is given by (Bennett *et al.*, 1954)

$$\sigma_{\phi_{\text{err}}} = \frac{\sqrt{\sum_{j=1}^{M} F_j \left(x_j - \bar{x}\right)^2}}{\sum_{j=1}^{M} F_j - 1}, \tag{8.22}$$

where F_j is the corresponding frequency count of the sample data element x_j and $\bar{x}$ is the sample mean of data elements obtained by

$$\bar{x} = \frac{\sqrt{\sum_{j=1}^{M} F_j \, x_j}}{\sum_{j=1}^{M} F_j}. \tag{8.23}$$

In order to obtain the typical phase error (mean of the standard deviation of the phase error $\overline{\sigma_{\phi_{\text{err}}}}$), the computation of Equation 8.22 should be repeated many times (say, set $k = 1, 2, \ldots, K$) and then needs to take the mean among them as

$$\overline{\sigma_{\phi_{\text{err}}}} = \sqrt{\sum_{k=1}^{K} \sigma^2_{\phi_{\text{err}_k}} \Big/ K}, \tag{8.24}$$

where $\sigma^2_{\phi_{\text{err}_k}}$ is the variance of the phase error for the kth set. Then, as usual the uncertainty is occurred in the result. In order to obtain the uncertainty of the obtained result $\overline{\sigma_{\phi_{\text{err}}}}$ in Equation 8.24, we use Equation 8.5 since it is assumed that the error in the correlation function due to the random jitter is following a Gaussian distribution. Thus, the standard error for $\overline{\sigma_{\phi_{\text{err}}}}$ is given by

$$\text{SE}(\sigma_{\phi_{\text{err}}}) = \pm \frac{\text{std}(\sigma_{\phi_{\text{err}}})}{\sqrt{K}}, \tag{8.25}$$

where std(.) is the standard deviation of $\sigma_{\phi_{\text{err}}}$ among the K sets which can be calculated as

$$\text{std}(\sigma_{\phi_{\text{err}}}) = \sqrt{\frac{\sum_{k=1}^{K} \left(\sigma_{\phi_{\text{err}_k}} - \overline{\sigma_{\phi_{\text{err}}}}\right)^2}{K - 1}}, \tag{8.26}$$

where $\sigma_{\phi_{\text{err}_k}}$ is the standard deviation of the phase error for the kth set.

Hence the measurement of the typical phase error ϕ_{err} (mean of the standard deviation of the phase error among the K sets) with the standard error (uncertainty) is found by

$$\sigma_{\phi_{\text{err}}} = \overline{\sigma_{\phi_{\text{err}}}} \pm \frac{\text{std}(\sigma_{\phi_{\text{err}}})}{\sqrt{K}}, \tag{8.27}$$

Now, substituting Equations 8.24 and 8.26 into Equation 8.27, we have

$$\sigma_{\phi_{\text{err}}} = \sqrt{\frac{\sum_{k=1}^{K} \sigma^2_{\phi_{\text{err}_k}}}{K}} \pm \sqrt{\frac{\sum_{k=1}^{K} \left(\sigma_{\phi_{\text{err}_k}} - \sqrt{\sum_{k=1}^{K} \sigma^2_{\phi_{\text{err}_k}} \Big/ K} \right)^2}{K\,(K-1)}}. \tag{8.28}$$

This is the corresponding estimation for the phase error with the uncertainty due to the presence of random jitter in the correlation function.

8.3 Testing the Model by Simulated Data

In most real implementations, the camera is in homodyne operation ($f_l = f_s = f$), therefore the model (Equation 8.21) is tested only for homodyne case. The random jitter is assumed to be following a Gaussian distribution. The zero means ($\mu_l = \mu_s = 0$) is chosen for the distribution since it can be controlled by an offset adjustment. For the RMS values of the RJ, we choose the set of values as 21 pairs (σ_l, σ_s). In order to generalise the result, the amounts for these RMS pairs are chosen that slightly different in the light and shutter signal such as [(0,0), (50, 51), (100, 101), ... (950, 951), (1000, 1001)] ps.

Since each setup takes relatively large execution time, the analysis of each setup is performed only for a single and fixed integration period ($T = 1$ ms). We chose this amount because most of the present AMCW ToF cameras operate under this integration period. For the purpose of analysis, the two ToF phase shifts ($\phi = \pi/6$ and $\pi/3$) are considered throughout the simulation. However, the number of samples during the integration period is more important to identify in the evaluation of the model. In order to identify the sufficient number of samples (steps in the integral) for the simulation, the following computation is carried out.

8.3.1 Calculation of Sufficient Number of Samples

Let us consider the modulation frequency f and integration period T for any setup. Then, the number of cycles in the integration period is given by

$$N_{cyl,T} = fT \text{ cycles.} \tag{8.29}$$

Now, the number of samples per cycle N should satisfy the Nyquist criteria (i.e., at least a double of $N_{cyl,T}$) and thus,

$$N = \frac{N_{int}}{N_{cyl,T}} = \frac{N_{int}}{fT}, \tag{8.30}$$

where $N_{int} \gg 2N_{cyl,T}$ is a sufficient number of samples chosen in the integration period for the simulation. This N_{int} is the corresponding number of steps for the integration period for the model.

8.3.2 Simulation Setup

The model (Equation 8.21) is evaluated for eight modulation frequencies in the range of $f = 30$ to 1000 MHz with fixed integration period $T = 1$ ms throughout the simulations. In order to maintain the fixed number of samples per cycle (N = 100 each), the number of samples in the integration period N_{int} is chosen accordingly. This 100 is a sufficient number of samples per cycle with the chosen integration period for each modulation frequency. Trapezoidal integration is used throughout the simulation since it is a straightforward method. From Chapter 7, we found that trapezoidal integration (or the Romberg integration) is not very accurate for the calculations of complex integrals. But, the accuracy of this integration is not heavily important. However, by comparing, the execution time among these two numerical methods (see Table 7.7), we chose trapezoidal integration for our purpose.

The MCS is performed for 500 independent evaluations of the model for each setup. Then, the standard deviation of the corresponding histogram (or KDE) is used for analysing the result of the phase error obtained ($\sigma_{\phi_{\text{err}}}$). In order to analyse the uncertainty of the resultant phase error, thirty repetitions are performed for each simulation setup. The simulation setup is visualised in Figure 8.2 and all corresponding parameters of the simulation set up are tabulated in Table 8.1.

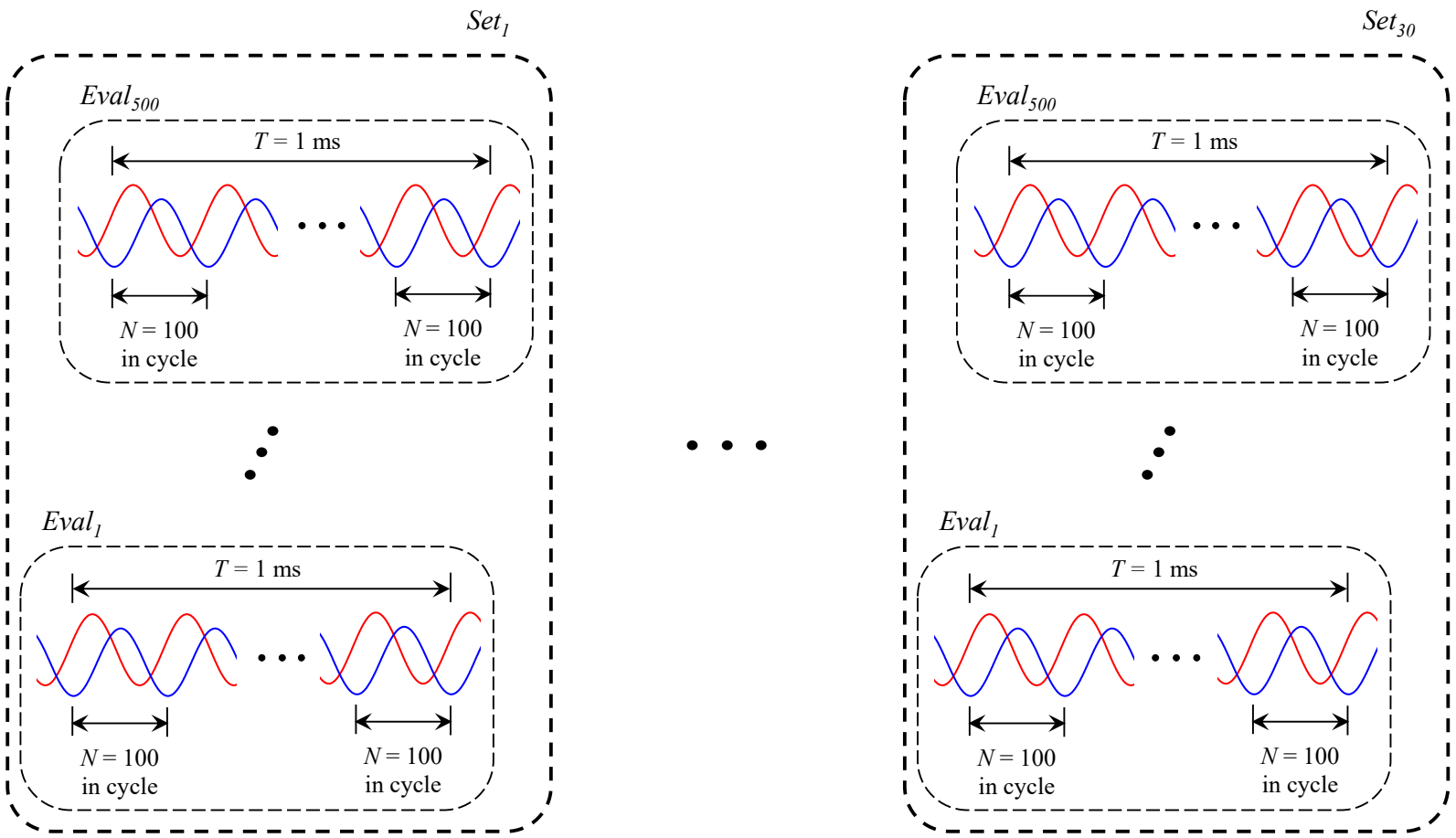

Figure 8.2: Illustration of the simulation setup for the analysis of random jitter in the correlation function.

Table 8.1: Parameters of the simulation setup

Time of flight system			
Integration period, $T = 1$ ms	Number of samples		
Modulation frequency, f (MHz)	in the T, N_{int}		per cycle, N
$f_{30} = 30$	3	$\times 10^6$	100 —by using Equation 8.30 $\left(N = \frac{N_{int}}{fT}\right)$
$f_{50} = 50$	5		
$f_{100} = 100$	10		
$f_{200} = 200$	20		
$f_{400} = 400$	40		
$f_{600} = 600$	60		
$f_{800} = 800$	80		
$f_{1000} = 1000$	100		
Random jitter with Gaussian distribution			
Means (ps)	$\mu_l = \mu_s = 0$		
Standard deviations (ps) 21 RMS pairs (σ_l, σ_s)	$\big[(0, 0); (50, 51); (100, 101); \ldots$ $\ldots (950, 951); (1000, 1001)\big]$		
Other parameters - Number of:			
Independent evaluations for the MCS of the model, nEval = 500			
Repetitions in order to analyse the uncertainty of the model, nSet = 30			

8.4 Results and Discussion

By using the Monte Carlo simulation the corresponding set of data is generated and then these data are simulated by using two non-parametric estimations stated in Section 8.1.6 (see Section C.4 in Appendix C for Matlab script). Figures 8.3 and 8.4 show the corresponding probability density functions by the two estimations with the ToF phase shifts $\phi = \pi/6$ and $\pi/3$, separately, for the first and last two modulation frequencies, respectively, in Table 8.1 due to the random jitter of a pair of RMS $(\sigma_l, \sigma_s) = (50, 51)$ ps with a single set. In addition, the relevant standard deviation of the phase error (i.e., $\sigma_{\phi_{\mathrm{err}_k}}, k = 1$) for each case is also pointed on the captions of both figures. By comparison of the standard deviations, it is observed that the phase errors at high modulation frequencies are larger than low modulation frequencies.

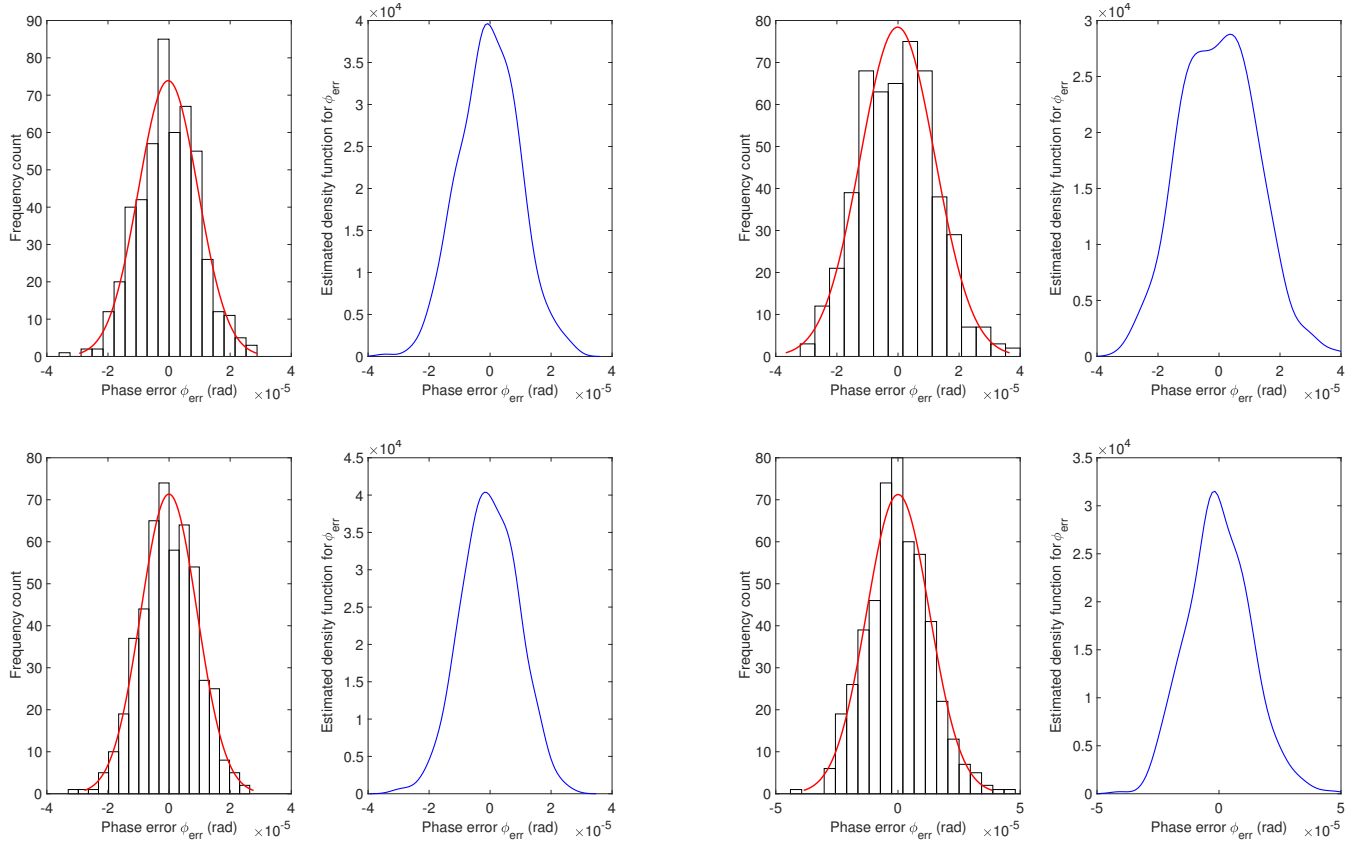

Figure 8.3: PDF for the phase error ϕ_{err} when (a) $f = 30$ and (b) $f = 50$ MHz, for a pair of $(\sigma_l, \sigma_s) = (50, 51)$ ps, for ToF phase shifts (top) $\phi = \pi/6$ and (bottom) $\phi = \pi/3$ rad, using 500 independent evaluations of MCS with a single set by using (left of (a) and (b)) histogram with curve fitting and (right of (a) and (b)) KDE. Standard deviation of the phase error $\sigma_{\phi_{\text{err}_1}}$ (in $\times 10^{-5}$ rad) for (a)(top) 0.97, (a)(bottom) 0.92, (b)(top) 1.22 and (b)(bottom) 1.29.

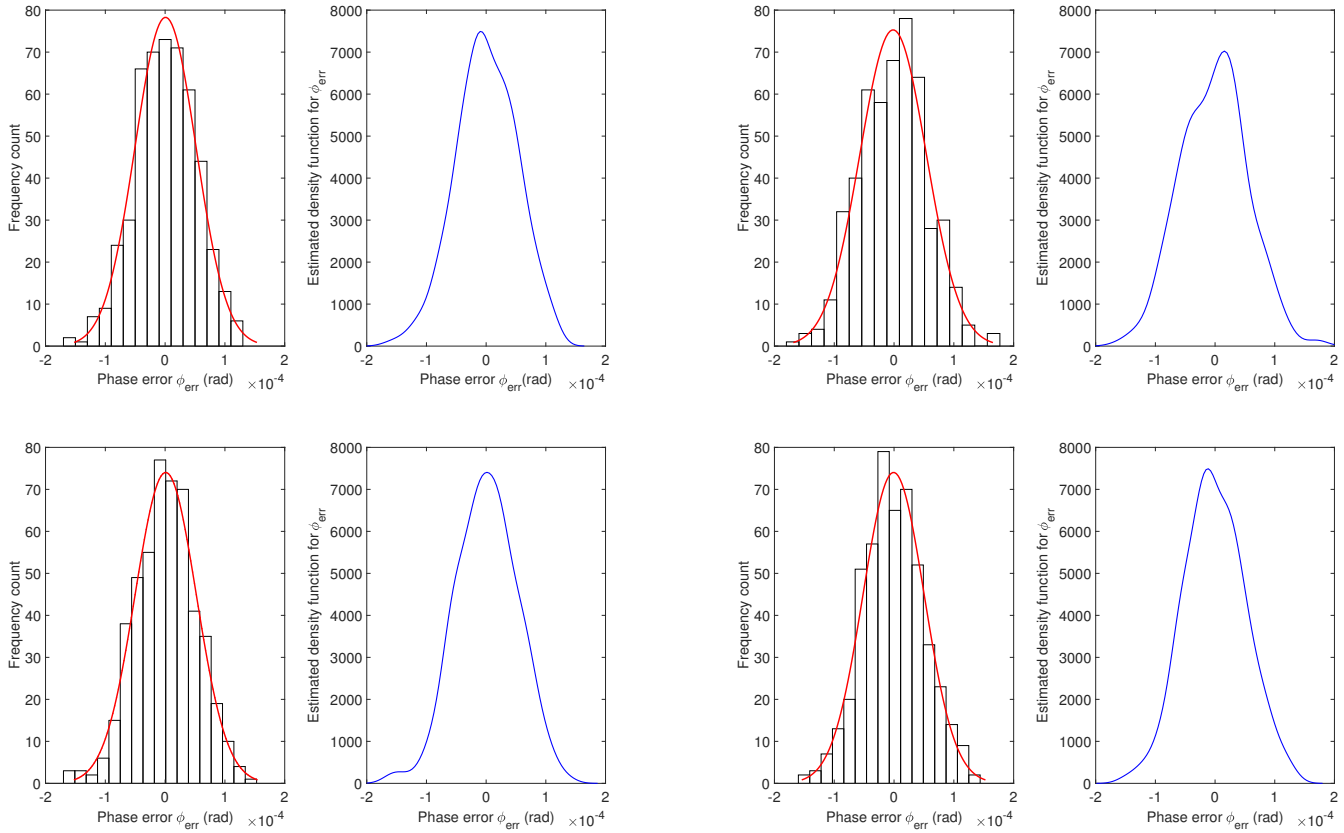

Figure 8.4: PDF for the phase error ϕ_{err} when (a) $f = 800$ and (b) $f = 1000$ MHz, for a pair of $(\sigma_l, \sigma_s) = (50, 51)$ ps, for ToF phase shifts (top) $\phi = \pi/6$ and (bottom) $\phi = \pi/3$ rad, using 500 independent evaluations of MCS with a single set by using (left of (a) and (b)) histogram with curve fitting and (right of (a) and (b)) KDE. Standard deviation of the phase error $\sigma_{\phi_{\text{err}_1}}$ (in $\times 10^{-5}$ rad) for (a)(top) 5.10, (a)(bottom) 5.12, (b)(top) 5.56 and (b)(bottom) 5.12.

Similarly, one can obtain these estimations for other modulation frequencies as well. Table 8.2 tabulates the corresponding standard deviation of the phase error for all eight modulation frequencies and two ToF phase shifts by performing 500 independent evaluations of MCS each with a pair of RMS $(\sigma_l, \sigma_s) = (50, 51)$ ps for a single set.

Table 8.2: Standard deviation of phase error for each modulation frequency with a RMS pair of $(\sigma_l, \sigma_s) = (50, 51)$ ps and 500 independent MCS for a single set for the two ToF phase shifts

f (MHz)	Parameters used	$\sigma_{\phi_{\text{err}_1}}$ (in $\times 10^{-5}$ rad) for	
		$\phi = \pi/6$	$\phi = \pi/3$
30	$T = 1$ ms	0.97	0.92
50	$(\sigma_l, \sigma_s) = (50, 51)$ ps	1.22	1.29
100		1.72	1.72
200		2.43	2.43
400	Independent MCS	3.60	3.40
600	with	4.20	4.56
800	nEval = 500,	5.10	5.12
1000	nSet = 1	5.56	5.12

The standard deviation of the phase error increases when the modulation frequency increases. In addition, for the same modulation frequency with a single set, the phase errors are not reasonably changed for the two ToF phase shifts chosen and there is no pattern among them. Note that the results for each setup are with a single set. In each setup, an independent MCS is performed for each phase shift.

Now, thirty repetitions are performed to estimate the uncertainty of the phase error for all 21 RMS pairs (σ_l, σ_s). First, let us consider the first three modulation frequencies for the two ToF phase shifts. Figure 8.5 shows the typical phase error which is computed by the mean of the standard deviation against the RMS of the injected random jitter for $f = 30$, 50 and 100 MHz with 500 independent MCS for each evaluation. For the same frequency, the corresponding results for both ToF phase shifts are approximately similar (compare each (left) and (right) sub plots in Figure 8.5, separately).

For each of these three frequencies, an approximately linear relationship between the RMS of RJ and phase error has occurred. For $f = 100$ MHz, a slightly curving upward (see Figure 8.5(c)) can be seen by the naked eye. For

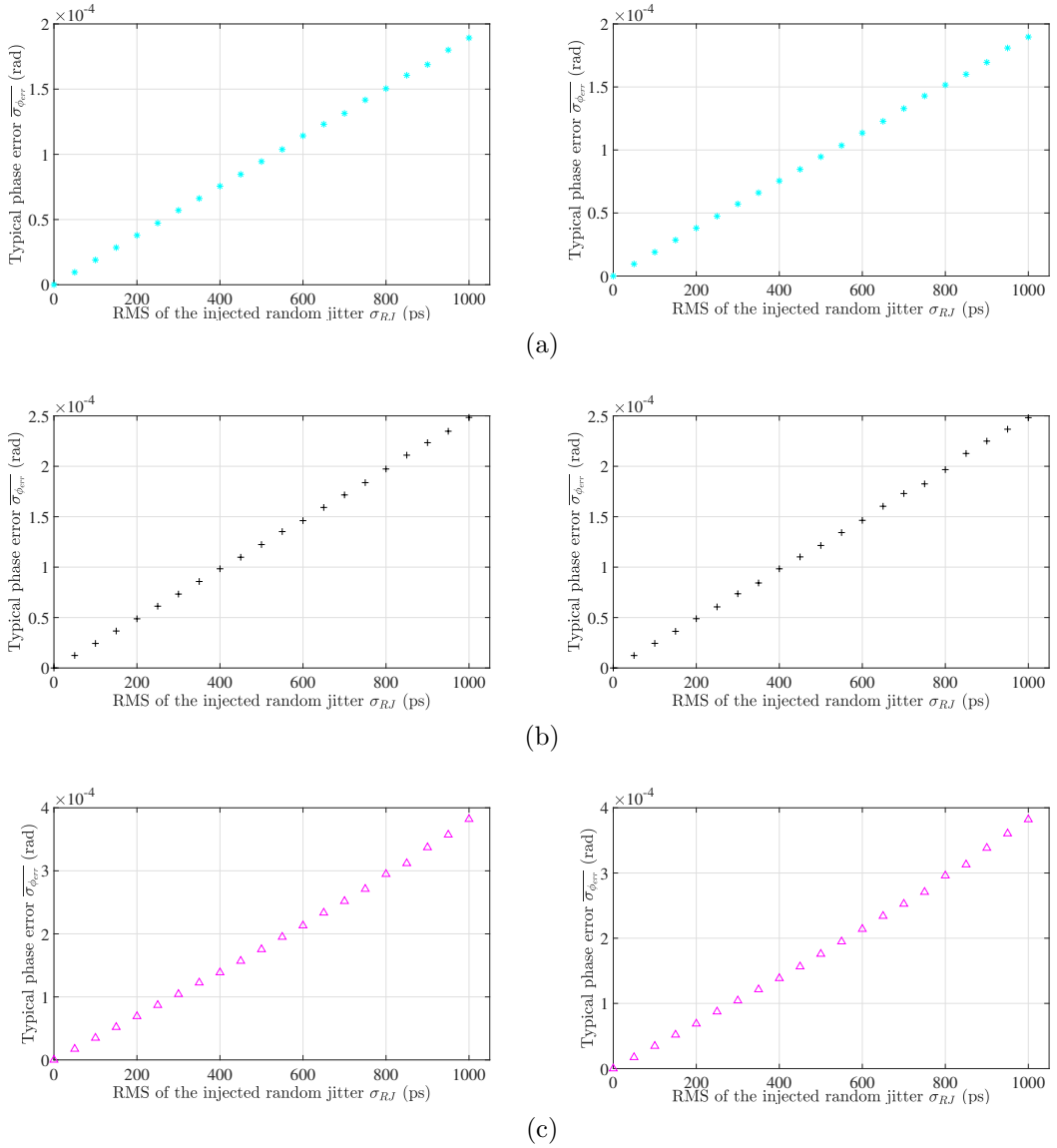

Figure 8.5: Typical phase error $\overline{\sigma_{\phi_{\text{err}}}}$ against the RMS of random jitter when the modulation frequency f (MHz): (a) 30, (b) 50 and (c) 100, for the ToF phase shifts ϕ: (left) $\pi/6$ and (right) $\pi/3$ rad, by using 500 independent MCS with the integration period $T = 1$ ms and 30 repetitions.

the maximum RMS of RJ (i.e., $\sigma_{RJ} = 1000$ ps), the first three modulation frequencies $f = \{30, 50, 100\}$ MHz are given $\overline{\sigma_{\phi_{\text{err}}}} = \{189.26, 248.45, 384.89\}$ μrad of the (typical) standard deviation of phase errors, respectively. These are relatively very low values that influence range measurements. Thus, for those three modulation frequencies, the RJ is unable to impact range measurements, even its RMS is a relatively large value 1000 ps each. Now, it is interesting to see whether this behaviour is the same for the rest of the modulation frequencies in Table 8.1.

Let us consider the behaviour of the RJ when f is increased. Figure 8.6 compares (typical phase error) the mean of the standard deviation of the phase error $\overline{\sigma_{\phi_{\text{err}}}}$ against the RMS of random jitter σ_{RJ} for all modulation frequencies chosen (see Table 8.1) for the ToF phase shift $\phi = \pi/6$. Note that in order to compare the results, the corresponding results for the first three modulation frequencies (each (left) sub plots in Figure 8.5) are also included in the figure. In practice, we can measure the phase error to about 10000th of a cycle (i.e., $2\pi/10^4 \approx 0.6283$ mrad) in the system. So, the corresponding line of the phase error $\overline{\sigma_{\phi_{\text{err}}}} = 10^{-4}$ rad criterion for all RMS values is also marked (see line - - - -) on the figure. The analysis of the intersection points between each curve with the $2\pi/10^4$ radian line is interesting.

It is clear that curves are behaving in non linear shapes when f increases. Also, for each modulation frequency f, the corresponding $\overline{\sigma_{\phi_{\text{err}}}}$ increases when σ_{RJ} increases. Among the two cameras experimented with in Chapter 5, it was found the maximum random jitter with RMS of $\sigma_{\text{RJ}} = (159.6 \pm 0.1)$ ps in MESA SR4000. For the purpose of analysis, lets first consider the RMS of σ_{RJ} = 200 ps for each modulation frequency in the figure. Then, for the typical phase error of $\overline{\sigma_{\phi_{\text{err}}}} = 0.1$ mrad criterion is starting to occur at least from f = 200 MHz while for $\overline{\sigma_{\phi_{\text{err}}}} = 1$ mrad criterion of error is occurring at $\sigma_{\text{RJ}} \approx 950$ ps. In addition, the phase error $\overline{\sigma_{\phi_{\text{err}}}} = 0.1$ mrad criterion occurred at least from $\sigma_{\text{RJ}} = \{500, 400, 300\}$ ps for the modulation frequencies $f = \{30, 50, 100\}$ MHz, respectively.

In contrast, when the modulation frequency is $f \geq 200$ MHz, there is a rising trend of the typical phase error at the RMS $\sigma_{\text{RJ}} = 300$ ps for the rest of the modulation frequencies. An example, for $f = 400$ MHz, the sharp rising of $\overline{\sigma_{\phi_{\text{err}}}}$ occurred at the RMS σ_{RJ} = 300 ps. For the last four modulation frequencies, the phase error $\overline{\sigma_{\phi_{\text{err}}}} = 1$ mrad criterion is starting to occur from the RMS $\sigma_{\text{RJ}} \approx \{550, 375, 300, 240\}$ ps, respectively. Furthermore, when f = 600 MHz the typical phase error $\overline{\sigma_{\phi_{\text{err}}}}$ is dramatically increased up to 1 rad at the RMS $\sigma_{\text{RJ}} = 850$ ps and then shows stable behaviour for the rest of the RMS values. This similar behaviour is occurred at $\sigma_{\text{RJ}} = 650$ and 550 ps for the modulation frequencies $f = 800$ and 1000 MHz, respectively.

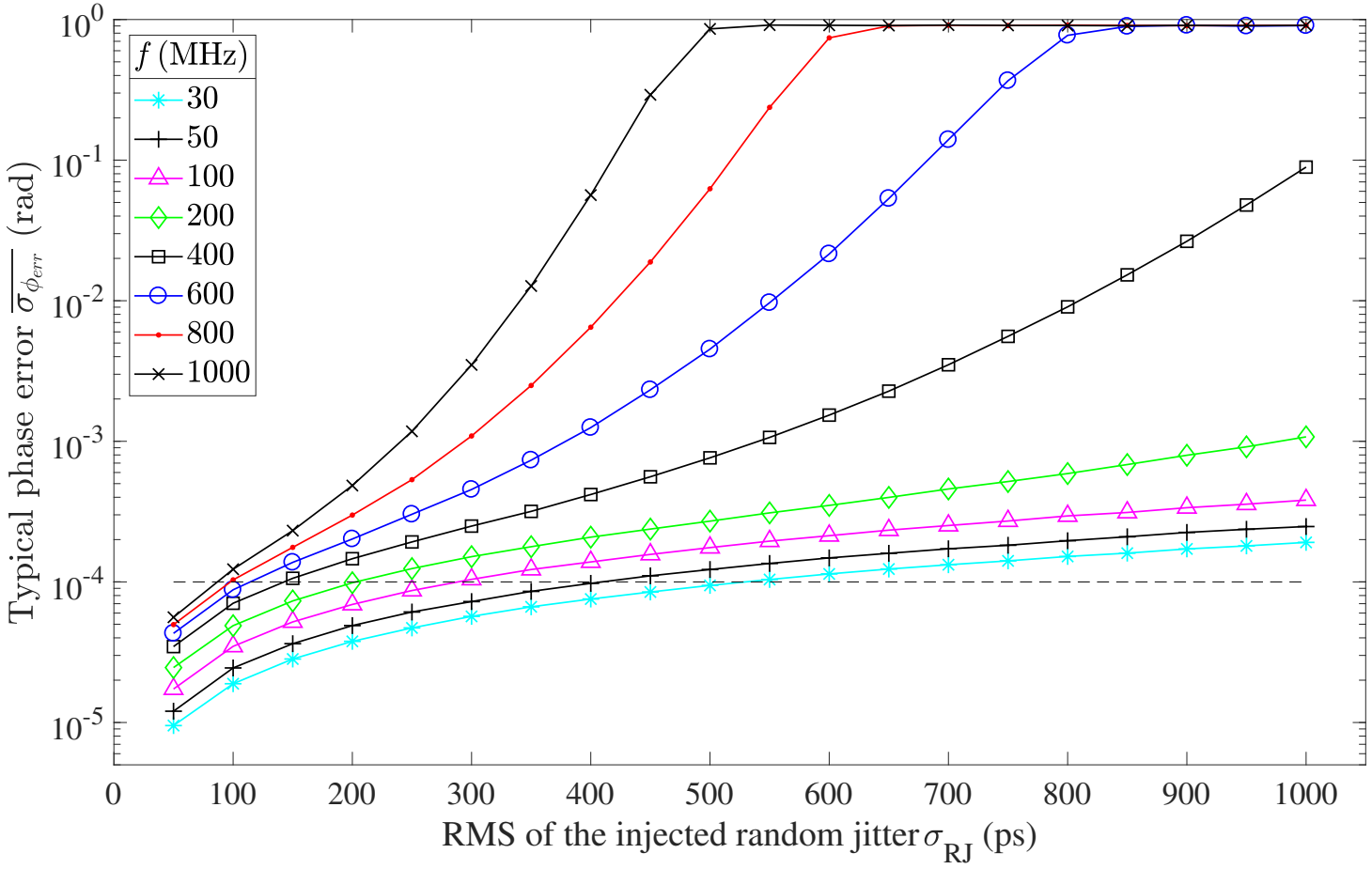

Figure 8.6: Typical phase error $\overline{\sigma_{\phi_{\mathrm{err}}}}$ against the RMS of random jitter for modulation frequencies in Table 8.1 for a ToF phase shift $\phi = \pi/6$ by using 500 independent Monte Carlo simulation with $T = 1$ ms and 30 repetitions. The line - - - - indicates the phase error $\overline{\sigma_{\phi_{\mathrm{err}}}} = 10^{-4}$ rad criterion. The uncertainties of the plotted points are smaller than the width of a line.

Figure 8.7 shows when the random jitter affect the measurement of phase against the modulation frequency, by using the corresponding data in Figure 8.6. So, the upper side of the fitted curve is the corresponding affecting area on range measurements due to presence of random jitter. It is clear that at $f = \{30,\ 50,\ 100\}$ MHz, the error can tolerate the RJ with RMS $\sigma_{\text{RJ}} = \{530, 410, 288\}$ ps while at $f = \{800, 1000\}$ MHz only $\sigma_{\text{RJ}} = \{97, 87\}$ ps can be tolerated, respectively. Thus, the random jitter in two ToF cameras experimented in Chapter 5 is unable to influence range measurements (since $\sigma_{\text{RJ}} = (159.6 \pm 0.1)$ ps and (40.37 ± 0.04) ps for $f = 30$ and 50 MHz, respectively). For currently available AMCW ToF flight range imaging cameras (for $f < 100$ MHz), the random jitter has not a measurable effect on range measurement. But increasing the modulation frequency further, the random jitter has a measurable affect on phase, thus in range. As examples, 400 MHz with random jitter of 140 ps and 600 MHz with 115 ps have measurable affect on ranging (see Figure 8.7).

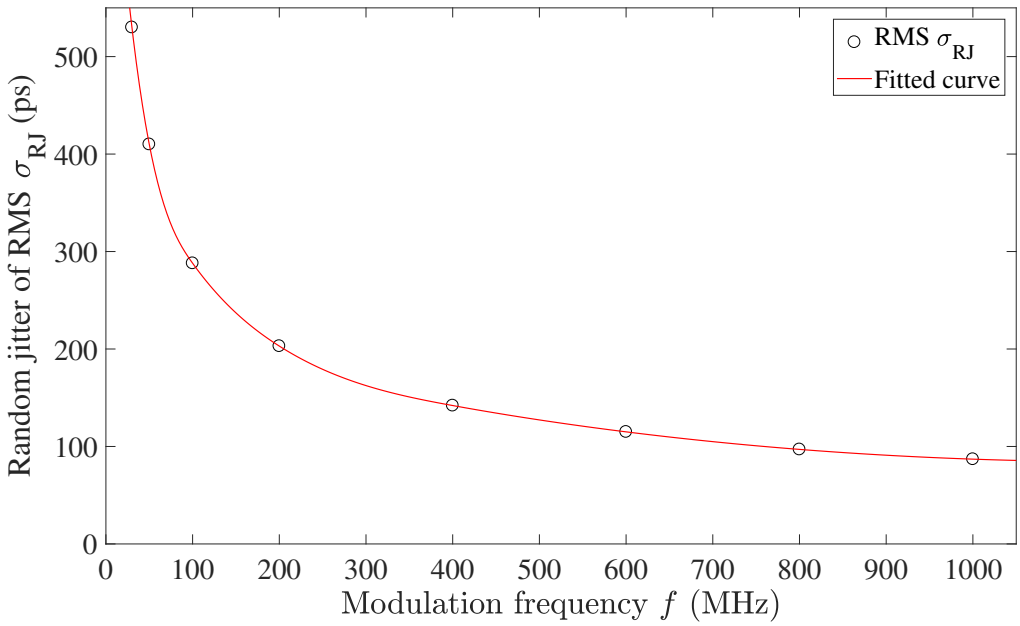

Figure 8.7: The domain of the RJ that affects the measurement of phase obtained by using Figure 8.6 with the phase error $\overline{\sigma_{\phi_{\text{err}}}} = 10^{-4}$ rad criterion. Above the curve random jitter has a potentially measurable affect on ranging.

Now the standard deviation of the range error for each corresponding typical phase error can be computed by using the fundamental relation of the ToF ranging (i.e., Equation 2.1). As an example, from Figure 8.6, for $f = 30$ MHz, the standard deviations of phase errors when the random jitter pairs of RMS

$(\sigma_l, \sigma_s) = \{(200, 201), (400, 401), (600, 601), (800, 801), (1000, 1001)\}$ ps are given as $\sigma_{\phi_{\text{err}}} \approx \{3.777, 7.555, 11.398, 15.172, 19.103\} \times 10^{-5}$ rad, respectively, for the ToF phase shift $\phi = \pi/6$. Then, the standard deviations of corresponding range errors (typical) can be computed as $\sigma_{d_{\text{err}}} \approx \{0.03, 0.06, 0.09, 0.12, 0.15\}$ mm, respectively, which are an approximately linear relationship as shown in Figure 8.5(a)(left). These values are extremely insignificant in their influence on range measurements. That is, even in the presence of maximum RMS $(\sigma_l, \sigma_s) = (1000, 1001)$ ps of random jitter is unable to sufficiently influence range measurements when $f = 30$ MHz (since $\sigma_{d_{\text{err}}} \approx 0.15$ mm). Similarly, with Figure 8.6 and Equation 2.1, the calculated typical range errors for each modulation frequency for the selected five RMS pairs of random jitter can be computed as shown in Table 8.3. Note that these values are rounded to two decimal places and the shaded cells are the potentially measurable amounts.

Table 8.3: The typical range error (standard deviation $\sigma_{d_{\text{err}}}$ in mm) computed by using Figure 8.6 with $\overline{\sigma_{\phi_{\text{err}}}} = 10^{-4}$ rad criterion and Equation 2.1, due to the selected RMS of random jitter σ_{RJ} in the correlation model for all modulation frequencies. The shaded cells are the only potentially measurable $\sigma_{d_{\text{err}}}$ amounts

f (MHz)	Range error $\sigma_{d_{\text{err}}}$ (mm)	Injected random jitter of RMS pair (σ_l, σ_s) in ps				
		(200, 201)	(400, 401)	(600, 601)	(800, 801)	(1000, 1001)
30		0.03	0.06	0.09	0.12	0.15
50		0.02	0.05	0.07	0.09	0.12
100		0.02	0.03	0.05	0.07	0.09
200		0.01	0.02	0.04	0.07	0.13
400		0.01	0.03	0.09	0.54	5.32
600		0.01	0.05	0.85	30.69	35.97
800		0.01	0.19	22.09	27.22	27.08
1000		0.01	1.35	21.71	21.62	21.69

It is straightforward to see, among the values σ_{RJ} chosen in the table, the standard deviation of range errors $\sigma_{d_{\text{err}}}$ systematically decreased (except for $(\sigma_l, \sigma_s) = (1000, 1001)$ ps when $f = 200$ MHz) up to the modulation frequency $f = 200$ MHz while they are dramatically increased from $f = 400$ MHz. At $f = 400$ MHz, the potential measurable amount $\sigma_{d_{\text{err}}} = 5.32$ mm is starting to occur with the presence of $\sigma_{\text{RJ}} = 1$ ns. However, it is well clear that the measurable range errors $\sigma_{d_{\text{err}}}$ started to occur for low RMS values when the modulation frequency is increased (see the shaded cells of the table). As examples at

$f = \{600, 800, 1000\}$ MHz, the range errors are $\sigma_{d_{\text{err}}} = \{30.69, 22.09, 21.71\}$ mm when the random jitter as $\sigma_{\text{RJ}} = \{800, 600, 600\}$ ps, respectively. Note that the range errors are approximately the same ($\sigma_{d_{\text{err}}} \approx 27$ mm) for the last selected two RMS pairs $\sigma_{\text{RJ}} = \{800, 1000\}$ when $f = 800$ MHz while they are approximately the same ($\sigma_{d_{\text{err}}} \approx 22$ mm) for the last selected three RMS pairs $\sigma_{\text{RJ}} = \{600, 800, 1000\}$ when $f = 1000$ MHz.

8.4.1 Uncertainty Analysis of the Results

Figure 8.8 shows the uncertainty (standard error) as error bars by using Equation 8.25 for the corresponding results shown in Figure 8.6 for each modulation frequency. The uncertainty values (length of the error bars) are increasing when the modulation frequency increases. In addition, within the same modulation frequency, the uncertainty is also increased when the RMS of random jitter increases. This is verified in Figure 8.9 which compares the corresponding uncertainty (standard error) for each modulation frequency and each RMS of random jitter. It is seen that for the first four frequencies, the uncertainty is less than 10^{-5} rad when the random jitter is greater than 500 ps while for the last three frequencies it is in the range (10^{-3}–10^{-2}) rad when the random jitter is greater than 800 ps.

With the presence of maximum random jitter (i.e., RMS $\sigma_{\text{RJ}} = 1000$ ps), the uncertainty range is approximately (1–6) μrad for the first four frequencies while it is (0.6–4) mrad for the frequencies 400 and 600 MHz. This milliradian range for the standard error has relatively large deviations with respect to the typical phase errors obtained (compare Figures 8.6 and 8.9, especially for the last three modulation frequencies). That is, thirty repetitions are not significant enough for the uncertainty analysis of the results when f increases. Thus, in order to increase the accuracy of the results, it needs more repetitions than the current value ($\gg 30$). Then, as usual, the execution time for each simulation set up will be increased accordingly.

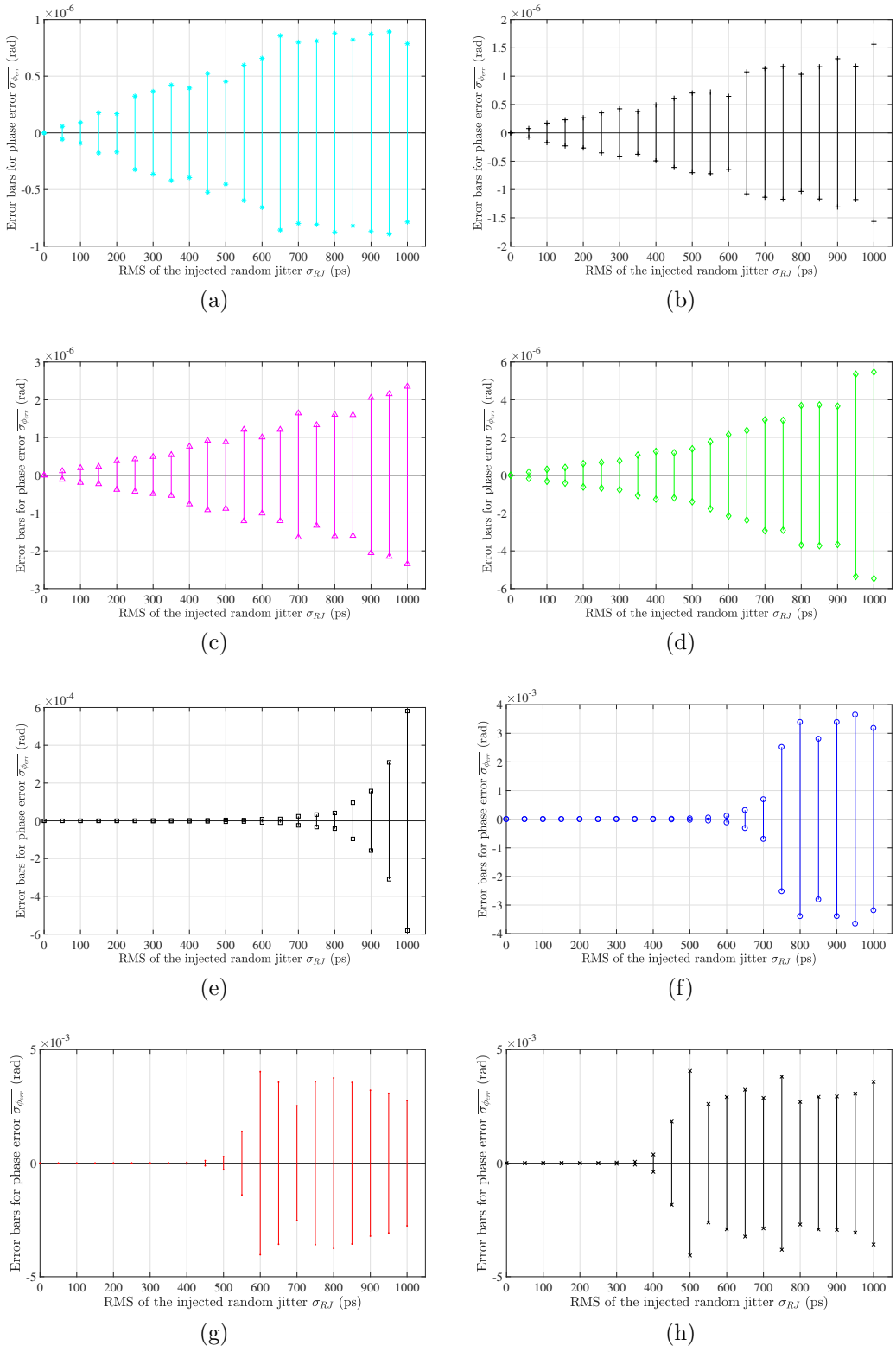

Figure 8.8: Uncertainty SE($\sigma_{\phi_{\text{err}}}$) of the typical phase error $\overline{\sigma_{\phi_{\text{err}}}}$ against the RMS of the random jitter by using Equation 8.25 with 30 repetitions for modulation frequency f (MHz): (a) 30, (b) 50, (c) 100, (d) 200, (e) 400, (f) 600, (g) 800 and (h) 1000, when $\phi = \pi/6$ and $T = 1$ ms.

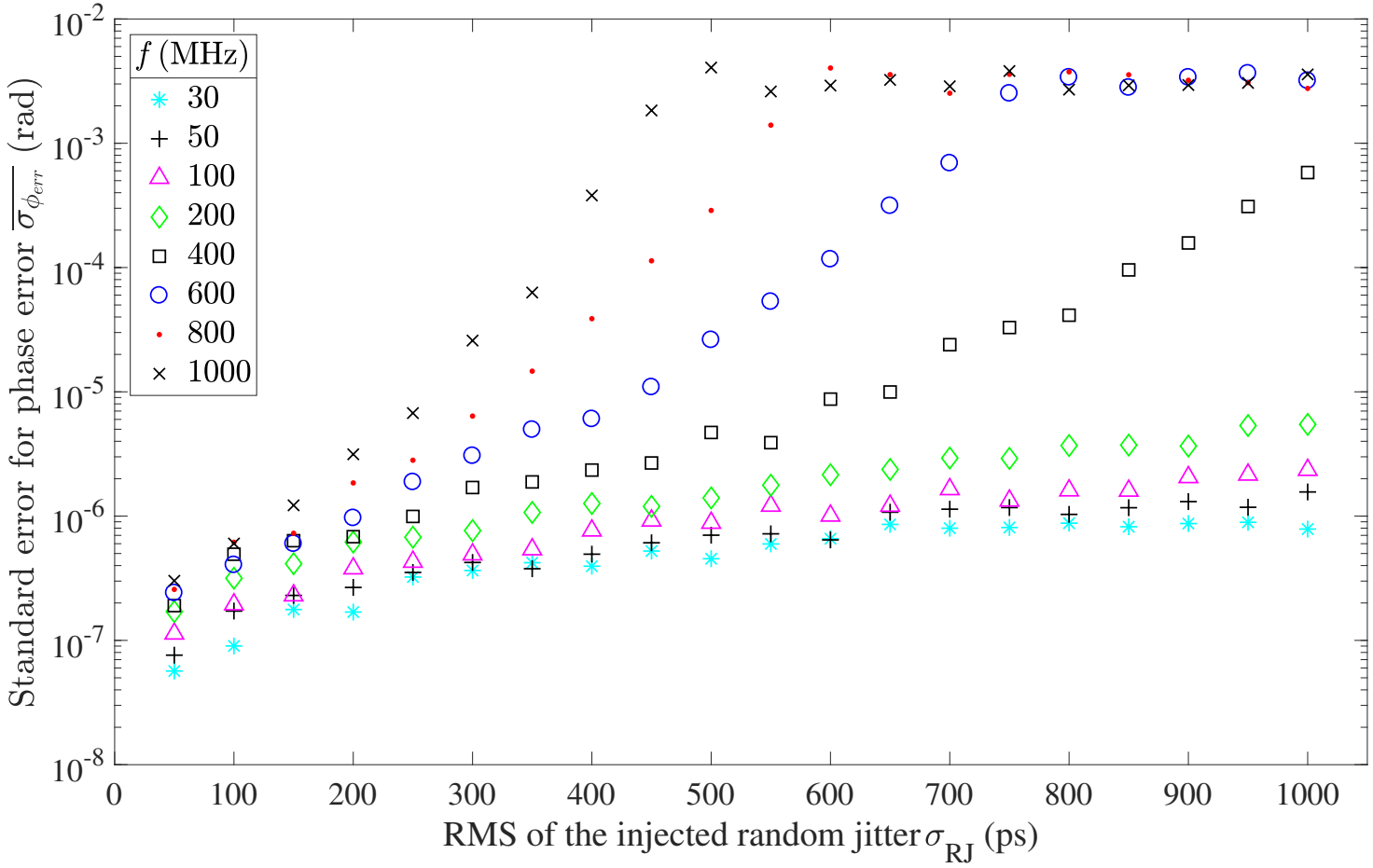

Figure 8.9: Comparison of the uncertainty (standard error) for the typical phase error $\overline{\sigma_{\phi_{\mathrm{err}}}}$ against the RMS of the random jitter by using Equation 8.25 with the repetitions nSet = 30 for all modulation frequencies when ToF phase shift $\phi = \pi/6$ and the integration period $T = 1$ ms.

8.4.2 Execution Time for the Simulation

Table 8.4 shows the approximate execution time in hours for the main results obtained in this chapter that corresponding to Figure 8.6. Note that these amounts are rounded up to the nearest two decimal places. All simulation are implemented with MATLAB R2019a (The MathWorks Inc.) and are executed on a Linux server of configuration: the Linux kernel 4.9.0−6−amd64 with x86−64 architecture, the operating system Debian GNU/Linux 9 (stretch), the memory 128.0 GB RAM and 32 logical cores.

For first six modulation frequencies, the two set up were concurrently executed while last two frequencies were executed one after other due to the limitation of the memory of the server. All 16 cores are used for each modulation frequency.

Table 8.4: Approximate execution time for simulations

f (MHz)	Parameters used: N_{int}	Parameters used: Others	Time (in hours)
30	3		5.89
50	5	$T = 1$ ms, $\phi = \pi/6$, $N = 100$,	9.90
100	10	$\mu_l = \mu_s = 0$ ps,	20.44
200	20	$(\sigma_l, \sigma_s) = [(0,0); (50,51); \ldots$	39.78
400	40	$\times 10^6$ $\ldots (950,951); (1000,1001)]$ ps	100.46
600	60	Independent MCS with nEval = 500	150.11
800	80	for number of repetitions nSet = 30	158.64
1000	100		214.43

In order to minimise the execution time for simulations we used the *parfor* command (parallel for loop in MATLAB) for the variable corresponding to the evaluations of 500 independent MCS (i.e., the variable 'nEvl' in script "genMCsRJ.m" in Appendix C.4). This *parfor* command generates different random number streams for all evaluation of MCS and for each modulation frequency. As usual, when the parameter N_{int} increases the execution time increases.

8.5 Chapter Remarks

The analysis of the influence of random jitter in the correlation function of AMCW ToF cameras was investigated in this chapter. It was assumed the random jitter in the emitted and shutter signals of the correlation function follow two separate Gaussian distributions. The Monte Carlo method would evaluated the correlation function with random jitter and non-parametric estimations used to obtain the PDF of the standard deviation of the phase error.

Due to low modulation frequencies of current AMCW ToF cameras (less than 100 MHz), we found that the random jitter is unable to sufficiently influence the range measurements even in the presence of relatively large random jitter. As examples, for the modulation frequencies $f = \{30,\ 50,\ 100\}$ MHz, the typical phase error $\overline{\sigma_{\phi_{\text{err}}}} = 0.1$ mrad criterion were starting to occur from $\sigma_{\text{RJ}} = \{500,\ 400,\ 300\}$ ps of random jitter, respectively. Then, the corresponding range errors for this typical phase error 0.1 mrad criterion are given by $\sigma_{d_{\text{err}}} \approx \{0.08,\ 0.05,\ 0.02\}$ mm, respectively which are not sufficient amounts to be detectable in range measurements. Even of RMS $\sigma_{\text{RJ}} = 1$ ns, the typical range errors (standard deviation) for first three modulation frequencies are $\sigma_{d_{\text{err}}} \approx \{0.15,\ 0.12,\ 0.09\}$ mm, respectively. If we take 10^{-4} rad criterion as when errors could be measured then at $f = \{30,\ 50,\ 100\}$ MHz can tolerate the $\sigma_{\text{RJ}} = \{530, 410, 288\}$ ps but at $f = \{600,\ 800,\ 1000\}$ MHz only $\sigma_{\text{RJ}} = \{115, 97, 87\}$ ps can be tolerated, respectively. However, at $f = 200$ MHz, the typical phase error of $\overline{\sigma_{\phi_{\text{err}}}} = 1$ mrad criterion (corresponding range error $\sigma_{d_{\text{err}}} \approx 0.12$ mm) was starting to occur but due to the large RMS $\sigma_{\text{RJ}} \approx$ 950 ps.

We found increasing of the modulation frequency above approximately 400 MHz with random jitter of 140 ps has a measurable effect on ranging when the criteria of the phase error 10^{-4} radian is chosen. This is further reduced when the modulation frequency 600 MHz is given the random jitter of 115 ps. In addition, by analysing the uncertainty of the results (the phase error $\overline{\sigma_{\phi_{\text{err}}}}$ hence the range error $\sigma_{d_{\text{err}}}$), we found that thirty repetitions of the simulation set up for higher RMS values especially with higher modulation frequencies are not sufficient. As examples, when the RMS $\sigma_{\text{RJ}} > 800$ ps, the typical phase errors are in the range of (0.6–4) mrad for the modulation frequencies 400 and 600 MHz which are relatively large values with respect to the corresponding $\overline{\sigma_{\phi_{\text{err}}}}$.

Chapter 9

Conclusions and Outlook

Three main sections of the research were covered in this thesis. These are the development of a common methodology for jitter extraction and calculation, an alternative cost effective technique for jitter measurement and the analysis of jitter influence on range measurements in AMCW ToF range imaging cameras. In addition, a comprehensive literature survey is provided that places the presented research in a context relevant to the task of understanding gaps in the noise and jitter investigation in the AMCW ToF range imaging cameras. Over the last couple of decades, these cameras are commercially available at reasonable prices and have been used in many applications. These cameras have relatively high error sources due to a variety of reasons. The reasonable noise investigations and a couple of studies for the jitter analysis on the AMCW ToF range imaging were found in the literature. These were thoroughly described in Chapters 2 and 3, which are the literature review section of this thesis.

Before this thesis, there was a huge gap in the analysis of jitter present in the AMCW ToF ranging systems, namely, the jitter extraction, the effect of jitter, what types and what amounts of jitter have more effect on range measurements related to the AMCW ToF ranging. Most of these were largely uninvestigated in the literature. Because of this lack of jitter investigation, the objective of this thesis became analysing, experimenting and designing theoretical models that have not been performed previously. Based on this undertaking, enhancements have been developed and successfully incorporated to significantly improve the quality of the achievements. Thus, this thesis has contributed to minimizing the above mentioned gaps as much as possible. These are analysed in the next two sections which correspond to jitter extraction with measurement explored in Chapters 4 to 6 and the jitter influence on

the AMCW ToF range imaging systems was inspected in Chapters 7 and 8 of this thesis.

Throughout this thesis, real and simulated data was used for empirical analysis and verification of algorithms. Thus, the algorithms and the results in this thesis can be supported to investigate the periodic and random jitter on the illumination signal in most of the AMCW ToF range imaging cameras. The remainder of this chapter is divided into two parts: a summary of the obtained results with achieved improvements. Next, some interesting extensions for future investigation on the jitter in AMCW ToF ranging are pointed out.

9.1 Summary of Findings

The extraction and measurement of jitter in AMCW ToF range imaging cameras were investigated in the second section of this thesis (Chapters 4 to 6). Since it is difficult to access signals inside the camera, the light source of the camera was investigated. An algorithm was proposed for real time jitter extraction on the emitted light source signal of the AMCW ToF range imaging cameras. The most important advantage of this proposed algorithm is that a reference clock signal is not needed to trigger the time measurement unit and Fourier analysis and some signal processing techniques are used instead. In addition, this algorithm is camera independent and can be used to extract jitter on both digital and analogue signals of any kind of shape (sinusoidal, triangular, rectangular). However, because the modulated light source does not carry a data stream, only RJ and PJ were decomposed from the illumination signal. Other types of jitter are only relevant to communication channels. In order to verify the proposed algorithm, first it was tested on simulated data and the results showed a reasonable accuracy in the jitter measurements. As examples, it was given (4.5 ± 0.3) ps and (4.93 ± 0.04) ps when we injected only a RJ of RMS 5 ps and only a PJ of 5 ps, respectively. However, it proved difficult sometimes to separate the PJ accurately when RJ is a large fraction of the total jitter.

Then, the proposed algorithm was experimentally tested with the emitted light signal of two AMCW ToF cameras, namely, MESA Imaging SR4000 and Softkinetic DS325. For control, a signal with the corresponding modulation frequency of the cameras was generated with a signal generator (HP Agilent 8648B) and measured with the oscilloscope. In order to control the uncertainties, 100 acquisitions for each experimental setup were captured. From the

experiments, the periodic jitter was found at two frequencies in both cameras. For the MESA SR4000, the PJ of frequencies of 0.064 and (5.09 ± 0.06) MHz with the amplitudes of (71.5 ± 0.3) and (14.0 ± 1.4) ps, respectively. For the DS325, PJ was found at (0.399 ± 0.003) and (2.905 ± 0.009) MHz with the amplitudes of (61.0 ± 5.2) and (36.3 ± 3.5) ps, respectively. Between the two cameras, a relatively larger random jitter was found in the SR4000 with RMS of (159.6 ± 0.1) ps than for the DS325 with RMS of (40.37 ± 0.04) ps. We found evidence of flicker noise in the MESA SR4000 camera which was found to behave as ($f^{-0.94\pm0.02} \approx 1/f$). As expected, there was no periodic jitter in the signal generator and we believe the oscilloscope measurements were very accurate.

Next, the real-time oscilloscope was replaced by a much cheaper measuring instrument, a SDR USB dongle, to measure the jitter on the same two depth cameras. This dongle is based on one of the emerging technologies in communication: software defined radio technology. Interesting results were found in the experiments. With the comparison of the results from the oscilloscope, we were able to obtain some accurate results with the limitations of the measuring device. They are (1) the SDR dongle can be used to measure the periodic and random jitter only up to half of the intermediate-frequency (IF) obtained from the down shift of the amplified radio frequency (e.g., RF = 30 MHz) with the local oscillator (e.g., LO = 29.6 MHz) which can be substantially less than the Nyquist frequency (e.g., 3.2/2 = 1.6 MHz) of the dongle, (2) when the sampling frequency is less (i.e., if the number of sample points is an insufficient amount in a cycle), then this SDR dongle cannot be used for jitter measurement since the signal is not properly (smoothly) represented. In that situation, it can give incorrect jitter amounts. From the experiments, for SR4000, the periodic jitter at (62.5 ± 1.1) kHz with the amplitude (63.5 ± 1.8) ps and random jitter with RMS of (70.0 ± 0.2) ps are found which verifies the above limitation (1) where the frequencies are less than half of the IF, that is, (30 − 29.6) MHz/2 = 200 kHz. However, due to the above limitation (2), the experiment on the DS325 camera with this dongle was not carried out. In order to calculate the jitter amounts, it was needed to use the ratio of the number of samples per cycle between the oscilloscope and SDR dongle.

The period and random jitter influence on the range measurements is reported in Chapters 7 and 8, respectively. An analytical model to investigate the influence of the periodic jitter on the range measurements under the heterodyne and homodyne operations in AMCW ToF range imaging cameras was

obtained with the help of the Fourier analysis and some standard mathematical functions. The obtained model was tested with simulated data. We found that the phase difference of the periodic jitter between the emitted light and shutter signals of the camera $\phi^s_{_{PJ}}$, the modulation frequency f, the integration period T, the amplitude of the periodic jitter A_{PJ} and the relationship of the periodic jitter frequency f_{PJ} to the modulation frequency are the factors that influence the periodic jitter on range measurements. However, the influence can be compensated by adjusting the integration period of the camera.

For the chosen phase errors $\phi_{\mathrm{err}} = \{0.1, 0.01, 0.001\}$ rad the periodic jitter influences range measurements when the integration period $T = 0.01$ ms for certain amplitudes of the periodic jitter A_{PJ} and modulation frequencies f_{PJ}. When the periodic jitter is at $f_{\mathrm{PJ}} = 4.9261$ MHz (in Figure 7.5) and at $f_{\mathrm{PJ}} = 5$ MHz (in Figure 7.13), there is evidence that the starting influence range of $[A_{\mathrm{PJ}}, f_{\mathrm{PJ}}]$ is proportional to the T with slightly different amounts in each f_{PJ}. Since, the two AMCW ToF cameras used have low modulation frequencies (30 MHz for SR4000 and 50 MHz for DS325) with low amplitudes of periodic jitter ($A_{\mathrm{PJ}} = (71.5 \pm 0.3)$ and (14.0 ± 1.4) ps for SR4000 while $A_{\mathrm{PJ}} = (61.0 \pm 5.2)$ and (36.3 ± 3.5) ps for DS325), we concluded that the periodic jitter in the light sources of each camera do not influence range measurements.

We are recommending when the integration period $T = 0.01$ ms and the modulation frequency of the camera is $f = 200$ MHz then the amplitude of the PJ should be $A_{\mathrm{PJ}} < 700$ ps while when $f = 1000$ MHz it should be $A_{\mathrm{PJ}} < 180$ ps. For the middle values of the parameters, the periodic jitter does not influence when $A_{\mathrm{PJ}} < 400$ ps for $f = 400$ MHz in order to prevent the phase errors of $\phi_{\mathrm{err}} = 0.001$ and 0.01 rad on range measurements. In addition, these recommended values of A_{PJ} for modulation frequency f should be further reduced when the integration period of the camera is reduced. Thus, the periodic jitter influences current AMCW ToF ranging cameras (since $f <$ 100 MHz) if the integration period $T \leq 1$ μs. In future, the depth sensor manufacturers will increase the resolution range of ToF cameras by using high modulation frequencies and very high frame rates which are the factors that affect integration periods of the cameras.

In Chapter 8, the stochastic model for the correlation function of the AMCW range imaging was investigated to identify the influence of the random jitter on range measurements. It was assumed that the random jitter follows the Gaussian distribution. The simulated data was used with the help of 500 independent evaluations of the Monte Carlo method to estimate the

result for the model obtained. Two non-parametric estimations were used to identify the PDF for the standard deviation of the phase error $\sigma_{\phi_{\text{err}}}$. Thirty repetitions for each setup with the independent evaluations were performed for various parameters such as modulation frequency f, RMS of random jitter σ_{RJ} and fixed integration period $T = 1$ ms. For the random jitter, slightly different RMS amounts (σ_l, σ_s) for light and shutter signals were used for each setup throughout the simulations. However, for the mean of the random jitter (μ_l, μ_s), zero values were chosen since they are unbiased with data hence the phase error can be settled by an offset adjustment.

We found that the random jitter is not sufficiently influenced in current AMCW ToF cameras since their modulation frequencies are relatively low (less than 100 MHz). By analysis, the standard deviation of the phase error (typical) from the stochastic model was evident that the random jitter is starting to influence range measurements when $f = 400$ MHz with random jitter of 140 ps has a measurable affect on ranging for the phase error of 10^{-4} rad criterion and this RMS amount is further reduced to 115 ps when the modulation frequency 600 MHz. As examples, the measurable typical range error $\sigma_{d_{\text{err}}} \approx \{5.32, 30.69, 22.09, 21.71\}$ mm occurred for $f = \{400, 600, 800, 1000\}$ MHz when the random jitter of RMS $\sigma_{\text{RJ}} = \{1000, 800, 600, 600\}$ ps, respectively.

9.2 Future Investigations

During the last decade, the ToF range imaging cameras have significantly improved and have been used in various applications from agricultural sectors to engineering industries. With the improvement of the technology to build the depth sensor, novel applications of ToF range imaging will increase. At present, more researchers are mainly focused on the noise investigation in these cameras. However, from this thesis, we found that the jitter significantly influences range measurements therefore it is worth further investigating jitter in ToF range imaging systems. Several investigations could be extended to further perform the ToF range imaging systems due to the jitter influence on measurements as follows.

The proposed methodology in Chapters 4 and 5 could be extended to correct range measurements after extracting and measuring the RJ and PJ in the light signal of the camera. This will be very useful since the available jitter can be compensated before the measurement. Since for a particular configuration of the AMCW camera (e.g., with default modulation frequency and integra-

tion period), the periodic and random jitter in the illumination source is fixed amounts which can be computed with the proposed methodology. Then, considering the benchmark numerical results in Chapters 7 and 8 for the influence of the periodic and random jitter on range measurements, respectively, can be applied for compensating of the measurement. In addition, the proposed algorithm may be applied to extract the jitter in other types of ToF range imaging cameras such as pulse based and pseudo-noise based modulation cameras. This methodology can be used for jitter measurement in any kind of application where the reference clock signal cannot be accessed.

A cheaper SDR USB dongle with the proposed algorithm for jitter extraction in ToF cameras at lower frequencies in the RF signal was investigated in Chapter 6. The high sample rates and high quality of SDRs can be used to explore the relatively large range of frequencies of the PJ and RJ in the light source of the AMCW ToF cameras by setting a suitable local oscillator frequency to get a large intermediate frequency (less than the Nyquist frequency) in the dongle. Also, this concept may be used to find the jitter in the light source of the aforementioned two modulation types of ToF range imaging cameras as well as in any other relevant applications. In addition, it may possible to modify the DSP engine in the dongle which is a software based controller in order to get maximum benefit but this may not be a straightforward process.

In Chapter 7, the influence of the periodic jitter on range measurements was investigated. Can we compensate the PJ amount in the first phase step (by determining and correcting it) before it proceeds to the second phase step and so on, in the correlation function within the integration period? With the influence of the PJ in each phase step a constant (a fixed amount), then it can be further analysed with the crosstalking between phase steps, during the integration period. But if it is not a constant (i.e., random behaviour), then it will be difficult to compensate for the influence of the PJ on range measurements. Thus, this is a more challenging task for future investigation that arises from Chapter 7. On the other hand, here the periodic jitter at a single frequency was considered. But in practice, the ToF cameras may have periodic jitter at multiple frequencies. Then, it is very interesting to know how the analytical model will change accordingly. Will the influence be linear or non-linear and will it be partially or fully cancel on range measurements? So, some interesting questions arise from this future investigation.

A finite number of evaluations of the Monte Carlo simulation were used to investigate the influence of random jitter on range measurements in Chapter 8.

With increasing the number of simulations, it is surprisingly effective to estimate the better result than the current one. In order to understand the impact of uncertainty of the results obtained, it is necessary to analyse the stochastic model for the full range of possible outcomes, to get much more accurate results. On the other hand, all simulations were done at fixed integration period $T = 1$ ms and it is interesting to investigate the behaviour of the random jitter for various T, especially for less than 1 ms integration period since now the depth sensor manufacturers are trying to develop the AMCW ToF cameras with short integration periods. However, according to the central limit theorem, the Gaussian distribution was assumed for random jitter in the correlation function. But is it true, maybe another known or unknown distribution? This study can be further investigated by choosing a different standard distribution or prediction one for the random jitter.

Another interesting extension of this study is what kind of behaviour occurs when both periodic and random jitter present in the correlation function. Will it be possible to obtain a comprehensive analytical model to investigate their influence on range measurements?

References

Abramowitz, M. and I. A. Stegun. *Handbook of mathematical functions: with formulas, graphs, and mathematical tables*, volume 55. Courier Corporation (1965).

Anthonys, G., M. J. Cree, and L. Streeter. Jitter extraction in a noisy signal by fast Fourier transform and time lag correlation. In: *Applied Mechanics and Materials*, volume 884, pp. 113–121. Trans Tech Publ (2018a).

Anthonys, G., M. J. Cree, and L. Streeter. Signal processing approaches for jitter extraction in time-of-flight range imaging cameras. In: *12th International Conference on Signal Processing and Communication Systems (ICSPCS)*, pp. 1–9. Cairns, Australia (2018b).

Anthonys, G., M. J. Cree, and L. Streeter. Jitter measurement in digital signals by using software defined radio technology. In: *2019 IEEE International Instrumentation and Measurement Technology Conference (I2MTC)*, pp. 1–5. Auckland, New Zealand (2019).

Balakrishnan, V. All about the Dirac delta function (?). *Resonance*, **8(8)**, pp. 48–58 (2003).

Beheim, G. and K. Fritsch. Range finding using frequency-modulated laser diode. *Applied Optics*, **25(9)**, pp. 1439–1442 (1986).

Bennett, C. A., N. L. Franklin, *et al. Statistical analysis in chemistry and the chemical industry*. Wiley (1954).

Bevington, P. R. and D. K. Robinson. *Data reduction and error analysis for the physical sciences*. McGraw-Hill, third edition (2003).

Bhandari, A., A. Kadambi, R. Whyte, C. Barsi, M. Feigin, A. Dorrington, and R. Raskar. Resolving multipath interference in time-of-flight imaging via modulation frequency diversity and sparse regularization. *Optics letters*, **39(6)**, pp. 1705–1708 (2014).

Blackman, R. B. and J. W. Tukey. The measurement of power spectra from the point of view of communications engineering Part I. *The Bell System Technical Journal*, **37(1)**, pp. 185–282 (1958).

Blais, F. Review of 20 years of range sensor development. *Journal of Electronic Imaging*, **13(1)**, pp. 231–244 (2004).

Blais, F., J. A. Beraldin, and S. F. El-Hakim. Range error analysis of an integrated time-of-flight, triangulation, and photogrammetric 3d laser scanning system. In: *Laser Radar Technology and Applications V*, volume 4035, pp. 236–248. International Society for Optics and Photonics (2000).

Blitzstein, J. K. and J. Hwang. *Introduction to probability*. Chapman and Hall/CRC (2014).

Boucher, R. and J. Hassab. Analysis of discrete implementation of generalized cross correlator. *IEEE Transactions on Acoustics, Speech, and Signal Processing*, **29(3)**, pp. 609–611 (1981).

Busemeyer, L., D. Mentrup, K. Möller, E. Wunder, K. Alheit, V. Hahn, H. Maurer, J. Reif, T. Würschum, J. Müller, *et al.* BreedVision — A multi-sensor platform for non-destructive field-based phenotyping in plant breeding. *Sensors*, **13(3)**, pp. 2830–2847 (2013).

Büttgen, B., F. Lustenberger, P. Seitz, *et al.* Pseudonoise optical modulation for real-time 3-d imaging with minimum interference. *IEEE Transactions on Circuits and Systems I: Regular Papers*, **54(10)**, pp. 2109–2119 (2007).

Büttgen, B., T. Oggier, M. Lehmann, R. Kaufmann, and F. Lustenberger. CCD/CMOS lock-in pixel for range imaging: Challenges, limitations and state-of-the-art. *1st range imaging research day*, pp. 21–32 (2005).

Carobbi, C. F. and M. Cati. The absolute maximum of the likelihood function of the Rice distribution: Existence and uniqueness. *IEEE Transactions on Instrumentation and Measurement*, **57(4)**, pp. 682–689 (2008).

Céspedes, I., Y. Huang, J. Ophir, and S. Spratt. Methods for estimation of subsample time delays of digitized echo signals. *Ultrasonic imaging*, **17(2)**, pp. 142–171 (1995).

Chapra, S. C. and R. P. Canale. *Numerical Methods for Engineers*, volume 7. McGraw-Hill New York (2015).

Chiabrando, F., R. Chiabrando, D. Piatti, and F. Rinaudo. Sensors for 3D imaging: Metric evaluation and calibration of a CCD/CMOS time-of-flight camera. *Sensors*, **9(12)**, pp. 10080–10096 (2009).

Cohen, R. Jitter and signal noise in frequency sources. Technical report, Raltron Electronics Corp, Miami, Florida 33172, U.S.A. (2005).

Conroy, R. M., A. A. Dorrington, R. Künnemeyer, and M. J. Cree. Range imager performance comparison in homodyne and heterodyne operating modes. In: *Three-Dimensional Imaging Metrology, Proc. SPIE*, volume 7239, pp. 1–10 (2009).

Consultative Committee for Space Data Systems. Pseudo-Noise (PN) Ranging Systems (2014).

Cosart, L. D., L. Peregrino, and A. Tambe. Time domain analysis and its practical application to the measurement of phase noise and jitter. *IEEE Transactions on Instrumentation and Measurement*, **46(4)**, pp. 1016–1019 (1997).

Dahlquist, G. and A. Bjorck. *Numerical Methods in Scientific Computing: Volume 1*, volume 103. Society for Industrial and Applied Mathematics (2008).

Dal Mutto, C., P. Zanuttigh, and G. M. Cortelazzo. *Time-of-flight cameras and Microsoft Kinect™*. Springer Science & Business Media (2012).

Davenport, D. M. Wireless communication with a mobile asset employing dynamic configuration of a software defined radio (2005). US Patent 6,937,877.

Dorrington, A., J. Godbaz, M. Cree, A. Payne, and L. Streeter. Separating true range measurements from multi-path and scattering interference in commercial range cameras. In: *IS&T/SPIE Electronic Imaging, Proc. SPIE*, volume 7864, pp. 1–10 (2011).

Dou, Q. and J. A. Abraham. Jitter decomposition by time lag correlation. In: *Proceedings of the 7th International Symposium on Quality Electronic Design*, pp. 525–530. IEEE Computer Society (2006).

Falie, D. and V. Buzuloiu. Noise characteristics of 3D time-of-flight cameras. In: *2007 International Symposium on Signals, Circuits and Systems*, volume 1, pp. 1–4. IEEE (2007).

Foix, S., G. Alenya, and C. Torras. Lock-in time-of-flight (tof) cameras: A survey. *IEEE Sensors Journal*, **11(9)**, pp. 1917–1926 (2011).

Franks, L. and J. Bubrouski. Statistical properties of timing jitter in a pam timing recovery scheme. *IEEE Transactions on Circuits and Systems*, **21(4)**, pp. 489–496 (1974).

Freedman, D. and P. Diaconis. On the histogram as a density estimator: L_2 theory. *Probability theory and related fields*, **57(4)**, pp. 453–476 (1981).

Freedman, D., Y. Smolin, E. Krupka, I. Leichter, and M. Schmidt. Sra: Fast removal of general multipath for tof sensors. In: *Computer Vision–ECCV 2014*, pp. 234–249. Springer (2014).

Fuchs, S. and G. Hirzinger. Extrinsic and depth calibration of tof-cameras. In: *Computer Vision and Pattern Recognition, 2008. CVPR 2008. IEEE Conference on*, pp. 1–6 (2008).

Fuchs, S. and S. May. Calibration and registration for precise surface reconstruction with time-of-flight cameras. *Int. J. Intell. Syst. Technol. Appl.*, **5(3/4)**, pp. 274–284 (2008).

Fuchs, S., M. Suppa, and O. Hellwich. Compensation for multipath in tof camera measurements supported by photometric calibration and environment integration. In: *Computer Vision Systems*, pp. 31–41. Springer (2013).

Fürsattel, P., S. Placht, M. Balda, C. Schaller, H. Hofmann, A. Maier, and C. Riess. A comparative error analysis of current time-of-flight sensors. *IEEE Transactions on Computational Imaging*, **2(1)**, pp. 27–41 (2016).

Ganapathi, V., C. Plagemann, D. Koller, and S. Thrun. Real time motion capture using a single time-of-flight camera. In: *2010 IEEE Computer Society Conference on Computer Vision and Pattern Recognition*, pp. 755–762. IEEE (2010).

Garcia, A. L. *Numerical methods for physics*. Prentice Hall Englewood Cliffs, NJ, second edition (2000).

Geller, M. and E. Ng. A table of integrals of the error function. ii. additions and corrections. *J. Res. Natl. Bur. Stand.*, **75**, pp. 149–163 (1971).

Geller, M. and E. W. Ng. A table of integrals of the exponential integral. *Journal of Research of the National Bureau of Standards B*, **73B(3)**, pp. 1–20 (1969).

Godbaz, J. P., M. J. Cree, and A. A. Dorrington. Understanding and ameliorating non-linear phase and amplitude responses in AMCW lidar. *Remote Sensing*, **4(1)**, pp. 21–42 (2011).

Godbaz, J. P., M. J. Cree, and A. A. Dorrington. Closed-form inverses for the mixed pixel/multipath interference problem in AMCW lidar. In: *IS&T/SPIE Electronic Imaging*, pp. 829618–829618. International Society for Optics and Photonics (2012).

Gudmundsson, S. A., H. Aanæs, and R. Larsen. Environmental effects on measurement uncertainties of time-of-flight cameras. In: *Signals, Circuits and Systems, 2007. ISSCS 2007. International Symposium on*, volume 1, pp. 1–4. IEEE (2007).

Hall, P. S., P. Gardner, and A. Faraone. Antenna requirements for software defined and cognitive radios. *Proceedings of the IEEE*, **100(7)**, pp. 2262–2270 (2012).

Hancock, J. and S. Draving. Jitter-understanding it, measuring it, eliminating it; part 2: Jitter measurements. *High Frequency Electronics*, pp. 20–28 (2004).

Hancock, J. *et al.* Jitter-understanding it, measuring it, eliminating it; part 1: Jitter fundamentals. *High Frequency Electronics*, **4(4)**, pp. 44–50 (2004).

Hansard, M., S. Lee, O. Choi, and R. P. Horaud. *Time-of-flight cameras: principles, methods and applications*. Springer Science & Business Media (2012).

Härdle, W. *et al. Smoothing techniques: with implementation in S*. Springer Science & Business Media (1991).

Haykin, S. S. and M. Moher. *An introduction to analog and digital communications*. John Wiley & Sons, second edition (2007). ISBN 9780471432227.

He, Y., B. Liang, Y. Zou, J. He, and J. Yang. Depth errors analysis and correction for time-of-flight (tof) cameras. *Sensors*, **17(1)**, p. 92 (2017).

Henry, P., M. Krainin, E. Herbst, X. Ren, and D. Fox. Rgb-d mapping: Using depth cameras for dense 3d modeling of indoor environments. In: *12th International Symposium on Experimental Robotics (ISER*. Citeseer (2010).

Horaud, R., M. Hansard, G. Evangelidis, and C. Ménier. An overview of depth cameras and range scanners based on time-of-flight technologies. *Machine vision and applications*, **27(7)**, pp. 1005–1020 (2016).

Hosking, R. H. *Software-Defined Radio Handbook*. Pentek Inc, 12th edition (2016).

Hussmann, S. and T. Edeler. Pseudo-four-phase-shift algorithm for performance enhancement of 3D-TOF vision systems. *IEEE Transactions on Instrumentation and Measurement*, **59(5)**, pp. 1175–1181 (2010).

Hussmann, S., A. Hermanski, and T. Edeler. Real-time motion supression in tof range images. In: *Instrumentation and Measurement Technology Conference (I2MTC), 2010 IEEE*, pp. 697–701. IEEE (2010).

Hussmann, S., A. Hermanski, and T. Edeler. Real-time motion artifact suppression in tof camera systems. *IEEE Transactions on Instrumentation and Measurement*, **60(5)**, pp. 1682–1690 (2011).

Hussmann, S., F. Knoll, and T. Edeler. Modulation method including noise model for minimizing the wiggling error of tof cameras. *IEEE Transactions on Instrumentation and Measurement*, **63(5)**, pp. 1127–1136 (2014).

Jähne, B. *Computer vision and applications*: *a guide for students and practitioners*. Elsevier (2000).

Jamtsho, S. and D. D. Lichti. Modelling scattering distortion in 3D range camera. *International Archives of Photogrammetry, Remote Sensing and Spatial Information Sciences*, **38(5)**, pp. 299–304 (2010).

Jimenez, D., D. Pizarro, and M. Mazo. Single frame correction of motion artifacts in pmd-based time of flight cameras. *Image and Vision Computing*, **32(12)**, pp. 1127–1143 (2014).

Jiménez, D., D. Pizarro, M. Mazo, and S. Palazuelos. Modeling and correction of multipath interference in time of flight cameras. *Image and Vision Computing*, **32(1)**, pp. 1–13 (2014).

Jin, X.-L. and S.-Q. Zeng. Design of 3D tof camera system based on CW modulation technique. In: *2016 13th IEEE International Conference on Solid-State and Integrated Circuit Technology (ICSICT)*, pp. 373–375 (2016).

Johnson, J. B. Thermal agitation of electricity in conductors. *Nature*, **119(2984)**, p. 50 (1927).

Jondral, F. K. Software-defined radio: basics and evolution to cognitive radio. *EURASIP journal on wireless communications and networking*, **2005(3)**, pp. 275–283 (2005).

Jongenelen, A. P., A. D. Payne, D. A. Carnegie, A. A. Dorrington, and M. J. Cree. Development of a real-time full-field range imaging system. In: *Recent Advances in Sensing Technology*, pp. 113–129. Springer (2009).

Kahlmann, T. and H. Ingensand. Calibration and development for increased accuracy of 3D range imaging cameras. *Journal of Applied Geodesy*, **2(1)**, pp. 1–11 (2008).

Kahlmann, T., F. Remondino, and H. Ingensand. Calibration for increased accuracy of the range imaging camera swissranger ^{TM}. In: *Image Engineering and Vision Metrology*, volume 36 of *3*, pp. 136–141 (2006).

Karp, J. S., S. Surti, M. E. Daube-Witherspoon, and G. Muehllehner. The benefit of time-of-flight in pet imaging: Experimental and clinical results. *Journal of nuclear medicine: official publication, Society of Nuclear Medicine*, **49(3)**, p. 462 (2008).

Kawala-Sterniuk, A., M. Podpora, M. Pelc, M. Blaszczyszyn, E. J. Gorzelanczyk, R. Martinek, and S. Ozana. Comparison of smoothing filters in analysis of EEG data for the medical diagnostics purposes. *Sensors*, **20(3)**, p. 807 (2020).

Kim, Y. M., D. Chan, C. Theobalt, and S. Thrun. Design and calibration of a multi-view tof sensor fusion system. In: *Computer Vision and Pattern Recognition Workshops, 2008. CVPRW '08. IEEE Computer Society Conference on*, pp. 1–7 (2008).

Klose, R., J. Penlington, and A. Ruckelshausen. Usability study of 3D time-of-flight cameras for automatic plant phenotyping. **69**, pp. 93–105 (2009).

Kolb, A., E. Barth, R. Koch, and R. Larsen. Time-of-flight cameras in computer graphics. In: *Computer Graphics Forum*, volume 29, pp. 141–159. Wiley Online Library (2010).

Kraft, H., J. Frey, T. Moeller, M. Albrecht, M. Grothof, B. Schink, H. Hess, and B. Buxbaum. 3D-camera of high 3D-frame rate, depth-resolution and background light elimination based on improved PMD (photonic mixer device)-technologies. *OPTO, Nuernberg, May* (2004).

Krishnan, S. R. and C. S. Seelamantula. On the selection of optimum Savitzky-Golay filters. *IEEE transactions on signal processing*, **61(2)**, pp. 380–391 (2012).

Kuo, A., T. Farahmand, N. Ou, S. Tabatabaei, and A. Ivanov. Jitter models and measurement methods for high-speed serial interconnects. In: *Test Conference, 2004. Proceedings. ITC 2004. International*, pp. 1295–1302. IEEE (2004).

Kuo, A., R. Rosales, T. Farahmand, S. Tabatabaei, and A. Ivanov. Crosstalk bounded uncorrelated jitter (buj) for high-speed interconnects. *IEEE Transactions on Instrumentation and measurement*, **54(5)**, pp. 1800–1810 (2005).

Kuyel, T. Method and system for measuring jitter (2003). US Patent 6,640,193.

Lackey, R. and D. W. Upmal. Speakeasy: the military software radio. *IEEE Communications Magazine*, **33(5)**, pp. 56–61 (1995).

Lange, R. and P. Seitz. Solid-state time-of-flight range camera. *IEEE Journal of Quantum Electronics*, **37(3)**, pp. 390–397 (2001).

Lange, R., P. Seitz, A. Biber, and R. Schwarte. Time-of-flight range imaging with a custom solid state image sensor. In: *Laser Metrology and Inspection*, volume 3823, pp. 180–192. International Society for Optics and Photonics (1999).

Langmann, B., K. Hartmann, and O. Loffeld. Depth camera technology comparison and performance evaluation. In: *ICPRAM (2)*, pp. 438–444 (2012).

Laufer, C. and E. J. Hoffman. *The Hobbyist's Guide to the RTL-SDR: Really Cheap Software Defined Radio: A Guide to the RTL-SDR and Cheap Software Defined Radio by the Authors of the RTL-SDR.com Blog*. Carl Laufer (2016).

Lee, S. Time-of-flight depth camera motion blur detection and deblurring. *IEEE Signal Processing Letters*, **21(6)**, pp. 663–666 (2014).

Li, L. Time-of-flight camera - an introduction. Technical report, Texas Instruments - Technical White Paper, Dallas, Texas 75265, U.S.A. (2014).

Li, M. *Jitter, Noise, and Signal Integrity at High-speed*. Prentice Hall Press, Upper Saddle River, NJ, USA, first edition (2007). ISBN 9780132429610.

Li, M. P., J. Wilstrup, R. Jessen, and D. Petrich. A new method for jitter decomposition through its distribution tail fitting. In: *International Test Conference 1999. Proceedings (IEEE Cat. No. 99CH37034)*, pp. 788–794. IEEE (1999).

Lindner, M. and A. Kolb. Lateral and depth calibration of PMD-distance sensors. In: *Proceedings of the Second International Conference on Advances in Visual Computing - Volume Part II*, ISVC'06, pp. 524–533. Springer-Verlag, Berlin, Heidelberg (2006). ISBN 3-540-48626-7, 978-3-540-48626-8.

Lindner, M. and A. Kolb. Compensation of Motion Artifacts for Time-of-Flight Cameras. *Lecture Notes in Computer Science*, **5742**, p. 16 (2009).

Lindner, M., I. Schiller, A. Kolb, and R. Koch. Time-of-flight sensor calibration for accurate range sensing. *Comput. Vis. Image Underst.*, **114(12)**, pp. 1318–1328 (2010).

Liu, X. and K. Fujimura. Hand gesture recognition using depth data. In: *6th International Conference on Automatic Face and Gesture Recognition*, p. 529. IEEE (2004).

Lottner, O., A. Sluiter, K. Hartmann, and W. Weihs. Movement artefacts in range images of time-of-flight cameras. In: *2007 International Symposium on Signals, Circuits and Systems*, volume 1, pp. 1–4 (2007).

Lyons, R. G. *Understanding Digital Signal Processing*. Pearson Education, Inc., Boston, MA, USA, third edition (2011).

Maeland, E. On the comparison of interpolation methods. *IEEE transactions on medical imaging*, **7(3)**, pp. 213–217 (1988).

Marco, J., Q. Hernandez, A. Munoz, Y. Dong, A. Jarabo, M. H. Kim, X. Tong, and D. Gutierrez. DeepToF: off-the-shelf real-time correction of multipath interference in time-of-flight imaging. *ACM Transactions on Graphics (ToG)*, **36(6)**, p. 219 (2017).

May, S., B. Werner, H. Surmann, and K. Pervolz. 3d time-of-flight cameras for mobile robotics. In: *Intelligent Robots and Systems, 2006 IEEE/RSJ International Conference on*, pp. 790–795. IEEE (2006).

McCarthy, A., N. J. Krichel, N. R. Gemmell, X. Ren, M. G. Tanner, S. N. Dorenbos, V. Zwiller, R. H. Hadfield, and G. S. Buller. Kilometer-range, high resolution depth imaging via 1560 nm wavelength single-photon detection. *Optics express*, **21(7)**, pp. 8904–8915 (2013).

Mitola, J. Software radios: Survey, critical evaluation and future directions. *IEEE Aerospace and Electronic Systems Magazine*, **8(4)**, pp. 25–36 (1993).

Moller, T., H. Kraft, J. Frey, M. Albrecht, and R. Lange. Robust 3D measurement with pmd sensors. In: *In: Proceedings of the 1st Range Imaging Research Day at ETH*, pp. 3–906467 (2005).

Monson, T. C., J. W. Grantham, S. W. Childress, J. T. Sackos, R. O. Nellums, and S. M. Lebien. Characterization of scannerless ladar. In: *Laser Radar Technology and Applications IV*, volume 3707, pp. 409–421. International Society for Optics and Photonics (1999).

Moon, U.-K., K. Mayaram, and J. T. Stonick. Spectral analysis of time-domain phase jitter measurements. *IEEE Transactions on Circuits and Systems II: Analog and Digital Signal Processing*, **49(5)**, pp. 321–327 (2002).

Moring, I., T. Heikkinen, R. Myllyla, and A. Kilpela. Acquisition of three-dimensional image data by a scanning laser range finder. *Optical engineering*, **28(8)**, p. 288897 (1989).

Mufti, F. and R. Mahony. Statistical analysis of signal measurement in time-of-flight cameras. {*ISPRS*} *Journal of Photogrammetry and Remote Sensing*, **66(5)**, pp. 720 – 731 (2011).

Mure-Dubois, J. and H. Hügli. Real-time scattering compensation for time-of-flight camera. In: *Proceedings of the ICVS Workshop on Camera Calibration Methods for Computer Vision Systems* (2007).

Nguyen, K., E. Fisher, A. Walton, and I. Underwood. An experimentally verified model for estimating the distance resolution capability of direct time of flight 3D optical imaging systems. *Measurement Science and Technology*, **24(12)**, p. 125001 (2013).

Nitzan, D., A. E. Brain, and R. O. Duda. The measurement and use of registered reflectance and range data in scene analysis. *Proceedings of the IEEE*, **65(2)**, pp. 206–220 (1977).

Oppenheim, A. V., R. W. Schafer, and J. R. Buck. *Discrete-time Signal Processing (2nd Ed.)*. Prentice-Hall, Inc., Upper Saddle River, NJ, USA (1999). ISBN 0-13-754920-2.

Oprisescu, S., D. Falie, M. Ciuc, and V. Buzuloiu. Measurements with tof cameras and their necessary corrections. In: *Signals, Circuits and Systems, 2007. ISSCS 2007. International Symposium on*, volume 1 (2007).

Orfanidis, S. *Introduction to Signal Processing*. Prentice Hall (1996).

Pang, H., J. Zhu, and W. Huang. Jitter decomposition by fast Fourier transform and time lag correlation. In: *Communications, Circuits and Systems, 2009. ICCCAS 2009. International Conference on*, pp. 365–368. IEEE (2009).

Patrin, J. and M. Li. Comparison and correlation of signal integrity measurement techniques. *DesignCon 2002* (2002).

Payne, A. D. *Development of a full-field time-of-flight range imaging system*. Ph.D. thesis, The University of Waikato (2008).

Payne, A. D., A. A. Dorrington, M. J. Cree, and D. A. Carnegie. Improved measurement linearity and precision for amcw time-of-flight range imaging cameras. *Appl. Opt.*, **49(23)**, pp. 4392–4403 (2010).

Persson, P.-O. and G. Strang. Smoothing by Savitzky-Golay and Legendre filters. In: *Mathematical systems theory in biology, communications, computation, and finance*, pp. 301–315. Springer (2003).

Pfeifer, N., D. Lichti, J. Böhm, and W. Karel. 3D cameras: Errors, calibration and orientation. In: *TOF Range-Imaging Cameras*, pp. 117–138. Springer (2013).

Piatti, D. and F. Rinaudo. SR-4000 and CamCube3.0 time of flight (ToF) cameras: Tests and comparison. *Remote Sensing*, **4(4)**, pp. 1069–1089 (2012).

Randall, R. B. *Frequency Analysis*. Brül & Kjor, third edition (1987).

Rapp, H., M. Frank, F. Hamprecht, and B. Jhne. A theoretical and experimental investigation of the systematic errors and statistical uncertainties of time-of-flight-cameras. *Int. J. Inte. Sys. Tech. and Appl.*, **5(3/4)** (2008).

Remondino, F. and D. Stoppa. *TOF Range-Imaging Cameras*. Springer Publishing Company, Incorporated (2013). ISBN 3642275222, 9783642275227.

Rice, S. Mathematical analysis of random noise-conclusion. *Instruments and Measurements, IEEE Transactions on*, **24**, pp. 46–156 (1945).

Robert, C. and G. Casella. *Monte Carlo statistical methods*. Springer Science & Business Media (2013).

Rohatgi, V. K. and A. M. E. Saleh. *An introduction to probability and statistics*. John Wiley & Sons (2015).

Rosenblatt, M. Remarks on some nonparametric estimates of a density function. *The Annals of Mathematical Statistics*, pp. 832–837 (1956).

Säckinger, E. *Broadband circuits for optical fiber communication*. John Wiley & Sons (2005).

Sadeghi, M. and F. Behnia. Optimum window length of Savitzky-Golay filters with arbitrary order. *arXiv preprint arXiv:1808.10489* (2018).

Salzer, H. Formulas for calculating the error function of a complex variable. *Mathematical Tables and Other Aids to Computation*, **5(34)**, pp. 67–70 (1951).

Sarbolandi, H., D. Lefloch, and A. Kolb. Kinect range sensing: Structured-light versus Time-of-Flight Kinect. *Computer vision and image understanding*, **139**, pp. 1–20 (2015).

Sarbolandi, H., M. Plack, and A. Kolb. Pulse based time-of-flight range sensing. *Sensors*, **18(6)** (2018).

Savitzky, A. and M. J. E. Golay. Smoothing and differentiation of data by simplified least squares procedures. *Analytical Chemistry*, **36(8)**, pp. 1627–1639 (1964).

Schäfer, H., F. Lenzen, and C. S. Garbe. Model based scattering correction in time-of-flight cameras. *Optics express*, **22(24)**, pp. 29835–29846 (2014).

Schamm, T., M. Strand, T. Gumpp, R. Kohlhaas, J. M. Zollner, and R. Dillmann. Vision and tof-based driving assistance for a personal transporter. In: *Advanced Robotics, 2009. ICAR 2009. International Conference on*, pp. 1–6. IEEE (2009).

Schmidt, M. and B. Jähne. Efficient and robust reduction of motion artifacts for 3d time-of-flight cameras. In: *3D Imaging (IC3D), 2011 International Conference on*, pp. 1–8. IEEE (2011).

Schwarte, R. Method and apparatus for determining the phases and/or amplitude information of an electromagnetic wave (1997).

Seiter, J., M. Hofbauer, M. Davidovic, and H. Zimmermann. Investigation of the distance error induced by cycle-to-cycle jitter in a correlating time-of-flight distance measurement system. *Optical Engineering*, **53(7)**, pp. 073104–073104 (2014).

Semiconductor, D. Clock (CLK) jitter and phase noise conversion. Technical report, Application Note 3359 (2007).

Servin, M., J. C. Estrada, and J. A. Quiroga. The general theory of phase shifting algorithms. *Opt. Express*, **17(24)**, pp. 21867–21881 (2009).

Sharma, V. K., J. N. Tripathi, R. Nagpal, S. Deb, and R. Malik. A comparative analysis of jitter estimation techniques. In: *Electronics, Communication and Computational Engineering (ICECCE), 2014 International Conference on*, pp. 125–130. IEEE (2014).

Shinagawa, M., Y. Akazawa, and T. Wakimoto. Jitter analysis of high-speed sampling systems. *IEEE Journal of Solid-State Circuits*, **25(1)**, pp. 220–224 (1990).

Silverman, B. W. *Density estimation for statistics and data analysis*. Chapman and Hall/CRC (1998).

Souders, T. M., D. R. Flach, C. Hagwood, and G. Yang. The effects of timing jitter in sampling systems. In: *Instrumentation and Measurement Technology Conference, 1989. IMTC-89. Conference Record., 6th IEEE*, pp. 199–203. IEEE (1989).

Soutschek, S., J. Penne, J. Hornegger, and J. Kornhuber. 3-d gesture-based scene navigation in medical imaging applications using time-of-flight cameras (2008).

Spirig, T., P. Seitz, O. Vietze, and F. Heitger. The lock-in CCD-two-dimensional synchronous detection of light. *IEEE Journal of quantum electronics*, **31(9)**, pp. 1705–1708 (1995).

Strand, O. N. A method for the computation of the error function of a complex variable. *Mathematics of computation*, **19(89)**, pp. 127–129 (1965).

Streeter, L. Stochastic calculus analysis of optical time-of-flight range imaging and estimation of radial motion. *Journal of the Optical Society of America A*, **34(7)**, pp. 1063–1072 (2017).

Streeter, L. Time-of-flight range image measurement in the presence of transverse motion using the Kalman filter. *IEEE Transactions on Instrumentation and Measurement*, **67(7)**, pp. 1573–1578 (2018).

Streeter, L., M. J. Cree, A. Dorrington, *et al.* A strategy for the correction of effects of jitter in amcw lidar images. In: *Image and Vision Computing New Zealand (IVCNZ), 2013 28th International Conference of*, pp. 500–505. IEEE (2013).

Streeter, L. and A. A. Dorrington. Coded exposure correction of transverse motion in full-field range imaging. *Optical Engineering*, **53(10)**, p. 102109 (2014).

Streeter, L. and A. A. Dorrington. Simple harmonic error cancellation in time of flight range imaging. *Optics Letters*, **40(22)**, pp. 5391–5394 (2015).

Tarczynski, A. and N. Allay. Spectral analysis of randomly sampled signals: suppression of aliasing and sampler jitter. *IEEE Transactions on Signal Processing*, **52(12)**, pp. 3324–3334 (2004).

Taylor, J. R. *An Introduction to Error Analysis*. University Science Books, Sausalito, California (1997).

Tong, J., J. Zhou, L. Liu, Z. Pan, and H. Yan. Scanning 3d full human bodies using kinects. *IEEE transactions on visualization and computer graphics*, **18(4)**, pp. 643–650 (2012).

Tuttlebee, W. *Software defined radio: origins, drivers and international perspectives*. Wiley, first edition (2002).

Tuttlebee, W. H. Software-defined radio: facets of a developing technology. *IEEE Personal Communications*, **6(2)**, pp. 38–44 (1999).

Tuttlebee, W. H. *Software defined radio: enabling technologies*. John Wiley & Sons (2003).

Vivó-Truyols, G. and P. J. Schoenmakers. Automatic selection of optimal Savitzky-Golay smoothing. *Analytical chemistry*, **78(13)**, pp. 4598–4608 (2006).

Whyte, R., A. Bhandari, L. Streeter, M. J. Cree, and A. A. Dorrington. Time frequency duality of time-of-flight range cameras for resolving multi-path interference. In: *Proceedings of the 29th International Conference on Image and Vision Computing New Zealand*, pp. 247–252. ACM, New York, NY, USA (2014a).

Whyte, R., L. Streeter, M. Cree, and A. Dorrington. Review of methods for resolving multi-path interference in time-of-flight range cameras. In: *Sensors Conference, 2014 IEEE*, pp. 629–632. Valencia, Spain (2014b).

Whyte, R., L. V. Streeter, M. J. Cree, and A. A. Dorrington. Resolving multiple propagation paths in time of flight range cameras using direct and global separation methods. *Optical Engineering*, **54(11)**, pp. 1–9 (2015).

Whyte, R. Z., A. D. Payne, A. A. Dorrington, and M. J. Cree. Multiple range imaging camera operation with minimal performance impact. In: *Image Processing: Machine Vision Applications III*, volume 7538, p. 75380I. International Society for Optics and Photonics (2010).

Wu, M., G. Chen, and D. Chen. ADC jitter estimation using a single frequency test without requiring coherent sampling. *IEICE Electronics Express*, **9(18)**, pp. 1485–1491 (2012).

Wu, M., Z. Liu, and D. Chen. Extracting random jitter and sinusoidal jitter in adc output with a single frequency test. *IEICE Electronics Express*, **12(20)**, pp. 20150742–20150742 (2015a).

Wu, M., Z. Liu, L. Xu, and D. Chen. Accurate and cost-effective technique for jitter and noise separation based on single-frequency measurement. *Electronics Letters*, **52(2)**, pp. 106–107 (2015b).

Yamaguchi, T. J., M. Ishida, H. X. Hou, D. Armstrong, K. Takayama, and M. Soma. An FFT-based jitter separation method for high-frequency jitter testing with a 10x reduction in test time. In: *Test Conference, 2007. ITC 2007. IEEE International*, pp. 1–8. IEEE (2007).

Yamaguchi, T. J., M. Soma, D. Halter, R. Raina, J. Nissen, and M. Ishida. A method for measuring the cycle-to-cycle period jitter of high-frequency clock signals. In: *VLSI Test Symposium, 19th IEEE Proceedings on. VTS 2001*, pp. 102–110. IEEE (2001).

Yamaguchi, T. J., M. Soma, M. Ishida, T. Watanabe, and T. Ohmi. Extraction of peak-to-peak and rms sinusoidal jitter using an analytic signal method. In: *VLSI Test Symposium, 2000. Proceedings. 18th IEEE*, pp. 395–402. IEEE (2000).

Yamaguchi, T. J., M. Soma, L. Malarsie, M. Ishida, and H. Musha. Timing jitter measurement of 10 Gbps bit clock signals using frequency division. In: *VLSI Test Symposium, 2002.(VTS 2002). Proceedings 20th IEEE*, pp. 207–212. IEEE (2002).

Zanuttigh, P., G. Marin, C. Dal Mutto, F. Dominio, L. Minto, and G. M. Cortelazzo. *Time-of-Flight and Structured Light Depth Cameras: Technology and Applications*. Springer (2016).

Zhang, Z. A flexible new technique for camera calibration. *IEEE Transactions on Pattern Analysis and Machine Intelligence*, **22**, pp. 1330–1334 (2000).

Zhao, A.-X., X.-J. Tang, Z.-H. Zhang, and J.-H. Liu. The parameters optimization selection of Savitzky-Golay filter and its application in smoothing pretreatment for FTIR spectra. In: *2014 9th IEEE Conference on Industrial Electronics and Applications*, pp. 516–521. IEEE (2014).

Appendix A

Mathematical Functions

Here we briefly introduce the Bessel function, error function and monotonic property of invertible functions that mainly used in Chapter 7.

A.1 Bessel function

Let i be the imaginary unit for complex $z = x + iy$, where $x, y \in \mathbb{R}$. One of the solution of the differential equation

$$z^2 \frac{d^2\omega}{dz^2} + z\frac{d\omega}{dz} + \left(z^2 - \nu^2\right)\omega = 0 \tag{A.1}$$

is $J_{\pm\nu}(z)$, the Bessel functions of the first kind with indices $\pm\nu$. This is a regular function of z throughout the z-plane cut along the negative real axis, and for fixed $z(\neq 0)$ is an entire function of ν. When ν is a integer (i.e., $\pm m$), then ν has no branch point and is an entire function of z. One of the integral representation of the Bessel function of the first kind of order m is given by (Abramowitz and Stegun, 1965)

$$J_m(x) = \frac{1}{2\pi}\int_{-\pi}^{\pi} e^{i(x\sin\theta - m\theta)}\, d\theta, \tag{A.2}$$

where θ is any angle in unit of radians by convention.

A.2 Error function

The error function encountered in integrating the normal distribution which is a normalized form of the Gaussian function. The error function erf(z) of the argument z (real or complex) with respect to η, defined by (Abramowitz and

Stegun, 1965)

$$\text{erf(z)} \equiv \frac{2}{\sqrt{\pi}} \int_0^z e^{-\eta^2}\, d\eta. \tag{A.3}$$

Some useful properties of error function (Geller and Ng, 1969, 1971; Strand, 1965; Salzer, 1951) are

$$\text{erf}(0) = 0, \quad \text{erf}(\infty) = 1, \quad \text{erf}(-z) = -\text{erf}(z). \tag{A.4}$$

A.3 Monotonic in Functions

An invertible function $y = g(x)$ on an interval (a, b) is:

- decreasing if $\forall x_1, x_2 \in (a, b) : x_1 < x_2 \implies g(x_1) \geq g(x_2)$;
- strictly decreasing if $\forall x_1, x_2 \in (a, b) : x_1 < x_2 \implies g(x_1) > g(x_2)$;
- increasing if $\forall x_1, x_2 \in (a, b) : x_1 < x_2 \implies g(x_1) \leq g(x_2)$;
- strictly increasing if $\forall x_1, x_2 \in (a, b) : x_1 < x_2 \implies g(x_1) < g(x_2)$.

If a function $y = g(x)$ is invertible on the interval (a, b) and belongs to one of the above types, this function is called monotonic on the given interval.

Appendix B

Statistical Theorems

In this appendix, we point out some definitions and proofs of the standard statistical main theorems used in Chapter 8. Besides, some useful formulas for calculating the uncertainty of the measurements is presented.

B.1 Definitions

This section includes the theorem of the *law of the unconscious statistician* (LOTUS) with definitions of the *cumulative distribution function* (CDF) of a continuous random variable.

B.1.1 Law of the Unconscious Statistician (LOTUS)

In order to find the expected value of a function $g(X)$ of continuous random variable X when the probability distribution of X is known but does not known the same for $g(X)$, then we can use the law of the unconscious statistician (LOTUS) theorem. Thus, the expected value of any function $g : \mathbb{R} \to \mathbb{R}$ of the variable X is given by

$$\mathbb{E}[g(X)] = \int_{-\infty}^{\infty} g(x) f_X(x)\, dx. \tag{B.1}$$

B.1.2 Cumulative Distribution Function of a Random Variable

The CDF of a continuous random variable X is another method to describe the distribution of random variables and is defined as

$$F_X(x) = \mathrm{P}(X \leq x), \qquad \text{for} \quad \forall x \in \mathbb{R}, \tag{B.2}$$

where $\mathrm{P}(X \leq x)$ is the probability that the random variable X is less than or equal to the element x.

B.2 Proofs

This section focuses the proof of some theorems, namely, LOTUS and the Gaussian integral.

B.2.1 LOTUS Theorem

If X is a continuous random variable with probability density function $f_X(x)$; then the mean of any function $g : \mathbb{R} \to \mathbb{R}$ is given by

$$\mathbb{E}[g(X)] = \int_{-\infty}^{\infty} g(x) f_X(x)\, dx, \tag{B.3}$$

where $y = g(x)$ for $\forall x \in \mathbb{R}$. Let $Y = g(X)$ is a strictly monotonic function (i.e., $g(x)$ is differentiable with its inverse $g^{-1}(y)$ is also monotonic) and the derivative is given by

$$\frac{d}{dy}\Big(g^{-1}(y)\Big) = \frac{1}{g'(g^{-1}(y))}, \tag{B.4}$$

By using the change of variables method, the right side of Equation B.1 can be formulated

$$\int_{-\infty}^{\infty} g(x) f_X(x)\, dx = \int_{-\infty}^{\infty} y\, f_X(g^{-1}(y)) \frac{1}{g'(g^{-1}(y))}\, dy \tag{B.5}$$

Also, we have

$$x = g^{-1}(y) \quad \to \quad dx = \frac{1}{g'(g^{-1}(y))} \qquad (\because \text{Equation B.4}). \tag{B.6}$$

On the other hand, from the cumulative distribution function, we have

$$\begin{aligned} F_Y(y) = \mathrm{P}(Y \leq y) = \mathrm{P}(g(X) \leq y) &= \mathrm{P}(X \leq g^{-1}(y)) \\ &= F_X(g^{-1}(y)). \end{aligned} \tag{B.7}$$

Then, by the chain rule, the PDF of Y is given by

$$f_Y(y) = f_X(g^{-1}(y)) \frac{1}{g'(g^{-1}(y))}. \tag{B.8}$$

Then from Equations B.5 and B.8, we have

$$\begin{aligned}\int_{-\infty}^{\infty} g(x) f_X(x)\, dx &= \int_{-\infty}^{\infty} y\, f_Y(y)\, dy \\ &= \mathbb{E}[Y] \qquad (\because \text{by definition}) \\ \therefore \int_{-\infty}^{\infty} g(x) f_X(x)\, dx &= \mathbb{E}[g(X)]. \end{aligned} \tag{B.9}$$

□

B.2.2 Gaussian integral

The Gaussian integral (also the probability integral) is related to the erf(.) which is the integral of one-dimensional Gaussian function over $(-\infty, \infty)$ as

$$I = \int_{-\infty}^{\infty} e^{-x^2} dx. \tag{B.10}$$

It can be computed using the combining of two one-dimensional Gaussian variables. Then

$$I^2 = \int_{-\infty}^{\infty} e^{-x^2} dx \int_{-\infty}^{\infty} e^{-y^2} dy = \int_{-\infty}^{\infty} \int_{-\infty}^{\infty} e^{-(x^2+y^2)} dx\, dy.$$

Transform to polar coordinates, $x^2 + y^2 = r^2$ and $dx\, dy = r\, dr\, d\theta$, we have

$$I = \sqrt{\int_0^{2\pi} \int_0^{\infty} e^{-r^2} r\, dr\, d\theta} = \sqrt{2\pi \left. \frac{e^{-r^2}}{-2} \right|_0^{\infty}} = \sqrt{\pi}. \tag{B.11}$$

□

Note that this integral can be used to find the corresponding area of a normal distribution for the given interval such as $\mu \pm \sigma, \mu \pm 2\sigma$ and $\mu \pm 3\sigma$ that result approximately 68.27%, 95.45% and 99.73% of the distribution, respectively.

B.3 Uncertainty of the Measurements

The repeating measurements allow to know a better idea of the actual value and also enable to characterize the uncertainty of the measurement. Let $\{x_1, x_2, x_3, \ldots\ x_N, \text{where } N \in \mathbb{Z}^+\}$ are the measurements from an experiment by repeating N times. Table B.1 shows some useful expressions for calculating uncertainty of measurements (Taylor, 1997; Bevington and Robinson, 2003).

Table B.1: Used expressions for uncertainty calculation

(Typical) The average of all measurements $x_{\text{avg}} = \frac{1}{N}\sum_{i=1}^{N} x_i$			
Uncertainty	*for* / *where*	$N \leq 10$	$N > 10$
	a measurement δx when $x = \{x_1, x_2, \dots x_N\}$	$\delta x = \frac{\max(x)-\min(x)}{2}$	$\sigma = \sqrt{\frac{\sum_{i=1}^{N}(x_i - x_{\text{avg}})^2}{N}}$
	the mean δx_{avg}	$\frac{\delta x}{\sqrt{N}}$	$\frac{\sigma}{\sqrt{N}}$
With confidence level of 68.27%, the measured value $x_m = x_{\text{avg}} \pm \delta x_{\text{avg}}$			

The average of the measured values with uncertainty $x_{m_{\text{avg}}}$	$x_{m_{\text{avg}}} = \frac{1}{M}\sum_{j=1}^{M}\left(x_{\text{avg}_j} \pm \delta x_{\text{avg}_j}\right)$

Appendix C

Specific Matlab Scripts

C.1 Jitter Measurements on Simulated Data

This section is corresponding to Chapter 4 that tested the proposed algorithm described in Section 4.2. This includes two files, one for generating the simulation data and other for extracting the jitter in those simulated signals.

C.1.1 Generating simulation data - genSG10to50.m

```
%% Generating simulation data for check the propsed algorithm:
%% File name: genSG10to50.m --> includes for RJ, PJ and RJ + PJ;
%% Prepared by Gehan Anthonys - on September, 2017;

%% Parameters as for oscilloscope:
sampRate = 8e9;          % 8 GSa/s
Ts = 1/sampRate;         % 125 ps
tt = (0:1:2^14-1)*Ts;    % 65536 = 2^16 data points
lenTT = length(tt);
amplSig = 1;
modFreq = (10:10:50)*1e+6;
%% 1 --> RJ only, 2 --> PJ only, 3 --> both.
boolPjRjBoth = 3;
switch boolPjRjBoth
    case 1
        foldName = 'withRJ\20sets\';
    case 2
        foldName = 'withPJ\20sets\';
    case 3
        foldName = 'withRJ+PJ\20sets\';
end
% for RJ
if boolPjRjBoth == 1 || boolPjRjBoth == 3
    lenPts = lenTT/16 + 1;  % no of random numbers: 4097 for ../16
    rmsRJ = 5e-12;  % rms: 5, 10, 20, 30, 40, 50 ps
    valRJ = rmsRJ*randn(1, lenPts); % with 5ps (rms) RJ
    for k = 1:lenPts - 1
        coeff = polyfit([tt(16*(k-1)+1), tt(16*k)],[valRJ(k), valRJ(k+1)], 1);
        interPts{k} = coeff(1)*tt(16*(k-1)+1:16*k) + coeff(2);
    end
    horzIntRJ = interPts{1};
    for k = 2:length(interPts)
        horzIntRJ = horzcat(horzIntRJ, interPts{k});
    end
    intpolRJ = horzIntRJ;   % rms 5ps of RJ
    %%     To check the RJ:
    figure; plot(tt, intpolRJ, '.-'); grid on;
```

```
38      % XOR --
39      consRJ = repmat(rmsRJ, 1, lenTT);   % const rms 5ps of RJ, but the jitter
40          % will be cancelled out even the 1st element set to 0,
41      consRJ(1) = 0;  % since ideal and data signals aligned with 1st element,
42          % THEN, nearly ALL POINTS ARE EXACTLY ALINGED. Therfore, this is USELESS.
43      % XOR --
44      halfConsRJ = horzcat(zeros(1, lenTT/2), repmat(rmsRJ, 1, lenTT/2));
45          % half zero + half const rms 5ps of RJ
46  end
47
48  % for PJs
49  if boolPjRjBoth == 2 || boolPjRjBoth == 3
50      amplPJ1 = 5e-12;  % ampl: 5, 10, 20, 30, 40, 50 ps
51      freqPJ1 = 4.37e+6;
52      amplPJ2 = 0;
53      freqPJ2 = 10e+6;
54  end
55
56  nSet = 20;      % no of data sets
57  for nn = 1:nSet
58      for ii = 3:3
59          switch boolPjRjBoth
60              case 1      % with RJ only
61                  vol = amplSig*sin(2*pi*modFreq(ii)*(tt + intpolRJ));
62                      % with rms value of RJ, XOR --
63                  % vol = amplSig*sin(2*pi*modFreq(ii)*(tt + consRJ));
64                      % with const rms 5ps of RJ, XOR --
65                  % vol = amplSig*sin(2*pi*modFreq(ii)*(tt + halfConsRJ));
66                      % with half const rms 5ps of RJ
67              case 2      % with PJs only
68                  vol = amplSig*sin(2*pi*modFreq(ii)*(tt + amplPJ1*cos(2*pi*freqPJ1*tt) +
                        amplPJ2*cos(2*pi*freqPJ2*tt)));
69              case 3      % with (PJ + RJ)
70                  vol = amplSig*sin(2*pi*modFreq(ii)*(tt + amplPJ1*cos(2*pi*freqPJ1*tt) +
                        intpolRJ));
71              otherwise   % WITHOUT jitter
72                  vol = amplSig*sin(2*pi*modFreq(ii)*tt);
73          end
74          %%      To check the RJ:
75          figure; plot(tt, vol, '.-'); grid on;
76          data = [tt', vol'];
77          pathDir = strcat('E:\GA\Matlab\JitterAnalysis\wavesSR\jitsCalculation\SR4000\sSG8\
                ', foldName); % sSG6, sSG7, sSG8
78          cd(pathDir);
79          filename = strcat('sSG', num2str(10*ii), '_8GSa', num2str(nn),'.csv');
80          csvwrite(filename, data, 0, 0);
81      end
82  end
83  pathDir = 'E:\GA\Matlab\JitterAnalysis\wavesSR\jitsCalculation\SR4000\';
84  cd(pathDir);
85  %% End of the file: genSG10to50.m ----------
```

C.1.2 Extracting the jitter - rstSG10to50.m

```
1   %% Extracting the jitter which the simulated data by genSG10to50.m
2   %% File name: rstSG10to50.m --> includes for RJ, PJ and RJ + PJ;
3   %% Prepared by Gehan Anthonys - on September, 2017;
4   %%
5   %% DATA SAVED in .xlsx are NOT in t-domain, they are in f-domain abs(jitter) values, i.e.
        mean jitter of FFT spectra
6
7   clear all;
8   folTOF = 8;
9   dataDir = strcat('E:\GA\Matlab\JitterAnalysis\wavesSR\jitsCalculation\SR4000\sSG', num2str
        (folTOF), '\');
10  cd(dataDir);
11  spltDataDir = strsplit(dataDir, '\');
12  simData = 1;      % set 1 for simulation (generated) data and 0 for SigGen data
13  nSet = 20;
14  sigFrq = (10:10:50)*1e+6;
15
16  ifSmth = 0;       %% 1 for smoothing, 0 for NOT --> specially for simulated data only
17  ifWndw = 0;       %% 1 for windowing, 0 for NOT, before fft of jitter
18
19  if ifWndw == 1
20      strWndw = ', with windowing';
```

```
21      crrctFctrEny = sqrt(8/3);  % for Hann, energy
22      crrctFctrAmp = 2;          % for Hann, amplitude
23  else
24      strWndw = ', without windowing';
25      crrctFctrEny = 1;
26      crrctFctrAmp = 1;          % for Hann, amplitude
27  end
28  for i = 1:5
29      if simData == 1             % simulation (generated) data
30          sheet = strcat('sSG', num2str(i*10));
31          if ifSmth == 1
32              if ifWndw == 1
33                  dataSG = abs(xlsread('rstWndwSimSG10to50.xlsx', sheet, 'B:B'));
34                      % in order to generalise take the absolute
35              else
36                  dataSG = abs(xlsread('rstNoWndwSimSG10to50.xlsx', sheet, 'B:B'));
37              end
38          else
39              if ifWndw == 1
40                  dataSG = abs(xlsread('rstWndwSimSG10to50wo.xlsx', sheet, 'B:B'));
41              else
42                  dataSG = abs(xlsread('rstNoWndwSimSG10to50wo.xlsx', sheet, 'B:B'));
43              end
44          end
45      else
46          sheet = strcat('SG', num2str(i*10));        % Sig Gen data
47          if ifWndw == 1
48              dataSG = abs(xlsread('rstWndwSG10to50.xlsx', sheet, 'B:B'));        % Sig Gen
                    data: fft
49          else
50              dataSG = abs(xlsread('rstNoWndwSG10to50.xlsx', sheet, 'B:B'));      % Sig Gen
                    data: fft
51          end
52      end
53      valFfSG{i} = dataSG;
54      lenFfSG(i) = length(dataSG);
55      meanFfSG(i) = mean(dataSG);
56      stdFfSG(i) = std(dataSG);
57      rmsFfSG(i) = rms(dataSG);
58
59      trshldLvlDataSG = meanFfSG(i);
60
61      jFrq = sigFrq(i)*(0 : lenFfSG(i) - 1)/lenFfSG(i);
62      jFrqHlf = sigFrq(i)*(0 : lenFfSG(i)/2 - 1)/lenFfSG(i);
63
64      maxFfSG(i) = max(dataSG);
65
66      %% To find the area under the curve (total, RJ, PJ) by using fft
67      % To CHECK: whether have the PJ or not, in the signals
68      figure;
69      plot(jFrqHlf/1e+6, dataSG(1:end/2)*1e+12, 'o-', jFrqHlf/1e+6, repmat(trshldLvlDataSG,
            1, lenFfSG(i)/2)*1e+12, '.-');
70      grid on;
71
72      sheet = 'SET.A';    %'SET.A - for RJ, 'SET.B - for PJ, 'SET.C - for RJ+PJ
73      if strcmp(upper(sheet), 'SET.A') == 1
74          thrshld = 3;
75      else
76          thrshld = 1;
77      end
78
79      indMaxFfSG(i) = find(dataSG == maxFfSG(i), 1, 'first'); % peak index,
80                                                              % (i.e. @ PJ)
81      if indMaxFfSG(i) < length(jFrqHlf) && fix(maxFfSG(i)./meanFfSG(i)) > thrshld
82          % if more than 3, ASSUMED exist PJ. 'fix: Round toward zero'
83          existPJ = 1;
84          freqMaxSG(i) = jFrqHlf(indMaxFfSG(i));
85          indPrevMax(i) = indMaxFfSG(i) - 1;
86          indNextMax(i) = indMaxFfSG(i) + 1;
87
88          indsLvlPrevMax = find(dataSG(1:indMaxFfSG(i)) > trshldLvlDataSG);
89          indsLvlNextMax = find(dataSG(indMaxFfSG(i):end/2) > trshldLvlDataSG);
90          % to find prev index wrt max
91          if isempty(find(diff(indsLvlPrevMax) == 1, 1))
92              indPrevMax(i) = indsLvlPrevMax(end) - 1;
93          else
94              for aa = length(indsLvlPrevMax):-1:1
```

```
95                  if dataSG(indsLvlPrevMax(aa) - 1) > trshldLvlDataSG
96                      indPrevMax(i) = indPrevMax(i) - 1;
97                  else
98                      break;
99                  end
100             end
101         end
102         % to find next index wrt max
103         if isempty(find(diff(indsLvlNextMax) == 1, 1, 'last'))
104             indNextMax(i) = indMaxFfSG(i) + 1;
105         else
106             for zz = 1:length(indsLvlNextMax)
107                 if dataSG(indMaxFfSG(i) + indsLvlNextMax(zz)) > trshldLvlDataSG
108                     if dataSG(indMaxFfSG(i) + indsLvlNextMax(zz)) < dataSG(indMaxFfSG(i) +
                            indsLvlNextMax(zz) - 1)
109                         indNextMax(i) = indNextMax(i) + 1;
110                     else
111                         indNextMax(i) = indNextMax(i) - 1;
112                         break;
113                     end
114                 else
115                     break;
116                 end
117             end
118         end
119     else
120         existPJ = 0;
121         freqMaxSG(i) = 0;
122         indPrevMax(i) = 1;
123         indNextMax(i) = floor(lenFfSG(i)/2);
124         dataLvlPJ_RJ = 0;
125     end
126     %% To find the PSD of partial RJ,
127     %% we need the intermediate points inside the PJ bar -
128     %% --- by using linear interpolation
129     intpolPartRJ{i} = interp1([jFrqHlf(indPrevMax(i)) jFrqHlf(indNextMax(i))], ...
130                               [dataSG(indPrevMax(i)) dataSG(indNextMax(i))], ...
131                               jFrqHlf(indPrevMax(i):indNextMax(i)));
132
133     %% Calculating areas & power of the signal
134     %% Half: total area under the curve (ie. PJ + RJ)
135         areaFfSG(i) = 1*trapz(dataSG(1:end/2));
136         %% Total power spectrum
137         psFfSG(i) = sum(dataSG(1:end/2).*dataSG(1:end/2));      % by half
138         psFfSG_A(i) = sum(dataSG(1:end/2));     % by amplitude, by half
139         psFfSG_byFull(i) = 1*sum(dataSG.*dataSG);       % by full,
140             % BOTH ARE SAME when twice of half as, sqrt(2*...)
141
142     if existPJ == 1
143         figure;
144         plot(jFrqHlf/1e+6, dataSG(1:end/2)*1e+12, 'o-', 'color', 'blue'); grid on;
145         if indNextMax(i) <= length(jFrqHlf)
146             hold on; plot(jFrqHlf(indPrevMax(i):indNextMax(i))/1e6, intpolPartRJ{i}*1e12,
                    '+-');
147             xlabel('Frequecy (MHz)'); ylabel('Amplitude (ps)');
148             legend(strcat(num2str(sigFrq(i)/1e6),' MHz'), 'interpolated level');
149         end
150         hold on;
151         fill(jFrqHlf(indPrevMax(i):indNextMax(i))/1e6, dataSG(indPrevMax(i):indNextMax(i))
                *1e12, 'b');
152
153         % OR, direct calculation from plot (half side)
154         lenPJpart = length(dataSG(indPrevMax(i):indNextMax(i)));
155         psPJFfSG(i) = sum(dataSG(indPrevMax(i):indNextMax(i)).*dataSG(indPrevMax(i):
                indNextMax(i)) - ...
156                                                         intpolPartRJ{i}'.*intpolPartRJ{i}');
157         psPJFfSG_A(i) = sum(dataSG(indPrevMax(i):indNextMax(i)) - intpolPartRJ{i}');    %
                by amplitude
158     else
159         figure;
160         plot(jFrqHlf/1e+6, dataSG(1:end/2)*1e+12, 'o-', 'color', 'blue'); grid on;
161         xlabel('Frequecy (MHz)'); ylabel('Amplitude (ps)');
162         legend(strcat(num2str(sigFrq(i)/1e6), ' MHz'));
163
164         lenPJpart = 0;
165         psPJFfSG(i) = 0;
166         psPJFfSG_A(i) = 0;
```

```
167      end
168      psdRJFfSG(i) = psFfSG(i) - psPJFfSG(i);
169      psdRJFfSG_A(i) = psFfSG_A(i) - psPJFfSG_A(i);
170  end
171  meanFfSG;
172  stdFfSG;
173
174  %% Total jitter, from spectrum
175  rmsFfSgnl = rmsFfSG.*sqrt(lenFfSG);
176      % from spectrum, to check the accuracy of total jitter,
177  ampFfSgnl = sqrt(2)*rmsFfSgnl;
178      % This should be EQUAL to 'calAmpFfSG' given by 'sqrt(signal's POWER)'
179  %% with correction factor
180  rmsFfSgnl_cF = rmsFfSG.*sqrt(crrctFctrEny).*sqrt(lenFfSG);
181      % corrected on Nov 17, 2018 --> factor should in sqrt()
182  ampFfSgnl_cF = sqrt(2)*rmsFfSgnl_cF
183  %%
184  %% Calculating jitter parameters:
185  % NOTE: FROM THE SPECTRUM IT GIVES "RMS value of each freq of time signal",
186  % therefore, to get the amplitude we need to MULTIPLE by sqrt(2) for PJ and
187  % for Total J. But for RJ it can be get as it is, since RJ measured in RMS
188  %% ------ on Jan 31, 2018.
189
190  % Total jitter
191  if strcmp(upper(sheet), 'SET.A') == 1
192          %'SET.A - for RJ, 'SET.B - for PJ, 'SET.C - for RJ+PJ
193      calRmsFfSG = sqrt(2*psFfSG);        % since two sided
194      calRmsFfSG_cF = sqrt(2*psFfSG)*sqrt(crrctFctrEny)
195          % corrected on Nov 17, 2018 --> factor should in sqrt()
196  else                        % 'SET.B' or 'SET.C'
197      calAmpFfSG = sqrt(2)*sqrt(2*psFfSG);        % since two sided
198      calAmpFfSG_cF = sqrt(2)*sqrt(2*psFfSG)*sqrt(crrctFctrEny)
199          % corrected on Nov 17, 2018 --> factor should in sqrt()
200  end
201
202  %% for PJ --> [ampl (or rms), freq], by (in f and PSD - domains)
203  freqPJSG = freqMaxSG
204  % by PSD is given amplitude, but spectrum is given the rms amounts
205  calAmplPJSG = sqrt(2)*sqrt(2*psPJFfSG);         % since two sided
206  calAmplPJSG_cF = sqrt(2)*sqrt(2*psPJFfSG)*sqrt(crrctFctrEny)
207          % corrected on Nov 17, 2018 --> factor should in sqrt()
208
209  %% for RJ --> [rms], by (in f and PSD - domains)
210  if strcmp(upper(sheet), 'SET.B') == 1       % if PJ only --> SET.B
211      calRmsRJSG = 0;
212      calRmsRJSG_cF = 0
213  elseif strcmp(upper(sheet), 'SET.A') == 1         % if RJ only --> SET.B
214          calRmsRJSG = sqrt(2)*sqrt(2*psdRJFfSG)      % since two sided
215      calRmsRJSG_cF = sqrt(2)*sqrt(2*psdRJFfSG)*crrctFctrEny
216      else             % if PJ + RJ  --> SET.C
217      calRmsRJSG = sqrt(2*psdRJFfSG)      % since two sided
218      calRmsRJSG_cF = sqrt(2*psdRJFfSG)*crrctFctrEny
219          % corrected on Nov 17, 2018 --> factor should in sqrt()
220  end
221  %%
222  %%  for ploting
223  for i = 1:5
224      padFfSG{i} = num2cell(padarray(valFfSG{i}(1:end/2), (max(lenFfSG)-lenFfSG(i))/2, 0, '
           post'));
225  end
226  dataSG10 = cell2mat(padFfSG{1});
227  dataSG20 = cell2mat(padFfSG{2});
228  dataSG30 = cell2mat(padFfSG{3});
229  dataSG40 = cell2mat(padFfSG{4});
230  dataSG50 = cell2mat(padFfSG{5});
231
232  jFs = 30e+6;
233  jffN =  max(lenFfSG);
234  jFreq = jFs*(0 : jffN-1)/jffN;
235  jFreqHalf = jFs*(0 : jffN/2-1)/jffN;
236
237  if simData == 1       % simulation (generated) data
238      deviceSG = 'Simulation data : ';
239      measureDev = 'using computer';
240  else              % for Sig Gen data
241      deviceSG = 'Sig/Gen Agilent 8648B : ';
242      measureDev = ' by using oscilloscope: Hp infiniium 2.25 GHz, 8 GSa/s';
```

```
243 end
244 textStr = num2str(calRmsRJSG);
245
246 %% FFT spectrum for all together, THIS is better
247 figure;
248 plot(jFreqHalf/1e+6, dataSG10*1e+12, 'o-', 'color', 'blue'); hold on;
249         %text(1, 13, num2str(calRmsRJSG(1)), 'FontSize', 16);
250 plot(jFreqHalf/1e+6, dataSG20*1e+12, '+-', 'color', 'magenta'); hold on;
251         %text(6,12, num2str(calRmsRJSG(2)), 'FontSize', 16);
252 plot(jFreqHalf/1e+6, dataSG30*1e+12, 's-', 'color', 'green'); hold on;
253         %text(11,11, num2str(calRmsRJSG(3)), 'FontSize', 16);
254 plot(jFreqHalf/1e+6, dataSG40*1e+12, 'p-', 'color', 'red'); hold on;
255         %text(16,10, num2str(calRmsRJSG(4)), 'FontSize', 16);
256 plot(jFreqHalf/1e+6, dataSG50*1e+12, 'x-', 'color', 'cyan'); grid on;
257         %text(21,9, num2str(calRmsRJSG(5)), 'FontSize', 16);%ylim([0 5]*1)
258 title({[deviceSG, 'FFT spectrum (1st half) of the total jitter (mean) of data sets: ',
     num2str(nSet), ' @ ', cell2mat(spltDataDir(end-1))], ...
259             [measureDev, ' for 10 MHz to 50 MHz', strWndw]}, 'FontSize', 12);
260 xlabel('Frequency (MHz)','FontSize', 24,'FontWeight','bold');
261 ylabel('Amplitude (ps)','FontSize', 24,'FontWeight','bold');
262 legend({'10 MHz', '20 MHz', '30 MHz', '40 MHz', '50 MHz'}, 'FontSize', 20);
263 set(gca,'FontSize',20);
264 %%
265 %% save the data
266 if simData == 1     % simulation (generated) data
267     if ifWndw == 1
268         xlsName = 'rstWndwSimAEF.xlsx';
269             % with windowing before fft of jitter
270     else
271         xlsName = 'rstNoWndwSimAEF.xlsx';
272     end
273     [Num,Txt,Raw] = xlsread(xlsName, sheet);
274     nRows = size(Raw,1);
275     dataAtOut =  strcat('A', num2str(nRows+1));
276     dataCal = [sigFrq; freqPJSG; calAmplPJSG; calRmsRJSG];
277
278     xlswrite(xlsName, dataCal', sheet, dataAtOut);
279 end
280 dataDir = 'E:\GA\Matlab\JitterAnalysis\wavesSR\jitsCalculation\SR4000\';
281 cd(dataDir);
282 %% End of the file: rstSG10to50.m ----------
```

C.2 Capturing multiple sets of data from two oscilloscopes

In order to control the uncertainty of the experimental results, multiple data needs to be captured. This section is corresponding to Chapter 5 which multiple sets of data is captured from the oscilloscope and saved automatically to a computer. For medium speed oscilloscope (Keysight Infiniium S-Series DSOS604A High Definition), the automation process can be set up on the device while for low speed oscilloscope (HP Infiniium 54846B) it is needed to connect via USB/GBIP interface with a Matlab script. The multiple sets of data from the two cameras and the signal generator are captured by the two oscilloscopes, separately.

Since the two cameras are getting warm due to the running of a long period, the light signals of the cameras are not captured continuously. Instead, approximately 30 minutes of slots are used for data capturing in each camera. Cameras were switched off for cooling process between slots of data capturing.

C.2.1 DSOS604A High Definition, 6 GHz and 20 GSa/s

This is a medium speed oscilloscope and can automate to capture the continuously. The following sequence is used to capture and store the data, select:

(1) the 'Trigger' tab;
(2) on 'Trigger Action ...';
(3) the box next to 'Perform Multipurpose On Trigger';
(4) the number of times that needs to save on a trigger under 'Max no Of Actions';
(5) the 'Setup ...' in the 'Multipurpose On Trigger' section;
(6) the 'QuickWaveform' under the 'Multipurpose' drop down list;
(7) the file format and the location to save the files.

The files are saved in the Comma-separated values (*.csv) format.

C.2.2 HP Infiniium 54846B, 2.25 GHz and 8 GSa/s

This is a low speed oscilloscope and can connect via USB/GBIP interface to capture the multiple signals continuously with the following Matlab script.

```
% 03 May, 2017 ------------------
% To collect the data from HP infinnium 54846B oscilloscope via USB/GBIP interface:
% Capturing 65536 points for SR4000/ DS325/ SigGen 8648B using the oscilloscope
%% ------------------------------

clc     %Clear the MATLAB command window
clear   %Clear the MATLAB variables

% Setup:
instrumentConnected = true;
% Ignore the instrument when doing a test:
if instrumentConnected
    % Instrument
    visaObjOscope = visa('agilent','GPIB0::7::INSTR');
    % Set the buffer size
    visaObjOscope.InputBufferSize = 100000;
    % Set the timeout value
    visaObjOscope.Timeout = 10;
    % Set the Byte order
    visaObjOscope.ByteOrder = 'littleEndian';
    % Open the connection
    fopen(visaObjOscope);
end

for k = 501:1050        % Use 500 acquisition slots (taken ~30 mins), since the camera is
    bit heating.
    if instrumentConnected
        fprintf(visaObjOscope, ':DISK:STOR CHAN1, "F:\\SR400\\SR30_8GSa%d.csv", TEXT, XYP,
            ON', k);
    end
    pause(4);           % About 3.3 sec needs to store each file for SR4000 & DS325
end

if instrumentConnected
    % Check for any instrument errors
    instrumentError = query(visaObjOscope,':SYST:ERR?')

    % Close the instrument
    fclose(visaObjOscope);
end
```

C.3 Romberg integration algorithm

This is used in Chapter 7 that evaluating the influence of the periodic jitter in range measurements by using one of the numerical approaches used. This Matlab function computes the integral using the Romberg integration method.

```
function [R] = rombf(f,a,b,N)
% 18 June, 2019 ---------------
% Rombergs method for computing the integral of function f in the range [a,b] using
% at most k Richardson extrapolations. Stop when q extrapolations have been performed.
% Inputs:
%       f - function,
%       a,b - lower and upper bound of the integral
%       N - Romberg table N by N with 2^(N-1) panels.
% Output:
%       R - Romberg table with R[N, N} is the best estimate of the value of the integral.
%
% An example:
%       [R] = rombf(corrFun, -tau/2, tau/2, rmbgN); with number of panels = 2^(rmbgN-1).
%
% Thus, if rmbgN = 18 then number of panels is 2^(17) = 131072.
% % -------------------------

h = b - a; np = 1;

% First term R(1,1)
R(1,1) = h*(feval(f,a) + feval(f,b))/2;
for i = 2:N
    h = h/2;
    np = 2*np;
    sum = 0;              % Compute midpoint sum
    for k = 1:2:np-1
        sum = sum + feval(f, a + k*h);
    end
    % First column entry R(i,1)
    R(i,1) = R(i-1,1)/2 + h*sum;
    m = 1;
    % Other columns R(i,2) , ... ,R(i,i)
    for k = 2:i           % Repeated Richardson extrapolation
        m = 4*m;
        R(i,k) = R(i,k-1) + (R(i,k-1) - R(i-1,k-1))/(m - 1);
    end
end
```

C.4 Monte Carlo simulation

This is corresponding to Chapter 8 that evaluating the influence of the random jitter in range measurements. This consists two files, one for generating data with Monte Carlo method and obtaining the PDF using non parametric estimations. Other file is for generating the results of the phase error and analysing the uncertainty of the results.

C.4.1 Generating data with MCS - genMCsRJ.m

```
% %  July 04, 2019
% % -- Related to the chapter 8 of thesis --> 'genMCsRJ.m'
% % This is for analyse the effect of the random jitter (RJ)
% % (i.e., epsS & epsL (random variates)) on range measurements by frequency domain.
% % Light function is funL = cos(2*pi*frqL*(t + epsL) - phiToF)
% % Shutter function is funS = cos(2*pi*frqS*(t + epsS) + theta)
```

```
7
8  clear all;
9
10 nTrpz = 60e6;            % [3 5 20 ...]*1e6;  % number of steps in 'trapz' integration
11 nEval = 500;             % The number of function evaluations
12 nSet = 30;               % Repeating the number of set for uncertainty calculation
13 setNo = 1:nSet;          % for x axis plot
14
15 T = 1e-3;                % integration period in sec (FIXED)
16 phiToF = (0:6)*pi/6;     % ToF phase shift in rad
17 rad2deg(phiToF)
18 frqL = 600e6;            % mod frequency of light signal --> [30 50 200 ... 1000] MHz
19 frqS = frqL;             % mod frequency of shutter signal --> [30 50 200 ... 1000] MHz
20
21 % Random jitter parameters
22 muL = 0e-12;             % mean in sec
23 sgmL = (0:50:1000)*1e-12;               %[0 50 100 200 400 ... 1000]*1e-12;     % std dev
       in sec
24 muS = 0e-12;             % mean in sec
25 sgmS = [0 sgmL(2:end) + 1e-12]; %[0 51 101 201 401 ... 1001]*1e-12;     % std dev in sec
26
27 tt = linspace(-T/2, T/2, nTrpz);
28
29 % --- Run the correlation function
30 ifRJ = 1;   % 1 for RJ
31 for ii = 2:3%length(phiToF)                % 0 30 60 ... degrees
32     tic;              % starting the time
33     for nL = 2:2%length(sgmL)              % 0 50 100 ... ps
34         for nS = nL %2:2:4%length(sgmS)
35             for nSt = 1:nSet
36                 parfor nEvl = 1:nEval
37                     esL = muL + randn(nTrpz,1)*sgmL(nL);
38                     esS = muS + randn(nTrpz,1)*sgmS(nS);
39                     if ifRJ == 0
40                         funI = @(tt) exp(2i*pi*frqS*tt).*cos(2*pi*frqL*tt - phiToF(ii));
41                     else
42                         funI = exp(2i*pi*frqS*(tt + esS')).*cos(2*pi*frqL*(tt + esL') -
                               phiToF(ii));
43                     end
44                     angIone = angle(pi*trapz(tt, funI'));
45                     errAngPhi(nEvl) = abs(angIone) - abs(phiToF(ii));
46                 end
47                 stdErrAngPhi(nSt) = std(errAngPhi);
48 %%  Plotting the density estimations
49                 % {
50 %% for histogram
51                 optBWhist = 2/nEval^(1/3)*iqr(errAngPhi);
52                 if sgmL(nL) == 0
53                     noBinsHist = 1;
54                 else
55                     noBinsHist = floor((max(errAngPhi) - min(errAngPhi))/optBWhist);
56                 end
57 %% for kde
58                 optBWkde = 1.06/nEval^(1/5)*min(stdErrAngPhi(nSt), iqr(errAngPhi)/1.34);
59                 xPos = min(errAngPhi); %min
60                 yPosH = max(hist(errAngPhi, noBinsHist));
61                 yPosK = max(ksdensity(errAngPhi));
62
63                 figure;
64                 subplot(1,2,1); hh = histfit(errAngPhi, noBinsHist); % hist(errAngIone,
                       noBinsHist, 'Normalization','pdf');
65                 hh(1).FaceColor = 'b';
66                 text(xPos, yPosH, strcat('\sigma_{\phi_{err}} =  ', num2str(stdErrAngPhi))
                       , 'FontSize', 14);
67                 title(['Histogram for the PDF of phase error \phi_{err} for \phi = ',
                       num2str(phiToF(ii)), ' rad']);
68                 xlabel('Phase error \phi_{err} (rad)'); ylabel('Frequency count');
69                 set(gca,'FontSize',20);
70                 [yVal, xVal] = ksdensity(errAngPhi, 'width', optBWkde);
71                 subplot(1,2,2); plot(xVal, yVal, 'LineWidth', 1.5, 'Color', 'b');
72                 text(xPos, yPosK, strcat('\sigma_{\phi_{err}} =  ', num2str(stdErrAngPhi))
                       , 'FontSize', 14);
73                 title(['KDE for the PDF of phase error \phi_{err} for \phi = ', num2str(
                       phiToF(ii)), ' rad']);
74                 xlabel('Phase error \phi_{err} (rad)'); ylabel('Estimated density function
                        for \phi_{err}'); set(gca,'FontSize',20);
75                 %}
```

```
%% In order to calculate the uncertainty we need "(mean +/- std err)" of the standard deviation of phase error
                muErrAngPhi(nSt) = mean(errAngPhi);
                varErrAngPhi(nSt) = var(errAngPhi);
            end
        end
%% meanStdErr... are same for both methods, but for uncStdErr... this method is not given correct answer:
%%      Since, "sqrt(mean(sum of var))" not EQUAL "mean(sum of std)" ---> see Chapter 8
        meanStdErrAngPhi1(nL) = mean(stdErrAngPhi);
        uncStdErrAngPhi1(nL) = std(stdErrAngPhi)/sqrt(length(stdErrAngPhi));
%%          OR
        meanStdErrAngPhi(nL) = sqrt(sum(varErrAngPhi)/length(varErrAngPhi));
        uncStdErrAngPhi(nL) = sqrt(sum((stdErrAngPhi - sqrt(sum(varErrAngPhi)/length(varErrAngPhi))).^2))/length(varErrAngPhi);

        %% Plotting std. dev. of the phase error by nSet wise (i.e., repetition wise)
        %{
                figure;
                plot(setNo, stdErrAngPhi{nL}, '.-'); grid on;
                title(strcat('Standard deviation of the phase error \phi_{err} for the number of sets : ', ...
        num2str(nSet), ' for \phi = ', num2str(phiToF(ii)), ' rad when f_{mod} = ', num2str(fl/1e6), ...
                        ' MHz, \sigma_l = ', num2str(sgmL(nL)*1e12), ' ps and \sigma_s =', num2str(sgmS(nS)*1e12), ' ps'));
                xlabel('Set number'); ylabel('Standard deviation of phase error \sigma_{\phi_{err}}');
                text(max(setNo)/2, max(stdErrAngPhi{nL}), ...
        strcat('Standard deviation = ', num2str(meanStdErrAngPhi(nL)), ' \pm ', num2str(uncStdErrAngPhi(nL))));
        %}
    end
    endT = toc;                             % completing time
        strT = strcat(num2str(endT/60), ' mins');
    valPhiToF = phiToF(ii);
%% Plotting uncertainty of the std. dev. of the phase error by sigL wise -->
    %% as STD_\phi_err = \mu_{std of \phi_err} \pm \unc_{std of \phi_err}
    % {
    figure;
    plot(sgmL*1e12, meanStdErrAngPhi, 'o', 'LineWidth', 1, 'MarkerSize', 10, 'color', 'b'); grid on;
%     eBar = errorbar(sgmL*1e12, meanStdErrAngPhi, uncStdErrAngPhi, 'o', 'LineWidth', 1, 'MarkerSize', 10, 'color', 'b'); grid on;
    title(strcat('Uncertainty of the standard deviation of the phase error \phi_{err} by sigL wise with sets : ', ...
                num2str(nSet), ' for \phi = ', num2str(valPhiToF), ' rad when f_{mod} = ', num2str(frqL/1e6), ' MHz'));
    xlabel('RMS of the injected random jitter \sigma_{RJ} (ps)');
    ylabel('Typical phase error $\overline{\sigma_{\phi_{err}}}$ (rad)', 'interpreter', 'latex');
    set(gca,'FontSize',20); xlim([0 1050]);
    text(0, 0, strT);
    %}
    %% Save the work space as a .mat file
    % {
    filename = strcat('phaErrRJ', num2str(rad2deg(valPhiToF)), 'deg ', num2str(frqL/1e6), 'MHz', num2str(nSet), 'sets.mat');
    dataDir = 'E:\GA\Matlab\JitterAnalysis\wavesSR\jitsCalculation\SR4000\mcsRJ\'; cd(dataDir);
    save(filename, 'nSet', 'frqL', 'sgmL', 'sgmS', 'valPhiToF', 'stdErrAngPhi', 'meanStdErrAngPhi', 'uncStdErrAngPhi', 'strT', '-v7.3');
    %}
end

dataDir = 'E:\GA\Matlab\JitterAnalysis\wavesSR\jitsCalculation\SR4000\'; cd(dataDir);
```

C.4.2 Results with uncertainty - rstMCsRJ.m

```
%% Modified on September 12, 2019
%% -- Related to the chapter 8 of thesis --> 'rstMCsRJ.m'
%% This is for --->
%% (1) to plot the phase error for all frequencies on same graph and
%% (2) to analyse the uncertainty of the resulted phase individually

clear all; close all;
```

```
8
9  phaToF = [30 60];                                % ToF phase shift
10 modFrq = [30 50 100 200 400 600 800 1000];          % Modulation frequencies in MHz
11 dataDir = 'E:\GA\Matlab\JitterAnalysis\wavesSR\jitsCalculation\SR4000\mcsRJ\'; cd(dataDir)
       ;
12 symMrk = {'*-c', '+-k', '^-m', 'd-g', 's-b', 'o-y', '.-r', 'x-k'};
13 symMrkUnc = {'*c', '+k', '^m', 'dg', 'sy', 'ob', '.r', 'xk'};
14 for pp = 1:length(phaToF)
15     matName = strcat('phaErrRJ', num2str(phaToF(pp)), '*30sets.mat');
16     matFiles = dir(matName);
17     %% (1) to plot the phase error - - -
18     figure;
19     for qq = 1:length(matFiles)
20         matNameFrqWise = strcat('phaErrRJ', num2str(phaToF(pp)), 'deg', num2str(modFrq(qq)
               ), 'MHz30sets');
21         load(matNameFrqWise);
22         meanStdErr(qq, :) = meanStdErrAngPhi;
23         uncStdErr(qq, :) = uncStdErrAngPhi;
24         rmsRJ(qq, :) = sgmL;
25         modFrq(qq) = frqL;
26 %         plot(rmsRJ(qq, :)*1e12, meanStdErr(qq, :), symMrk{qq}, 'LineWidth', 1, '
       MarkerSize', 10, 'color', symMrk{qq}(end));
27         semilogy(rmsRJ(qq, :)*1e12, meanStdErr(qq, :), symMrk{qq}, 'LineWidth', 1, '
               MarkerSize', 10, 'color', symMrk{qq}(end));
28 %         errorbar(rmsRJ(qq, :)*1e12, meanStdErr(qq, :), uncStdErr(qq, :), symMrk{qq}, ...
29 %                                     'LineWidth', 1, 'MarkerSize', 10, 'color', symMrk{qq}(
       end));
30         strLegNum{qq} = num2str(frqL/1e6); hold on;
31     end
32     hanLegNum = legend(strLegNum, 'Location', 'northwest', 'FontSize', 20, 'interpreter',
           'latex'); legNumTtl = get(hanLegNum,'Title');
33     set(legNumTtl,'String', '{\it f} (MHz)', 'FontWeight', 'normal', 'FontSize', 20, '
           interpreter', 'latex');
34     xlabel('RMS of the injected random jitter $\sigma_{RJ}$ (ps)', 'interpreter', 'latex')
           ;
35     ylabel('Typical phase error $\overline{\sigma_{\phi_{err}}}$ (rad)', 'interpreter', '
           latex');
36     set(gca,'FontSize',20); xlim([0 1050]); hold off;
37
38     %% (2) to analyse the uncertainty
39 %%     Individual plot
40     %{
41     for qq = 1:length(matFiles)
42         figure;
43         rmsVals = [rmsRJ(qq, :)*1e12, rmsRJ(qq, :)*1e12];
44         uncVals = [uncStdErr(qq, :), -uncStdErr(qq, :)];
45 %%  As stems
46         stem(rmsVals, uncVals, symMrk{qq}, 'LineWidth', 1, 'MarkerSize', 10, 'color',
               symMrk{qq}(end));
47 %% XOR
48         semilogy(rmsVals, uncVals, symMrk{qq}, 'LineWidth', 1, 'MarkerSize', 10, 'color',
               symMrk{qq}(end));
49 %% XOR
50 %%  As error bars
51         errorbar(rmsRJ(qq, :)*1e12, meanStdErr(qq, :), uncStdErr(qq, :), symMrk{qq}, ...
52                 'LineWidth', 1, 'MarkerSize', 10, 'color', symMrk{qq}(end)); grid on;
53         xlabel('RMS of the injected random jitter $\sigma_{RJ}$ (ps)', 'interpreter', '
               latex');
54         ylabel('Error bars for phase error $\overline{\sigma_{\phi_{err}}}$ (rad)', '
               interpreter', 'latex');
55         set(gca,'FontSize',25); xlim([0 1050]); %ylim([-5e-4 5e-4]);
56         title(strcat('Uncertainty of the mean of standard deviation of the phase error \
               overline{\sigma_{\phi_{err}}} (rad) ', ...
57             num2str(nSet), 'sets for \phi = ', num2str(valPhiToF), ' rad when f_{mod} =
                   ', strLegNum{qq}, ' MHz'),'FontSize', 10);
58     end
59     hold off;
60     %}
61         %%     Plot the corresponding 0.1 mrad phase error for RJ against Mod freq.
62     %{
63     modFrq = [30 50 100 200 400 600 800 1000];       %in MHz
64     sgmRJ = [530,410,288,203,142,115,97,87];  % in ps
65     figure;
66     plot(modFrq, sgmRJ, 'ok', 'MarkerSize', 10); hold on;
67     legend('RMS \sigma_{RJ}', 'Fitted curve');
68     xlabel('Modulation frequency $f$ (MHz)', 'interpreter', 'latex');
69     ylabel('Random jitter of RMS $\sigma_{RJ}$ (ps)', 'interpreter', 'latex');
```

```
    set(gca,'FontSize',25, 'FontName', 'Times New Roman'); xlim([0 1050]); ylim([0 550]);
    %}
%%%%%%%%%%%%%%%%%%%%%%
    %% (2) to analyse the uncertainty
%%      Individual plot
    %{
    for qq = 1:length(matFiles)
        figure;
        rmsVals = [rmsRJ(qq, :)*1e12, rmsRJ(qq, :)*1e12];
        uncVals = [uncStdErr(qq, :), -uncStdErr(qq, :)];
%%  As stems
        stem(rmsVals, uncVals, symMrk{qq}, 'LineWidth', 1, 'MarkerSize', 10, 'color', symMrk{qq}(end));
                set(gca,'yscal','log');
%% XOR
%%  As error bars
%         errorbar(rmsRJ(qq, :)*1e12, meanStdErr(qq, :), uncStdErr(qq, :), symMrk{qq}, ...
%                   'LineWidth', 1, 'MarkerSize', 10, 'color', symMrk{qq}(end));
        grid on;
        xlabel('RMS of the injected random jitter $\sigma_{RJ}$ (ps)', 'interpreter', 'latex');
        ylabel('Error bars for phase error $\overline{\sigma_{\phi_{err}}}$ (rad)', 'interpreter', 'latex');
        set(gca,'FontSize',25, 'FontName', 'Times New Roman'); xlim([0 1050]);
        title(strcat('Uncertainty of the mean of standard deviation of the phase error \overline{\sigma_{\phi_{err}}} (rad) ', ...
             num2str(nSet), 'sets for \phi = ', num2str(valPhiToF), ' rad when f_{mod} = ', strLegNum{qq}, ' MHz'), 'FontSize', 10);
    end
    hold off;
    %}
%%      All plots in same figure
    %{
    figure;
    for qq = 1:length(matFiles)
        rmsVals = [rmsRJ(qq, :)*1e12, rmsRJ(qq, :)*1e12];
        uncVals = [uncStdErr(qq, :), -uncStdErr(qq, :)];
        plot(rmsVals, uncVals, symMrk{qq}, 'LineWidth', 1, 'MarkerSize', 10, 'color', symMrk{qq}(end));
        set(gca,'yscal','log'); hold on;
        strLegUnc{qq} = strLegNum{qq};
    end
    hanLegUnc = legend(strLegUnc, 'Location', 'northwest', 'FontSize', 20, 'interpreter', 'latex');
    legUncTtl = get(hanLegUnc,'Title');
    set(legUncTtl,'String', '{\it f} (MHz)', 'FontWeight', 'normal', 'FontSize', 20, 'interpreter', 'latex');
    xlabel('RMS of the injected random jitter $\sigma_{RJ}$ (ps)', 'interpreter', 'latex');
    ylabel('Standard error for phase error $\overline{\sigma_{\phi_{err}}}$ (rad)', 'interpreter', 'latex');
    set(gca,'FontSize',20); xlim([0 1050]); %ylim([-5e-4 5e-4]);
    title(strcat('Uncertainty of the mean of standard deviation of the phase error \overline{\sigma_{\phi_{err}}} (rad) ', ...
           num2str(nSet), 'sets for \phi = ', num2str(valPhiToF), ' rad when f_{mod} = ', strLegUnc{1}, ' to ', ...
           strLegUnc{end}, ' MHz'), 'FontSize', 10); hold off;
    %}
end

%% Calculating corresponding range errors when sigmaRJ = [200 400 600 800 1000] ps
fMod = 1e6*[30; 50; 200; 400; 600; 800; 1000];          % Modulation frequency in Hz
pErr = [3.777e-5 7.555e-5 1.140e-4 1.517e-4 1.910e-4;
        4.890e-5 9.767e-5 1.482e-4 1.963e-4 2.476e-4;
        6.914e-5 1.387e-4 2.131e-4 2.947e-4 3.820e-4;
        9.864e-5 2.081e-4 3.501e-4 5.897e-4 1.076e-3;
        1.462e-4 4.184e-4 1.536e-3 9.044e-3 8.917e-2;
        2.019e-4 1.252e-3 2.149e-2 7.719e-1 9.047e-1;
        2.988e-4 6.477e-3 7.406e-1 9.128e-1 9.080e-1;
        4.846e-4 5.640e-2 9.099e-1 9.063e-1 9.093e-1];      % Phase error in radian

c = 299792458;                              % Speed of light ms^(-1)

dErr_mm = (c*pErr./4/pi./fMod)*1e3         % range error in mm
dErr_Rmm = round(dErr_mm, 2)               % range error round to 2 decimal places (mm)

dataDir = 'E:\GA\Matlab\JitterAnalysis\wavesSR\jitsCalculation\SR4000\'; cd(dataDir);
```

Appendix D

Maple Simulations

In this appendix, some expressions obtained in Chapter 7 are verified by using the mathematical tool, Maple ver 16.02 by Maplesoft is included.

D.1 Correlation model without periodic jitter

```
restart
Parameters(f_l, f_s, Θ, ϕ, T) :
with(inttrans) :
u := Heaviside : rect := t → ( u(t + T/2) − u(t − T/2) ) :
T := 1 :
plot(rect(t), t = -1 ..1, thickness = 2) :

with(DynamicSystems) :

nonDCpart := ∫_{-T/2}^{T/2} cos(2·π·f_l·t − ϕ)·exp(I·2·π·f_s·Θ·t) dt
```

$$-\frac{1}{2}\,\frac{1}{\pi\left(\Theta^2 f_s^2 - f_l^2\right)}\left(\left(-\mathrm{I} f_s \Theta\cos\left(\pi f_l\right)\cos\left(\phi\right) + \mathrm{I} f_s \Theta\sin\left(\pi f_l\right)\sin\left(\phi\right) + f_l\sin\left(\pi f_l\right)\cos\left(\phi\right)\right.\right. \tag{1}$$
$$+ f_l\cos\left(\pi f_l\right)\sin\left(\phi\right) + \mathrm{I}\,\mathrm{e}^{2\mathrm{I}\pi\Theta f_s} f_s\Theta\cos\left(\pi f_l\right)\cos\left(\phi\right) + \mathrm{I}\,\mathrm{e}^{2\mathrm{I}\pi\Theta f_s} f_s\Theta\sin\left(\pi f_l\right)\sin\left(\phi\right)$$
$$\left.\left. + \mathrm{e}^{2\mathrm{I}\pi\Theta f_s} f_l\sin\left(\pi f_l\right)\cos\left(\phi\right) - \mathrm{e}^{2\mathrm{I}\pi\Theta f_s} f_l\cos\left(\pi f_l\right)\sin\left(\phi\right)\right)\mathrm{e}^{-\mathrm{I}\pi\Theta f_s}\right)$$

```
FTnonDCpart := fourier(rect(t)·cos(2·π·f_l·t − ϕ), t, 2·π·f_s·Θ)
```

$$\frac{\sin\left(\pi\Theta f_s + \pi f_l\right)\mathrm{e}^{\mathrm{I}\phi}}{2\,\pi\Theta f_s + 2\,\pi f_l} + \frac{\mathrm{e}^{-\mathrm{I}\phi}\sin\left(\pi\Theta f_s - \pi f_l\right)}{2\,\pi\Theta f_s - 2\,\pi f_l} \tag{2}$$

```
DCpart := ∫_{-T/2}^{T/2} exp(I·2·π·f_s·Θ·t) dt
```

$$-\frac{\frac{1}{2}\,\mathrm{I}\left(-1 + \mathrm{e}^{2\mathrm{I}\pi\Theta f_s}\right)\mathrm{e}^{-\mathrm{I}\pi\Theta f_s}}{\pi f_s\Theta} \tag{3}$$

```
FTDCpart := fourier(rect(t), t, 2·π·f_s·Θ)
```

$$\frac{\sin\left(\pi\Theta f_s\right)}{\pi\Theta f_s} \tag{4}$$

D.2 Correlation model with periodic jitter

```
restart;
Parameters(f_l, f_s, Θ, ϕ, T, A_pj, f_pj, β_l, β_s, n, m) :

with(inttrans) :
u := Heaviside : rect := t→u(t + T/2) − u(t − T/2) :

T := 1 :
lt := cos(2·π·f_l·(t + A_pj·sin(2·π·f_pj·t)) − ϕ)
```

$$\cos\left(-2\,\pi f_l\left(t + A_{pj}\sin\left(2\,\pi f_{pj}\,t\right)\right) + \phi\right) \tag{1}$$

```
eTht := exp(I·f_s·2·π·Θ·t)
```

$$e^{2\,I f_s\,\pi\Theta t} \tag{2}$$

```
eJt := exp(I·2·π·f_s·Θ·A_pj·sin(2·π·f_pj·t + ϕ_pj^s))
```

$$e^{2\,I\pi f_s\,\Theta A_{pj}\sin\left(2\,\pi f_{pj}\,t + \phi_{pj}^{s}\right)} \tag{3}$$

```
nonDCpart := ∫_{-T/2}^{T/2} lt·eJt·eTht dt
```

$$\int_{-\frac{1}{2}}^{\frac{1}{2}} \cos\left(-2\,\pi f_l\left(t + A_{pj}\sin\left(2\,\pi f_{pj}\,t\right)\right) + \phi\right) e^{2\,I\pi f_s\,\Theta A_{pj}\sin\left(2\,\pi f_{pj}\,t + \phi_{pj}^{s}\right)} e^{2\,I f_s\,\pi\Theta t}\,dt \tag{4}$$

```
FTnonDCpart := fourier(rect(t)·cos(2·π·(f_l + n·f_pj)·t − ϕ), t, 2·π·(f_s·Θ + m·f_pj))
```

$$-\frac{\sin\left(\pi\left(f_s\,\Theta + m f_{pj}\right) - \pi f_l - \pi\, n f_{pj}\right) e^{-I\phi}}{-2\,\pi\left(f_s\,\Theta + m f_{pj}\right) + 2\,\pi f_l + 2\,\pi\, n f_{pj}} + \frac{\sin\left(\pi\left(f_s\,\Theta + m f_{pj}\right) + \pi f_l + \pi\, n f_{pj}\right) e^{I\phi}}{2\,\pi\left(f_s\,\Theta + m f_{pj}\right) + 2\,\pi f_l + 2\,\pi\, n f_{pj}} \tag{5}$$

Note that the sifting property is defined by (Oppenheim *et al.*, 1999)

$$\int_{-\infty}^{\infty} \delta(t-a)\, g(t)\, dt = g(a), \tag{D.1}$$

where $g(t)$ is continuous function and finite at $g(a)$. Then, using Equation D.1, Equations (2) and (5) in Appendix D.1 and D.2, respectively, can be shown as

$$\begin{aligned}
&\frac{e^{i\phi}}{2}\operatorname{sinc}(\pi(\Theta f_s + f_l)) + \frac{e^{-i\phi}}{2}\operatorname{sinc}(\pi(\Theta f_s - f_l)) \\
&\qquad = \frac{e^{i\left(\frac{\Theta f_s}{-f_l}\right)\phi}}{2}\operatorname{sinc}(\pi(\Theta f_s + f_l)) + \frac{e^{-i\left(\frac{\Theta f_s}{f_l}\right)\phi}}{2}\operatorname{sinc}(\pi(\Theta f_s - f_l)) \\
&\qquad = \frac{e^{-i\left(\frac{\Theta f_s}{f_l}\right)\phi}}{2}\left[\operatorname{sinc}(\pi(\Theta f_s + f_l)) + \operatorname{sinc}(\pi(\Theta f_s - f_l))\right],
\end{aligned} \tag{D.2}$$

and

$$\begin{aligned}
&\frac{e^{-i\phi}}{2}\operatorname{sinc}(\pi(f_s\Theta - f_l + (m-n)f_{\mathrm{PJ}})) + \frac{e^{i\phi}}{2}\operatorname{sinc}(\pi(f_s\Theta + f_l + (m+n)f_{\mathrm{PJ}})) \\
&\qquad = \frac{1}{2}e^{-i\left(\frac{f_s\Theta + m f_{\mathrm{PJ}}}{f_l + n f_{\mathrm{PJ}}}\right)\phi}\Big[\operatorname{sinc}(\pi(f_s\Theta + m f_{\mathrm{PJ}} - f_l - n f_{\mathrm{PJ}})) \\
&\qquad\qquad + \operatorname{sinc}(\pi(f_s\Theta + m f_{\mathrm{PJ}} + f_l + n f_{\mathrm{PJ}}))\Big].
\end{aligned} \tag{D.3}$$